AN ABSTRACT OF THE THESIS OF

<u>Kyozo Ueyoshi</u>   for the degree of   <u>Doctor of Philosophy</u>

in <u>Atmospheric Sciences</u>   presented on <u>1 March 1985</u>

Title: <u>Numerical Simulation of Planetary Boundary-Layer Evolution and</u>

<u>Mesoscale Flow over Irregular Terrain under Daytime Heating Conditions</u>

Redacted for Privacy

Abstract approved:_____

 Prof. James W. Deardorff

The influence of irregular terrain on the evolution of the daytime planetary boundary layer (PBL) and meso-β scale dry circulations is studied using two three-dimensional hydrostatic σ-coordinate models with different approaches for the PBL parameterizations; the 4-layer model uses the mixed-layer (bulk-layer) approach, while the 7-layer model adopts the eddy-diffusivity (multi-layer) approach. Numerical experiments are carried out under the conditions of a dry, sunny summer day with moderate prevailing westerly winds blowing over gently sloping idealized hills in a domain of 150 km on a side. The results from the two models are compared and their performances are evaluated.

The behaviors of the mean PBL depth and inversion strength are analytically described using a simple one-point mixed-layer model. Counterclockwise rotation of the mean PBL winds with time observed in both model results can be explained only when the non-zero momentum flux at the PBL top is taken into account. However, stresses associated with entrainment at the PBL top are not sufficient to pull the cold air out of the valleyes so as to result in breakup of the early morning stable layer, as is suggested in a previous study.

The regions of weak winds that persist in the morning PBL are

attributed largely to the baroclinic effect of horizontal variations of potential temperature θ in the PBL, while the effect of surface drag is quite small in these areas. Significant differences in the flow patterns near the surface in two results suggest the importance of the local pressure gradient force associated with terrain irregularities. The effect of horizontal θ advection is also significant in helping reduce the PBL θ anomalies and promote breakup of the stable layer.

The well-mixed assumption generally applies quite well to the development of the θ profiles, while for momentum it seems valid only during the peak of convective mixing and the eddy-diffusivity approach is probably preferable for a better description of the low-level flows. The fields of the PBL top height obtained using different procedures in the two models are found to correspond fairly well to each other.

Mass-flux convergence associated with terrain irregularities and resulting changes in the wind fields are shown to play a key role in the midday PBL height patterns. The development of the PBL structure as revealed by the θ cross sections obtained from either model corresponds favorably to that indicated by idealized cross sections previously constructed from observed data. The formation of a region of mass-flux convergence and accompanying updrafts near the surface on the leeward side of a mountain, processes which are likely to be important in terrain-induced cloud initiations, seem to be simulated.

Numerical Simulation of Planetary Boundary-Layer Evolution
and Mesoscale Flow over Irregular Terrain
under Daytime Heating Conditions

by

Kyozo Ueyoshi

A THESIS

submitted to

Oregon State University

in partial fulfillment of
the requirements for the
degree of

Doctor of Philosophy

Completed 1 March 1985

Commencement June 1985

APPROVED:

Redacted for Privacy

Professor of Atmospheric Sciences in charge of major

Redacted for Privacy

Chairman of Department of Atmospheric Sciences

Redacted for Privacy

Dean of Graduate School

Date thesis is presented <u>1 March 1895</u>

Typed by Michelle Holcomb and Naomi Zielinski for <u>Kyozo Ueyoshi</u>

ACKNOWLEDGMENTS

I wish to express my gratitude to Drs. James W. Deardorff and Young-June Han for their guidance, patience, and encouragement throughout the course of this research. Without their support of my work this dissertation would never have been completed.

Appreciation is also extended to the other members of my doctral committee, Drs. W.C. Denison, C.A. Paulson, and C.R.N. Rao for reading the thesis and for their helpful criticisms and suggestions.

I would like to thank Dr. W.L. Gates for kindly making available to me the computing facilities at the Climatic Research Institute, Oregon State University. I also gratefully acknowledge free use of the Amdahl computer at the National Aeronautics and Space Administration High Speed Computing Facility (NHSCF).

I am indebted to Messrs. R. Mobley and W. McKie for their indespensable assistance in various aspects of computing and graphics, and particularly for making remote job entry to NHSCF possible. I also wish to thank Dr. D.A. Randall for his continued interest in this research and for sorting out cumbersome remote-access problems with NHSCF.

The final version of this dissertation was expertly typed by Ms. M. Holcomb and Ms. N. Zielinski.

TABLE OF CONTENTS

LIST OF FIGURES

NUMERICAL SIMULATION OF PLANETARY BOUNDARY-LAYER EVOLUTION AND MESOSCALE FLOW OVER IRREGULAR TERRAIN UNDER DAYTIME HEATING CONDITIONS

1. INTRODUCTION

1.1 Statement of Problem

The interactions between the earth's surface and the overlying atmospheric flow occur through the planetary boundary layer (PBL) of variable depth which acts as a sink for momentum and a source for heat and moisture. These interactions ultimately result in redistributions of the surface fluxes through a much deeper depth of overlying atmosphere where they can effect changes in atmospheric features on scales much larger than those of turbulent motions characterizing the PBL (Smith and Carson, 1977). As discussed by Driedonks and Tennekes (1981), a physically realistic treatment of the PBL for incorporation in both long-range (over 2 weeks) and medium-range (3 - 12 days) atmospheric numerical forecasting models is quite important since the interactions between the PBL and the air motion above would affect the climatological mean state as well as synoptic-scale motions (Bhumralkar, 1976; Miyakoda and Sirutis, 1977; Louis, 1979). For short-range predictions (0 - 2 days), on the other hand, it is generally known that processes in the PBL would not greatly influence the large-scale motions. The behavior of phenomena on smaller scales, however, is generally more affected by processes in the PBL associated with the local boundary conditions, and a proper representation of the PBL processes for

incorporation in a forecasting model is again essential for realistic simulations of such features.

Simulations of terrain-induced phenomena on meso-β scales (20-200 km; Orlanski, 1975) present such a case in which horizontal inhomogeneities associated with the local boundary conditions, which include variable terrain, horizontal differential heating and surface fluxes, play a key role. Terrain-induced mesoscale phenomena include sea and land breezes, mountain-valley winds, mountain waves, hydraulic jumps, lake effects, and urban circulations (Pielke, 1981). In study of these mesoscale atmospheric features, understanding the vertical structure of the PBL itself in terms of various meteorological quantities is often as much of interest as examining the mean horizontal variations.

One of the objectives of this research is to evaluate various effects of complex terrain and surface heating on the PBL structure and mesoscale circulations under simple idealized conditions. Specifically, we examine the daytime development of the PBL on the meso-β scale, under the condition of a typical dry summer day with moderate geostrophic forcing superimposed over gently sloping terrain. This study is our initial effort to develop a three-dimensional (3-D) mesoscale model suitable for simulations of a broad range of meso-β scale phenomena on time scales of 0 - 2 days. Our goal here is therefore to better understand first order effects rather than to reproduce specific processes occurring in the interaction of terrain with air flow aloft.

As discussed by Lenschow et al. (1979) and illustrated by a study of Deardorff, Ueyoshi and Han [hereafter referred to as DUH]

(1984), relatively gentle variations of terrain on order of meso-β scales can cause significant local variations in temperature, winds, humidity and depth of the PBL, particularly in the initial stages of development of the daytime convective boundary layer. Lenschow et al. (1979) asserted that these local variations, on the small end of meso-β scale, may be greater in magnitude than daytime synoptic variations on the meso-α scale (200 - 2000 km).

Terrain-induced inhomogeneity, therefore, significantly affects representation of observed surface data and creates great complexity in their use for synoptic analyses and climate studies. Moreover, from a practical point of view, its effect is significant on local diffusion of pollutants, wind-energy generation and agriculture (Warner et al., 1978; Lenschow et al., 1979). On the other hand, the particular importance of an accurate knowledge of the PBL depth in describing the interactions between the boundary layer and the overlying atmosphere in a large-scale model has been emphasized by Suarez et al. (1983).

In order to accomplish the above objective there is a need for a parameterization scheme that is relatively simple but would give an accurate description of the effects of subgrid-scale processes on the PBL features on resolvable scales. In particular, representations of vertical transport of momentum, heat and moisture require a special care in view of their importance in determining the PBL as well as mesoscale flow structures. In a mesoscale model or general circulation model (GCM), however, the resolution of the model grid is often too coarse to resolve processes in the PBL, and the influence of these subgrid-scale processes usually must be retrieved

by relating them to resolvable variables that carry available information.

There are in general two approaches to incorporating the subgrid-scale effects within the PBL into a model. One is to assume certain flux profiles within the PBL and relate the surface fluxes to the calculated variables at the lowest level of the model. In this approach, a representation of bulk properties of the PBL as a whole is needed. Another approach is to resolve the vertical profiles of the fluxes within the PBL explicitly by placing several layers below, say, 800 mb.

The basis for the first approach (the bulk-layer or mixed-layer approach) is that in the developing convectively unstable boundary layer the intense turbulent mixing creates a potential temperature profile virtually independent of height (see Fig. 4.1), while making an assumption of simple profiles of turbulent fluxes within the PBL possible. This "well-mixed" layer is usually capped by a thin inversion, represented by a step discontinuity in the potential temperature profile, and a deep stable free atmosphere above it (Carson, 1973).

The PBL parameterization scheme proposed by Deardorff (1972) for a GCM is an example of the bulk-layer approach. In this scheme, similarity theory is used to obtain the surface fluxes as functions of resolvable variables. A time-dependent height of the PBL, required for estimating the above fluxes, is explicitly predicted. The rate of entrainment at the PBL top is a function of the surface heat and momentum fluxes and the inversion strength.

On the other hand, in the second approach (the multi-layer or

eddy-diffusivity approach) the surface fluxes are generally obtained using similarity theory, while a first-order closure (K-theory) is utilized above the surface layer. A mesoscale model developed by Anthes and Warner (1978) gives an example of this approach. In this model, the parameterization scheme proposed by Busch et al. (1976) was adopted, in which the depth of the PBL needed for the prediction of a time-dependent mixing length is diagnosed using the potential temperature lapse rate.

Recently, a PBL parameterization scheme based on the bulk-layer approach has been developed by Suarez and Arakawa (1979) and Suarez et al. (1983) for a GCM, while a scheme that takes the multi-layer approach has been presented by Louis (1979) for a medium-range fore-casting model. In adopting the bulk-layer approach, Suarez et al. (1983) have argued that in the clear unstable case the well-mixed assumption makes use of a relatively simple scheme sufficient to describe the PBL fluxes without a fine resolution. They also argue that the transition between the turbulent region in the PBL and the overlying atmosphere is even more distinct when the PBL is topped with a stratocumulus deck. In these situations the PBL may be regarded as a distinct and clearly identifiable region in which the description of the turbulent fluxes can be greatly simplified with the use of the well-mixed assumption. When the turbulence is weak and the transition is gradual, the second approach should be more suitable. However, as long as the parameterization can account for the bulk properties of the latter situation, the detailed flux profiles should be of secondary importance as far as large-scale circulations are concerned.

On the other hand, Louis (1979) preferred a detailed PBL representation over a bulk-layer method. He argues that auxiliary time-dependent variables needed in a bulk approach such as the depth of the PBL and temperature discontinuity at the PBL top are rather difficult to be initialized or verified, and might result in incorrect feedbacks in the model. In Louis' scheme, therefore, K-theory is applied to express directly the fluxes above the surface layer, while similarity theory is utilized to obtain the surface fluxes.

The problem of accurately predicting the PBL depth, on the other hand, has been handled in Suarez and Arakawa's (1979) scheme by introducing a modified σ-coordinate in which both the PBL top and the earth's surface are coordinate surfaces. By adopting this coordinate system, as discussed by Suarez et al. (1983), the PBL bulk properties at the PBL top can be directly predicted, thereby reducing uncertainty that might lead to a less accurate representation of the interactions between the PBL and the flow aloft.

One of the major drawbacks on the bulk-type approach is that the assumptions made concerning the character of the PBL below a well-defined top are not always appropriate for the observed boundary layer, although it has an advantage of being economical (ECMWF, 1982). The well-mixed assumption should best apply for potential temperature because of a strong coupling between stratification and convective mixing (Mahrt and Lenschow, 1976). This assumption, however, is less justified for specific humidity since the entrainment of dry air at the PBL top and the generally more moist surface tend to create a gradient. Wind profiles are

least independent of height because of horizontal pressure gradients (Pielke, 1981). Furthermore, turbulence at night is seldom strong enough to maintain the well-mixed assumption, thus requiring a separate treatment of nighttime conditions (Tennekes and Driedonks, 1981). On the other hand, Pielke (1973) chose the multi-layer approach in modeling of the sea breeze because the well-mixed layer capped by an upper stable layer is seldom observed during the summer over south Florida and also because the internal vertical structure of the PBL cannot be resolved, as is necessary in the case of modeling of the sea breeze.

The multi-layer approach that makes use of K-theory, on the other hand, has a shortcoming in that there is no solid physical basis yet for assuming a flux-gradient relationship for all conditions of turbulent transfer within the PBL. Furthermore, there is no sufficient physical basis either for expressing a turbulent transfer coefficient or a mixing length as functions of the variables on resolvable scales.

In principle, with the multi-layer approach an increased number of vertical levels and a higher horizontal resolution, along with the possible use of a higher-order closure parameterization, presumably allow a better representation of subgrid-scale processes within the PBL. In reality, however, the amount of computer resources necessary to implement such a model poses a practical limit.

Considering the physical differences in these two approaches that might significantly alter mesoscale features of our interest, as well as from the viewpoint of economy, it is therefore of great

importance to assess feasibility of adopting one approach over the other in a mesoscale model. As the second objective of this research, we thus develop two types of 3-D models, one with the bulk-layer approach based on Suarez and Arakawa's (1979) scheme and the other with the multi-layer approach based on Louis' (1979) formulation, and examine their performances in conjunction with the first objective described earlier.

1.2 Previous Studies

The bulk-layer approach was first utilized for simulations of terrain-induced mesoscale phenomena by Lavoie (1972) in a single layer model of the PBL. He recognized that under strong wind shear or thermal convection the well-mixed assumption allows the values at a single level to describe the PBL sufficiently. The model consisted of a surface layer, a well-mixed layer capped by an inversion, and a deep relatively stable air aloft. The time-dependent calculations were limited to the mixed-layer variables including its depth, while interactions with the surface and the overlying stable layer were parameterized. Lavoie (1972, 1974) has applied the model successfully to simulate the steady-state structure of snowstorms over the lee shores of Great Lakes and also the air flow over the Hawaiian Islands.

Keyser and Anthes (1977) have modified Lavoie's model in an attempt to produce short-range forecasts of low-level flow patterns. A terrain-following coordinate, parameterizations for entrainment of heat and momentum at the PBL top and convective adjustment were introduced. The model was successful in resolving a

number of transient features in the daytime PBL over the middle Atlantic States with a considerable degree of realism. Raddatz and Khanderkar (1979) also applied Lavoie's model successfully to simulation of upslope enhanced extreme rainfall events over the Canadian western plains.

A version of Keyser and Anthes' model has been used by Han et al. (1982) to study dry mesoscale motions in the well-mixed layer over a domain with hilly terrain of 150 km on a side. They found that for the idealized conditions treated (no horizontal temperature gradients, no surface heating, no entrainment, and no pressure adjustment aloft), the topography quickly induces a steady state flow pattern by means of surface friction. The flow pattern, however, is shown to vary significantly depending on model parameters such as the Rossby and Froude numbers. The above study was extended by DUH (1984) to include the more realistic case of a heated, growing daytime mixed layer containing horizontal variations of potential temperature. The model also included three layers above the mixed layer so that pressure adjustments aloft can be accounted for. The structure of the model is based on Suarez and Arakawa's (1979) work described earlier. The bulk aerodynamic formulation is used for the surface fluxes with constant bulk transfer coefficients. The fluxes at the PBL top are parameterized using the scheme proposed by Deardorff (1973). The depth of the mixed layer is allowed to increase with time through the mechanism of entrainment. The flow patterns found in this study were typically unsteady due particularly to the relaxation of the frictional force as the mixed layer deepened irregularly, and to the

presence of horizontal gradients in potential temperature. The effect of hydrostatic form drag associated with interactions of the mean flow, terrain and horizontal temperature gradients was also found to be significant in determining the flow patterns.

Kaplan et al. (1982) used a bulk-layer parameterization scheme based on a generalized similarity theory (Chang, 1981) in a mesoscale model whose domain covers most of North America with realistic terrain. In this scheme, which is a revision of that proposed by Deardorff (1972), the entrainment rate and the inversion strength were calculated, and the PBL depth was predicted using different formulations for stable and unstable cases. Some of the meteorological variables were calculated by techniques similar to those suggested by Phillips (1974). However, the pressure gradient force was not in a perturbation form, which appeared to cause noise development near the regions of strong terrain gradients. This subject will be further elaborated later.

There exists in the literature a large number of mesoscale models utilizing the multi-layer, eddy-diffusivity approach. Here numerical studies dealing with circulations over irregular terrain will be briefly reviewed.

The 3-D σ-coordinate model developed by Anthes and Warner (1974) covering a 150 x 150 km domain in New Mexico is among the earliest models with realistic bottom topography. They investigated, using a cross-section version, the effects of vertical and horizontal resolutions and variations of the upper surface. Their experiments have shown that when the top pressure surface is 400 mb or less the results are rather similar in the lower

troposphere, and that the effect of the inversion is to perturb the low-level flow to a greater extent than when it is not present.

Mahrer and Pielke (1975) conducted a numerical study of air flow over a mountain using a two-dimensional (2-D) mesoscale model in a terrain-following coordinate system. K-theory was used for the PBL formulation in which the turbulent transfer coefficients were calculated using the method proposed by O'Brien (1970), while the top of the PBL was determined using Deardorff's (1974) scheme. The model was later generalized by Mahrer and Pielke (1976) to a 3-D model to study the influence of a local heat source on the large-scale prevailing flow. Mahrer and Pielke (1977a) further included in this model the parameterization of the surface heat budget and radiative fluxes. The integrations were performed for the area with smoothed topography utilized by Anthes and Warner (1974). Under the conditions of a dry, summer afternoon with a prevailing westerly wind of 5 ms^{-1}, the development of strong horizontal convergence zones downwind of local terrain maxima corresponded well to observations.

The effect of terrain slope on solar and infrared radiation was also included in this model since a study using a 2-D version (Mahrer and Pielke, 1977b) showed that even small slopes could influence mesoscale circulations significantly. The results of the 3-D model also indicated a strong correlation of the simulated surface temperature with the terrain elevation and aspect. Clark and Gall (1982) also incorporated the sun's zenith angle and the effect of sloping terrain in a similar manner in a 3-D model in a terrain-following coordinate system covering a 50 x 50 km domain.

However, their experiments showed that the introduction of terrain
slope in the sun's zenith angle calculations did not cause
significant changes in the low-level vertical velocity field despite
the relatively steep slope angle present in the smoothed real
topography.

Anthes and Warner (1978) developed a 3-D σ-coordinate model in
which both the eddy-diffusivity approach presented by Busch et al.
(1976) and the bulk-layer approach based on Deardorff (1972) were
implemented as two options. In the bulk approach, the lowest layer
was assumed to comprise the PBL so that its depth was approximately
constant. Experiments with a 2-D version across the Appalachian
terrain showed that a large-amplitude internal oscillation in the
PBL associated with a geostrophic initialization can be greatly
reduced if surface friction is included in the initialization.

Warner et al. (1978) conducted an experiment using real
synoptic data in the above 3-D bulk model to successfully produce a
12 h forecast covering the eastern United States. An experiment
using the model with the multi-layer approach was performed to
obtain a qualitative estimate of the perturbations that can be
generated by variable terrain and surface heating on upper-end
meso-α scales (~2000 km). Surprisingly large deviations in low-
level wind direction and amplitude were observed in the regions of
relatively gentle terrain slopes, under adiabatic, inviscid and
low-wind conditions. They stressed the significance of light-wind
regimes on the mesoscale. For example, stagnation of an air mass
with calm winds poses the potential for the development of high
air-pollution concentrations due to low ventilation. Also under

these conditions, the effects of orographic and thermal forcing can be more easily identified. The significance of an accurate estimate of the PBL depth from a practical viewpoint was demonstrated using a ventilation factor (the product of the PBL depth and mean wind).

Channeling effects were observed in Warner et al.'s experiments using a 30 x 30 km domain with idealized smooth hills under an inviscid and stable stratified condition. The stagnation of the flow observed upwind and downwind of an isolated model mountain was attributed to an effect of pressure forces induced by the mountain rather than a surface-drag effect since the model was inviscid. Channeling of the low-level flow along lower elevations was also seen in simulations of the sea breeze over the southern British Isles performed by Carpenter (1979), who used a non-hydrostatic mesoscale model, and in experiments by Allard and Derome (1974) in the valleys in eastern Canada.

In order to attain an increased resolution near the surface and still retain the advantages of a uniform grid, Nickerson (1979) adopted a transformed σ-coordinate based on Kalnay de Rivas' (1972) proposal. In his model, the diffusion coefficients were computed using O'Brien's (1970) profile in which the PBL depth was set equal to 1 km. The model was used for simulations of air flow and terrain-induced cloud cover over the islands of Hawaii.

A turbulent-closure model based on a set of second-moment turbulent equations was used by Yamada (1978) for simulations of mesoscale flow over Gaussian mountains in a domain of 600 km on a side. However, Pielke (1981) argued that higher-order closure representations have not improved simulations of the resolvable

variables in the PBL over those obtained using the best first-order
representations.

Anthes et al. (1980) performed a comparison of the mean PBL
structure as predicted by the mixed-layer model of Keyser and Anthes
(1977) with the multi-level model of Anthes and Warner (1978).
Experiments with cross-section versions of the models revealed that
when horizontal inhomogeneities associated with differential heating
over complex terrain are introduced, the mixed-layer model in
general appears to have distinct limitations. They concluded that
for these conditions, a multi-level model seems to be essential to
the realistic prediction of flow within the PBL, since adjustments
in the mass-wind field above the PBL produce important effects on
the pressure gradient within the PBL.

1.3 Brief Description of the Models

In order to contrast the present research with the previous
studies, it may be useful to describe briefly our basic models
here. A version of the 3-D hydrostatic model developed for a
previous study of terrain-induced mesoscale motions (DUH, 1984)
represents the model utilizing the bulk-layer approach. In this
model, the lowest model layer comprises an assumed PBL or well-mixed
layer of variable depth. As mentioned earlier, this is accomplished
by introducing a modified σ-coordinate. Above the PBL are three
additional layers of uniform thickness in σ extending up to the
pressure 400 mb (see Fig. 2.1a). The horizontal domain is square
with 150 km on a side. The grid interval is 10 km in both x- and
y-directions. The cyclic boundary conditions are employed on both

west-east and north-south boundaries. An idealized irregular model terrain embodying cyclic lateral boundary conditions is used (Figs. 5.1 and 5.2). Hereafter this model will be referred to as the "M4" model.

In the second model utilizing the multi-layer approach proposed by Louis (1979), a commonly-used version of the σ-coordinate is used. The model atmosphere is divided into 7 layers between the surface and the top of the atmosphere placed at 400 mb (see Fig. 2.1b). The spacing of the vertical grid is uneven so that the lowest portion of the atmosphere corresponding to the PBL can be resolved into several layers. The domain size, the grid increment, lateral boundary conditions and the variable topography are identical to those in the above M4 model. Hereafter this model will be referred to as the "L7" model.

Major features implemented in both the M4 and L7 models are:

(i)   the potential enstrophy and energy conserving finite-difference scheme developed by Arakawa and Lamb (1981);

(ii)   the adiabatic reference atmosphere proposed by Phillips (1974) to reduce the truncation errors in pressure gradient force terms;

(iii)   the bulk transfer coefficients based on the formulation of Louis (1979) that requires no special treatment for the free convection regime and also is appropriate for very stable conditions; and

(iv)   the energy balance equation which utilizes a linear

relation between the soil heat flux at the surface and

the net radiation deduced from field experiments.

The descriptions of these features and the models will be given in

more detail in the following chapters.

In the next chapter, basic governing equations for both models

are described. The parameterization scheme of the PBL is presented

in Chapter 3. The behaviors of the bulk transfer coefficients

adopted are tested and evaluated. In Chapter 4, the finite-

difference schemes are explained in association with the PBL

parameterization schemes. The potential enstrophy and energy

conserving scheme is tested and its performance is compared against

that of an energy conserving scheme. The effectiveness of the

reference atmosphere implemented in our models is also checked.

Boundary and initial conditions are described in Chapter 5. In

Chapter 6, the results of numerical experiments are presented. The

experiments are performed under the condition of a typical dry

summer day with moderate prevailing winds over gentle hills in

mid-latitudes. The time evolutions of meteorological variables and

quantities of our major interest are evaluated in the forms of

domain averages, horizontal patterns and vertical cross sections, as

well as using simple models. Interrelationships among these

quantities are examined. Also in this chapter, the results from the

M4 and L7 models are compared. Summary and conclusions of this

research are presented in Chapter 7.

2. BASIC GOVERNING EQUATIONS

2.1 <u>Outline</u>

The basic governing equations are described in this chapter in
the forms which are appropriate for the difference equations to be
used in our numerical modeling. The finite-difference schemes
adopted for the vertical differencing for the M4 and L7 models, as
they will be described in Chapter 4, are those derived by Suarez and
Arakawa (1979) and Arakawa and Suarez (1983), respectively, both of
which preserve integral properties of the continuous equations
listed below:

(A) the pressure gradient force generates no circulation of
vertically integrated momentum along a contour of the
surface topography (conservation of circulation under
inviscid conditions);

(B) the energy conversion term has the same form in both the
thermodynamic and the kinetic energy equation (total
energy conservation under adiabatic processes); and

(C) the global mass integral of the potential temperature is
conserved under adiabatic conditions (conservation of
total enthalphy under adiabatic processes).

The horizontal scheme that will be utilized in our modeling
(Arakawa and Lamb, 1981) is consistent with these vertical
finite-difference schemes in that in deriving the scheme an emphasis
has been placed on the conservation of integral constraints of the
continuous equations such as potential enstrophy and total energy.
Since more detailed derivations of equations and constraints can be

found in Arakawa and Lamb (1977 and 1981), Suarez and Arakawa
(1979), and Arakawa and Suarez (1983), we present in this chapter
only the basic equations relevant to our modeling in the forms which
are consistent with the above-mentioned finite-difference schemes to
be utilized.

In general the equations appropriate for the atmospheric
motions above the PBL or the mixed layer in the M4 model also apply
to the entire atmosphere of the L7 model. The equations for the M4
model only differ from those for the L7 model in that the pressure
at the PBL top, p_B, is added as a prognostic variable and the form
of the pressure gradient term in the PBL must be modified. Also $\pi\dot\sigma$
which will be defined later in this chapter has a slightly different
form. Therefore repetition of equations will be kept to the minimum
when there is no risk of confusion. The same applies to the
description of the finite-difference scheme in Chapter 4.

2.2 Vertical Coordinate

a. The M4 model. A modified version of the σ-coordinate
system originally proposed by Phillips (1957) is used for the
vertical coordinate in the M4 model.

We define

$$
\sigma = \begin{cases}
\dfrac{p-p_T}{p_B-p_T} & \text{for } p_T \le p \le p_B \qquad (2.1a) \\[3ex]
\dfrac{p-p_B}{p_S-p_B} + 1 & \text{for } p_B \le p \le p_S \qquad (2.1b)
\end{cases}
$$

where p is the pressure, p_T is the constant pressure at the top of

the model atmosphere, p_B is the pressure at the PBL top, p_S is the pressure at the earth's surface (see Fig. 2.1).

With the following definition of

$$\pi = \begin{cases} \pi_L \equiv p_B - p_T & \text{for } 0 \le \sigma < 1 & (2.2a) \\ \\ \pi_M \equiv p_S - p_B & \text{for } 1 < \sigma \le 2 & (2.2b) \end{cases}$$

we may write p as:

$$p = \begin{cases} p_T + \sigma\pi_L & \text{for } 0 \le \sigma < 1 & (2.3a) \\ \\ p_B + (\sigma-1)\pi_M & \text{for } 1 \le \sigma \le 2 & (2.3b) \end{cases}$$

Taking the differential in the vertical under constant time we obtain from Eqs. (2.3a) and (2.3b):

$$dp = \pi d\sigma \qquad (2.4)$$

for all σ except at $\sigma = 1$ where π is not uniquely defined. The material time derivative in the σ-coordinate is

$$\frac{D}{Dt} = \left(\frac{\partial}{\partial t} + \underset{\sim}{V}\right)_\sigma + \dot{\sigma}\frac{\partial}{\partial\sigma} \qquad (2.5)$$

where $\underset{\sim}{V}$ is the horizontal velocity and $\dot{\sigma} \equiv D\sigma/Dt$ is the σ-coordinate vertical velocity. The vertical pressure velocity ω is then obtained from (2.3a), (2.3b), and (2.5):

$$\omega = \begin{cases} \pi\dot{\sigma} + \sigma\left(\frac{\partial}{\partial t} + \underset{\sim}{V} \cdot \nabla\right)\pi & \text{for } 0 \le \sigma < 1 \quad (2.6a) \\ \\ \pi\dot{\sigma} + (\sigma-1)\left(\frac{\partial}{\partial t} + \underset{\sim}{V} \cdot \nabla\right)\pi + \left(\frac{\partial}{\partial t} + \underset{\sim}{V} \cdot \nabla\right)p_B & \text{for } 1 < \sigma \le 2 \quad (2.6b) \end{cases}$$

The relationship between gradients ∇_p and ∇_σ is given by

$$\nabla_p = \nabla_\sigma + \nabla_p \sigma \frac{\partial}{\partial\sigma} \qquad (2.7)$$
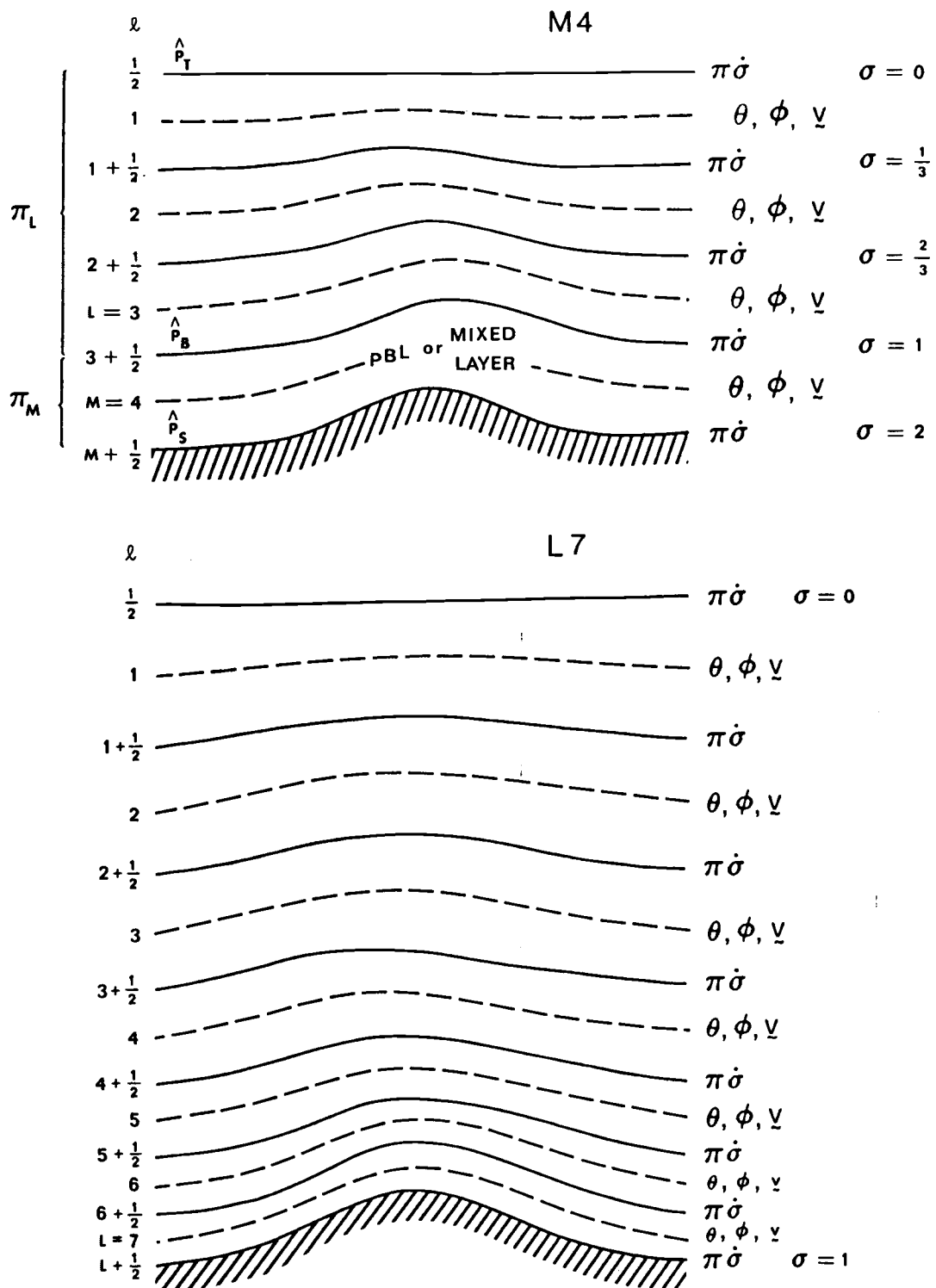
Fig. 2.1. The vertical grid structures of the M4 (top) and L7 (bottom) models, showing distributions of the prognostic variables. Solid lines indicate "half levels," while dashed lines show "full levels." See text in Sec. 4.1.1.

Operating ∇_p on (2.3a) and (2.3b) and substituting the results in (2.7) we find

$$
\nabla_p = \begin{cases}
\nabla_\sigma - \dfrac{\sigma}{\pi}\,\nabla\pi\,\dfrac{\partial}{\partial\sigma} & \text{for } 0 \le \sigma < 1 \quad (2.8a) \\[4mm]
\nabla_\sigma - \dfrac{1}{\pi}\,[(\sigma-1)\nabla\pi + \nabla p_B]\,\dfrac{\partial}{\partial\sigma} & \text{for } 1 < \sigma \le 2 \quad (2.8b)
\end{cases}
$$

b. <u>The L7 model</u>. The σ-coordinate used in the L7 model is obtained by replacing p_B by p_S in (2.1a), (2.2a) and (2.3a):

$$
\sigma = \frac{p-p_T}{p_S-p_T} \qquad \text{for } p_T \le p \le p_S \qquad (2.9)
$$

$$
\pi = p_S - p_T \qquad \text{for } 0 \le \sigma \le 1 \qquad (2.10)
$$

$$
p = p_T + \sigma\pi \qquad \text{for } 0 \le \sigma \le 1 \qquad (2.11)
$$

Similarly, we obtain from (2.6a) and (2.8a):

$$
\omega = \pi\dot\sigma + \sigma(\frac{\partial}{\partial t} + \underset{\sim}{V} \cdot \nabla)\pi \qquad \text{for } 0 \le \sigma \le 1 \qquad (2.12)
$$

$$
\nabla_p = \nabla_\sigma - \frac{\sigma}{\pi}\nabla\pi\frac{\partial}{\partial\sigma} \qquad \text{for } 0 \le \sigma \le 1 \qquad (2.13)
$$

Eqs. (2.4) and (2.5) are also valid in the L7 model.

2.3 Continuity Equation

a. <u>The M4 model</u>. The continuity equation in the p-coordinate $\nabla_p \cdot \underset{\sim}{V} + \partial\omega/\partial p = 0$ can be expressed with the use of (2.4), (2.6) and (2.8) as

$$
\frac{\partial\pi}{\partial t} + \nabla_\sigma \cdot (\pi\underset{\sim}{V}) + \frac{\partial(\pi\dot\sigma)}{\partial\sigma} = 0 \qquad (2.14)
$$

It is assumed that the top of the atmosphere ($\sigma = 0$) and the ground surface ($\sigma = \sigma_S = 2$) are material surfaces so that

$$(\pi\dot{\sigma})_{\sigma=0} = 0 \qquad\qquad (2.15)$$

$$(\pi\dot{\sigma})_{\sigma=\sigma_S=2} = 0 \qquad\qquad (2.16)$$

At the PBL top where $\sigma = 1$, $(\pi\dot{\sigma})_{\sigma=1}$ represents the rate at which mass is added to the PBL from the free atmosphere above. Thus we may write

$$(\pi\dot{\sigma})_{\sigma=1} = \rho_B g w_e \qquad\qquad (2.17)$$

where g is the acceleration of gravity, $\rho_B w_e$ is the entrainment rate of mass into the PBL, ρ_B is the density, and subscript B denotes a quantity at the PBL top. Since we consider only the boundary layer on a typical clear, dry day and no cloud moisture or boundary-layer moisture is modeled, no upward mass flux into cumulus clouds through the PBL top is treated here. Thus, integrating (2.14) in σ by making use of (2.15)-(2.17) yields the equations for p_S, p_B, and $\pi\dot{\sigma}$:

$$\frac{\partial p_S}{\partial t} = -\nabla \cdot \int_0^{\sigma_S=2} (\pi\underline{V})\, d\sigma \qquad\qquad (2.18)$$

$$\frac{\partial p_B}{\partial t} = -\nabla \cdot \int_0^1 (\pi\underline{V})\, d\sigma - \rho_B g w_e \qquad\qquad (2.19)$$

$$\pi\dot{\sigma} = -\nabla \cdot \int_0^\sigma (\pi\underline{V})\, d\sigma - \sigma \frac{\partial p_B}{\partial t} \qquad\qquad (2.20)$$

and thus we have

$$\frac{\partial}{\partial t}(p_S - p_B) = -\nabla \cdot \int_1^{\sigma_S=2} (\pi\underline{V})\, d\sigma + \rho_B g w_e \qquad\qquad (2.20a)$$

b. <u>The L7 model</u>. Eq. (2.14) is also valid in the L7 model.
The boundary conditions (2.15) and (2.16), and the equation for p_S
are applicable to the L7 model if we set $\sigma = \sigma_S = 1$:

$$(\pi\dot\sigma)_{\sigma=0} = 0$$

$$(\pi\dot\sigma)_{\sigma=\sigma_S=1} = 0 \tag{2.21}$$

$$\frac{\partial p_S}{\partial t} = -\nabla \cdot \int_0^\sigma (\pi\underset{\sim}{V})d\sigma \tag{2.22}$$

The equation for $\pi\dot\sigma$ is now written as

$$\pi\dot\sigma = -\nabla \cdot \int_0^{\sigma_S=1}(\pi\underset{\sim}{V})d\sigma - \sigma\frac{\partial p_S}{\partial t} \qquad \text{for } 0 \le \sigma \le 1 \tag{2.23}$$

Since the PBL top is not a σ-coordinate surface Eqs. (2.17) and
(2.19) are not used in the L7 model.

2.4 Equation of State

It is assumed that the model atmosphere is an ideal gas so that
the equation of state takes the form $\alpha = RT/p$, where α is the
specific volume, T is the temperature, and R is the gas constant for
which the value for dry air is used in our models. The use of Eq.
(2.4) and the potential temperature defined by $\theta = T/P$ in the above
expression for α gives

$$\alpha = c_p \theta \frac{\partial P}{\partial p} \tag{2.24}$$

where

$$P \equiv (\frac{p}{p_{00}})^\kappa \tag{2.25}$$

is the Exner pressure, p_{00} is a reference pressure, $\kappa = R/c_p$, and
c_p is the specific heat at constant pressure.

2.5 Hydrostatic Equation

The hydrostatic equation $d\phi = -\alpha dp$ can be redefined after application of (2.4) as

$$\frac{\partial \phi}{\partial \sigma} = -\pi d \qquad (2.26)$$

or using (2.24) we can write

$$d\phi = -c_p \theta \, dP \qquad (2.27)$$

where ϕ is the geopotential.

2.6 First Law of Thermodynamics

The first law of thermodynamics takes the form in terms of the potential temperature:

$$\left(\frac{\partial}{\partial t} + \underset{\sim}{V} \cdot \nabla\right)_\sigma \theta + \dot\sigma \frac{\partial \theta}{\partial \sigma} = \frac{1}{\pi} \frac{g}{c_p} \frac{\partial H}{\partial \sigma} \qquad (2.28)$$

where H is the sensible heat flux due to the subgrid scale turbulent motion, the form of which will be specified later. The flux form of (2.28) can be obtained by making use of (2.14):

$$\left(\frac{\partial}{\partial t}\right)_\sigma (\pi\theta) + \nabla_\sigma \cdot (\pi\underset{\sim}{V}\theta) + \frac{\partial}{\partial \sigma} (\pi\dot\sigma\theta) = \frac{g}{c_p} \frac{\partial H}{\partial \sigma} \qquad (2.29)$$

2.7 Momentum Equation

a. The M4 model. The horizontal component of the momentum equation in vector form may be written

$$\frac{D\underset{\sim}{V}}{Dt} + f\underset{\sim}{k} \times (\underset{\sim}{V} - \underset{\sim}{V}_g) = -\nabla_p \phi + \frac{g}{\pi} \frac{\partial \underset{\sim}{\tau}}{\partial \sigma} \qquad (2.30)$$

where $\underset{\sim}{V}_g$ is the geostrophic wind, f is the Coriolis parameter, $\underset{\sim}{k}$ is the vertical unit vector, and $\underset{\sim}{\tau}$ is the flux of momentum due to the sub-grid scale turbulent motion whose form will be specified

later. The horizontal finite-difference scheme that will be used in our modeling (Arakawa and Lamb, 1981) requires (2.30) written in vector invariant form:

$$\left(\frac{\partial}{\partial t}\right)_\sigma \underset{\sim}{V} + \dot\sigma \frac{\partial \underset{\sim}{V}}{\partial \sigma} + q\underset{\sim}{k} \times (\pi \underset{\sim}{V}) + \underset{\sigma}{\nabla}(1/2\ \underset{\sim}{V}^2) =$$
$$-\nabla_p \phi + f\underset{\sim}{k} \times \underset{\sim g}{V} + \frac{g}{\pi}\frac{\partial \underset{\sim}{\tau}}{\partial \sigma} \tag{2.31}$$

where $q \equiv (f+\zeta)/\pi$, and $\zeta \equiv \underset{\sim}{k} \cdot \nabla_\sigma \times \underset{\sim}{V}$ is the relative vorticity. Here Eq. (2.5) has been used in place of D/Dt.

Applying (2.8a) to ϕ and using (2.26) the pressure gradient force can be expressed as

$$-\nabla_p \phi = -\nabla_\sigma \phi + \frac{\sigma}{\pi}\left(\frac{\partial \phi}{\partial \sigma}\right)\nabla\pi \tag{2.32}$$

$$= -\nabla_\sigma \phi - \sigma\alpha\nabla\pi \qquad \text{for } 0 \leq \sigma < 1 \tag{2.33}$$

Since P is a function of π only for $0 \leq \sigma < 1$, we may write Eq. (2.24) as

$$\alpha = c_p \frac{\theta}{\sigma}\left(\frac{\partial P}{\partial \pi}\right)_\sigma \tag{2.34}$$

Thus we obtain from (2.33)

$$-\nabla_p \phi = -\nabla_\sigma \phi - c_p \theta\left(\frac{\partial P}{\partial \pi}\right)_\sigma \nabla\pi \qquad \text{for } 0 \leq \sigma < 1 \tag{2.35}$$

In the PBL $-\nabla_p \phi$ takes the form by the use of (2.8b):

$$-\nabla_p \phi = -\nabla_\sigma \phi - \frac{1}{\pi}[\phi - \frac{\partial((\sigma-1)\phi)}{\partial\sigma}\nabla\pi - \frac{\partial\phi}{\partial\sigma}\nabla p_B] \tag{2.36}$$

Here we have used the identity $(\sigma-1)\ \partial\phi/\partial\sigma = (\partial/\partial\sigma)[(\sigma-1)\phi] - \phi$.

b. <u>The L7 model</u>. Eqs. (2.30)-(2.31) are also valid in the L7 model. For the pressure gradient force Eqs. (2.32)-(2.35) can be used with $0 \leq \sigma \leq 1$.

3. PARAMETERIZATION OF THE PLANETARY BOUNDARY LAYER

3.1 Determination of Turbulent Fluxes

The parameterization scheme for the turbulent surface layer is based on the Monin-Obukhov (1954) similarity hypothesis, which has been widely accepted as a basis for relating the mean vertical gradients of wind speed and temperature in the surface layer to the corresponding surface turbulent fluxes (Deardorff, 1972; Pielke, 1973; Busch et al., 1976; Anthes and Warner, 1978) and is well supported by observational studies (Arya and Sundrarajan, 1976; Businger et al., 1971; Dyer and Hicks, 1970; Hicks, 1976; Garrett, 1978). The Monin-Obukhov similarity theory predicts that the non-dimensional wind speed and potential temperature are universal functions ϕ_M and ϕ_H of the stability parameter z/L:

$$\frac{kz}{u_*} \frac{\partial u(z)}{\partial z} = \phi_M\left(\frac{z}{L}\right) \tag{3.1}$$

$$\frac{kz}{\theta_*} \frac{\partial \theta(z)}{\partial z} = \phi_H\left(\frac{z}{L}\right) \tag{3.2}$$

where

$$L \equiv \frac{\bar{\theta}}{k} \frac{u_*^2}{g\theta_*} \tag{3.3}$$

is the Monin-Obukhov length, $U(z)$ and $\theta(z)$ are the mean wind speed and the potential temperature at the height z, respectively, $\bar{\theta}$ is a mean potential temperature in the surface layer, and k is the von Karman constant. The friction velocity u_* and the scaling temperature θ_* are defined in terms of the mean vertical surface eddy fluxes of momentum and sensible heat:

$$u_*^2 = -(\overline{u'w'})_s \qquad\qquad (3.4)$$

$$u_*\theta_* = -(\overline{w'\theta'})_s \qquad\qquad (3.5)$$

where the overbar denotes time average, the prime the deviation from the average, and the subscript s indicates the value at the surface. The forms of ϕ_M and ϕ_H are generally determined empirically from the field experiments.

3.1.1 Bulk Transfer Coefficients

We use the bulk aerodynamic formulation (Deardorff, 1968) to relate the mean vertical turbulent fluxes of momentum and sensible heat across the surface, τ/ρ and $H/\rho c_p$, to values of the mean variables, U and θ, in the surface layer which are explicitly represented in the numerical model:

$$\frac{\tau}{\rho} \equiv (\overline{u'w'})_s = -C_D U^2(z) \qquad\qquad (3.6)$$

$$\frac{H}{\rho c_p} \equiv (\overline{w'\theta'})_s = -C_H U(z)[\theta(z) - \theta_s] \qquad\qquad (3.7)$$

where C_D and C_H are the bulk transfer coefficients for momentum and sensible heat, respectively. It is noted that $(\overline{u'w'})_s$ is oriented along the wind direction at height z. Although (3.6) and (3.7) give no more than mathematical definitions of C_D and C_H, they are in general functions of height, stability and surface roughness, and the Monin-Obukhov similarity theory described earlier is used here to estimate C_D and C_H as functions of the model variables and parameters.

Combining Eqs. (3.4) with (3.6), and (3.5) with (3.7) gives

$$C_D = \frac{u_*^2}{U^2(z)} \tag{3.8}$$

$$C_H = \frac{u_* \theta_*}{U(z)[\theta(z) - \theta_s]} \tag{3.9}$$

Integration of (3.1) and (3.2) from the surface roughness height z_0 to a measurement height z gives

$$\frac{k}{u_*} U(z) = \int_{\zeta_0}^{\zeta} \frac{\phi_M(\zeta')}{\zeta'} d\zeta' \equiv \Phi_M(\zeta, \zeta_0) \tag{3.10}$$

$$\frac{k}{\theta_*}[\theta(z) - \theta_s] = \int_{\zeta_0}^{\zeta} \frac{\phi_H(\zeta')}{\zeta'} d\zeta' \equiv \Phi_H(\zeta, \zeta_0) \tag{3.11}$$

where $\zeta = z/L$ is the stability parameter and $\zeta_0 = z_0/L$. Therefore, from (3.8)-(3.11) the bulk transfer coefficients C_D and C_H are specified in terms of Φ_M and Φ_H:

$$C_D = \frac{k^2}{\Phi_M^2(\zeta, \zeta_0)} \tag{3.12}$$

and

$$C_H = \frac{k^2}{\Phi_M(\zeta, \zeta_0) \Phi_H(\zeta, \zeta_0)} \tag{3.13}$$

However, since our objective is to express C_D and C_H directly as functions of the known model variables U and θ, we need to seek an alternative way to specify them. If we define the bulk Richardson number, Ri_B, for the layer from the surface to height z as

$$Ri_B = \frac{g}{\bar{\theta}} \frac{z\Delta\theta}{U^2(z)} \tag{3.14}$$

where $\Delta\theta \equiv \theta(z) - \theta_s$, then ζ can be written by using (3.3), (3.10) and (3.11) as

$$\zeta = \alpha Ri_B \tag{3.15}$$

where

$$\alpha \equiv \frac{\Phi_M^2(\zeta,\zeta_0)}{\Phi_H(\zeta,\zeta_0)} \tag{3.16}$$

Substitution of (3.15) for ζ in (3.16) formally gives

$$\alpha = \frac{\Phi_M^2(\alpha Ri_B, \alpha Ri_B z_0/z)}{\Phi_H(\alpha Ri_B, \alpha Ri_B z_0/z)}$$

$$= (\alpha, Ri_B, z_0/z) \tag{3.17}$$

Therefore, for given z and z_0 we can find α by numerical iterations from (3.17), and hence ζ from (3.15). Finally, C_D and C_H can be obtained from (3.12) and (3.13) as functions of Ri_B.

3.1.2 Analytical Formulation of Bulk Transfer Coefficients

There are numerous formulae for ϕ_M and ϕ_H that have been proposed in the literature, and an authoritative review of major universal functions is given by Yaglom (1977). On the other hand, Dyer (1974) reviewed flux-profile relationships based on observational studies and concluded that those of Dyer and Hicks (1970) offer the most convincing flux profile description, while Carson and Richards (1978) examined the universal functions for stable conditions proposed by several investigators and argued that the formulation of Hicks (1976) is that best suited to the numerical modeling of fluxes in stable surface-layer conditions.

Since numerical solution of (3.17) by iterations is a rather time consuming process in a numerical model, it is desirable to seek

simple analytical or diagnostic expressions for C_D and C_H to replace (3.12) and (3.13) and attempt to explicitly describe the turbulent fluxes in terms of known quantities. Based on the formulation derived by Businger et al. (1971), Louis (1979) has proposed such a method that improves computational efficiencies, which we have adopted here in our modeling as presented below.

Businger et al. (1971) derived the following empirical formulae for ϕ_M and ϕ_H by analyzing the surface-layer wind and temperature profiles from the Kansas experiment:

For stable conditions ($\zeta > 0$)

$$\phi_M = 1 + \beta\zeta \qquad (3.18)$$

$$\phi_H = r + \beta\zeta \qquad (3.19)$$

while for unstable conditions ($\zeta < 0$)

$$\phi_M = (1-\gamma_M\zeta)^{-1/4} \qquad (3.20)$$

$$\phi_H = r(1-\gamma_H\zeta)^{-1/2} \qquad (3.21)$$

where constants are $r = 0.74$, $\beta = 4.7$, $\gamma_M = 15$ and $\gamma_H = 9$. On the other hand, following Paulson (1970) and Baker and Baxter (1975), Eqs. (3.10) and (3.11) can be written

$$\Phi_M(\zeta,\zeta_0) = \ln(\frac{z}{z_0}) - \psi_M(\zeta) + \psi_M(\zeta_0) \qquad (3.22)$$

$$\Phi_H(\zeta,\zeta_0) = \ln(\frac{z}{z_0}) - \psi_H(\zeta) + \psi_H(\zeta_0) \qquad (3.23)$$

With the use of (3.18)-(3.21) functions ψ_M and ψ_H for stable conditions are expressed as

$$\psi_M(\zeta) = -\beta\zeta \qquad (3.24)$$

$$\psi_H(\zeta) = -\frac{\beta}{r}\zeta \tag{3.25}$$

and for unstable conditions we have

$$\psi_M(\zeta) = \ln[(\frac{1+\xi^2}{2})(\frac{1+\xi}{2})^2] - 2\tan^{-1}\xi + \frac{\pi}{2} \tag{3.26}$$

$$\psi_H(\zeta) = 2\ln(\frac{1+\eta}{2}) \tag{3.27}$$

where $\xi = (1-\gamma_M\zeta)^{1/4}$ and $\eta = (1-\gamma_H\zeta)^{1/2}$. Substituting (3.22) and (3.23) for ϕ_M and ϕ_H in (3.12) and (3.13) and using (3.15)-(3.17), we can formally write

$$C_D = c^2 f_M(Ri_B, z/z_0) \tag{3.28}$$

$$C_H = \frac{c^2}{r} f_H(Ri_B, z/z_0) \tag{3.29}$$

where $c^2 = [k/\ln(z/z_0)]^2$ is the transfer coefficient under neutral conditions.

By using (3.18)-(3.21) Louis (1979) has computed the values of $c^2 f_M$ and $c^2 f_H/r$ numerically as functions of Ri_B for various values of z/z_0 as a parameter. If simple analytical expressions can be found to fit these values of the computed transfer coefficients, the need to do iterative computation at every time step of the integration could be avoided.

For unstable conditions ($Ri_B < 0$) we require that there must be a finite heat flux in the free convection limit ($U \to 0$). For near-neutral conditions ($Ri_B \simeq 0$), the behavior of f_M and f_H depends on the slope of the flux-profile relationship near neutrality. With these constraints Louis (1979) and Louis et al. (1982) have found that in unstable conditions the following

analytical formulae fit reasonably well the computed curves:

$$f_M = 1 - \frac{2bRi_B}{1+3abc^2(z/z_0)^{1/2}|Ri_B|^{1/2}} \qquad (3.30)$$

$$f_H = 1 - \frac{3bRi_B}{1+3abc^2(z/z_0)^{1/2}|Ri_B|^{1/2}} \qquad (3.31)$$

where $a = b = 5$.

In the case of stable conditions ($Ri_B > 0$), ζ can be expressed as an explicit function of Ri_B by using (3.15), (3.16) and (3.22)-(3.25) (Baker and Baxter, 1975). With Businger et al.'s (1971) formulation for ϕ_M and ϕ_H, C_D and C_H decrease monotonically as Ri_B (> 0) increases and vanish at a critical value of $Ri_B \simeq 0.21$. However, Louis (1979) reported that the use of the original Businger formulation or its simpler approximate form in the stable case would produce physically unrealistic results: once Ri_B exceeds its critical value of ~0.21, the ground becomes energetically disconnected from the model atmosphere and starts cooling by radiation at a rate faster than observations actually indicate. At the same time the model atmosphere would not cool as fast as it would in the real atmosphere due to the lack of sensible heat directed downward into the ground. It is, however, unlikely that the mean flux over a grid box which covers an extensive area of 100 km^2 in our numerical model or up to 10^5 km^2 in some GCMs would be zero even in the most stable conditions (Carson and Richards, 1978). In fact, observational evidence suggests that intermittent turbulence exists even in the situations in which Ri_B exceeds its critical value (Kondo et al., 1978). In numerical modeling, therefore, allowing small but finite fluxes would be more acceptable

than the vanishing of fluxes beyond a very small value of Ri_B.

By taking these points into consideration the following forms of f_M and f_H for stable conditions have been proposed by Louis (1979) and Louis et al. (1982) that would give more realistic representations of turbulent fluxes under stable conditions:

$$f_M = \frac{1}{1 + 2bRi_B(1 + d \cdot Ri_B)^{-1/2}} \qquad (3.32)$$

$$f_H = \frac{1}{1 + 3bRi_B(1 + d \cdot Ri_B)^{1/2}} \qquad (3.33)$$

where $b = d = 5$. Further details of their derivations can be found in the references mentioned above.

3.1.3 Derived Bulk Transfer Coefficients

Once the values of $U(z)$, $\Delta\theta$, z and z_0 are specified, Ri_B can be obtained from (3.14). Then C_D and C_H can be found from (3.28) and (3.29) with the use of (3.30)-(3.33) as functions of Ri_B.

The derived curves for C_D and C_H as function of Ri_B for $z/z_0 = 111$, 500, and 5000 are given in Fig. 3.1. Here, we take $g/\bar{\theta} = 0.033$ ms^{-2}K^{-1} following Carson and Richards (1978). For the purpose of comparison, those obtained using Businger et al.'s (1971) universal functions by means of numerical iterations are also plotted. It is seen that with the Businger formulation the transfer coefficients in stable conditions decrease very rapidly from its neutral value $c^2 = [k/\ln(z/z_0)]^2$ as Ri_B increases and vanish at the critical Richardson number $Ri_{BC} \approx 0.21$. Here we used the von
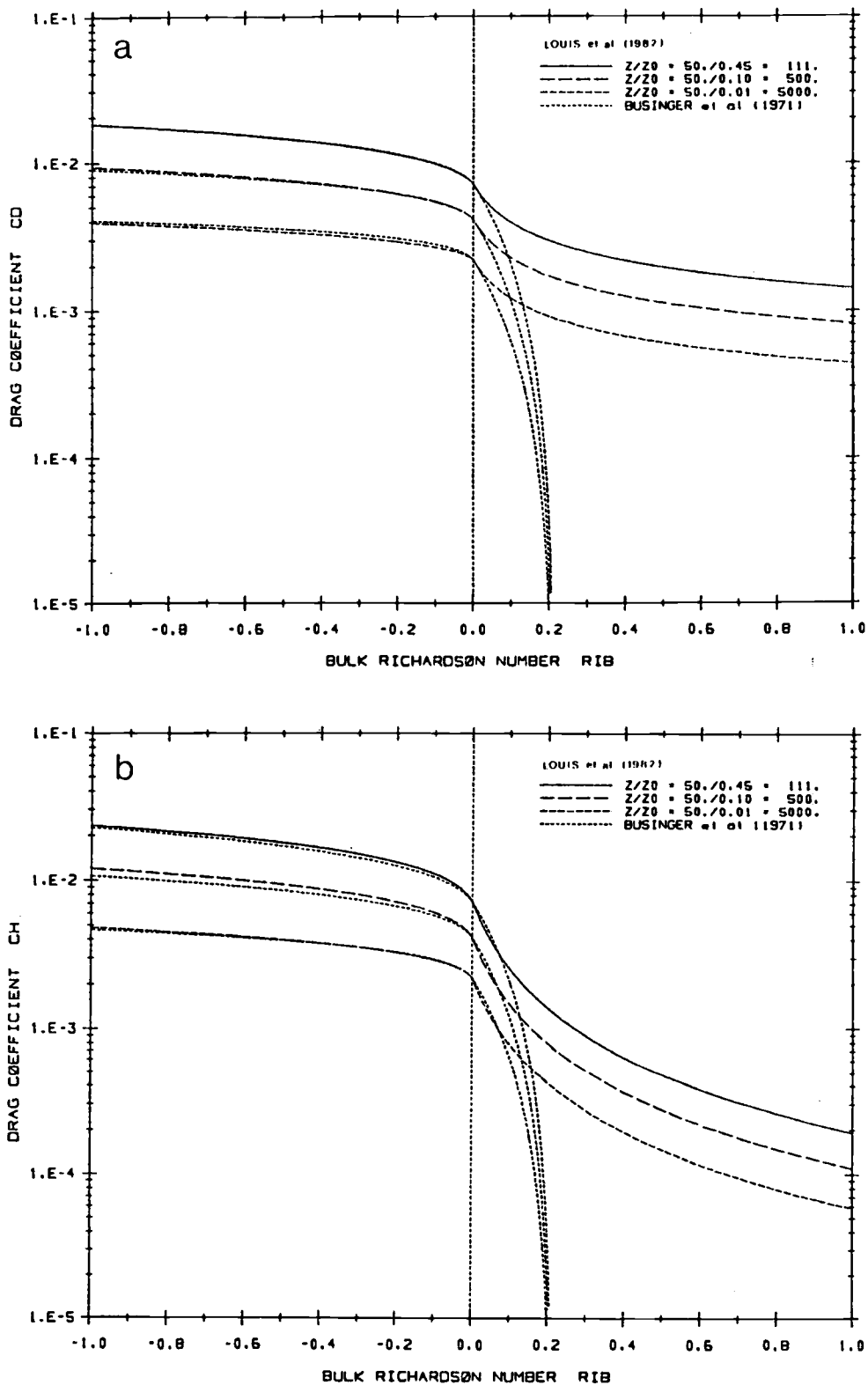
Fig. 3.1. The bulk transfer coefficients (a): C_D, and (b): C_H for the Louis formulation as functions of the bulk Richardson number Ri_B with $z = 50$ m and $z_0 = 0.01$, 0.10 and 0.45m. In both cases, fine dotted curves that converge as Ri_B approaches 0.21 are for the Businger formulation.

Karman constant $k = 0.40$. Therefore, no turbulent fluxes exist for $Ri_B > 0.21$. On the other hand, the Louis formulae give C_D and C_H tending towards asymptotes as $Ri_B \rightarrow \infty$. This allows small but finite turbulent fluxes for very stable conditions for which $Ri_B \gg Ri_{BC}$ and satisfies the need for estimating fluxes representative over the area of a grid element in a numerical model. In unstable conditions, the Louis formulae are very close to the Businger formulation for all values of z/z_0 used, indicating that Louis' explicit analytical functions are good approximation to the Businger formulation at least for the moderately unstable case.

3.1.4 Derived Surface Turbulent Fluxes

a. Stable case. The relationship between the surface momentum flux and the model variables $U(z)$ and $\theta(z)$ for the Louis formulation is displayed in Fig. 3.2a for stable conditions. For comparison purpose, the same relationship obtained for the Businger formula is given in Fig. 3.2b.

It is seen that there exists an extensive zero-flux region where $Ri_B > Ri_{BC}$ in the Businger formula, while the Louis formulation has no zero-flux region since there is no critical Ri_B in his formulation. In very stable weak-wind conditions the values depicted in Fig. 3.2a are quite small and physically insignificant. For moderate-wind conditions the Louis formulation gives weak stress in the range of $0.10 \sim 0.15$ Nm^{-2} under existence of strong temperature contrasts of over 10 K, the conditions which may not be too common. Therefore, it seems that the differences between these two formulae are insignificant.
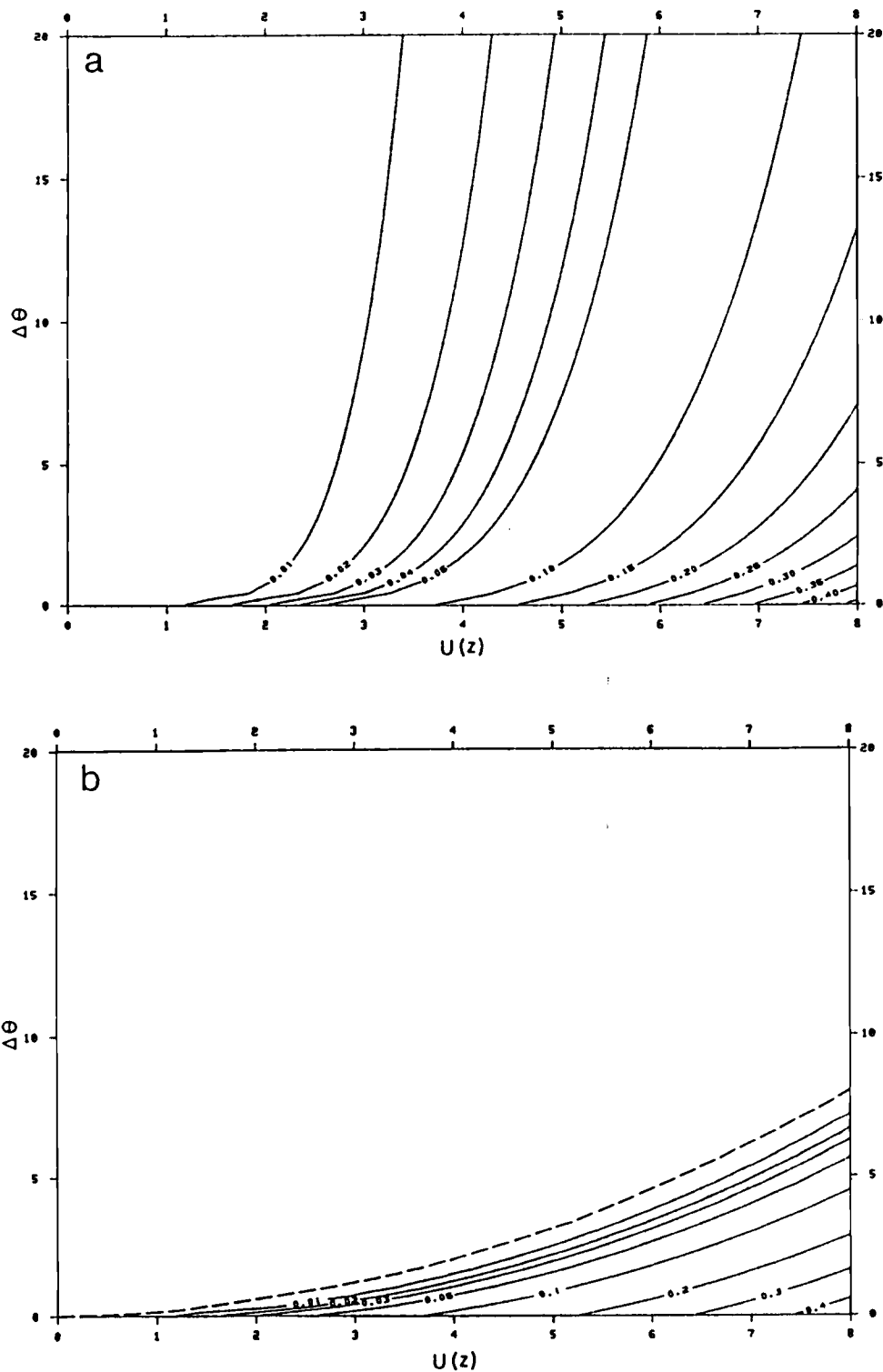
Fig. 3.2. Isopleths of $-\tau/\rho$ (m^2s^{-2}) for stable conditions $(Ri_B > 0)$ as functions of $U(z)$ (ms^{-1}) and $\Delta\theta(K) = \theta(z) - \theta_s$ with $z = 50$ m and $z_0 = 0.45$ m. (a): the Louis formulation, and (b): the Businger formulation. Broken line in (b) indicates $Ri_B(crit) = 0.21$.

Isopleths of the surface sensible heat flux $H/\rho c_p$ given by
(3.7) are illustrated in Figs. 3.3a and b for the Louis and the
Businger formulae, respectively. Each isopleth of the Businger
formulation has a local turning point at $Ri_B \simeq 0.07$ at which $U(z)$
takes a minimum value, while turning points of the isopleths of the
Louis formula line up along the isopleth $Ri_B \simeq 1.5$. For small
$Ri_B < 0.07$ the isopleths of $H/\rho c_p$ for both formulations nearly
coincide.

As is noted by Carson and Richards (1978), for a given $U(z)$ the
magnitude of $H/\rho c_p$ increases from zero in neutral conditions to a
minimum value as $\Delta\theta$ increases from zero to a large value. However,
in very stable conditions, it decreases to zero again in the
Businger formulation or to a small but finite value in the Louis
formula. On the other hand, the eddy stress decreases monotonically
from its maximum in neutral conditions to zero (the Businger case)
or to a small but non-zero value (the Louis case) in very stable
conditions. Therefore, the same value of $H/\rho c_p$ can be achieved in
weakly or very stable conditions corresponding to two different
values of the surface eddy stress u_*.

An important feature that Louis (1979) has intended to achieve
in his derivation of an analytical formula is evident in Fig. 3.3.
In the Businger case the isopleths of $H/\rho c_p$ become asymptotic to
the isopleth $Ri_B = Ri_{BC}$ so that the turbulent heat flux
decreases as Ri_B approaches Ri_{BC} and thus there is a dominant
region beyond the isopleth $Ri_{BC} \simeq 0.21$ of the $(U, \Delta\theta)$-plane for
which non-zero flux is inhibited. By contrast, there is no critical
Ri_B in the Louis case, and hence small but finite sensible heat
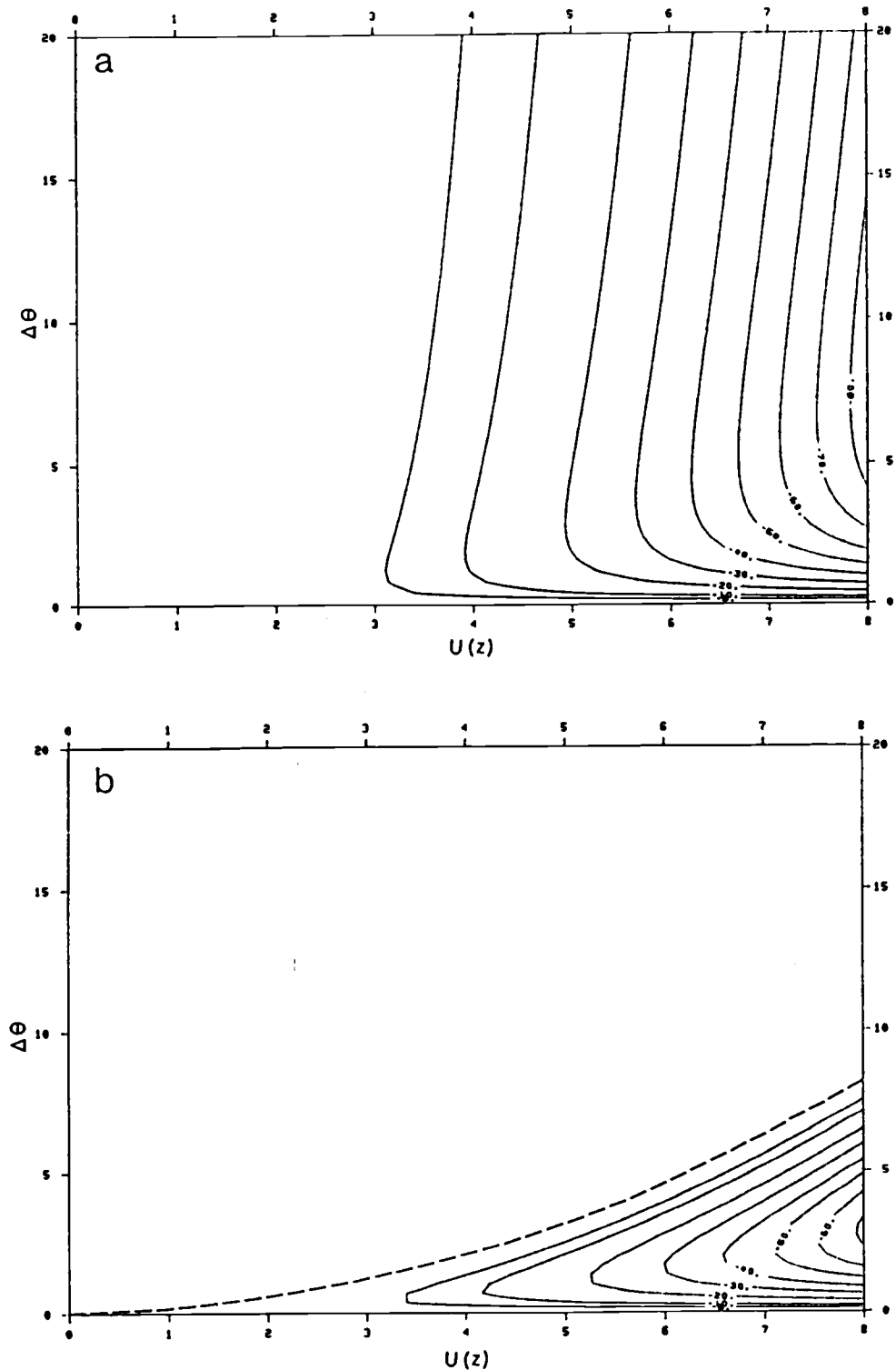
Fig. 3.3. Isopleths of $H/\rho C_p$ $(10^{-3}K\ ms^{-1})$ for stable conditions $(Ri_B > 0)$ as functions of $U(z)$ (ms^{-1}) and $\Delta\theta(K)$ with $z = 50\ m$ and $z_0 = 0.45m$. (a): the Louis formulation, and (b): the Businger formulation. Broken line in (b) indicates $Ri_B(crit) = 0.21$.

flux is allowed in the entire domain of the $(U, \Delta\theta)$-plane, which is an important feature more desirable than the vanishing of fluxes beyond a small critical Ri_B.

Comparison of the isopleths of the fluxes based on the Louis approach for $z = 10$ m, $z_0 = 0.1$ m and for $z = 100$ m, $z_0 = 0.1$ m (not shown) with those based on the Hicks formulation (Figs. 3-5 in Carson and Richards, 1978) reveals that both formulations exhibit nearly identical features except that Hicks formulation has $Ri_{BC} = 1.33$ but not with the Louis formulae. Therefore, we may argue that for stable conditions the Louis formulae can be compared favorably to the Hicks formulation (1976), but can be calculated at a faster speed without time-consuming numerical iterative procedures.

b. <u>Unstable case.</u> The isopleths of $H/\rho c_p$ in unstable conditions ($Ri_B < 0$) are displayed in Fig. 3.4a for the Louis formulation. It is seen that the isopleths consist of nearly straight lines slightly inclined upward as the wind speed decreases from moderate to zero. The upward heat flux does not vanish even when the mean wind becomes zero as it would if C_H were a constant. This is a desirable property in numerical modeling that describes free convection which is maintained by buoyant transport. Therefore, there is no need for restricting the wind speed used in the bulk aerodynamic formulation of the fluxes given by (3.6) and (3.7) to be above a certain minimum in order to realize the conditions of free convection, as is done in Washington and Williamson (1977), Ghan <u>et al</u>. (1982), and Mannouji (1982). Also we can avoid the necessity of
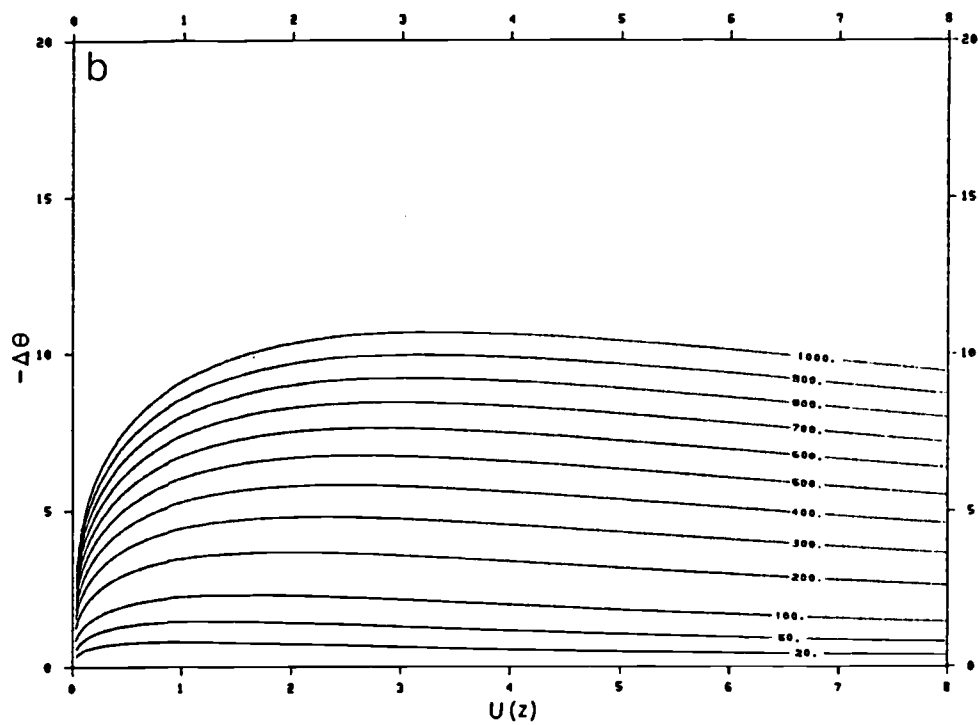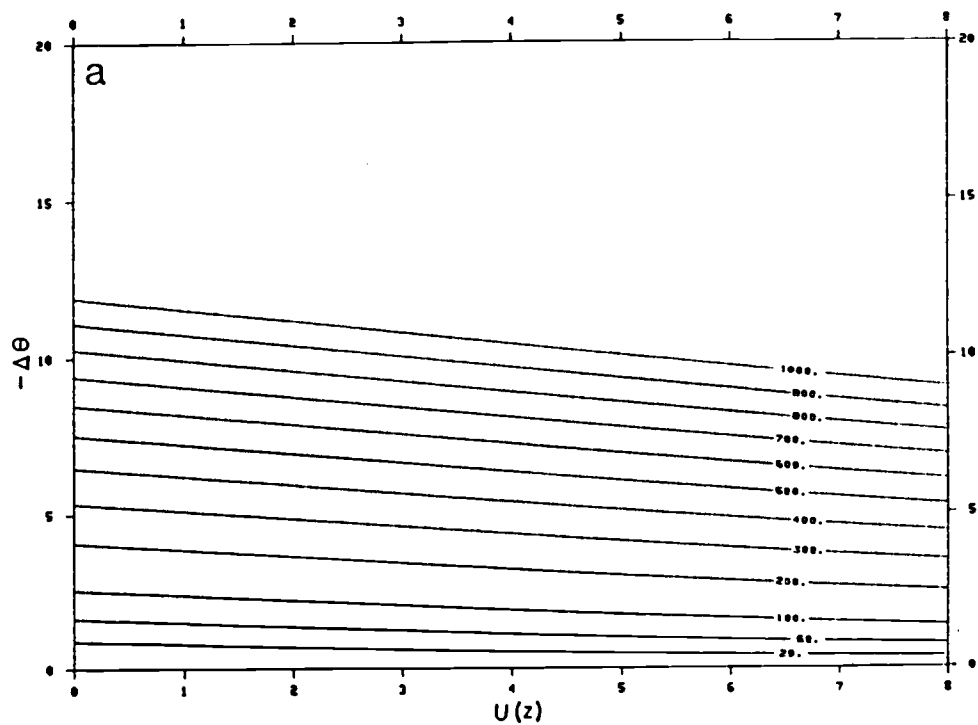
Fig. 3.4. As in Fig. 3.3. except for unstable conditions ($Ri_B < 0$). Note that the ordinates are now $-\Delta\theta = \theta_s - \theta(z)$.

specifying a separate heat flux formulation for free convection regime by making use of Townsend's (1964) free convection heat flux, as in Deardorff (1972) and Kaplan et al. (1982).

The isopleths of the heat flux for Businger's approach are depicted in Fig. 3.4b. For the mean wind above ~3 ms^{-1}, they are nearly straight lines, with slight dependence on the wind speed. However, for weak-wind conditions, the isopleths tend to converge to the (U = 0, -$\Delta\theta$ = 0) point. It is apparent that in very weak- or no-wind conditions the slight increase in the temperature difference -$\Delta\theta$ = θ_s - $\theta(z)$ brings about a large increase of the upward heat flux. Businger (1973) stated that in very stable no-wind conditions (3.21) does not seem to be supported by observed data and that in free convection regime where u_* vanishes ϕ_H should be re-defined in terms of the free-convective velocity w_* [see Eq. (3.56)] as is done in Deardorff (1972).

In conclusion, the Louis formulation also appears to give more realistic representation of the turbulent fluxes in unstable conditions than the Businger formulae, and particularly, in free convection regime there is no need for a special treatment of the turbulent heat flux.

3.1.5 Eddy Transfer Coefficients

The vertical turbulent fluxes above the surface layer in the L7 model are defined using eddy diffusivities as:

$$\frac{\tau}{\rho} = \overline{v'w'} = -K_M \frac{\partial v}{\partial z} \tag{3.34}$$

$$\frac{H}{\rho c_p} = \overline{w'\theta'} = -K_H \frac{\partial \theta}{\partial z} \tag{3.35}$$

where K_M and K_H are the eddy transfer coefficients for momentum and sensible heat, respectively. An explicit distribution for K_M and K_H that was proposed by O'Brien (1970) has been much used in mesoscale and urban boundary layer modeling (Bornstein, 1975; Pielke and Mahrer, 1975). Its cubic polynomial representation of K requires a knowledge of values of K and height at both the tops of the surface and boundary layers as well as the value of the gradient of K at the surface layer top. Although an explicit distribution of K may be simple to use once it has been determined by the use of the above-mentioned parameters which may have to be chosen ad hoc, it neither takes into account the distribution of the wind shear nor the thermal stability of the flow which is of prime importance since stability would inhibit vertical diffusion very effectively (Andre, 1982). An implicit model, on the other hand, attempts to overcome the necessity of making ad hoc assumptions concerning the structure of K by empirically expressing the eddy transfer coefficients as functions of wind shear and stability in the following form (Blackadar, 1979):

$$K_{M,H} = \ell_m^2 \left| \frac{\partial \underset{\sim}{V}}{\partial z} \right| f_{M,H}(Ri) \tag{3.36}$$

where ℓ_m is a mixing length that characterizes the scale of energy-containing eddies. A review of various formulations of the empirical functions f(Ri) is also given in Blackadar (1979).

The expressions of f for C_D and C_H given by (3.30)-(3.33) have been used in Louis (1979) for determination of f(Ri) in (3.36), except that Ri_B is replaced by the local Richardson number defined by

$$Ri = \frac{g}{\bar{\theta}} \frac{\frac{\partial \theta}{\partial z}}{\left|\frac{\partial \underaccent{\tilde}{V}}{\partial z}\right|^2} \qquad (3.37)$$

and in Eqs. (3.30) and (3.31) $c^2(z/z_0)^{1/2}$ is replaced by

$$(\frac{\ell_m}{\Delta z})^2 (\frac{\Delta z}{z})^{1/2} [(\frac{z+\Delta z}{z})^{1/3} - 1]^{3/2} \qquad (3.38)$$

after a dimensional argument, where Δz is the thickness of the model layer. The expression for the mixing length ℓ_m suggested by Blackadar (1962) is most widely used and has been adopted here:

$$\ell_m = \frac{\kappa z}{1 + \frac{\kappa z}{\lambda}} \qquad (3.39)$$

where the asymptotic mixing lengths λ used are 150 m for momentum and 450 m for sensible heat (Louis et al., 1982).

With the above choice of f(Ri), the turbulent fluxes above the surface layer are functions of vertical wind shear and thermal stability and consistent with the surface fluxes for similar conditions. Since the above scheme for vertical eddy diffusivities is applied throughout the model atmosphere including free convection regime, the dry convective adjustment is not necessary in the L7 model.

No explicit horizontal diffusion terms were included in our model equations which we found were not necessary in order to attain stability or smooth fields of prognostic variables.

3.2 Ground Surface Temperature

The ground surface temperature T_S in both the M4 and L7

models is computed using the surface energy balance equation. A number of methods to obtain T_S by using the energy balance equation have been proposed in the literature, and extensive reviews and evaluations of major approaches are given in Deardorff (1978) and Bhumralkar (1975). We have adopted the following form of the energy balance equation given in Deardorff (1978) which will be solved numerically using the procedure to be described in Section 3.2.2:

$$\epsilon_g \sigma_{SB} T_S^4 + H_{ST} + L \cdot E - (1-\alpha) S^{\downarrow} - \epsilon_a R_L^{\downarrow} = G \qquad (3.40)$$

where

E   = evapotranspiration rate

G   = ground (or soil) heat flux at the surface (positive when directed upward)

H_{ST} = sensible heat flux (positive when directed upward)

L   = latent heat of evaporation = 2.50×10^6 Jkg^{-1}

$R_L^{\downarrow}$ = longwave radiative flux directed downward

α = ground surface albedo = 0.15

ϵ_a = emissivity of the atmosphere = 0.80

ϵ_g = ground surface emissivity = 0.93

σ_{SB} = Stefan-Boltzmann constant

$S^{\downarrow}$ = shortwave radiative flux directed downward

$$= S_o \left(\frac{a_s}{r_s}\right)^2 T_{NET} \cos Z$$

S_o = solar constant = 1380 Wm^{-2}

a_S = average distance of the Earth from the Sun

r_S = distance of the Earth from the Sun at any given time

r_S/a_S = true geometric distance = 1.016 (June 21)

T_{NET} = net transmission

Z   = zenith angle

We chose constants given above that would be appropriate for a typical clear, dry day over a forested region in mid-latitudes. Following Pielke (1981) and Anthes and Warner (1978), the zenith angle is determined from

$$\cos Z = \sin\phi \sin\delta + \cos\phi \cos\delta \cos\omega_h \qquad (3.41)$$

where

ϕ = latitude = 45°N

δ = solar declination = 23°26' (June 21)

ω_h = solar hour angle = 15°[t_L - 12h]

t_L = local apparent time

Using the bulk aerodynamic formulation, the sensible heat flux is given by

$$H_{ST} = -\rho_a c_p C_H |\underset{\sim}{V}_a|(T_a - T_s) \qquad (3.42)$$

where subscript a denotes quantities near the ground, and the bulk transfer coefficient C_H will be computed using the method discussed in Section 3.1. The evapotranspiration rate E is assumed to have a sinusoidal representation:

$$E = C_{EV} \sin[\frac{\pi}{t_1-t_0}(t-t_0)] \qquad (3.43)$$

from sunrise (t_0) to sunset (t_1) while it is set to zero during nighttime, where constant c_{EV} = 1.132 x 10^{-4} kg $m^{-2}s^{-1}$ has been chosen so that the total evapotranspiration amounts to 4 mm day^{-1},

and t is time. As in Pielke (1981) and Kondratyev (1969), the effects of the sloping ground surface on the radiative flux have been taken into account in our modeling by replacing $S^\downarrow$ and $R_L^\downarrow$ by

$$\tilde{S}^\downarrow = S^\downarrow\frac{\cos i}{\cos Z}; \quad \tilde{R}_L^\downarrow = R_L^\downarrow \cos\alpha_G \tag{3.44}$$

where α_G is the angle of the slope, and $R_L^\downarrow$ is specified as $\sigma_{SB}T_a^4$. The angle of incidence of solar lays on the inclined surface, i, is obtained from

$$\cos i = \cos\alpha_G \cos Z + \sin\alpha_G \sin Z \cos(\beta_a - n_a) \tag{3.45}$$

and the solar and slope azimuths β_a and n_a are given by

$$\beta_a = \sin^{-1}[\frac{\cos\delta \cdot \sin\omega_h}{\sin Z}]$$

$$n_a = \frac{\pi}{2} - \tan^{-1}[\frac{\partial h_s}{\partial x}/\frac{\partial h_s}{\partial y}]$$

where h_s is the elevation of the ground surface.

For the net transmission, T_{NET}, at the ground surface in a cloudless and pollution-free atmosphere the empirical expression given also in Pielke (1981) has been adopted here:

$$T_{NET} = T_r - a_w \tag{3.46}$$

where

$$T_r = 0.485 + 0.515[1.041 - 0.16(\frac{0.949\times10^{-3}p+0.051}{\cos Z})^{1/2}] \tag{3.47}$$

with p being pressure (mb), and T_r accounts for molecular scattering and absorption by such gases as oxygen, ozone and carbon dioxide. Following McDonald (1960) and Atwater and Brown (1974), the absorptivity, a_w, of water vapor through a layer of water

vapor is given as

$$a_w = 0.077[\frac{w_p(p)}{cosZ}]^{0.30}$$

(3.48a)

where $w_p(p)$ is the precipitable water-vapor content (cm) of the atmosphere column above the pressure level p, and is defined by

$$w_p(p) = \frac{1}{\rho_w} \int_{p_T}^{p} \frac{q_m}{g} dp$$

(3.48b)

with ρ_w being the density of liquid water and q_m the mixing ratio. In our experiments $w_p(p)$ is specified as a constant in time and space (2 cm).

3.2.1 Ground Heat Flux

The ground heat flux at the surface, G, which is a fraction of the net radiation at the surface conducted into or out of the ground, is generally a function of such properties as soil and vegetation types, wetness as well as the stability of air near the ground. However, observational studies suggest that to a first-order approximation G can be expressed as a linear regression function of the net radiative flux R_N (Fuchs and Hadas, 1972; Idso et al., 1975; DeHeer-Amissah et al., 1981; Camuffo and Bernardi, 1982):

$$G = a_1 R_N + a_2$$

(3.49)

where a_1 and a_2 are proportionality constants, and

$$R_N \equiv \varepsilon_g \sigma_{SB} T_S^4 - (1-\alpha) \tilde{S}^{\downarrow} - \varepsilon_a \tilde{R}_L^{\downarrow}$$

(3.50)

The ground heat flux has been ignored (G = 0) in some GCMs

(Manabe et al., 1974; Gates et al., 1971). On the other hand, Nickerson and Smiley (1975) have proposed $a_1 = 0.19$ for $R_N < 0$ and $a_1 = 0.32$ for $R_N > 0$, while setting $a_2 = 0$ for all conditions, by analyzing the O'Neill data (Lettau and Davidson, 1957). Gadd and Keers (1970) have used $a_1 = 0.1$ for $R_N < 0$ and $a_1 = 0.5$ for $R_N > 0$ and $a_2 = 0$ for all R_N, while $a_1 = 0.1$ and $a_2 = 0$ for all R_N have been proposed by Burridge and Gadd (see Camuffo and Bernardi, 1982). On the other hand, Washington and Williamson (1977) have attempted to express G in terms of the sensible heat flux by writing $G = -1/3 \, H_{ST}$.

The second term a_2 in (3.49) represents the heat flux between the ground surface and the atmosphere when R_N vanishes, and may be caused by the temperature difference between them as well as the release of the latent heat from the ground (Camuffo and Bernardi, 1982). Field experiments mentioned earlier indicate that a_2 is generally a positive value in the range of 10~50 Wm^{-2}, which may not be ignored in the calculation of T_S when R_N is small. For the daily data of the O'Neill experiment, we found by applying linear regression analysis that a_1 varies from 0.185 to 0.297, and a_2 from 6 to 36 Wm^{-2}, while for the entire experiment period we obtained $a_1 = 0.220$ and $a_2 = 22.2$ Wm^{-2} (Fig. 3.5a). On the other hand, for days 33/34 of the Wangara experiment (Clarke et al., 1971), $a_1 = 0.343$ and $a_2 = 16.0$ Wm^{-2} were obtained (Fig. 3.5b). Recognizing large variabilities in a_1 and a_2 depending on the local conditions, as noted by Brutsaert (1982), we have chosen the values of a_1 and a_2 given in Deheer-Amissah et al. (1981):
$G = 0.356 \, R_N + 21$; and Camuffo and Bernardi (1982):
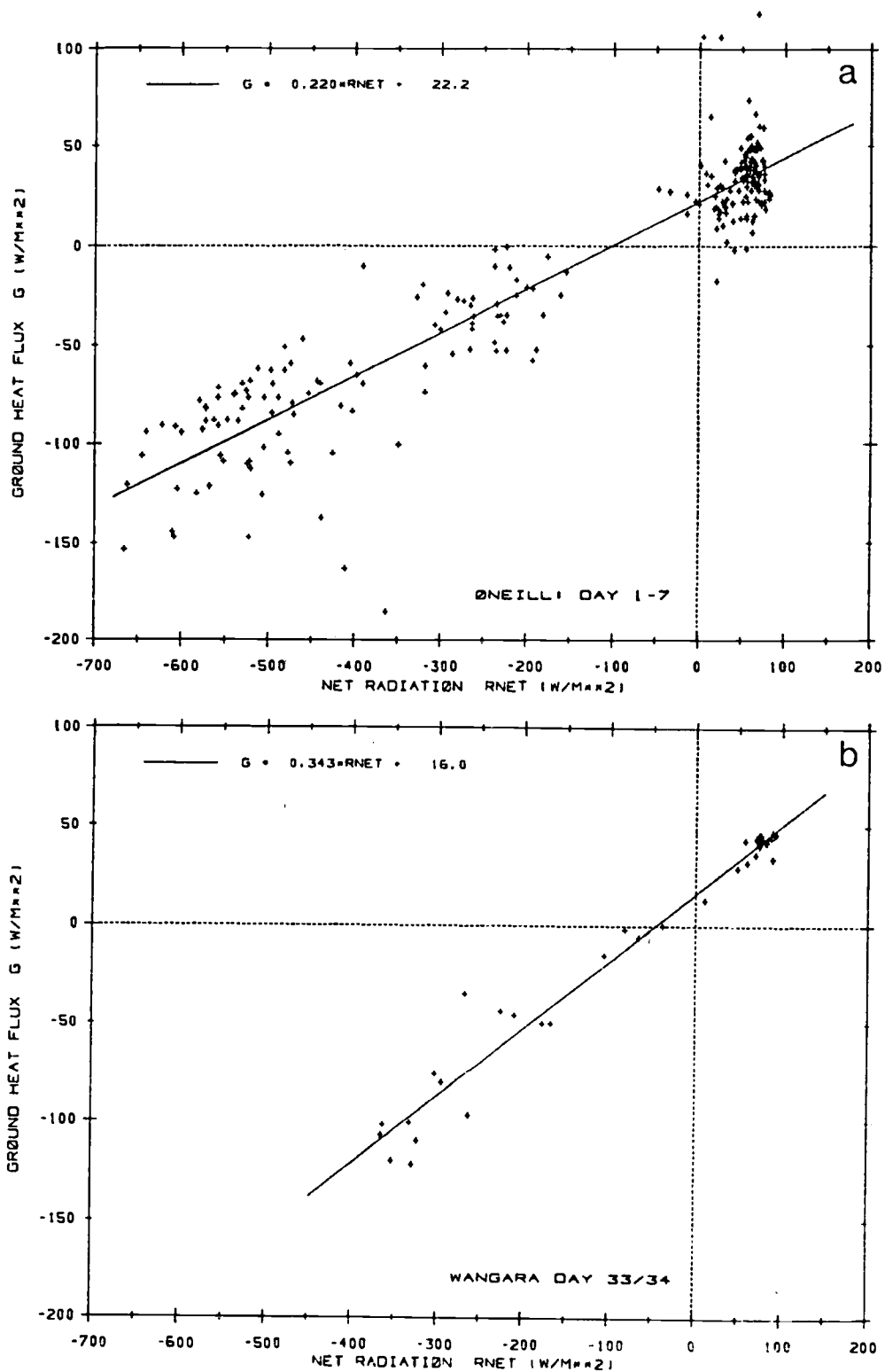
Fig. 3.5. Relationships between ground heat flux G and net radiation R_{NET} in units of watts m^{-2}. (a): days 1-7 of the O'Neill data, and (b): days 33-34 of the Wangara data.

$G = 0.34 \; R_N + 32$; as representative that are best suited to the situations in our modeling and have used $a_1 = 0.350$ and $a_2 = 25.0$, i.e.,

$$G = 0.35 \; R_N + 25(Wm^{-2}) \qquad \text{for all } R_N \qquad (3.51)$$

3.2.2 Numerical Methods

In Eq. (3.40) the term $\varepsilon_g \sigma_{SB} T_S^4$ is linearized in the following manner in order to avoid iterative procedures in calculations of T_S:

$$[T_S^{(n)}]^4 = [T_S^{(n-1)}]^3 \cdot [4T_S^{(n)} - 3T_S^{(n-1)}] \qquad (3.52)$$

where the superscript (n) refers to time step. Substituting (3.52) for $[T_S^{(n)}]^4$, (3.42) for H_{ST}, and (3.51) for G in (3.40) and making use of (3.50), we obtain

$$[T_S^{(n)} - T_a^{(n)}][4(1-a_1)\varepsilon_g \sigma_{SB} \{T_S^{(n-1)}\}^3 + \rho_a c_p C_H^{(n)} |\underset{\sim}{v}_a^{(n)}|]$$

$$= (1-a_1)[\varepsilon_g \sigma_{SB} \{T_S^{(n-1)}\}^3 (3T_S^{(n-1)} - 4T_a^{(n)}) + (1-\alpha)\tilde{S}^{\downarrow} + \varepsilon_a \tilde{R}_L^{\downarrow}]$$

$$-L \cdot E + a_2 \qquad (3.53)$$

where $T_a^{(n)} = P_a^{(n)} \theta_a^{(n)}$, with $P_a = (p_a/p_{00})^\kappa$. Here we have assumed that quantities in the atmosphere near the ground surface are vertically well-mixed so that the potential temperature near the surface θ_a can be replaced by the predicted potential temperature of the lowest layer.

3.3 PLanetary Boundary Layer Depth

In the M4 model we predict at each time step the pressures p_B

at the mixed-layer top and p_S at the ground surface as well as the potential temperature of the mixed layer, θ_M. Therefore, the depth h of the mixed layer can be obtained using the hydrostatic relation that will be defined in Section 4.1.3:

$$h = h_B - h_S = \frac{c_p}{g} \theta_M (P_S - P_B) \tag{3.54}$$

where h_B and h_S are the elevations of the mixed-layer top and the ground surface, respectively, while P_S and P_B are the values of (2.25) at h_B and h_S, respectively.

In the L7 model, however, there is no p_B predicted explicitly so that we must seek an alternative method to estimate h_B and hence h. Anthes and Warner (1978) used the potential temperature profile to estimate h in their high-resolution mesoscale model. The depth h is diagnosed as the first level at which the time-averaged potential temperature lapse rate exceeds a critical value of 1.3 x 10^{-3}K m^{-1}. Busch et al. (1976), on the other hand, chose the depth h as the first height above the ground at which the local Richardson number, Ri, given by (3.37) exceeds a critical value Ri_C = 0.25. Mahrt et al. (1982) also used a similar method in which the depth of the nocturnal boundary layer was estimated by linearly interpolating Ri, with the choice of Ri_C = 0.5. It has been found, however, that neither method gives satisfactory h fields in our 7-level model, due to the coarse vertical resolution. Another approach (Deardorff, 1974; Kaplan et al., 1982) that has been often used in the boundary layer modeling, which predicts h directly by using a prognostic equation, is also found difficult to use because of uncertainty of the potential temperature gradient or jump

immediately above h_B. Thus we have taken an approach that is a combination of both Anthes' and Busch's methods described above. The local Richardson number Ri at each interface level (level with a half-integer index $\ell-1/2$; see Fig. 2.1) is examined starting from the top layer. The height h_B is determined to lie within the layer confined between levels $\ell+1$ and $\ell-1$ when Ri exceeds for the first time a critical value Ri_C. The Ri_C used here is taken as unity to reflect the fact that it represents the average conditions over some vertical layer which may contain both stable and unstable region, although the values of Ri in the laboratories and observations at single ground sites are found to be near 0.25 (Ross and Orlanski, 1982). The potential temperature profile in layers $\ell+1$ and $\ell+2$, and that in layers $\ell-2$ and $\ell-1$ are then linearly extrapolated toward this layer and h_B is diagnosed as the level at which two temperature profiles coincides. A time average (usually 5 minutes) has been further taken in order to obtain a smooth varying behavior of h_B before each output.

3.4 Entrainment Rate Equation

As in a previous study of terrain-induced mesoscale motions in a heated, growing mixed layer (DUH, 1984), the following form of the entrainment rate equation will be used in the M4 model for w_e in (2.17):

$$w_e = \frac{0.24(w_*^3+3u_*^3)}{(g/\theta_M)\Delta\theta\cdot h+(w_*^3+3u_*^3)^{2/3}} \qquad (3.55)$$

where w_* is the mixed-layer free-convection velocity defined by

$$w_* \equiv [\frac{g}{\theta_M} \frac{H_S}{\rho_a c_p} h]^{1/3}$$ (3.56)

Here $\Delta\theta$ in this case is the discontinuity of θ across the top of the mixed layer. Furthermore, with the use of (3.4)-(3.7), the friction velocity, u_*, and the surface sensible heat flux, H_S, are determined from

$$u_* = C_D^{1/2} |\underset{\sim}{V}_M|$$ (3.57)

$$H_S = -\rho_a c_p C_H |\underset{\sim}{V}_M| (\theta_M - \theta_a)$$ (3.58)

where $\underset{\sim}{V}_M$ is the horizontal wind within the mixed layer of the M4 model.

4. FINITE-DIFFERENCE SCHEME

4.1 Vertical Differencing Schemes

The vertical differencing schemes adopted for the M4 and the L7 models are those derived by Suarez and Arakawa (1979) and Arakawa and Suarez (1983), respectively. The latter scheme is a generalization of the former and both satisfy some important integral constraints of the continuous equations given in Section 2.1. Additionally, both differencing schemes have been designed to satisfy the constraints which will be given in Section 4.1.3. Since detailed descriptions of the differencing schemes are given in Suarez and Arakawa (1979), Arakawa and Suarez (1983), and Suarez et al. (1983), only a brief summary of both schemes will be presented below along with the major features implemented in our models.

4.1.1 Vertical Grid Structure

a. The M4 model. The model atmosphere is divided into L (= 3) layers by L-1 levels of constant σ between the top of the model atmosphere ($\sigma = 0$) and the top of the planetary boundary layer (PBL) or mixed layer ($\sigma = \sigma_B = 1$), as shown in Fig. 2.1a. The horizontal wind components, potential temperature, geopotential and potential vorticity are defined for the layers at "full levels" identified by integer subscripts $\ell = 1,2,...,L$. The vertical velocity $\dot{\sigma}$ is represented at the interface "half levels" identified by $\sigma = 1/2, 1+1/2, ..., L+1/2$. A half-level variable will also be identified by a caret. The lowest layer between $\sigma = 1$ and $\sigma = 2$ is designated as the PBL or mixed layer and identified by integer

$M \equiv L+1$ (= 4). The top of the PBL (σ_B = 1) and the bottom of the atmosphere ($\sigma = \sigma_S$ = 2) are identified by half integers $M-1/2 \equiv L+1/2$ and $M+1/2$, respectively. The variable placement in the PBL is the same as in the layers above.

b. <u>The L7 model</u>. The vertical structure of the L7 model is shown in Fig. 2.1b. The above description of the vertical grid above the PBL top and variable placement for the M4 model also applies to the L7 model if we set L = 7. The bottom of the atmosphere is now at half level $L+1/2$ ($\sigma = \sigma_S$ = 1).

c. <u>The grid spacing</u>. Since one of our objectives is to compare the results from a multi-level model in which the PBL is represented by the lowest model layer (M4 model) with those from a conventional model with a relatively coarse resolution (L7 model), uniform spacing of the grids with 7 levels in the vertical in the L7 model would be unsatisfactory for this purpose because it would not resolve the lower part of the atmosphere reasonably well. To remedy the problem we have adopted in the L7 model an irregular grid with smaller spacing near the ground that has been proposed by Kalnay de Rivas (1972), who has found that projection of a uniformly spaced grid, $\xi_\ell = \ell \Delta \xi$, with $\Delta \xi \equiv 1/L$ = constant, onto a non-uniform grid, z_ℓ, by choosing a simple function $z_\ell = (\ell \Delta \xi)^2$ gives an approximation of the first and second derivatives, $\partial f/\partial z$ and $\partial^2 f/\partial z^2$, with second-order accuracy in $\Delta \xi$, where f is an arbitrary function. In our L7 model, this projection corresponds to

$$\hat{\sigma}_{\ell+1/2} = 1 - (\frac{L-\ell}{L})^2, \qquad \ell = 1, 2, \ldots, L-1 \qquad (4.1)$$

where $\hat{\sigma}_{\ell+1/2}$ represents the interface level (half level) between layers ℓ and $\ell+1$ (Fig. 2.1b). The values of $\hat{\sigma}_{\ell+1/2}$ and $(\delta\sigma)_\ell$ are given as follows:

$\ell+1/2$	$\hat{\sigma}_{\ell+1/2}$	$(\delta\sigma)_\ell$
1/2	0.	
		.2653
1+1/2	.2653	
		.2245
2+1/2	.4898	
		.1837
3+1/2	.6735	
		.1428
4+1/2	.8163	
		.1021
5+1/2	.9184	
		.0612
6+1/2	.9796	
		.0204
7+1/2	1.	

Here $(\delta\sigma)_\ell$ is the discrete vertical operator defined for any variable ψ:

$$(\delta\psi)_\ell = \psi_{\ell+1/2} - \psi_{\ell-1/2} \qquad (4.2a)$$

Similarly, we define

$$(\delta\psi)_{\ell+1/2} = \psi_{\ell+1} - \psi_\ell \qquad (4.2b)$$

which will be used throughout this chapter.

In the M4 model, on the other hand, the depth of the lowest layer increases as the turbulent fluxes in the PBL become more active during the daytime, reaching a maximum depth of about 2000 m by sunset, as will be shown in Chapter 6, while the thickness of each layer above the PBL top proportionally decreases, thus making the use of non-uniform grid spacing less meaningful. Therefore, it has been decided that we use an equally spaced vertical grid above

the PBL top in the M4 model with L = 3.

4.1.2 Continuity Equation

a. The M4 model. The finite-difference forms of (2.14) and (2.18)-(2.20) are

$$\frac{\partial \pi}{\partial t} + \nabla \cdot (\pi \underset{\sim}{V})_\ell + \left[\frac{\delta(\pi \dot{\sigma})}{\delta \sigma}\right]_\ell = 0 \qquad \text{for } \ell = 1, 2, \ldots, M \quad (4.3)$$

$$\frac{\partial p_S}{\partial t} = -\nabla \cdot \sum_{\ell'=1}^{M} (\pi \underset{\sim}{V} \delta \sigma)_{\ell'} \qquad (4.4)$$

$$\frac{\partial p_B}{\partial t} = -\nabla \cdot \sum_{\ell'=1}^{M} (\pi \underset{\sim}{V} \delta \sigma)_{\ell'} - \rho_B g w_e \qquad (4.5)$$

$$(\pi \dot{\sigma})_{\ell+1/2} = -\nabla \cdot \sum_{\ell'=1}^{\ell} (\pi \underset{\sim}{V} \delta \sigma)_{\ell'} - \hat{\sigma}_{\ell+1/2} \frac{\partial p_B}{\partial t} \quad \text{for } \ell = 1, 2, \ldots, L \quad (4.6)$$

b. The L7 model. Eq. (4.3) is also valid in the L7 model. The discrete forms of (2.22) and (2.23) are

$$\frac{\partial p_S}{\partial t} = -\nabla \cdot \sum_{\ell'=1}^{L} (\pi \underset{\sim}{V} \delta \sigma)_{\ell'} \qquad (4.7)$$

$$(\pi \dot{\sigma})_{\ell+1/2} = -\nabla \cdot \sum_{\ell'=1}^{\ell} (\pi \underset{\sim}{V} \delta \sigma)_{\ell'} - \hat{\sigma}_{\ell+1/2} \frac{\partial p_S}{\partial t} \quad \text{for } \ell = 1, 2, \ldots, L \quad (4.8)$$

4.1.3 Pressure Gradient Force and Hydrostatic Relation

In deriving the discrete forms of the pressure gradient force and the hydrostatic equation Arakawa and Suarez (1983) required that

(1) the constraints (A)-(C) given in Section 2.1 are satisfied;

(2) the hydrostatic equation for the thickness of the lowest layer depends only on the potential temperature at the lowest full level since the non-locality introduces errors

in the pressure gradient force and local accuracy of the hydrostatic equation (Schlesinger et al., 1981); and

(3) the pressure gradient force vanishes for three dimensionally isentropic atmosphere.

The discrete scheme of the pressure gradient force for the M4 model above the PBL derived by Suarez and Arakawa (1979) is identical to the corresponding scheme for the L7 model, and it can be proved that the scheme for the M4 model also satisfies the conditions listed above.

a. The M4 model. It has been found that the pressure gradient force $-\nabla_p \phi$ which meets the above requirements is

$$-\nabla_p \phi_\ell = -\nabla_\sigma \phi_\ell - c_p \theta_\ell \frac{\partial P_\ell}{\partial \pi} \nabla \pi \qquad \text{for } \ell=1,2,\ldots,L \qquad (4.9)$$

The form of P_ℓ is given by

$$P_\ell = \frac{1}{1+\kappa} \left[\frac{\delta(Pp)}{\delta p} \right]_\ell$$

$$= \frac{1}{1+\kappa} \left[\frac{\hat{P}_{\ell+1/2}\hat{p}_{\ell+1/2} - \hat{P}_{\ell-1/2}\hat{p}_{\ell-1/2}}{(\pi\delta\sigma)_\ell} \right] \qquad \text{for } \ell=1,2,\ldots,L \quad (4.10)$$

where $\hat{P}_{\ell+1/2} = (\hat{p}_{\ell+1/2}/p_{00})^\kappa$ from (2.25), and $(\delta p)_\ell = (\pi\delta\sigma)_\ell$ have been used. The above form of P_ℓ has also been proposed by Phillips (1974). Differenciating (4.10) with respect to π, we find

$$\frac{dP_\ell}{d\pi} = \frac{1}{(\pi\delta\sigma)_\ell} \left[\hat{\sigma}_{\ell+1/2}(\hat{P}_{\ell+1/2} - P_\ell) + \hat{\sigma}_{\ell-1/2}(P_\ell - \hat{P}_{\ell-1/2}) \right] \qquad (4.11)$$

The discrete form of the hydrostatic relation that satisfies the above requirements can be written

$$\phi_L - \hat{\phi}_{L+1/2} = c_p\theta_L(\hat{P}_{L+1/2} - P_L) \tag{4.12}$$

$$\phi_\ell - \phi_{\ell+1} = c_p\hat{\theta}_{\ell+1/2}(P_{\ell+1} - P_\ell) \qquad \text{for } \ell=1,2,\ldots,L \tag{4.13}$$

$$\hat{\phi}_{\ell-1/2} - \hat{\phi}_{\ell+1/2} = c_p\theta_\ell(\hat{P}_{\ell+1/2} - \hat{P}_{\ell-1/2}) \qquad \text{for } \ell=1,2,\ldots,L \tag{4.14}$$

and the potential temperature at half level is given by

$$\hat{\theta}_{\ell+1/2} = \frac{1}{(\delta P)_{\ell+1/2}} [(P_{\ell+1} - \hat{P}_{\ell+1/2})\,\theta_{\ell+1} + (\hat{P}_{\ell+1/2} - P_\ell)\,\theta_\ell]$$

$$\text{for } \ell=1,2,\ldots,L \tag{4.15}$$

It is noted that (4.12)-(4.14) are formally discrete analogues of Eq. (2.27).

For the lowest layer Eq. (2.36) is integrated from $\sigma_S = 2$ to $\sigma_B = 1$ to give

$$-\nabla_p\phi_M = -\nabla_\sigma\phi_M - \frac{1}{\pi}[(\phi_M - \hat{\phi}_S)\,\nabla\pi + (\hat{\phi}_B - \hat{\phi}_S)\,\nabla p_B] \tag{4.16}$$

where $\hat{\phi}_S \equiv \phi_{M+1/2}$ and $\hat{\phi}_B \equiv \phi_{M-1/2}$, and ϕ_M is assumed to represent the mean value of ϕ in the vertically well-mixed PBL. The hydrostatic equation takes the form

$$\phi_M - \hat{\phi}_S = c_p\theta_M(\hat{P}_S - P_M) \tag{4.17}$$

$$\hat{\phi}_B - \hat{\phi}_S = c_p\theta_M(\hat{P}_S - \hat{P}_B) \tag{4.18}$$

where $\hat{P}_S \equiv P_{M+1/2}$ and $\hat{P}_B \equiv P_{M-1/2}$.

b. <u>The L7 model</u>. As has been stated earlier, Eqs. (4.9)-(4.14) are also valid for the L7 model for $\ell = 1,2,\ldots,L$.

4.1.4 First Law of Thermodynamics

The discrete form of the thermodynamic equation (2.29) is

$$\frac{\partial}{\partial t}(\pi\theta)_\ell + \nabla \cdot (\pi\underset{\sim}{V}_\ell \theta_\ell) + [\frac{\delta(\pi\dot\sigma\theta)}{\delta\sigma}]_\ell = \frac{g}{c_p}[\frac{\delta H}{\delta\sigma}]_\ell \qquad (4.19)$$

which applies to both the M4 model for $\ell = 1,2,...,M$, and the L7 model for $\ell = 1,2,...,L$. The half level potential temperature $\hat\theta_{\ell+1/2}$ is given by (4.15). However, the treatment of H on the right side of (4.19) in the M4 model is quite different from that in the L7 model, as described below.

a. The M4 model. The turbulent sensible heat flux H is ignored in the layers above the PBL and therefore the right side of (4.19) is set to zero for $\ell = 1,2,...,L$. As we have discussed in Chapter 3, the form of H in the surface layer $H_S \equiv H_{M+1/2}$ is expressed as

$$H_S = -\rho_a c_p C_H |\underset{\sim}{V}_a|(\theta_a - \theta_S) \qquad (4.20)$$

where the variables with subscript a represent quantities near the surface. Since it is assumed that the PBL is a vertically well-mixed layer, we set $\underset{\sim}{V}_a = \underset{\sim}{V}_M$, $\theta_a = \theta_M$, and $\rho_a \simeq \rho_s = \rho_{M+1/2}$. The bulk transfer coefficient for sensible heat flux, C_H, will be computed by using the formula derived by Louis (1979), and Louis et al. (1982), as discussed in Section 3.1. For the height at which C_H is calculated, Tiedtke et al. (1979) used the height of the lowest full level z_M of their conventional σ-coordinate model. However, since z_M in the M4 model increases up to approximately 1000 m as the PBL grows during the daytime, it is not appropriate in the M4 model to treat the lower half of the lowest layer as the

surface layer and use Z_M for computing the transfer coefficient. Instead we have set $z_M = 50$ m = constant, which is the approximate height of the lowest full level in the L7 model. The ground surface temperature θ_S will be obtained by solving the energy balance equation (3.40) using the procedure described in Section 3.2.

For the layer immediately above the PBL we have

$$\frac{\partial}{\partial t} (\pi\theta_L) + \nabla \cdot (\pi\theta_\ell \underset{\sim}{V}_\ell) + \frac{1}{(\delta\sigma)_L} [(\pi\dot{\sigma}\hat{\theta})_{L+1/2} - (\pi\dot{\sigma}\hat{\theta})_{L-1/2}] = 0 \quad (4.21)$$

Here $\hat{\theta}_{L+1/2}$ represents the potential temperature immediately above the PBL top as shown in Fig. 4.1. The inversion or the interfacial entrainment layer, whose thickness is δ_{INV}, is not explicitly represented in the M4 model, but it is assumed that the M4 model represents the case in which $\delta_{INV} \rightarrow 0$ so that the potential temperature immediately above the PBL θ^+ should be independent of the mixed-layer potential temperature below. Therefore, θ^+ is determined by linearly extrapolating the potential temperatures θ_{L-1} and θ_{L-2} at full levels $\ell = L-1$ and $\ell = L-2$, respectively, downward to the half level $\ell+1/2 = L+1/2$ by using the hydrostatic relation (4.12)-(4.14), and $\hat{\theta}_{L+1/2}$ is set equal to θ^+ in (4.12).

For the PBL Eq. (4.19) is integrated from $\sigma_S = 2$ to $\sigma_B = 1$ using $(\delta\sigma)_M = 1$:

$$\frac{\partial}{\partial t} (\pi\theta_M) + \nabla \cdot (\pi\theta_M \underset{\sim}{V}_M) + [(\pi\dot{\sigma}\hat{\theta})_{M+1/2} - (\pi\dot{\sigma}\hat{\theta})_{M-1/2}] = \frac{g}{c_p} [H_{M+1/2} - H_{M-1/2}]$$

$$(4.22)$$

We have assumed here again that in the PBL quantities $\underset{\sim}{V}$ and θ are vertically well-mixed so that $\underset{\sim}{V}_M$ and θ_M represent the vertical
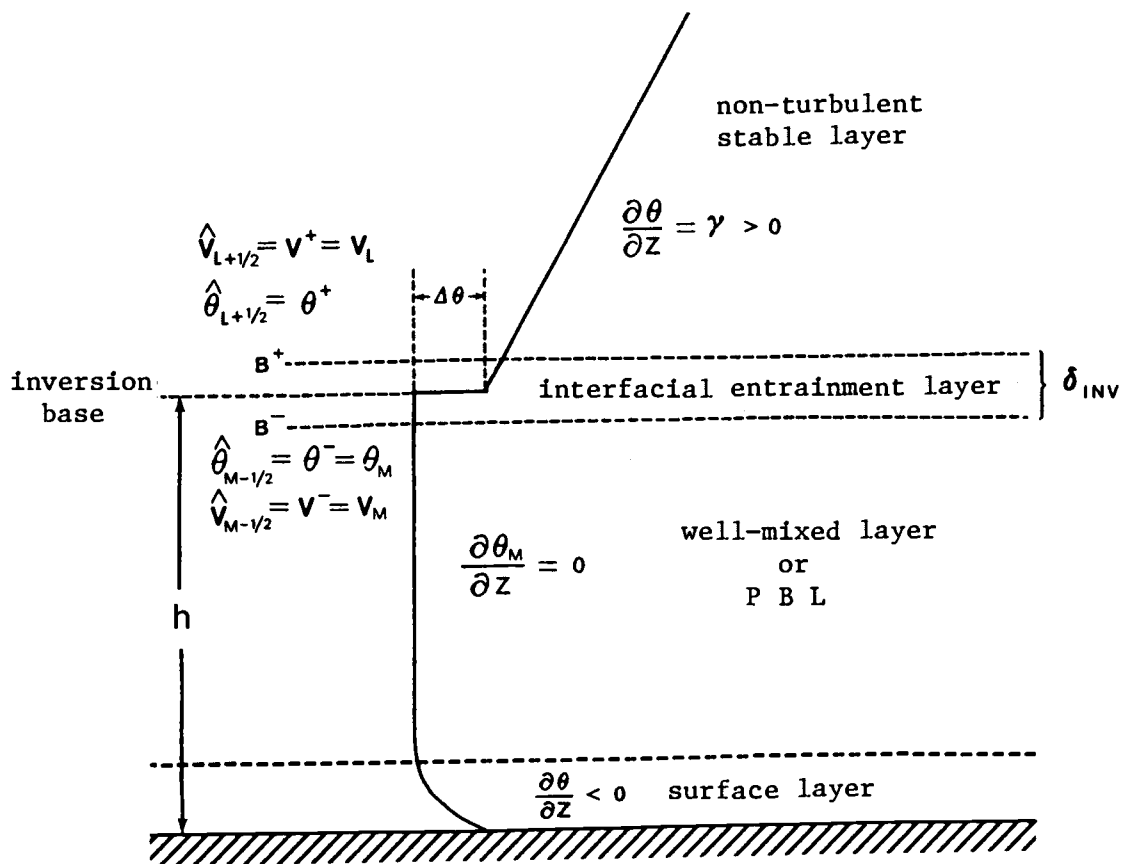
Fig. 4.1.   Schematic representation of the idealized potential temperature in and above a well-mixed boundary layer used in the M4 model.

mean of $\underset{\sim}{V}$ and θ in the PBL, respectively. Since $(\pi\dot{\sigma})_{M+1/2} = (\pi\dot{\sigma})_{\sigma_S=2} = 0$, we have

$$(\pi\dot{\sigma}\hat{\theta})_{M+1/2} = 0 \qquad (4.23a)$$

It is also assumed that $\hat{\theta}_{M-1/2}$ represents the potential temperature immediately below the inversion of infinitesimal thickness, θ^-, and from the well-mixed assumption we set $\hat{\theta}_{M-1/2} = \theta^- = \theta_M$. Furthermore, we assume following Carson (1973) and Tennekes (1973) that the turbulent heat flux at the top of the PBL is proportional to both the entrainment velocity w_e (positive when directed downward) and the temperature jump $\Delta\theta \equiv \theta^+ - \theta^-$ at the PBL top:

$$H_{M-1/2} = -\rho_B c_p w_e \Delta\theta = -\rho_B c_p w_e (\theta^+ - \theta_M) \qquad (4.23b)$$

which can also be derived from the budget equation for θ in the PBL (Suarez et al., 1983). Since $(\pi\dot{\sigma})_{\sigma=1}$ is defined by Eq. (2.17), we obtain:

$$(\pi\dot{\sigma}\theta)_{\sigma=1} = (\pi\dot{\sigma}\theta)_{M-1/2} = \rho_B g w_e \theta_M \qquad (4.23c)$$

Substitution of (4.20) and (4.23a)-(4.23c) into (4.22) finally gives

$$\frac{\partial}{\partial t}(\pi\theta_M) + \nabla \cdot (\pi\theta_M \underset{\sim}{V}_M) = \rho_B g w_e \theta^+ + \rho_a g C_H |\underset{\sim}{V}_M|(\theta_S - \theta_M) \qquad (4.24)$$

It is noted that in the above argument we have distinguished $\hat{\theta}_{M-1/2}$ from $\hat{\theta}_{L+1/2}$ by choosing $\hat{\theta}_{M-1/2} = \theta_M$ and $\hat{\theta}_{L+1/2} = \theta^+$, and also $H_{M-1/2}$ from $H_{L+1/2}$ by defining the former by (4.23b) while setting $H_{L+1/2} = 0$.

b. The L7 model. The flux H in the surface layer is specified by (4.20) as in the M4 model, but now we set $\underset{\sim}{V}_a = \underset{\sim}{V}_L$ and

$\theta_a = \theta_L$, while $H_S \equiv H_{L+1/2}$. The bulk transfer coefficient C_H is computed, as in Tiedtke et al. (1979), at the height of the lowest full level which stays approximately 50 m above the ground all the time, by using the Louis formulation discussed in Section 3.1. Above the surface layer the heat flux given by Eq. (3.35) is modified to allow for counter-gradient heat flux in weakly stable conditions (Deardorff, 1966):

$$\frac{H}{\rho c_p} = \overline{w'\theta'} = -K_H \left(\frac{\partial \theta}{\partial z} - \gamma_c \right) \tag{4.25}$$

where $\gamma_c = 0.65 \times 10^{-3}$ K m^{-1}. At the same time the gradient Richardson number, Ri, necessary to compute the eddy transfer coefficients K_M and K_H is modified accordingly:

$$Ri = \frac{g}{\bar{\theta}} \frac{\left(\frac{\partial \theta}{\partial z} - \gamma_c \right)}{\left(\frac{\partial V}{\partial z} \right)^2} \tag{4.26}$$

The discrete forms of H and Ri in σ-coordinate thus have the following expressions:

$$H_{\ell+1/2} = c_p (\rho K_H)_{\ell+1/2} \left[\rho g \left(\frac{\delta \theta}{\pi \delta \sigma} \right) - \gamma_c \right]_{\ell+1/2} \quad \text{for } \ell = 1, 2, \ldots, L-1 \tag{4.27}$$

$$(Ri)_{\ell+1/2} = \frac{g}{\bar{\theta}} \left(\frac{\pi \delta \sigma}{\rho g \delta V} \right)^2_{\ell+1/2} \left[\rho g \left(\frac{\delta \theta}{\pi \delta \sigma} \right) - \gamma_c \right]_{\ell+1/2}$$

$$\text{for } \ell = 1, 2, \ldots, L-1 \tag{4.28}$$

where the form of K_H has been defined in Section 3.1.5.

The potential temperature discontinuity $\Delta \theta$ in the L7 model is calculated using the following formula:

$$\Delta \theta = \max \begin{cases} \bar{\theta}^Z - \theta^+ \\ 0.15 \gamma h_B \end{cases} \tag{4.28a}$$

where $\bar{\theta}^z$ is the mass-weighted mean θ within the mixed layer as described in Section 3.3, θ^+ is the value of θ at the height h_B that is determined by linearly extrapolating two θ's at full levels immediately above h_B downward to h_B. γ is the lapse rate of θ aloft so determined, and the coefficient 0.15 was obtained by setting $A \simeq 0.2$ in (6.13).

4.1.5 Momentum Equation

In this section the differencing of the vertical advection and frictional force terms in the vector invariant form of the momentum equation given by (2.31) will be described. The differencing scheme of the pressure gradient force has already been presented in Section 4.1.3, while the other terms will be described in Section 4.2.

a. __The M4 model.__ The vertical advection term $\dot{\sigma}\, \partial \underset{\sim}{V}/\partial\sigma$ in Eq. (2.31) is expressed as

$$\frac{1}{(\pi\delta\sigma)_\ell} \left[(\pi\dot{\sigma})_{\ell-1/2} (\underset{\sim}{V}_\ell - \hat{\underset{\sim}{V}}_{\ell-1/2}) + (\pi\dot{\sigma})_{\ell+1/2} (\hat{\underset{\sim}{V}}_{\ell+1/2} - \underset{\sim}{V}_\ell) \right]$$

$$\text{for } \ell=1,2,\ldots,L-1 \qquad\qquad (4.29)$$

where

$$\hat{\underset{\sim}{V}}_{\ell+1/2} = \frac{1}{2} (\underset{\sim}{V}_\ell + \underset{\sim}{V}_{\ell+1}) \qquad \text{for } \ell=1,2,\ldots,L-1 \qquad (4.30)$$

We have assumed an inversion layer of infinitesmal thickness δ_{INV} immediately above the PBL top (see Fig. 4.1) which is not explicitly represented in the M4 model, and therefore we set for the layer $\ell = L$:

$$\hat{\underset{\sim}{V}}_{L+1/2} = \underset{\sim}{V}^+ = \underset{\sim}{V}_L \qquad\qquad (4.31)$$

The form of $\hat{\underset{\sim}{V}}_{\ell+1/2}$ given by (4.30) ensures conservation of kinetic

energy under adiabatic conditions, while Eq. (4.31) is the form of $\hat{V}_{\ell+1/2}$ obtained from an argument on preserving the continuity of total vertical flux of momentum (Suarez and Arakawa, 1979; Suarez et al., 1983). Similarly, we set $\hat{V}_{M-1/2} = V^- = V_M$ in Eq. (4.29) for the PBL (ℓ = M) using the vertically well-mixed assumption of the PBL properties, and thus by applying the boundary condition Eq. (2.16) the vertical advection term in the discrete form (4.29) vanishes for the lowest layer of the M4 model.

The momentum flux due to the subgrid-scale turbulent motion in the surface layer, τ_S, is given by

$$\tau_S \equiv \tau_{M+1/2} = -\rho_a C_D |V_M| V_M \tag{4.32}$$

Here we have again used the well-mixed assumption to set

$V_a = V_M$. The drag coefficient C_D will be calculated from the formula derived by Louis (1979) and Louis et al. (1982), as discussed in Section 3.1. The height at which C_D is calculated is defined in the same way as it is done for C_H discussed earlier in this chapter.

At the top of the PBL but below the infinitesmal inversion layer the turbulent momentum flux τ^- is defined by

$$\tau^- \equiv \tau_{M-1/2} = -\rho_B w_e \Delta V \tag{4.33}$$

where $\Delta V \equiv \hat{V}_{L+1/2} - \hat{V}_{M-1/2} = V_L - V_M$. Eq. (4.33) can be derived from the budget equation for V in the PBL (Suarez et al., 1983). On substituting (4.32) and (4.33) into the discrete form of the frictional force term in (2.31), $[(g/\pi)\delta\tau/\delta\sigma]_\ell$, we obtain for the PBL:

$$\left[\frac{g}{\pi}\frac{\delta\tau}{\delta\sigma}\right]_M = \frac{g}{\pi_M}\left[\rho_B w_e \Delta \underset{\sim}{V} - \rho_a C_D |\underset{\sim}{V}_M|\underset{\sim}{V}_M\right] \tag{4.34}$$

Here we have used $(\delta\sigma)_M = 1$.

On the other hand, the turbulent flux at the PBL top but above the infinitesmal inversion layer, $\underset{\sim}{\tau}^+$, is set

$$\underset{\sim}{\tau}^+ \equiv \underset{\sim}{\tau}_{L+1/2} = 0 \tag{4.35}$$

by assuming that there is no turbulence at this level and above. Therefore, we also have

$$\underset{\sim}{\tau}_{\ell+1/2} = 0 \quad \text{for } \ell = 1,2,\dots,L-1 \tag{4.36}$$

and the frictional force term in discrete form vanishes for layers $\ell = 1,2,\dots,L$.

b. <u>The L7 model</u>. The vertical advection term given by (4.29) applies to the L7 model for layers $\ell = 1,2,\dots,L$. Since quantities at the PBL top are not explicitly predicted, the half-level velocity given by (4.30) is valid for $\ell = 1,2,\dots,L-1$ in the L7 model. The turbulent flux of momentum in the surface layer takes the same form as (4.32):

$$\underset{\sim}{\tau}_S \equiv \underset{\sim}{\tau}_{L+1/2} = -\rho_a C_D |\underset{\sim}{V}_L|\underset{\sim}{V}_L \quad \text{for } L=7 \tag{4.37}$$

The drag coefficient C_D is computed by using the Louis scheme as in the M4 model, but at the height of the lowest full level as in the case of C_H.

The turbulent flux of momentum above the surface layer is given by Eq. (3.34) in Section 3.1, the discrete form of which is defined by

$$\underset{\sim}{\tau}_{\ell+1/2} = g\left[\rho^2 K_M \frac{\delta\underset{\sim}{V}}{\delta\sigma}\right]_{\ell+1/2} \quad \text{for } \ell = 1,2,\dots,L-1 \tag{4.38}$$

The form of K_M has been defined by Eq. (3.36) and the discrete Richardson number necessary to compute K_M is given by Eq. (4.28).

4.2 Horizontal Differencing Scheme

The horizontal differencing of the momentum equation and the continuity equation is based on the second-order potential enstrophy and total energy conserving scheme by Arakawa and Lamb (1981) for the shallow water system (hereafter referred to as the AL scheme). The scheme has been tested and compared with a total energy conserving scheme proposed by Sadourny (1975), the results of which will be given in Section 4.3. The horizontal differencing of the thermodynamic equation, on the other hand, utilizes the simplest second-order centered scheme. Since the derivation of the AL scheme involves extensive algebra we present in this section only the expressions relevant to our models.

4.2.1 Horizontal Grid Structure

The AL horizontal differencing scheme uses the so-called C-grid depicted in Fig. 4.2, which is staggered, and has an advantage of increasing the effective resolution by a factor of two. It also gives better simulations of the geostrophic adjustment as described by Mesinger and Arakawa (1976). The grid interval d is uniform in both the x- and y-directions and the distribution of the variables is as shown in Fig. 4.2. The quantities θ, ϕ, p, ω, and $\dot{\sigma}$ are defined at the "h" point, but $\dot{\sigma}$ is assigned to the "half" level, while other quantities are assigned to the "full" level in the vertical.
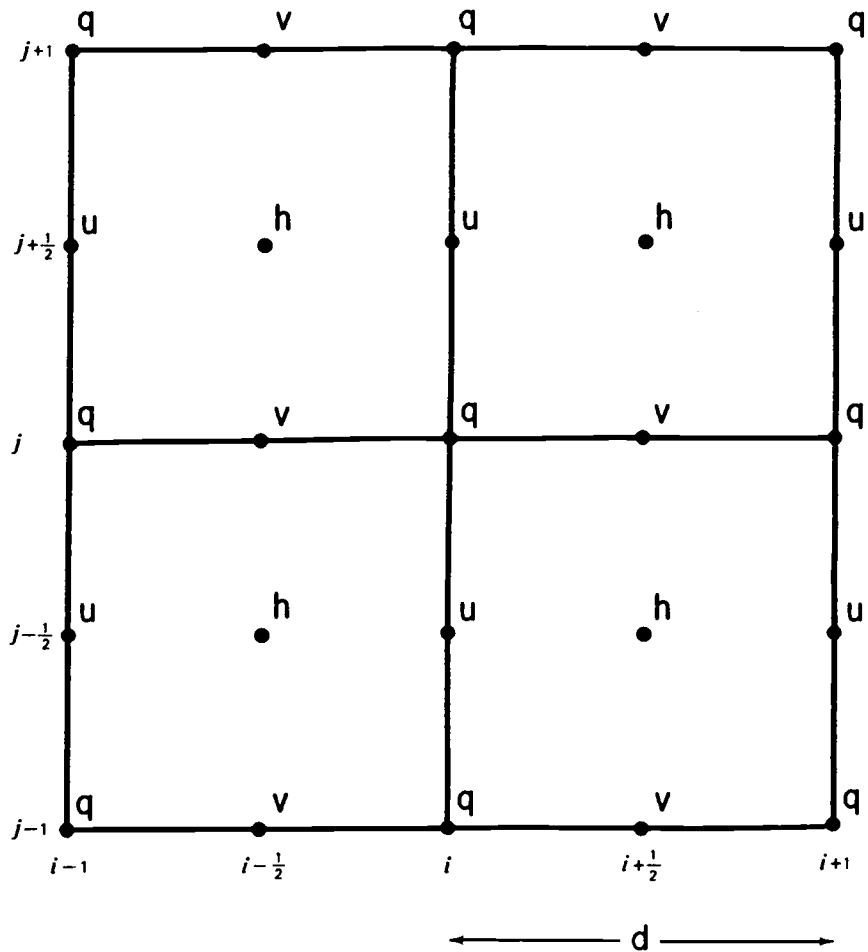
Fig. 4.2. Horizontal arrangement of the dependent variables on
"C" grid used in the AL scheme. The grid interval d is
uniform in both x- and y-directions.

4.2.2 Momentum Equations

The components of the momentum equation in vector invariant form given by Eq. (2.31) can be written under adiabatic frictionless conditions with $\underset{\sim}{V}_g = 0$ as:

$$\left(\frac{\partial}{\partial t}\right)_\sigma u - (\pi v)q + \left(\frac{\partial}{\partial x}\right)_\sigma [K+\phi] + (\pi\dot\sigma)\frac{\partial u}{\pi\partial\sigma} = 0 \qquad (4.39)$$

$$\left(\frac{\partial}{\partial t}\right)_\sigma v + (\pi u)q + \left(\frac{\partial}{\partial y}\right)_\sigma [K+\phi] + (\pi\dot\sigma)\frac{\partial v}{\pi\partial\sigma} = 0 \qquad (4.40)$$

where $K = 1/2(u^2+v^2)$, $q = (f+\zeta)/\pi$, and $\zeta = k\cdot\nabla_\sigma \times \underset{\sim}{V}$. We consider here the case in which $\pi\dot\sigma = 0$. Then Eqs. (4.39) and (4.40) can be expressed in general form as

$$\frac{\partial}{\partial t}u_{i,j+1/2} - \alpha_{i,j+1/2}v^*_{i+1/2,j+1} - \beta_{i,j+1/2}v^*_{i-1/2,j+1} - \gamma_{i,j+1/2}v^*_{i-1/2,j}$$

$$-\delta_{i,j+1/2}v^*_{i+1/2,j} + \varepsilon_{i+1/2,j+1/2}u^*_{i+1,j+1/2} - \varepsilon_{i-1/2,j+1/2}u^*_{i-1,j+1/2}$$

$$+ \frac{1}{d}[K_{i+1/2,j+1/2} - K_{i-1/2,j+1/2} + \phi_{i+1/2,j+1/2} - \phi_{i-1/2,j+1/2}] = 0$$

$$(4.41)$$

$$\frac{\partial}{\partial t}v_{i+1/2,j} + \gamma_{i+1,j+1/2}u^*_{i+1,j+1/2} + \delta_{i,j+1/2}u^*_{i,j+1/2} + \alpha_{i,j-1/2}u^*_{i,j-1/2}$$

$$+\beta_{i+1,j-1/2}u^*_{i+1,j-1/2} + \eta_{i+1/2,j+1/2}v^*_{i+1/2,j+1} - \eta_{i+1/2,j-1/2}v^*_{i+1/2,j-1}$$

$$+ \frac{1}{d}[K_{i+1/2,j+1/2} - K_{i+1/2,j-1/2} + \phi_{i+1/2,j+1/2} - \phi_{i+1/2,j-1/2}] = 0$$

$$(4.42)$$

where $u^*_{i+1,j+1/2} \equiv (\pi^{(u)}u)_{i+1,j+1/2}$ and $v^*_{i+1/2,j} \equiv (\pi^{(v)}v)_{i+1/2,j}$. α, β, γ, δ, ε, and η are linear functions of q, and superscripts u and v indicate that $\pi^{(u)}$ and $\pi^{(v)}$ are defined at the u- and v-points, respectively. K is defined at the h point. Undefined coefficients in (4.41) and (4.42) are determined by imposing the constraints discussed in Sections 2.1 and 4.1.3, and the resulting expressions for the coefficients are

$$\epsilon_{i+1/2,j+1/2} = \frac{1}{24}\left[q_{i+1,j+1} + q_{i,j+1} - q_{i,j} - q_{i+1,j}\right]$$

$$\eta_{i+1/2,j+1/2} = \frac{1}{24}\left[-q_{i+1,j+1} + q_{i,j+1} + q_{i,j} - q_{i+1,j}\right]$$

$$\alpha_{i,j+1/2} = \frac{1}{24}\left[2q_{i+1,j+1} + q_{i,j+1} + 2q_{i,j} + q_{i+1,j}\right]$$

$$\beta_{i,j+1/2} = \frac{1}{24}\left[q_{i,j+1} + 2q_{i-1,j+1} + q_{i-1,j} + 2q_{i,j}\right]$$

$$\gamma_{i,j+1/2} = \frac{1}{24}\left[2q_{i,j+1} + q_{i-1,j+1} + 2q_{i-1,j} + q_{i,j}\right]$$

$$\delta_{i,j+1/2} = \frac{1}{24}\left[q_{i+1,j+1} + 2q_{i,j+1} + q_{i,j} + 2q_{i+1,j}\right]$$

(4.43)

The "potential vorticity" q is now given by

$$q_{ij} = \frac{(f+\zeta)_{ij}}{\pi^{(q)}_{ij}} \tag{4.44}$$

where

$$\zeta_{ij} = \frac{1}{d}\left[u_{i,j-1/2} - u_{i,j+1/2} + v_{i+1/2,j} - v_{i-1/2,j}\right] \tag{4.45}$$

$$\pi^{(q)}_{ij} = \frac{1}{4}\left[\pi_{i+1/2,j+1/2} + \pi_{i-1/2,j+1/2} + \pi_{i-1/2,j-1/2} + \pi_{i+1/2,j-1/2}\right] \tag{4.46}$$

The quantities $\pi^{(u)}$ and $\pi^{(v)}$ are expressed as

$$\pi^{(u)}_{i,j+1/2} = \frac{1}{2}\left[\pi_{i+1/2,j+1/2} + \pi_{i-1/2,j+1/2}\right]$$

$$\pi^{(v)}_{i+1/2,j} = \frac{1}{2}\left[\pi_{i+1/2,j+1/2} + \pi_{i+1/2,j-1/2}\right] \tag{4.47}$$

The form of K is defined by

$$K_{i+1/2,j+1/2} = \frac{1}{4}\overline{\left[u^2_{j+1/2} + \frac{1}{4}(u_{j+3/2} + u_{j-1/2})^2\right]}^{i}_{i+1/2,j+1/2}$$

$$+ \frac{1}{4}\overline{\left[v_{i+1/2} + \frac{1}{4}(v_{i+3/2} + v_{i-1/2})^2\right]}^{j}_{i+1/2,j+1/2} \tag{4.48}$$

We use the above definition of kinetic energy instead of the more conventional 4-point definition of K (see Arakawa and Lamb, 1981) since we have found that Eq. (4.48) to some extent stabilizes the hydraulic jump-like phenomena that occur near the steep bottom topography in the M4 model when the lowest layer is shallow.

The scheme described above conserves total energy under adiabatic conditions. It also maintains conservation of the "potential enstrophy", defined by the global integral of $1/2\ q^2$ with respect to mass, under adiabatic conditions when $\pi\dot{\sigma} = 0$ and when no vorticity is generated by pressure gradient and frictional forces.

4.2.3 Integral Invariants

One of the major problems that has to be considered when selecting a finite-difference scheme for a numerical model is the computational stability of the method chosen. It is well known that aliasing errors generated by the nonlinearity of the horizontal advective processes cause the most serious numerical instabilities (Burridge, 1980). An aliasing error, which was first discussed by Phillips (1959), is due to the inability of the discrete grid to resolve wave lengths shorter than 2 grid intervals. Knowing only the values at grid points, a wave generated by a nonlinear interaction in the advective term that is shorter than the minimum resolvable wave length (2 grid intervals) is falsely represented as a wave of a longer wave length. Thus, a spurious energy inflow is expected to wave lengths that are slightly greater than the shortest resolvable wave length, and after a finite time of the numerical integration, the growth of energy through the feedback in the range

of these wave lengths can become beyond physically meaningful limit (Mesinger and Arakawa, 1976).

It has been known through the work of Fjortoft (1953), Arakawa (1966) and Lilly (1965) that in the discrete system the maintenance of the integral constraints satisfied by continuous equations plays an important role in preventing nonlinear instability in a nondivergent flow. In particular, it has been shown that the conservation of enstrophy or potential (absolute) enstrophy in nondivergent barotropic flows not only prevents nonlinear instability, but it is also essential for both reproducing the realistic exchanges of energy between different scales of motion and representing the dynamics correctly. Failure to conserve enstrophy or potential enstrophy in nondivergent barotropic flows leads to the spurious inflow of energy to shorter waves even when the total energy is conserved with some schemes, eventually resulting in a catastrophy (Arakawa and Lamb, 1977; Sadourny 1975; Fair weather and Navon, 1980). It is always possible through addition of artificial lateral diffusion schemes to control the false energy cascade by removing energy directly at the small scale end of the spectrum. However, doing so enhances the total amount of energy dissipation and removes erroneously energy from the atmospheric system we are investigating. Therefore, it is more desirable to obtain a realistic energy distribution through proper treatment of the nonlinear interactions, rather than by adding artificial viscosity.

Existence of steep mountains plays an important role in the generation and maintenance of the whole spectra of waves ranging from planetary scale to mesoscale. Recognizing that the mechanisms

for wave generation and subsequent evolution are nonlinear and involve smaller scales, Arakawa and Lamb (1981) have sought a finite-difference scheme whose dynamics represents properly even the nonlinear aspects of the flow over steep topography of a homogeneous fluid described by the shallow water equations. It can be shown that in such a flow each fluid parcel conserves the potential vorticity, $q \equiv (\zeta+f)/h$, during the advective processes over mountains:

$$\frac{Dq}{Dt} = 0 \tag{4.49}$$

where ζ is the relative vorticity, f is the Coriolis parameter, and h is the depth of the fluid. As shown below, this leads to conservation of the potential enstrophy $1/2\ hq^2$ in a closed domain:

$$\frac{d}{dt} \iint \frac{1}{2}\ hq^2\ dxdy = 0$$

and it is found that the enstrophy $(hq)^2$ is bounded, since

$$\iint (hq)^2\ dxdy < \iint \frac{h_{max}}{h} (hq)^2\ dxdy = h_{max} \iint hq^2\ dxdy = constant.$$

The quasi-two-dimensional, quasi-nondivergent motion such as one in the shallow water system approximately follows the laws of two-dimensional turbulence (Sadourny, 1975), and therefore energy cascade is restricted although h is variable, as it is in a purely two-dimensional flow. Conservation of the potential vorticity (4.49) does not always hold in the discrete system because large gradients in h as well as in $\zeta + f$ cause large truncation errors near steep mountains, thus preventing q from being conserved accurately. In fact, Arakawa and Lamb (1981) have found that when applied to the shallow water system, conventional differencing

schemes advect the potential vorticity poorly in the presence of steep topography. They also have found that an enstrophy conserving scheme for a purely two-dimensional flow does not necessarily guarantee conservation of potential enstrophy. To overcome these deficiencies, Arakawa and Lamb (1981) have developed a finite-difference scheme which is designed to conserve potential enstrophy as well as total energy. Following Arakawa and Lamb (1981), a summary of continuous integral constraints is given below which the new scheme is designed to maintain.

The governing shallow water equations for an incompressible inviscid fluid with a free surface can be written in the following vector invariant form:

$$\frac{\partial \underset{\sim}{V}}{\partial t} + q \underset{\sim}{k} \times \underset{\sim}{V}^* + (K+\phi) = 0 \tag{4.50}$$

$$\frac{\partial h}{\partial t} + \nabla \cdot \underset{\sim}{V}^* = 0 \tag{4.51}$$

where $\underset{\sim}{V}^*$ is the mass flux defined by $\underset{\sim}{V}^* = h\underset{\sim}{V}$, K is the kinetic energy, and ϕ is the geopotential of the free surface above sea (reference) level defined by $\phi = g(h+h_S)$, with h_S being the bottom surface height. Integrating (4.51) over a closed domain we obtain the conservation of mass:

$$\frac{d}{dt} \iint h \, dxdy = 0 \tag{4.52}$$

The kinetic energy equation is obtained by multiplying (4.50) by V^* and combining the result with (4.51):

$$\frac{\partial}{\partial t} (hK) + \nabla \cdot (\underset{\sim}{V}^*K) + \underset{\sim}{V}^* \cdot \nabla\phi = 0 \tag{4.53}$$

The potential energy equation can be found by multiplying (4.51) by ϕ:

$$\frac{\partial}{\partial t} [h(\frac{1}{2} gh + gh_S)] + \nabla \cdot (\underline{V}^* \phi) - \underline{V}^* \cdot \nabla\phi = 0 \qquad (5.54)$$

Adding (4.53) and (4.54) and integrating over the domain, we obtain

$$\frac{d}{dt} \iint [h(K + \frac{1}{2} gh + gh_S)] dxdy = 0 \qquad (4.55)$$

which expresses the conservation of total energy. The vorticity equation for this system is obtained from (4.50) and (4.51):

$$\frac{\partial}{\partial t} (hq) + \nabla \cdot (\underline{V}^* q) = 0 \qquad (4.56)$$

The equation of potential vorticity following a fluid parcel can be formed by subtracting (4.51) times q from (4.56) and dividing the result by h:

$$\frac{\partial q}{\partial t} + \underline{V} \cdot \nabla q = 0 \qquad (4.57)$$

Thus it can be seen that if q is constant everywhere, then there should be no time change of q. The equation for the potential enstrophy $1/2 \, hq^2$ can be derived by multiplying (4.51) by $1/2 \, q^2$ and (4.57) by hq and adding:

$$\frac{\partial}{\partial t} (\frac{1}{2} hq^2) + \nabla \cdot (\underline{V}^* \frac{1}{2} q^2) = 0 \qquad (4.58)$$

Integration of this equation over the domain results in

$$\frac{d}{dt} \iint \frac{1}{2} hq^2 \, dxdy = 0 \qquad (4.59)$$

which states conservation of potential enstrophy for the shallow water system. The differencing scheme developed by Arakawa and Lamb (1981) is designed to conserve the potential enstrophy as well as

the total energy. Furthermore, since the major objective of their deriving a new finite-difference scheme was to properly represent the flow over steep topography, the finite difference equations were required to satisfy the condition that when q is constant in space, then it cannot change in time. This requirement is important because, as described earlier, existence of high mountains causes large variations of gradients of ζ + f and h, which could result in large errors when the conventional schemes are used. Potential enstrophy conserving schemes have also been derived by other investigators such as Sadourny (1975) and Navon and Riphagen (1979). Sardourny's scheme is similar to that by Arakawa and Lamb (1981). However, it conserves the kinetic energy in the case of $\nabla \cdot \underset{\sim}{V}{}^* \neq 0$, while the potential enstrophy is conserved only for the flow with nondivergent mass flux $\nabla \cdot \underset{\sim}{V}{}^* = 0$, but not for the general flow.

4.2.4 Test Problem

Conservation of the quadratic invariant was tested for the Arakawa and Lamb (AL) scheme described earlier by numerically integrating the shallow-water equations with initial condition II used by Grammeltvedt (1969). The results are compared with those of a scheme derived by Sadourny (1975) that conserves the total energy but not the potential enstrophy (hereafter called the SE scheme).

Initial condition II employed by Grammeltvedt (1969) describes a westerly jet in an idealized barotropic flow in a cyclic channel on a β-plane with north-south perturbations of wavenumbers 1 and 3 along the zonal axis of the jet (Fig. 4.3). The same initial condition was also used by Gerrity et al. (1972) and Navon and
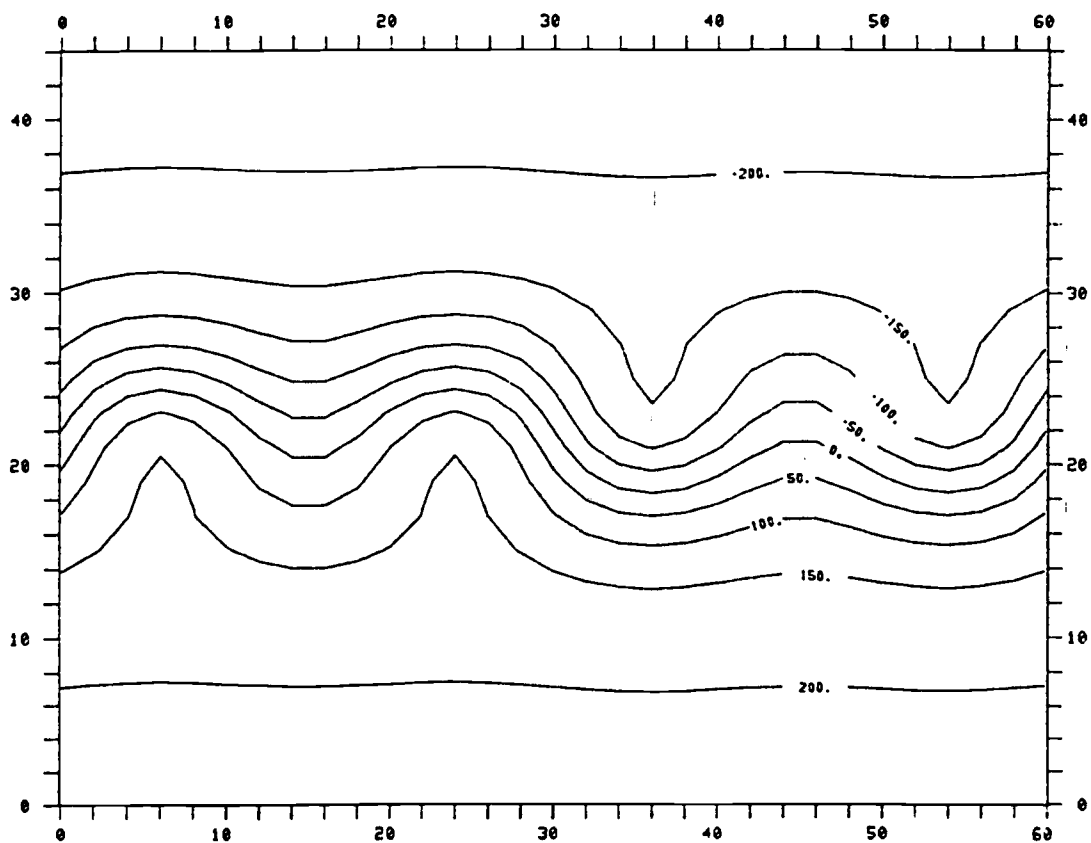
Fig. 4.3. Initial distribution of the height deviation relative to
the mean height of the free surface above mean sea level
(2000 m). Isopleths are drawn at 50 m intervals. The
domain is in units of 100 km.

Riphagen (1979) for testing fourth-order finite-difference schemes and by Cullen (1977) for finite-element schemes. The initial height field is given by

$$h + h_S = H_0 + H_1 \tanh \frac{9(y-D/2)}{2D}$$

$$+ H_2 \operatorname{sech}^2 \frac{9(y-D/2)}{D} [0.7 \sin(\frac{2\pi x}{L}) + 0.6 \sin(\frac{6\pi x}{L})]$$

where L is the channel length, D is the width. The boundary conditions are cyclic in the x-direction and the sides of the channel are rigid walls. The initial velocity fields are assumed to be geostrophic and are derived from the initial height field using the geostrophic approximation:

$$u = - \frac{g}{f} \frac{\partial(h+h_S)}{\partial y}, \quad v = \frac{g}{f} \frac{\partial(h+h_S)}{\partial x} .$$

In the numerical integration the following values were adopted:

D = 4400 km   L = 6000 km

H_0 = 2000 m H_1 = -220 m H_2 = 133 m

g = 10 ms^{-2} f_0 = 10^{-4}s^{-1} β = 1.5x10^{-11}s^{-1}m^{-1}

where $f = f_0 + \beta(y-D/2)$. The bottom topography was added to the above initial condition in order to test the efficiency of each scheme in the presence of non-uniform terrain. A narrow triangular ridge was placed at x = 3000 km which extended uniformly across the channel in the y-direction. The maximum height of the ridge was 1000 m and the width was 800 km at the bottom. Both the AL and SE schemes were integrated for 20 days, using the leap-frog method in time with a 5-minute time step. The Matsuno scheme was inserted every 30 time steps to eliminate the computational mode. The grid

size of 200 km was used in both the x- and y-directions, with 30 x 24 grid points inside the domain.

4.2.5 Results

The time evolutions of the integral invariants for the shallow-water equations i.e., total mass and energy, and potential enstrophy, are shown in Fig. 4.4 for the AL scheme (left) and the SE scheme (right). It is evident that both schemes maintain almost perfect conservation of mass (top figures). Total energy is also conserved within the limit of the machine truncation errors: total energy is 0.9999 relative to the starting value for the AL scheme and 0.9998 for the SE scheme at the end of day 20 (middle figures). On the other hand, the potential enstrophy increases linearly during the first 10 days for the SE scheme to 1.44 relative to the starting value, but it amplifies more rapidly during the next 10 days, reaching 3.49 at the end of the 20th day. Contrary to the SE scheme, the variations of the potential enstrophy for the AL scheme in time are confined to less than 1% of the starting value throughout the integration period. Note that the scales of the ordinates are different in the bottom figures.

The effects of maintaining conservation of the potential enstrophy for each scheme are evident in the relative vorticity patterns displayed in the Figs. 4.5 and 4.6. The initial vortices given in Fig. 4.5 are advected eastward over the mountain ridge across the channel at x = 3000 km. After 2 days of integrations the relative vortices for the SE scheme begin to disintegrate noticeably, while those for the AL scheme maintain most of the
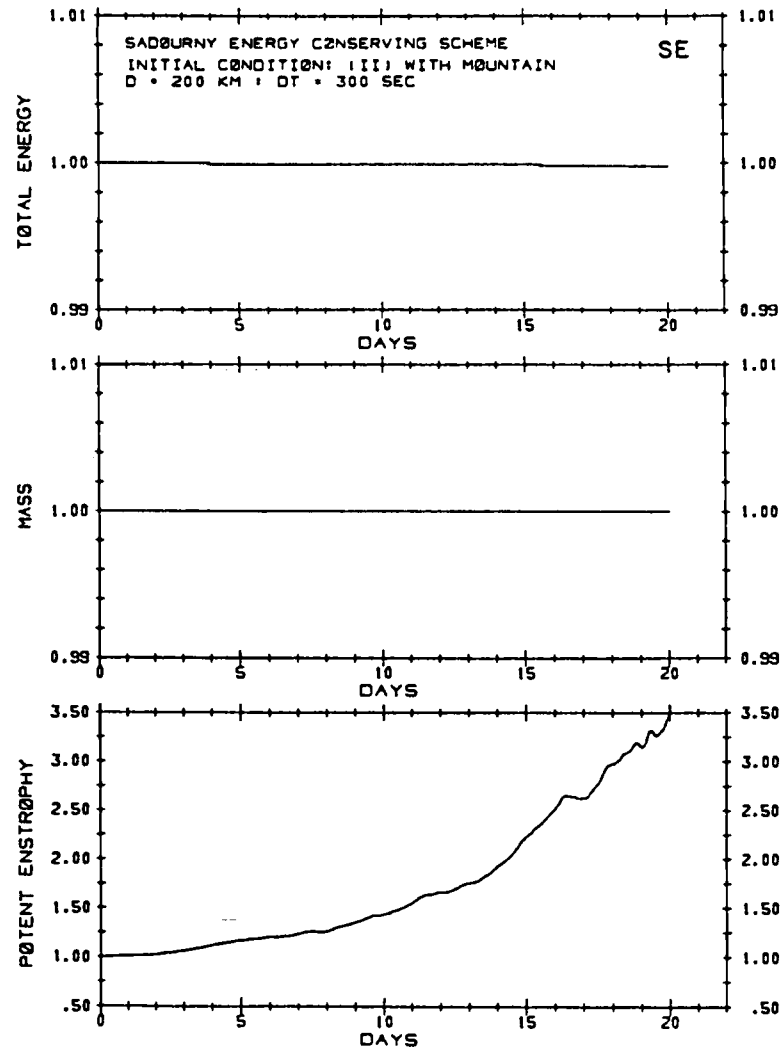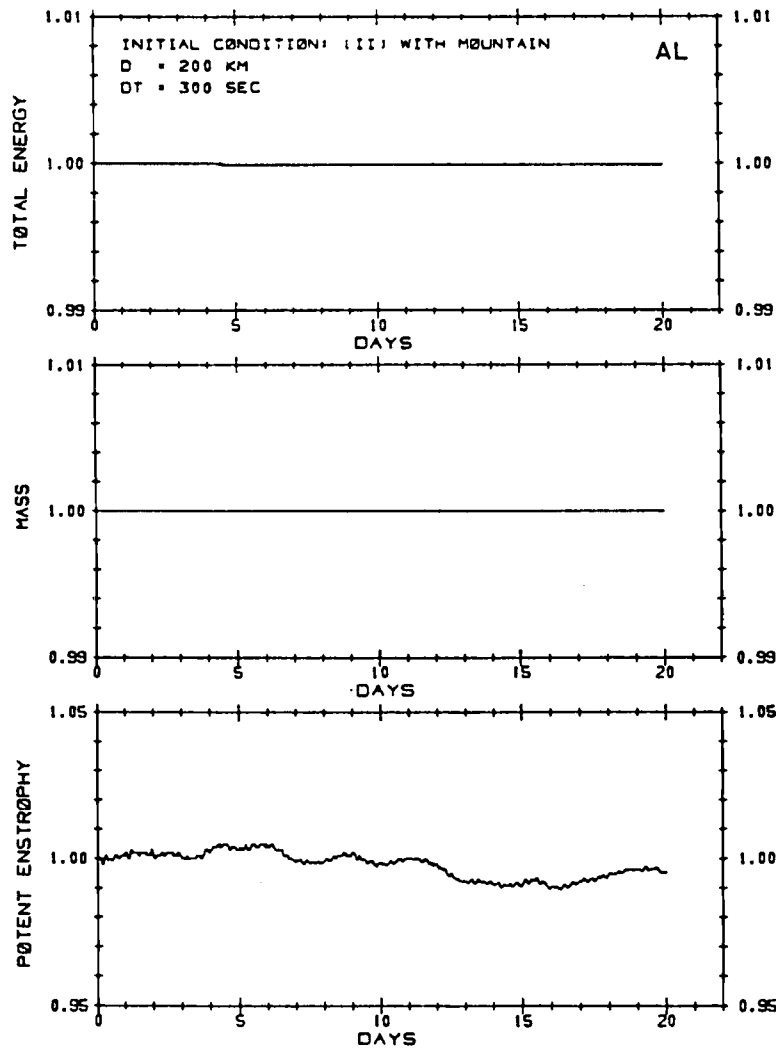
Fig. 4.4. The time evolution of total energy (top panel), mass (middle) and potential enstrophy (bottom) for the AL scheme (left panels) and the SE scheme (right). The scale of the ordinate is relative to the starting value, and the abscissa is in units of day.
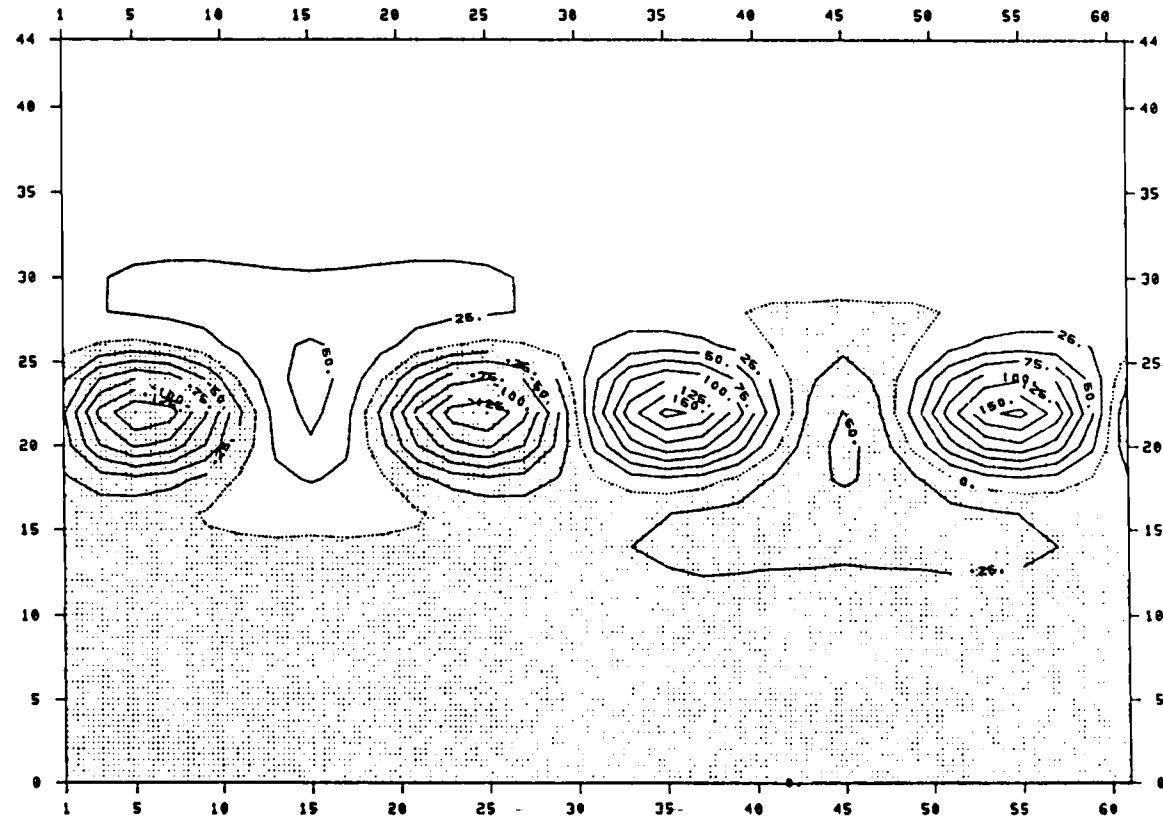
Fig. 4.5. The initial distributuion of the relative vorticity for both SE and AL schemes. Isopleths are drawn at $25 \times 10^{-6}\text{s}^{-1}$ intervals. The shaded area shows the domain of negative vortices. The domain is in units of 100 km.
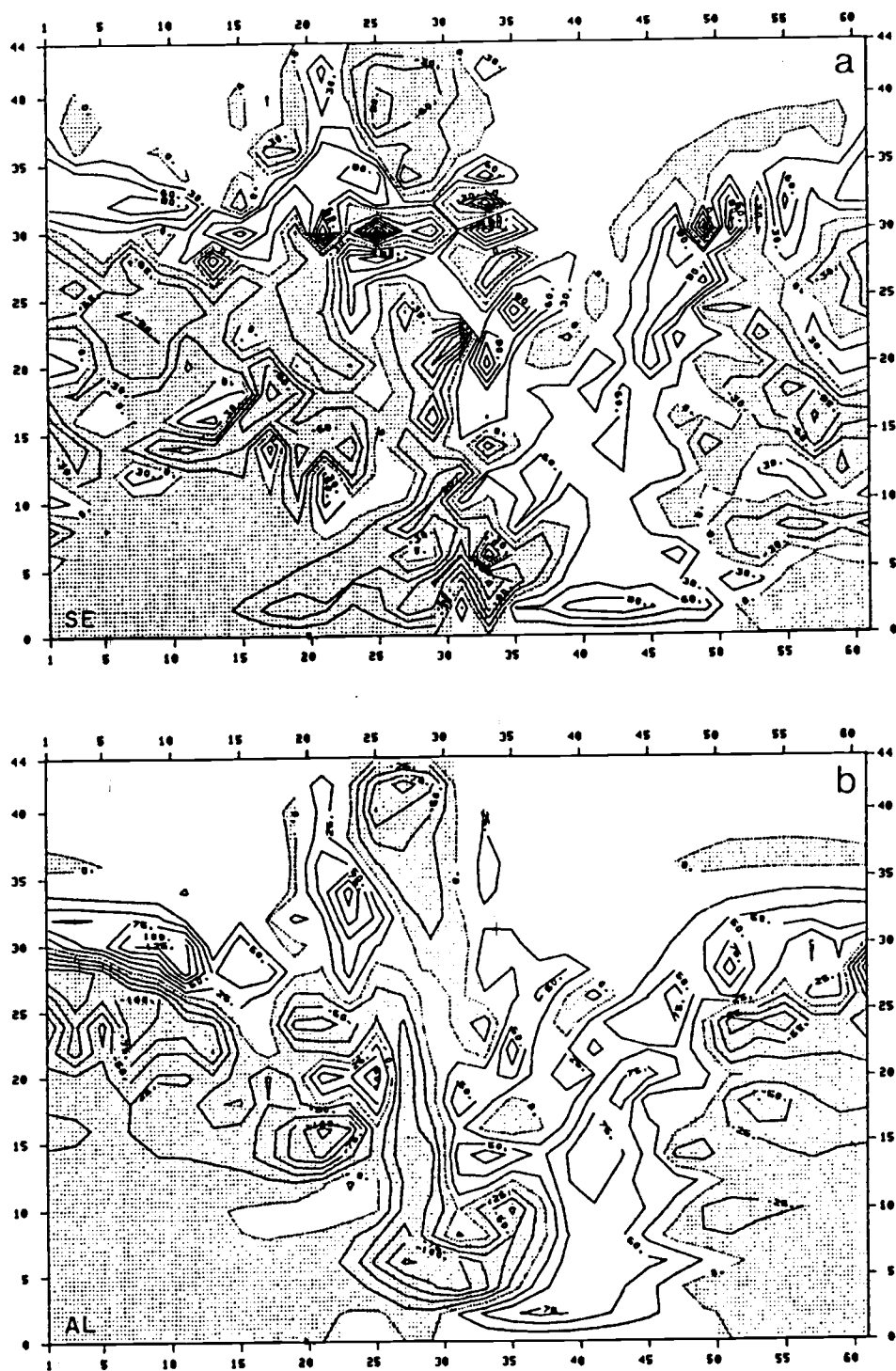
Fig. 4.6. As in Fig. 4.5 except that the fields are after 3 days for (a): the SE scheme, and (b): the AL scheme. Isopleths are drawn at $30 \times 10^{-6} s^{-1}$ intervals.

original vortices. The relative vorticity fields after 3 days are given in Fig. 4.6. The vortices for the SE scheme are considerably disoriented compared to those of the AL scheme, leaving little trace of the starting vorticity patterns, while the AL scheme still retains the major vortices from the initial condition. The extreme magnitude of the vortices generally begins to increase after 5 days as that of potential enstrophy does in the case of the SE scheme, and at the end of the 20th day it becomes over 3 times as large as the initial extreme magnitude. At the same time the size of the individual vortices approaches twice the grid interval. These vortices scatter over the channel without any organized pattern. On the other hand, the maximum magnitude of the vortices for the AL scheme remains within a limit of small fluctuations from the initial extremes throughout the integration period. Individual vortices tend to become smaller, approaching twice the size of the grid interval as in the case of the SE scheme, which seems to indicate the occurrence of 3-grid interval instability due to non-conservation of momentum of the AL scheme discussed in Hollingsworth et al. (1983), although the vortices are still grouped in large positive and negative cyclones even after 20 days. Inspection of the height fields reveals that both schemes produce similar patterns for the first 10 days. However, the height field after 15 days for the SE scheme shows considerable deterioration. It becomes completely disorganized after 20 days and the influence of the bottom ridge is hardly evident (Fig. 4.7a). By contrast, the height fields for the AL scheme are much smoother even after the 20-day integration (Fig. 4.7b).
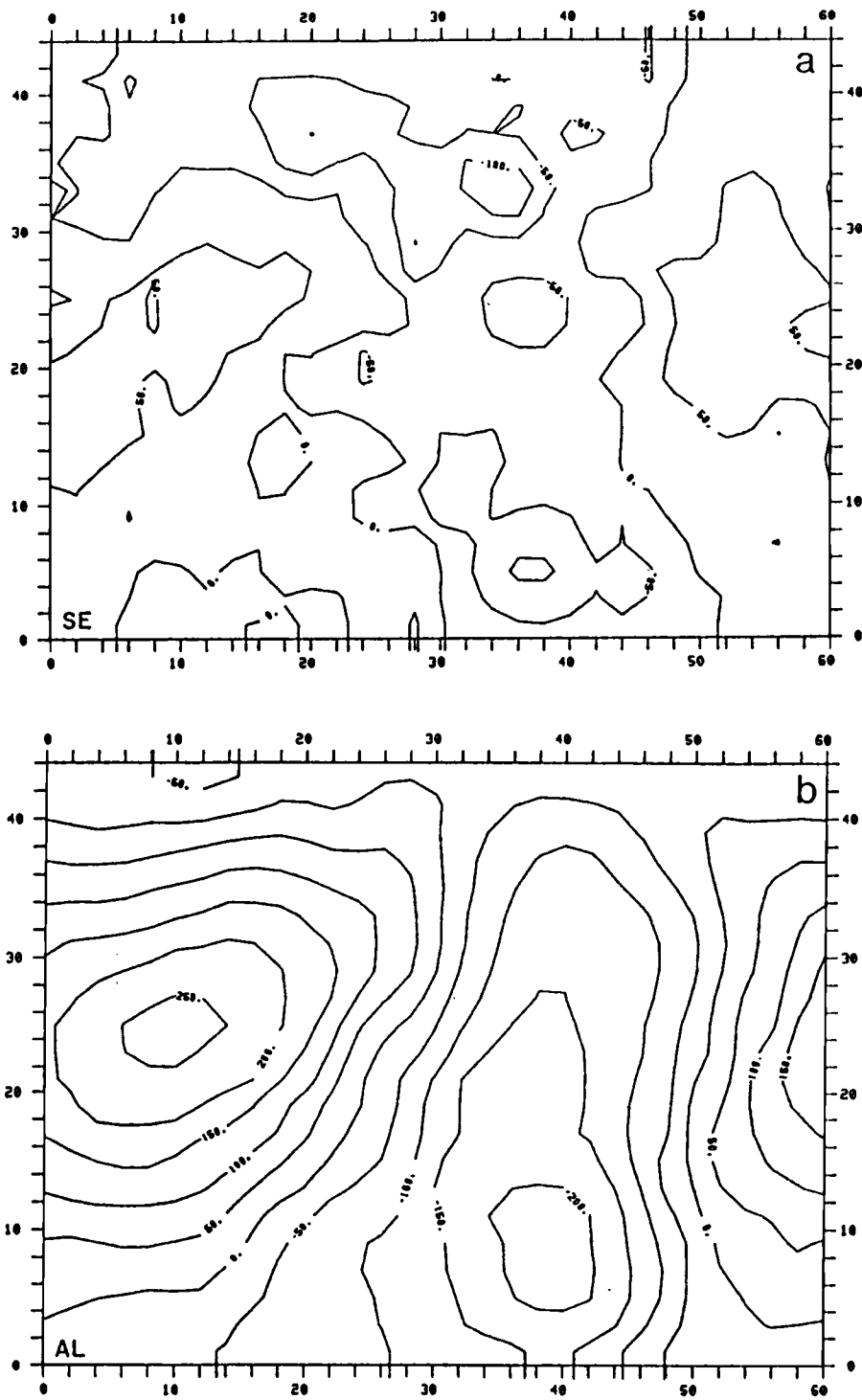
Fig. 4.7. As in Fig. 4.3 except that the fields are after 20 days for
(a): the SE schemes, and (b): the AL scheme.

The numerical experiments with both schemes reveal that the AL scheme which conserves the potential enstrophy as well as total energy is superior to the SE scheme which conserves the total energy only, in that conservation of the potential enstrophy inhibits a spurious energy cascade, thus leading to more realistic advection of the relative vorticity and the height fields and hence to better representation of the dynamics in the vicinity of the mountain.

Although the above experiments were carried out for a barotropic flow in a domain much larger than meso-β scale for a longer period of time than a period of up to 2 days we are primarily interested in, we can expect that the potential enstrophy conserving scheme of Arakawa and Lamb (1981) should perform equally well in representing the overall dynamics in a mesoscale domain for a shorter period of integrations.

Since local accuracy plays an important role in short-time mesoscale predictions, it is desirable that the AL scheme should also be tested for optimum accuracy in phase velocities and amplitudes along the lines of investigations that many workers have followed in the past (Navon and Riphagen, 1979; Cullen, 1977; Gretty et al., 1972; Williamson, 1969; Gustafsson, 1971).

4.3 Numerical Treatment of the Pressure Gradient Force

In the σ-coordinate system, the pressure gradient force, $-\nabla_p \phi$, consists of two terms as given in Eqs. (2.35) and (2.36). In the regions where the slope of terrain is steep and irregular, the individual terms on the right-hand side of Eqs. (2.35)-(2.36) tend to be large in magnitude but to have opposite signs, and thus

relatively small errors in these two terms could result in a large error in the pressure gradient force. For example, Sundqvist (1975) states that individual terms are 10-20 times greater than a typical value of their sum, and hence, a 1% deviation in temperature (2-3 C) would result in a 10% error in the pressure gradient force. In attempts to reduce this error, several methods have been proposed (e.g., Corby et al., 1972; Gary, 1973; Janijic, 1977; Nakamura, 1978; Tomine and Abe, 1982), while a review of selected approaches to this problem has been given by Mesinger (1982). Particularly, the concept of an <u>adiabatic reference atmosphere</u> was proposed by Phillips (1974) in an attempt to significantly reduce the effect of orographic truncation errors by allowing the geopotentials and the potential temperatures to be expressed as their deviations from this reference atmosphere. In the numerical models described here we follow Phillips' (1974) idea since it is consistent with the finite-difference scheme proposed by Suarez and Arakawa (1979) which we utilize in our models. A brief description of the adiabatic reference atmosphere and the results of its application to a simple model are presented below.

4.3.1 Adiabatic Reference Atmosphere

Phillips (1974) proposed an adiabatic reference atmosphere $\bar{\theta}$ and $\bar{\phi}(p)$ defined by

$$\theta = \theta' + \bar{\theta} \quad (\bar{\theta} = \text{constant}) \tag{4.60}$$

$$\phi = \phi' + \bar{\phi}(p) \tag{4.61}$$

$$\bar{\phi}(p) = \bar{\phi}_0 - c_p \bar{\theta} P \quad (\bar{\phi} = \text{constant}) \tag{4.62}$$

where $\bar{\theta}$ represents the reference potential temperature, which is a constant, $\bar{\phi}(p)$ is the reference geopotential which depends only on the pressure, and $\bar{\phi}_0$ is a constant. Thus, θ' and ϕ' are deviations of θ and ϕ from these references, respectively. $\bar{\theta}$ and $\bar{\phi}_0$ are given by

$$\bar{\theta} = \frac{\bar{\phi}(p_T) - \bar{\phi}(\langle p_S \rangle)}{c_p(\bar{P}_S - P_T)} \tag{4.63}$$

$$\bar{\phi}_0 = \frac{\bar{\phi}(p_T)\bar{P}_S - \bar{\phi}(\langle p_S \rangle)P_T}{\bar{P}_S - P_T} \tag{4.64}$$

where

$\bar{\phi}(p_T) = \langle \phi_T \rangle$: average (initial) ϕ at p_T,

$\bar{\phi}(\langle p_S \rangle) = \langle \phi_S \rangle$: average surface geopotential,

$\bar{P}_S = [\langle p_S \rangle / p_{00}]^\kappa$: average of (2.25) and $p_{00} = 1$,

and $\langle \ \rangle$ denotes domain average. Thus, Eqs. (4.60)-(4.64) give

$$\bar{\phi}(p) = \frac{\langle \phi_T \rangle(\bar{P}_S - P) + \langle \phi_S \rangle(P - P_T)}{\bar{P}_S - P_T} \tag{4.65}$$

We note that ϕ in the momentum equation given by (2.30) can be the actual geopotential or it can be the deviation, ϕ', defined in (4.61), since ϕ enters (2.30) only through $-\nabla_p\phi$. It is also noted that the thermodynamic equation (2.28) is unchanged if θ is replaced by θ' as defined in (4.60). The kinetic energy equation

$$\frac{\partial}{\partial t}\left(\pi \frac{1}{2}\underset{\sim}{V}^2\right) + \nabla_\sigma \cdot \left(\pi\underset{\sim}{V}\frac{1}{2}\underset{\sim}{V}^2\right) + \frac{\partial}{\partial\sigma}\left(\pi\dot{\sigma}\frac{1}{2}\underset{\sim}{V}^2\right)$$

$$= -\pi\underset{\sim}{V} \cdot \nabla_p\phi + \pi\underset{\sim}{V} \cdot \underset{\sim}{F} \tag{4.66}$$

is also valid if ϕ is replaced by ϕ'. Here $\underset{\sim}{F}$ represents the frictional force. It can be proven that the enthalpy equation, and the hydrostatic equation given by (2.27) are also unchanged if ϕ and θ are replaced by ϕ' and θ', respectively, provided that the absolute temperature, T, is at the same time replaced by T':

$$T' = T - P\bar{\theta} = T - \bar{T}(p) \qquad (4.67)$$

It was also shown by Phillips (1974) that the use of ϕ' and θ' along with T' would result in a well-defined energy integral. Thus, in the actual numerical simulations described in this research, we replace ϕ and θ by ϕ' and θ', respectively, whenever they appear in (2.27), (2.29) and (2.30) in an attempt to reduce the effects of orographic truncation errors in the pressure gradient force.

4.3.2 Numerical Experiments

To test the relevance of using the adiabatic reference atmosphere in our models several simple experiments were carried out following Phillips' (1974) calculations in which a two-column atmosphere in hydrostatic equilibrium was used, with the true value of the pressure gradient force equal to zero, i.e., $-\nabla_p\phi = 0$. The vertical variations of geopotential and potential temperature are defined as follows:

$$\phi \, [m^2 s^{-2}] = 1110 \, [0.95 + z\{72.43 + z(-6.9 + z)\}] \qquad (4.68)$$

and

$$\theta[K] = \frac{T}{P} = \frac{1}{RP} \frac{d\phi}{dz} = \frac{1110}{RP} \{72.43 + z(-13.8 + 3z)\} \qquad (4.69)$$

where $z \equiv -\ell n \, p$. Fig. 4.8 shows the structure of the 4-level model whose interfaces of the layers (half level) are located at σ
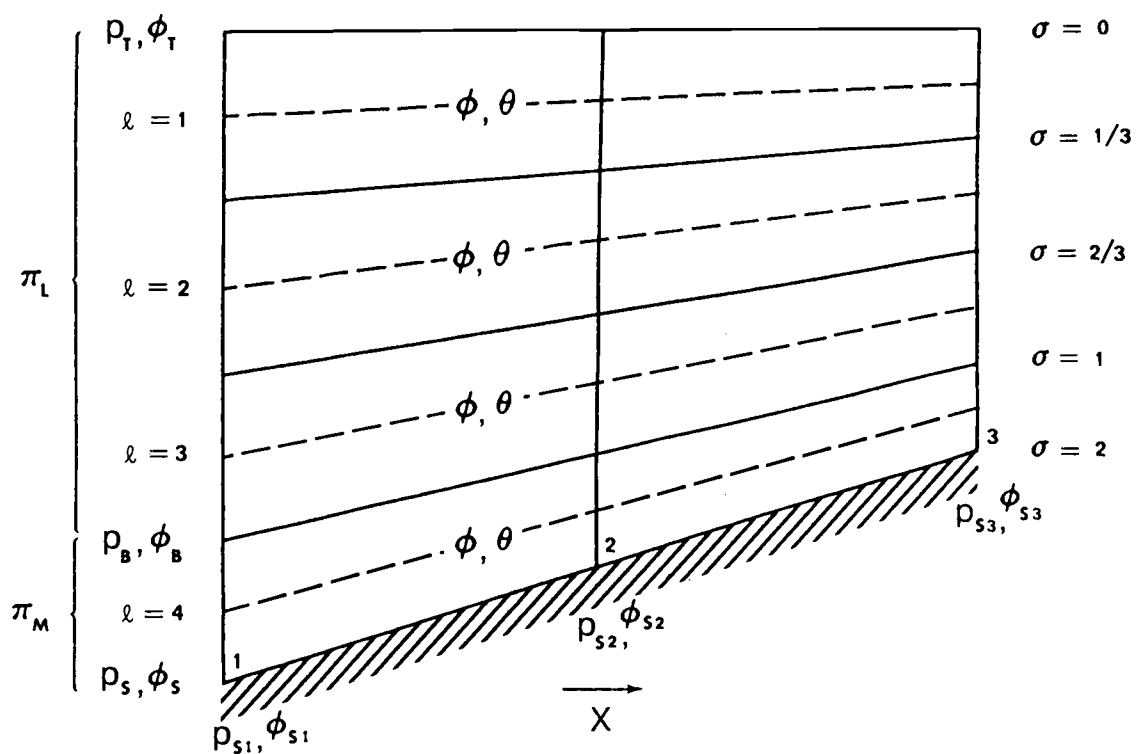
Fig. 4.8.   Schematic representation of the 4-level model of a 2-column atmosphere. Columns are located at points 1 and 3. The reference atmosphere is defined at point 2. $p_{s\ell}$, $\ell = 1$, 2, and 3, are the normalized surface pressures, and $\phi_{s\ell}$, $\ell = 1$, 2, and 3, are the geopotentials at the surface. See text.

surfaces 0, 1/3, 2/3, 1, and 2. We consider two columns located at points 1 and 3 (h grid points) along the direction of the x-axis on a sloping terrain. The reference atmosphere is defined at point 2 (u grid point) situated halfway between points 1 and 3. Here we also use spatial distributions of the dependent variables shown in Figs. 2.1 and 4.2. The normalized pressure at the ground level are $p_{S1} = 1.0$, $p_{S2} = 0.9$, $p_{S3} = 0.8$. At the PBL top where $\sigma = 1$, the values of pressures are $p_{B1} = 0.875$, $p_{B2} = 0.800$, and $p_{B3} = 0.725$. The pressure p_T at the top of the model atmosphere is 0.4. Thus, geopotentials at the surface are $\phi_{S1} = 1054.5$, $\phi_{S2} = 9441.478$, $\phi_{S3} = 18625.727$ $(m^2 s^{-2})$. The PBL consists of the lowest layer as in the 3-dimensional M4 model.

It is a common practice (Phillips, 1974) that in numerical predictions the initial input data is primarily the observed geopotential distribution rather than the temperature. However, in our experiments with the 3-dimensional models whose results will be discussed later, we use the "artificial" values of variables u, v, θ, etc., rather than observed values of these for initialization, and the initial values of geopotentials are diagnosed according to the hydrostatic relations, as presented in Section 4.1. Since the initial distribution of the potential temperatures is found to be important in our experiments, we will discuss here the effects of the use of the adiabatic reference atmosphere by using a "true" potential temperature distribution as input data, as given by (4.69), rather than that of geopotentials as input.

The pressure at the full level of each layer was determined from Eq. (4.10), and the "true" potential temperatures corresponding

to these levels were obtained using Eq. (4.69). Then, the hydrostatic relations Eqs. (4.13) and (4.17) were applied to obtain the geopotentials at the full level of each layer, assuming here that these geopotentials were defined at the levels $p_\ell = P^{1/\kappa}$, i.e., $\phi_\ell = \phi(P_\ell)$, for $\ell = 1,2,3$, and 4. The geopotential at the top of the model atmosphere necessary to define the adiabatic reference atmosphere at point 2 was also obtained by using the hydrostatic relation Eqs. (4.14) and (4.18). Therefore, geopotentials and pressures defined at the mid-point column 2 were used as averaged values necessary to calculate the reference values from Eqs. (4.63) and (4.64):

$$\bar{\theta} = 296.0790 \ (K)$$

$$\bar{\phi}_0 = 298476.0 \ (m^2 s^{-2})$$

Before carrying out tests on the adiabatic atmosphere, it should be worth while to examine the integral constraint (A) given in Section 2.1 and repeated below: the vertical integral of the horizontal pressure gradient force, $-\nabla_p \phi$, with respect to mass, is

$$-\frac{1}{g} \int_{p_T}^{p_S} \nabla_p \phi \, dp = -\frac{1}{g} [\nabla \int_{p_T}^{p_S} \phi \, dp - \phi_S \nabla p_S]$$

$$= -\frac{1}{g} [\nabla \int_{p_T}^{p_S} (\phi - \phi_S) \, dp + p_S \nabla \phi_S] \qquad (4.70)$$

Arakawa (1972) noted that the first term on the right-hand side of Eq. (4.70) is a gradient vector, and a line integral of its tangential component taken along an arbitrary closed curve on the sphere always vanishes. Therefore, only the second term contributes

to such a line integral provided that ϕ_S is variable. Thus, there can be any acceleration of the circulation of the vertically integrated momentum only when there is a non-horizontal bottom surface.

In our numerical experiments, we compute the difference in mass-weighted geopotentials described above for point 2 along a pressure surface between points 1 and 3:

$$\delta p_\ell \Delta \phi_\ell = (\pi \delta \sigma)_\ell \Delta \phi_\ell$$

where the apparent geopotentials, $\Delta \phi_\ell$, is defined by:

$$\Delta \phi_\ell \equiv - \Delta x (\frac{\partial \phi_\ell}{\partial x})_p$$

and Δx is the distance between points 1 and 3, taken as a unit distance (i.e., $\Delta x = 1$). The finite-difference scheme used in these experiments is identical to that used in the 3-dimensional M4 model described earlier in this chapter.

4.3.3 Results

Table 4.1a gives the results obtained by using total geopotentials and potential temperatures (we call it EXP M4T), while Table 4.1b shows the results for the case with the adiabatic reference atmosphere (EXP M4R). Column A gives the mass-weighted values of the first term in the pressure gradient force given by (4.9) or (4.16) for each layer,

$$-(\overline{\pi \delta \sigma})_\ell^x (\frac{\partial \phi}{\partial x})_\ell ,$$

while column B shows those of the second term,

Table 4.1. Values of $(\delta p)_\ell \Delta\phi_\ell$ (column C) and $\Delta\phi_\ell$ in units of $m^2 s^{-2}$.
(a) EXP M4T: using total geopotentials and potential temperatures for the 4-level model.
(b) EXP M4R: using the adiabatic reference atmosphere for the 4-level model.
(c) EXP M10T: as in (a) except for the 10-level model.
(d) EXP M10R: as in (b) except for the 10-level model.

Columns A and B show the mass-weighted values of the 1st and 2nd terms of the right side of (4.9) or (4.16), respectively. The 1st column from the left indicates the layer number ℓ; the 2nd and 3rd columns show the pressure and the value of σ at layer interface level $\ell-1/2$, respectively. See text.

	$\hat{p}_{l-1/2}$	$\hat{\sigma}_{l-1/2}$	A	B	C	$\overline{\delta p}_l^x$	$\Delta\phi_l$
a							
1	0.4000000	0.000000	-484.021	487.590	3.569	0.1333333	26.770
2	0.5333334	0.333333	-1215.330	1208.334	-6.996	0.1333333	-52.472
3	0.6666667	0.666667	-1724.095	1709.129	-14.966	0.1333333	-112.247
4	0.8000000	1.000000	-1607.512	1582.928	-24.584	0.1000000	-245.840
5	0.9000000	2.000000					
				SUM =	-42.977		
b							
1	0.4000000	0.000000	-10.543	15.968	5.425	0.1333333	40.684
2	0.5333334	0.333333	1.457	-0.139	1.318	0.1333333	9.885
3	0.6666667	0.666667	40.621	-40.615	0.005	0.1333333	0.038
4	0.8000000	1.000000	63.298	-64.258	-0.960	0.1000000	-9.599
5	0.9000000	2.000000					
				SUM =	5.788		
c							
1	0.1000000	0.000000	-40.902	41.176	0.274	0.0245731	11.134
2	0.1245731	0.039477	-136.532	136.371	-0.160	0.0306115	-5.242
3	0.1551846	0.088655	-258.093	257.239	-0.853	0.0381337	-22.375
4	0.1933182	0.149917	-414.098	412.323	-1.775	0.0475042	-37.371
5	0.2408224	0.226233	-615.707	612.751	-2.955	0.0591775	-49.941
6	0.3000000	0.321302	-877.535	873.138	-4.397	0.0737193	-59.640
7	0.3737193	0.439733	-1218.905	1212.690	-6.215	0.0918344	-67.678
8	0.4655537	0.587265	-1665.215	1656.682	-8.533	0.1144009	-74.587
9	0.5799546	0.771052	-2249.890	2238.375	-11.515	0.1425129	-80.801
10	0.7224675	1.000000	-3016.883	3001.503	-15.380	0.1775325	-86.634
11	0.9000000	2.000000					
				SUM =	-51.511		
d							
1	0.1000000	0.000000	-7.764	8.081	0.317	0.0245731	12.909
2	0.1245731	0.039477	-20.043	20.201	0.159	0.0306115	5.179
3	0.1551846	0.088655	-26.249	26.228	-0.020	0.0381337	-0.532
4	0.1933182	0.149917	-24.078	23.920	-0.159	0.0475042	-3.342
5	0.2408224	0.226233	-10.341	10.121	-0.220	0.0591775	-3.719
6	0.3000000	0.321302	19.338	-19.516	-0.178	0.0737193	-2.414
7	0.3737193	0.439733	70.937	-70.947	-0.010	0.0918344	-0.110
8	0.4655537	0.587265	152.611	-152.297	0.314	0.1144009	2.746
9	0.5799546	0.771052	275.484	-274.647	0.837	0.1425129	5.875
10	0.7224675	1.000000	454.713	-453.093	1.620	0.1775325	9.124
11	0.9000000	2.000000					
				SUM =	2.660		

$$-(\overline{\pi\delta\sigma})^X_\ell \, c_p \, \theta_\ell \, \frac{\partial P_\ell}{\partial \pi} \left(\frac{\partial \pi}{\partial X}\right)_\ell$$

for ℓ = 1, 2, and 3, and

$$-(\overline{\pi\delta\sigma})^X_\ell \left[\frac{1}{\pi}(\phi_M-\phi_S)\frac{\partial\pi}{\partial X} + (\phi_B-\phi_S)\frac{\partial P_B}{\partial X}\right]_\ell \left(\frac{\partial\pi}{\partial X}\right)_\ell$$

for ℓ = 4. The sum of these two terms is given in column C. It is apparent that the values in columns A and B are of large magnitude with opposite signs, whereas the sum of these terms results in a small value compared to individual terms, thereby tending to introduce large truncation errors. However, comparing the vertically summed value of column C, $\sum_{\ell=1}^{4}(\pi\delta\sigma)_\ell\Delta\phi_\ell$, for EXP M4R in Table 4.1b with that of EXP M4T in Table 4.1a, it is clear that the acceleration of circulation of the vertically integrated momentum due to truncation errors in the pressure gradient force has been considerably reduced with the use of the reference atmosphere, i.e., from -43.0 to 5.8 m^2s^{-2}, or to 14% of the error occurred in the case with total geopotentials. The last (8th) column in Tables 4.1a and b gives the values of the apparent geopotentials, $(\Delta\phi)_\ell$, between points 1 and 2, which can be obtained by dividing the values of column C by the pressure increment $(\overline{\delta p})^X_\ell$ for each layer given in the 7th column. If we suppose that the distance between points 1 and 3 is 200 km, the inclination of the ground surface is 1800 m/ 200 km, or 90 m/10 km, which is approximately equal to the steepest slope in the model terrain to be used in our 3-dimensional experiment (see Fig. 5.1). The value of $(\Delta\phi)_{\ell=4}$ = -9.6 m^2s^{-2} obtained for the PBL in the experiment with the reference atmosphere corresponds to a geostrophic wind of about 0.5 ms^{-1} in mid-latitudes. This value is relatively small for our 3-dimensional experiments

with an integration time-period of less than 24 h. On the other hand, the value of -245.8 m^2s^{-2} obtained for the apparent geopotential difference for the PBL in the experiment with total geopotentials corresponds to a geostrophic wind of about 12 ms^{-1}, which is intolerable even for the short-period experiments with our 3-dimensional model.

Additional experiments were carried out with a 10-level model very similar to that of Phillips' (1974). The results shown in Tables 4.1c and d are the experiments with total geopotentials (EXP M10T) and those with the reference atmosphere (EXP M10R), respectively. The potential temperature distributions were again used in these computations as input, and geopotentials were diagnosed using the hydrostatic relation, whereas Phillips (1974) used geopotentials defined by (4.68) as input data. The PBL consists of the lowest layer of this 10-level model as in the 4-level model discussed above. The interfaces of the layers at point 2 are located at equal intervals in $-\ell n \ p$ at point 2, and $p_T = 0.1$. The initial conditions at the ground surface are the same as in the 4-level model.

The vertical sums of the differences of the mass-weighted geopotentials, $\sum_{\ell=1}^{10} (\pi\delta\sigma)_\ell \Delta\phi_\ell$, given in column C of Tables 4.1c and d, were -51.5 m^2s^{-2} in EXP M10T and 2.66 m^2s^{-2} in EXP M10R. Thus, the use of the reference atmosphere reduced the truncation errors in the pressure gradient force to 5% of that obtained with total geopotentials. On the other hand, Phillips (1974) reported that the results with a simplified 10-level NMC model were 45.4 vs. 4.85 m^2s^{-2}, and thus the use of the reference atmosphere reduced the

errors to 10% of the total geopotential case.

The apparent geopotential difference $(\Delta\phi)_\ell$ between points 1 and 3 is given in the last column of Tables 4.1c and d. Within the PBL the difference is 9.12 m^2s^{-2} for EXP M10R, which gives a geostrophic wind of about 0.5 ms^{-1}, whereas the value of $(\Delta\phi)_{\ell=10}$ = -86.6 m^2s^{-2} for EXP M10T corresponds to a geostrophic wind of approximately 4.5 ms^{-1}.

The same computations were repeated with geopotentials defined by Eq. (4.68) as input for all four cases. The results were similar to those described above, although the errors in the sum of the mass-weighted geopotentials were somewhat larger in all four experiments if geopotentials were used as input. Thus, we can see from those experiments that the use of the adiabatic reference atmosphere considerably reduces the truncation errors in the pressure gradient force, and therefore results in the reduction of the false acceleration of the circulation of the vertically integrated momentum. Although we have tested the adiabatic reference atmosphere with only one typical potential temperature distribution and expect that the errors would be greater when the variations of potential temperatures are much large and irregular, particularly in the PBL during the daytime, the use of the reference atmosphere would give definitely better results compared to those obtained with total geopotentials. Hence, Phillips' (1974) adiabatic reference atmosphere will be used in our 3-dimensional experiments.

4.4 Implicit Differencing of Diffusion Equations

The layers near the ground in the vertical structure of the L7 model are rather thin in order to meet the condition that the PBL occupies at least two or three of the lowest layers. Therefore, the vertical diffusion terms in Eqs. (2.29) and (2.31) are treated implicitly in time to avoid numerical instability. To illustrate the procedure we take the following equation for the u-component of the horizontal wind in z-coordinate:

$$\frac{\partial u}{\partial t} = \frac{\partial}{\partial z} (K_M \frac{\partial u}{\partial z})$$

(4.71)

Following Richtmyer and Morton (1967), the discrete form of Eq. (4.71) may be written as:

$$\frac{u_\ell^{(n+1)} - u_\ell^{(n-1)}}{2\Delta t} = \frac{\xi[\delta(K_M \delta u)]_\ell^{(n+1)} + (1-\xi)[\delta(K_M \delta u)]^{(n-1)}}{(\Delta z)^2}$$

(4.72)

where superscript n refers to time step, and Δz the vertical grid size. The most commonly used Crank-Nicholson scheme has $\xi = 1/2$. However, we choose $\xi = 0.80$ following Peagle et al. (1976), a value that they argue would give a better treatment of shortwaves than the Crank-Nicholson scheme. Mahrer and Pielke (1978) also utilized the above implicit formulation with $\xi = 0.75$ for the simulation of the growth of the heated planetary boundary layer. The expanded form of (4.72) takes the following expression:

$$b_\ell u_{\ell-1}^{(n+1)} + a_\ell u_\ell^{(n+1)} + c_\ell u_{\ell+1}^{(n+1)} = d_\ell, \quad \ell=1,2,\ldots,L$$

(4.73)

where a_ℓ, b_ℓ, c_ℓ, and d_ℓ depend on quantities at the (n-1)st time step such as $u^{(n-1)}$, $v^{(n-1)}$, and $\theta^{(n-1)}$. The resulting

linear system of equations with a tridiagonal (Jacobi) coefficient matrix is solved by using the procedure described by Isaacson and Keller (1966).

4.5 Time Differencing Scheme

The time-stepping scheme used in the model is the leap-frog scheme. The Matsuno (Euler-backward) scheme is inserted periodically to avoid the separation of solutions due to the spurious computational mode. The time interval Δt used is 15s and a Matsuno step is inserted every 25 steps throughout the experiments.

5. BOUNDARY AND INITIAL CONDITIONS

5.1 Model Domain and Topography

The model domain is square whose size is 150 km in both x- and y-directions, and roughly corresponds to a grid box of a fine-resolution GCM. The horizontal grid mesh consists of 15 x 15 grid intervals with uniform grid increment, $d \equiv \Delta x = \Delta y = 10$ km.

The topography of the ground surface that has been adopted in our current models and also used in the previous experiments (Han et al., 1982; DUH, 1984) was generated using the technique proposed by Mandelbrot (1975). We start with a square domain of uniform altitude, then break it along a straight fault and displace the two sides vertically to form a cliff. This process is repeated a large number of times until a desired earth's relief is obtained. The positions of the faults and the heights of the cliffs are assumed random and mutually independent, the former being generated using uniform random numbers, and the height difference between any two points is a zero-mean Gaussian variable of finite variance. The resulting topography has been smoothed and adjusted to be cylcic in x and y as shown in Figs. 5.1 and 5.2. The mean terrain height $\langle h_s \rangle$ above sea-level (where the pressure, p_{so}, is taken as 1015 mb) is 511 m. Here and throughout this article we denote by $\langle \, \rangle$ the horizontal spatial average. The average one-dimensional spectrum of this terrain along either x or y approximately falls off with a -3 power-law slope over most of the limited wave number range and shows that the model topography has a majority of its terrain height variance at wavelengths longer than $2d = 20$ km (see Fig. 3 in
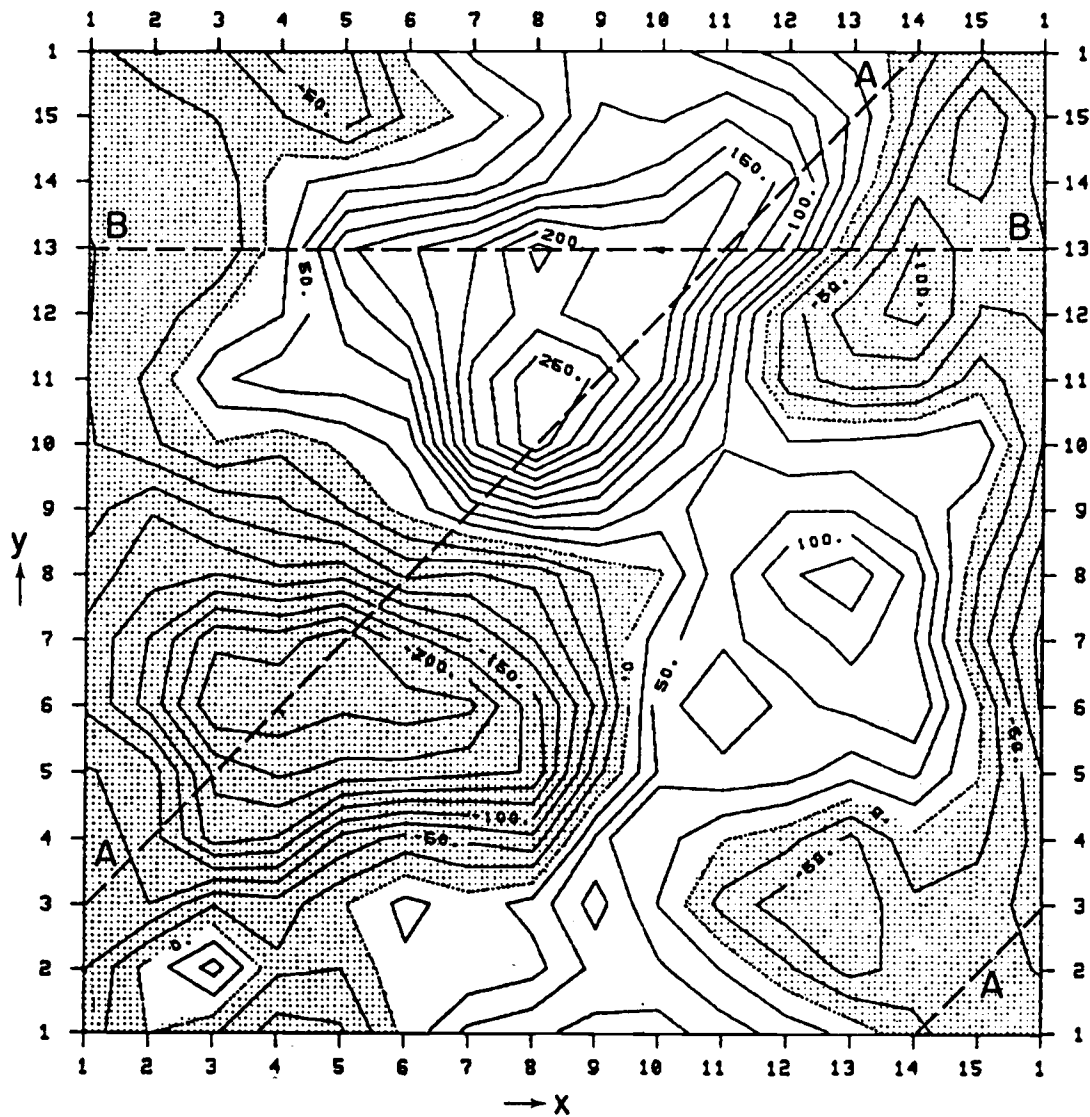
Fig. 5.1.   The terrain height utilized, relative to its mean height of
511 m.   Shaded regions denote below-average heights.
Contour interval is 25 m.   Tick marks with integers along
edges denote grid intervals along x and y, and a "site"
(grid point) is identified by a pair of integers.   The
broken line segments marked A and B are the two passes
along which vertical cross sections of Θ are taken, as
described in Chapter 6.
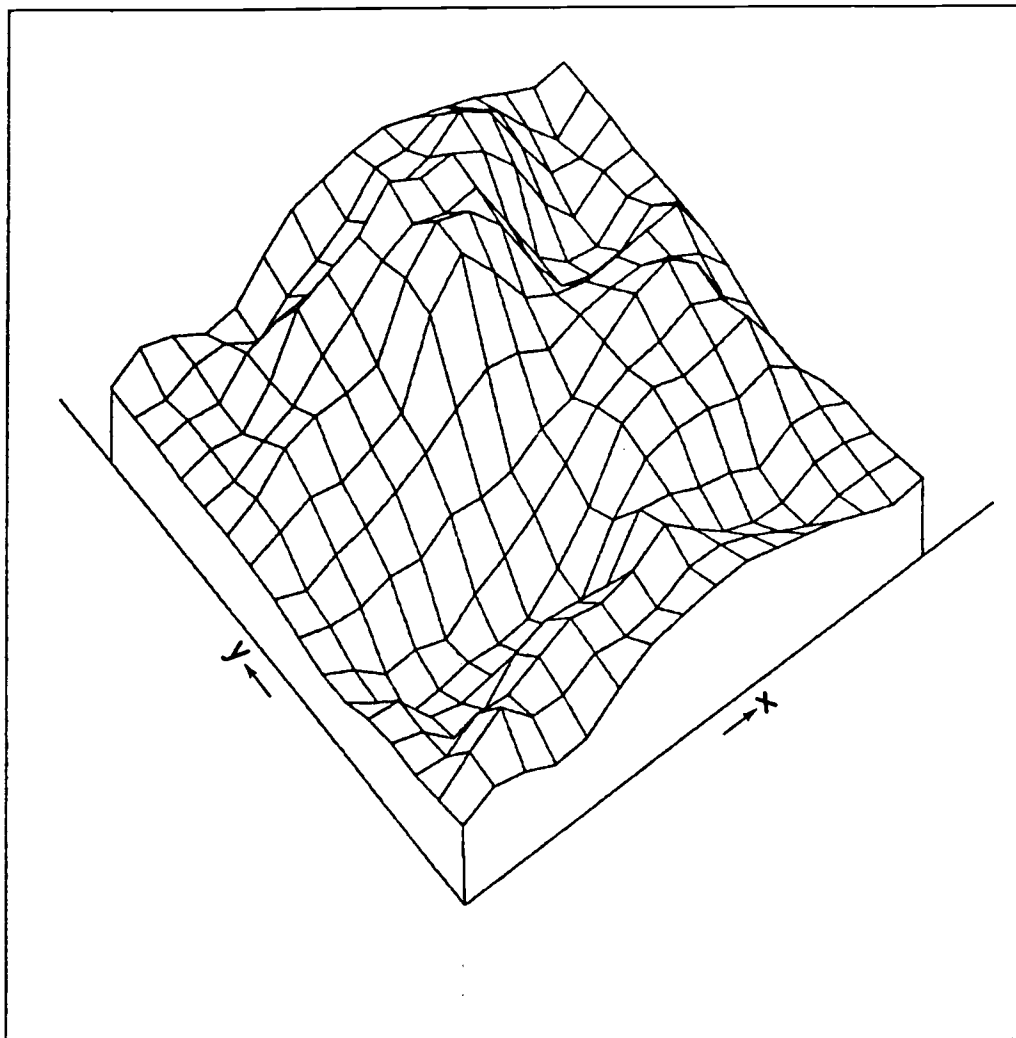
Fig. 5.2. Perspective view of the terrain profile used in the M4 and
L7 models. The viewing position is in the southwest
corner of the domain. The highest and the lowest
elevations are 272 m above and 249 m below the reference
level (511 m above sea level), respectively.

DUH, 1984). Therefore, with a choice of d = 10 km, the influence of subgrid-scale terrain variance, which would result in enhanced frictional and wave drag, may be neglected (Young and Pielke, 1983).

5.2 Lateral Boundary Conditions

The lateral boundary conditions employed are cyclic at both the north-south and east-west boundaries of the domain. With the use of these boundary conditions we can avoid ill-posedness at the boundaries which may result in serious errors in the interior domain in a limited-area mesoscale model (Anthes and Warner, 1978). The cyclic boundary conditions ensure that calculations at all grid points use the same finite-difference equations so that the truncation errors are of the same order everywhere and that globally averaged integral constraints are conserved under adiabatic frictionless conditions. Periodic boundary conditions, however, imply that solutions are infinitely repeated downstream, and with a relatively small domain being used as in the case of our models, disturbances generated in the interior of the domain can eventually return there after propagating downstream, passing through the cyclic boundaries. It is felt, however, that at this stage of our model development implementing a model with minimum complexity which will provide useful information under certain specialized conditions should be given the first priority. We plan to implement in our models nonperiodic, radiative boundary conditions proposed by, for example, Orlanski (1976), Camerlengo and O'Brien (1980), and Ross and Orlanski (1982) in the near future.

5.3 Top Boundary Condition

The choice of the upper pressure surface p_T has to be made in association with the vertical resolution of the model. If either the number of layers is too few, or the upper boundary is placed at too high a pressure, significant distortions in the solution may result (Anthes and Warner, 1974). However, due to the limited computer resources we can utilize, the number of layers that may used in our model is rather small. Since our prime interest is in simulating circulations in the lower troposphere and the PBL in particular, we place p_T at 400 mb by taking into consideration two-dimensional experiments by Anthes and Warner (1974) which have shown that p_T placed above 400 mb ($p_T > 400$ mb) in a 4-level model results in distorted circulations in the lower troposphere. The initial $\underset{\sim}{V}$ and θ profiles above the lowest layer that will be specified in Section 5.6 give the vertical wavelength L in terms of the Scorer parameter k_c:

$$L_w = \frac{2\pi}{k_c} = \frac{2\pi U}{(\frac{g}{\bar{\theta}} \frac{\partial \theta}{\partial Z})^{1/2}} \simeq 2.5 \text{ (km)} \tag{5.1}$$

where U and $\bar{\theta}$ are characteristic wind speed and potential temperature, respectively. With $p_T = 400$ mb the top of the model atmosphere is situated at an altitude slightly above 7000 m so that we can expect less than 2 information levels per wavelength in the vertical for the M4 model and less than 3 for the L7 model. Therefore, if strong mountain waves should develop the circulations in the lower troposphere may become significantly distorted due to the fact that the top of the model atmosphere is assumed to be a material

surface [see Eq. (2.15)] so that it is reflective. It is hoped that
a non-reflective upper boundary condition recently proposed by
Bongeault (1983) and Klemp and Durran (1983) will be implemented in
a future version of our models.

5.4 Introduction of Terrain and Temperature Variations

Since an abrupt change in the ground surface height introduces
transient gravity waves that may contaminate the physical aspects of
the solution we are interested in, the surface height is gradually
introduced as a linear function of time to minimize these undesir-
able accelerations. Following Mahrer and Pielke (1975), Deaven
(1976), and Klemp and Lilly (1978) who used similar procedures in
two-dimensional simulations of air flow over mountains, the initial
horizontal surface, located at the altitude of the averaged height,
$\langle h_S \rangle$ = 511 m, of the fully "grown" terrain depicted in Figs. 5.1
and 5.2, is slowly increased or decreased at each grid point by
1/Nth of $[h_S(x,y) - \langle h_S \rangle]$ each time step for N steps over 2 h
starting at 0100 LST (N is 480 with 15s time step).

At the same time the mountains are "growing," variations in the
horizontal θ field in the lowest layer in both models have been
introduced in the following manner. Starting with a uniform
$\theta = \theta(0100)$ = 282 K everywhere, we increase or decrease θ at each
grid point by 1/Nth of $[\theta(0300) - \theta(0100)]$ each time step for N
steps over 2 h so that θ and h_S are perfectly correlated. Here θ
stands for either $\theta_{M=4}$ for the M4 model or $\theta_{L=7}$ for the
L7 model, and the potential temperature at 0300 LST is given by

$$\theta(0300) = \theta(0100) + 1.5(K/100m)[h_s - \langle h_s \rangle] \qquad (5.2)$$

which implies $\langle \theta(0300) \rangle = \langle \theta(0100) \rangle = 282$ K. The potential temperature distribution given by (5.2) crudely simulates the result of nocturnal cool-air inflow toward the bottom of a basin along the slopes, combined with surface radiative cooling of air near the ground surface, that leads to penetration of the mountains up through horizontal θ-surfaces, and gives a maximum difference of 7.4 K between the lowest and highest altitudes in the model terrain. It was necessary to use a relatively small vertical change of 1.5 K/100 m in Eq. (5.2) in order to keep the static stability of the lowest two layers positive during the initial adjustment period, compared to 6.2 K/100 m in absolute temperature observed by Hocevar and Martsolf (1971) in a central Pennsylvania valley in clear April mornings or ~8 K/100 m in potential temperature measured by Magono and Nakamura (1982) in clear February mornings in a basin in the coldest region in Japan.

During the first 2 h of integrations the surface sensible heat flux H_S given by (4.20) was set to zero in (4.19), while H_{ST} in (3.42) and all other turbulent fluxes were kept turned on. After the mountains have stopped growing at 0300, another hour of integrations were performed until 0400, with H_S still being kept turned off, in order to remove the spurious accelerations and imbalances due to the introduction of the irregular terrain and temperature variations. At 0400 H_S in (4.19) was turned on although it was still negative (air to ground), and the sunrise defined as the first moment at which T_{NET} of Eq. (3.46) becomes positive at all grid

points occurred at 0425.

It may be questioned whether an adjustment time of 3 h is adequate for attaining quasi-steady-state fields free of spurious accelerations. Klemp and Lilly (1978) used a parameter tU/d_M as an indicator of initial adjustment time, where U and d_M are characteristic wind speed and mountain half-width, respectively. The value of tU/d_M for our experiments is 1.4 with t = 3 h, U = 5 ms^{-1} and $2d_M$ = 75 km (see DUH, 1984), while tU/d_M = 7.2, 5.4, and 5.0 for Mahrer and Pielke (1975), Deaven (1976), and Klemp and Lilly (1978), respectively. Although due to the limited computer resources the value of tU/d_M we used is smaller than those used by others, we have found that the fields of h + h_S and $\underset{\sim}{V}$ after 3 h of integrations of the M4 model resemble very closely those obtained after a 12 h integration of the 1-layer shallow water model under similar conditions (Han et al., 1982; DUH, 1984). Furthermore, 2-dimensional experiments by Anthes and Warner (1974) suggest that the major adjustment of the wind and mass fields to irregular terrain occurs in about 1 h, and therefore an initial adjustment time of 3 h was considered acceptable for our experiments.

5.5 Initial Pressures $\hat{p}_S$ and $\hat{p}_B$

The initial pressure at the sea surface, $\hat{p}_S$, where the geopotential height is assumed to be zero, is set equal to 1015 mb. Assuming that the air that would fill in the space between the sea surface and the average ground-surface height <h_S>, if the

mountain terrain were removed, is isentropic with potential
temperature θ, we obtain the surface pressure from the hydrostatic
relation (4.14) or (4.18):

$$\hat{p}_S = p_{SO} \left[1 - \frac{\langle \phi_S \rangle}{c_p \theta (p_{SO}/p_{OO})^\kappa} \right]^{1/\kappa} \qquad (5.3)$$

where θ is either $\theta_{M=4}$ or $\theta_{L=7}$, and $\langle \phi_S \rangle = g \langle h_S \rangle$. We also
set $p_{OO} = 1000$ mb in the Exner function defined by (2.25). In the
M4 model the pressure at the PBL top is then obtained from (4.18):

$$\hat{p}_B = \left[P_S - \frac{1}{c_p \theta} (\langle \phi_B \rangle - \langle \phi_S \rangle) \right]^{1/\kappa} \qquad (5.4)$$

where $\langle \phi_B \rangle = g \langle h_B \rangle$ is the mean geopotential at the PBL top with
$\langle h_B \rangle = 800$ m, and P_S is the value of (2.25) for $p = \hat{p}_S$.

5.6 Initial θ, T_S, h and $\underset{\sim}{V}$

The potential temperatures at full levels in the layers above
the lowest layer for both models were defined by

$$\theta_\ell = 5 \times 10^{-3}(z_\ell - 1623) + 291.5 \text{ (K)} \qquad (5.5)$$

where z_ℓ is the altitude (m) of the full level ℓ, and the average
lapse rate was set to 5×10^{-3}K m^{-1}. In the case of the M4 model
the PBL top is at half-level $\ell+1/2 = M-1/2$ and its initial height
was set to $h_B = \langle h_B \rangle = 800$ m so that the initial depth of the
PBL was h = $\langle h \rangle$ = $\langle h_B \rangle$ - $\langle h_S \rangle$ = 289 m. We have found earlier
that $\langle h \rangle$ in the M4 case not much smaller than 289 m would cause
hydraulic-jump-like phenomena on the lee side of the highest

peak in the model terrain (Houghton and Kasahara, 1968; Houghton and Isaacson, 1970) in early hours of integrations when the lowest layer is disconnected from the layers aloft under moderate wind ($\sim$5 ms^{-1}) and adiabatic conditions, and therefore $\langle h \rangle$ cannot be set to a smaller value. In the L7 model, on the other hand, there is no distinct PBL top and the initial PBL was assumed to consist of the lowest layer which was about 100 m thick, much less than that of the M4 model. However, to make the initial conditions for the L7 model as close as possible to those of the M4 model, the initial potential temperature at the second lowest level $\ell = L-1 = 6$ was redefined as the average of $\theta_{L=7}$ and θ_ℓ obtained from (5.5) at the height of full level $\ell = L-1$, which was about 250 m above the ground (see Fig. 2.1a). With the above distribution of potential temperature the PBL top was still assumed to be at half level $\ell+1/2 = L-1/2$ for the purpose of introducing θ variations and determining the initial $\underset{\sim}{V}$ field in the PBL of the L7 model. It is noted that in the M4 model the thickness of the lowest layer greatly varies horizontally after 3 h of integrations due to the fact that the PBL top is a material surface and rather flat, while in the L7 model it stays more or less the same ($\sim$100 m) in space and time.

Initial ground surface temperature T_S at 0100 LST was set to a value 2 K below the initial T_a determined from $T_a = P_a\theta_a$, where $\theta_a = \theta_{M=4} = \theta_{L=7} = 282$ K, and $P_a = P_s$. T_S was then diagnosed using (3.53) hereafter in which T_a during the initial 2 h of integrations was obtained from the forced value of θ in the lowest layer as discussed in Section 5.4.

The roughness length z_0 necessary to calculate C_D and C_H in

the bulk aerodynamic formulations was set to a constant value 0.45 m through the domain, a value appropriate to land surface (Randall, 1982). Initial values of C_D and C_H were set to their neutral values $[k/\ell n(z/z_0)]^2$, with z set equal to Min[50 m, $(\phi_B - \phi_S)/g]$ in the M4 case and to the height of the lowest full level ℓ = L in the L7 case throughout the entire integration period.

The conditions for velocity at the surface are non-slip conditions, while the vertical velocity $\overset{\cdot}{\sigma}$ is given by (2.16) or (2.21). The initial $\underset{\sim}{V}$ field in the lowest layer in each layer was obtained by assuming steady state and solving the equation of the Ekman balance between the frictional, Coriolis, and large-scale pressure gradient force terms:

$$f\underset{\sim}{k} \times (\underset{\sim}{V} - \underset{\sim}{V}_g) + \frac{C_D |\underset{\sim}{V}| \underset{\sim}{V}}{h} = 0 \qquad (5.6)$$

In the layers above the lowest layer the initial $\underset{\sim}{V}$ was assumed to be geostrophic so that $u_\ell = U_g$, $v_\ell = V_g$, where U_g and V_g are prescribed constants, i.e., $U_g = 5$ ms^{-1} and $V_g = 0$. This geostrophic forcing was imposed on all levels throughout the entire integration periods of both models.

6. RESULTS OF NUMERICAL EXPERIMENTS

6.1 General Considerations

The integrations of both the M4 and L7 models were carried out for 18 model-hours starting at 0100 LST, as described in Chapter 5, and ending at 1900 LST just before sunset. They were performed under the conditions of a typical, dry and clear summer day in mid-latitudes with moderate prevailing westerly winds of 5 ms^{-1} at all height levels. Although it is more desirable to carry out a longer period of the integrations and examine the results for, say, the second day, the results described below are for the first day of the integrations. This is because, in addition to our limited computer resources available, detrainment processes at the top of the mixed layer are not incorporated in the M4 model that would make the simulations of the diurnal cycle of boundary-layer evolution possible.

In describing the results, we use the horizontal fields of meteorological quantities on σ-surfaces. Although it is more customary to display the field of a variable at a constant height or pressure level, it is thought more convenient for our purposes to illustrate horizontal fields of variables on constant σ levels, considering the nature of the mixed layer for the M4 model and the gentle slopes of the model topography utilized. Thus, the results for L7 will also be shown on constant σ levels. For the same reason, we also take the domain average of a quantity on a σ-surface, and use the terms "domain average" and "layer average" interchangeably when there is no confusion.

In the following sections, we present a detailed analysis of
numerical results from both the M4 and L7 models in an attempt to
identify, among other features, the dynamical balances and the
forces which control the evolutions of the boundary-layer structure
and its flows.

6.2 Evolution of $<h>$ and $<\Delta\theta>$

A realistic knowledge of the evolution of the mixed-layer depth
h plays an essential part of atmospheric numerical forecasting
models and GCM's in which the boundary layer that couples the
atmosphere with the earth's surface through the turbulent transfer
of heat, momentum, and moisture is embedded. It is also important
for predicting the dispersion of atmospheric pollutants, which is
evidently limited by the height of the inversion "lid" (Tennekes,
1973). The inversion base depicted in Fig. 4.1 gradually rises as
the surface turbulent heat fluxes become vigorous during the course
of a clear sunny day because the warm air above the inversion base
is entrained into the turbulent convective layer below through the
strong agitation in the interface layer, which results from
bombarding and penetrating the stable layer by convective elements
originating in the surface layer (Carson, 1973).

The domain-averaged mixed-layer depth $<h>$ along with inversion
strength $<\Delta\theta>$ predicted by the M4 and L7 models are illustrated in
Figs. 6.1a and 6.1b, respectively. They represent the overall
evolutions of h and $\Delta\theta$ in the model domain which is approximately a
grid size of a fine-resolution GCM by eliminating such effects as
advection and mass flux divergence. Their evolutions are found to
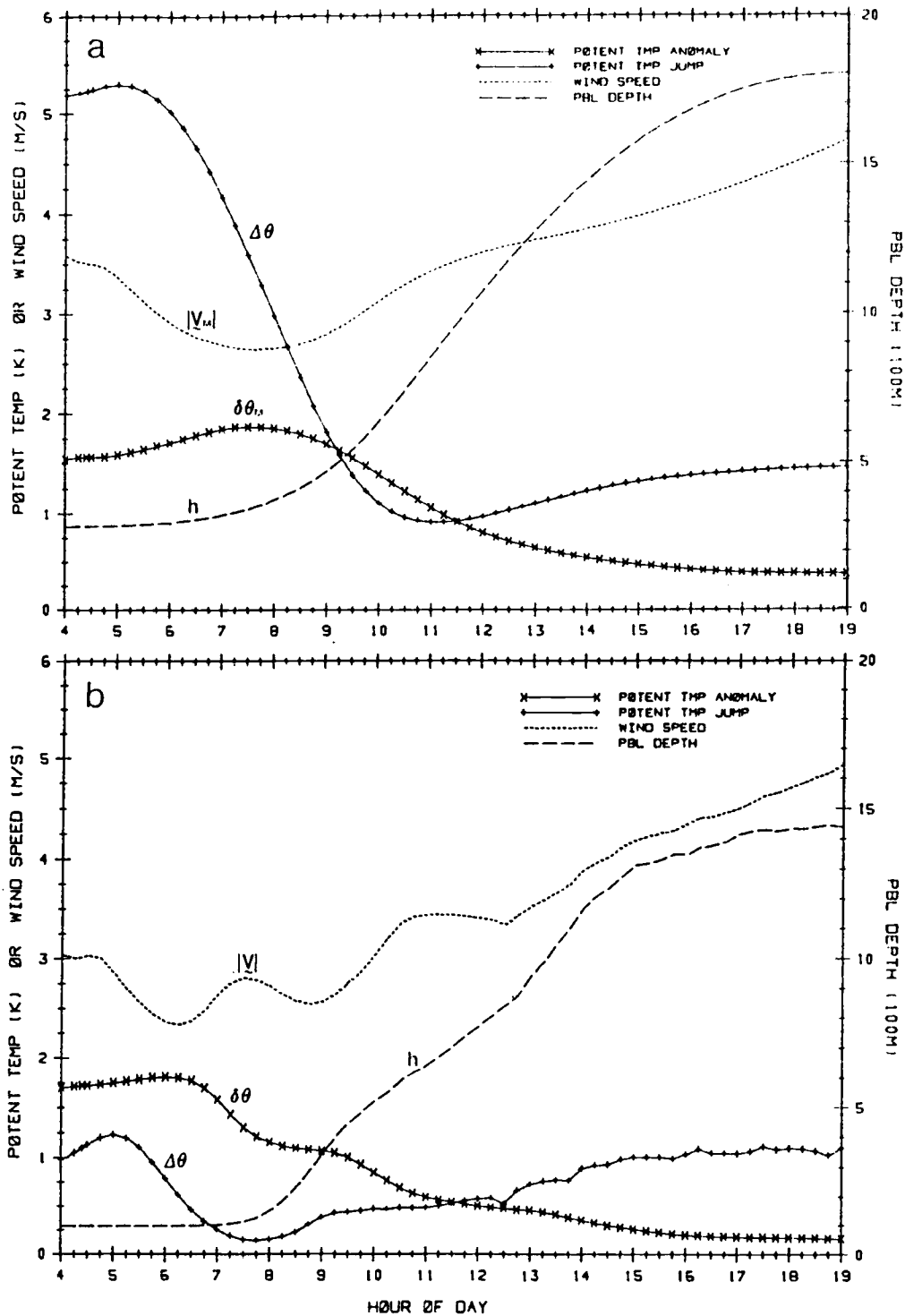
Fig. 6.1. (a): Domain averaged mixed-layer depth <h> (unit: 100m), potential temperature discontinuity at the inversion base <Δθ> (K); wind speed <|$\underset{\sim}{V}$|> (ms^{-1}) and rms horizontal potential temperature variability δθ (K) in the mixed layer, as functions of time of day for the M4 model. (b): As in (a) except for the L7 model, and <|$\underset{\sim}{V}$|> and δθ are for layer 7.

closely resemble those shown in Tennekes (1973) and Carson (1973),
who proposed simple one-point models of the convectively well-mixed
boundary layer, as depicted in Fig. 4.1, that relate h to $\Delta\theta$, the
surface heat flux $H(0,t)$ and the entrainment w_e. Since the
importance of $\Delta\theta$ in predicting h has also been recognized by other
investigators such as Lilly (1968), Mahrt and Lenschow (1976) and
Deardorff (1972), we attempt to explain the behavior of <h> and <$\Delta\theta$>
obtained from the M4 model by utilizing the models proposed by
Tennekes (1973) and Carson (1973).

We assume that the mixed layer consists of an incompressible
fluid of constant density. The time rate of change of h then can be
related to the entrainment rate w_e as follows:

$$\frac{\partial h}{\partial t} = -\nabla \cdot (h\underline{V}) + w_e \qquad (6.1a)$$

which is analogous to Eq. (2.20a). Here w_e is given by (3.55) and
is a function of $\Delta\theta$. We ignore large-scale subsidence as before.
Following Tennekes (1973), we further assume that the mixed layer is
within a horizontally homogeneous atmosphere on a horizontal plane,
as depicted in Fig. 4.1. Then (6.1a) can be written as

$$\frac{dh}{dt} = w_e \qquad (6.1b)$$

which is formally equivalent to the domain-averaged equation of
(6.1a), and the net rate of change of $\Delta\theta$ is given by

$$\frac{d\Delta\theta}{dt} = \gamma \frac{dh}{dt} - \frac{d\theta_M}{dt} \qquad (6.2)$$

where γ is the gradient of θ in the stable layer above the inversion base and is assumed to be independent of height and time. By assuming that it is independent of height, the heating rate of air in the mixed layer can be expressed as

$$\rho c_p \frac{d\theta_M}{dt} = - \frac{\partial}{\partial z} [\rho c_p H(z,t)] \qquad (6.3)$$

where $H(z,t) \equiv \overline{w'\theta'}$ is the turbulent heat flux at height z. Integrating (6.3) from $z = 0$ to h we obtain

$$\frac{d\theta_M}{dt} = \frac{1}{h} [H(0,t) - H(h,t)] \qquad (6.4)$$

The downward heat flux at the inversion base, $H(h,t)$, is related to $\Delta\theta$ and dh/dt by

$$\rho c_p \Delta\theta \frac{dh}{dt} = -\rho c_p H(h,t) \qquad (6.5)$$

which is equivalent to Eq. (4.23b). We note in (6.5) that the positive entrainment ($w_e > 0$) means downward heat flux at the mixed-layer top [$H(h,t) < 0$], and thus makes a positive contribution to the net rate of change of θ_M in (6.4). On substitution of (6.4) into (6.2) we find

$$\frac{d\Delta\theta}{dt} = \gamma \frac{dh}{dt} + \frac{1}{h} [H(h,t) - H(0,t)] \qquad (6.6)$$

and using (6.5) in (6.6) and rearranging the terms we obtain

$$h \frac{d\Delta\theta}{dt} + \Delta\theta \frac{dh}{dt} = \gamma h \frac{dh}{dt} - H(0,t) \qquad (6.7)$$

Using the equation for the kinetic energy of turbulence, Tennekes (1973) derived the following relation between the surface

heat flux and the heat flux at the inversion base in a strongly
unstable boundary layer:

$$H(h,t) = -AH(0,t) \qquad (6.8)$$

where the entrainment constant A was estimated to be 0.2.
Inspection of the entrainment rate equation (3.55) reveals that
(6.8) approximately holds under strong surface heating conditions
with the coefficient A ~0.2, although it is clear that a linear
relationship between H(0,t) and H(h,t) does not exist as far as
Eq. (3.55) is concerned. If we assume that (6.8) holds with a con-
stant A for a certain short time period, substitution of (6.8) into
(6.5) yields

$$\Delta\theta \, \frac{dh}{dt} = AH(0,t) \qquad (6.9)$$

Combining (6.7) with (6.9) and with the aid of $d\Delta\theta/dt =$
$d\Delta\theta/dh \, dh/dt$, we arrive at

$$h \, \frac{d\Delta\theta}{dh} + \alpha\Delta\theta - \gamma h = 0 \qquad (6.10)$$

where $\alpha = (1+A)/A$, the value of which becomes 6 for A = 0.2.
Integrating (6.10) with respect to h, we find the expression for the
inversion strength:

$$\Delta\theta = (\Delta\theta)_0 (\frac{h_0}{h})^{\alpha} + \frac{\gamma}{\alpha+1} \, h \, [1-(\frac{h_0}{h})^{\alpha+1}] \qquad (6.11)$$

where the subscript 0 denotes the initial values at time, t_0,
say. Integration of (6.7) with respect to t, on the other hand,
yields

$$(\Delta\theta)h = [(\Delta\theta)_0 h_0 - \frac{1}{2} \gamma h_0^2] + \frac{1}{2} \gamma h^2 - \int_{t_0}^{t} H(0,t)dt \qquad (6.12)$$

The terms in the square brackets represent the initial temperature deficit. If we assume $h = h_1 \gg h_0$ at $t = t_1 > t_0$ so that $(h_0/h_1)^\alpha \sim 0$, (6.11) becomes

$$\Delta\theta = \frac{\gamma}{\alpha+1} h = \frac{A}{1+2A} \gamma h \qquad \text{for } t \geq t_1 \qquad (6.13)$$

Then Eq. (6.12) can be expressed as

$$h^2 = -\frac{2(1+2A)}{\gamma}[(\Delta\theta)_0 h_0 - \frac{1}{2}\gamma h_0^2] + \frac{2(1+2A)}{\gamma} \int_{t_0}^{t} H(0,t)dt$$

$$\text{for } t \geq t_1 \qquad (6.14)$$

This implies that for $h \gg h_0$, the initial temperature deficit (the terms in the square brackets), rather than individual h_0 or $(\theta_M)_0$, is important for the evolutions of h and $\Delta\theta$ (Driedonks, 1982).

The discontinuity $\langle\Delta\theta\rangle$, plotted along with $\langle h\rangle$, $\langle|\underset{\sim}{V}_M|\rangle$ and the rms horizontal variability of θ_M in Fig. 6.1a, increases slightly after sunrise at 0425, and shows a local maximum at about 0500. This is because both $\langle H(0,t)\rangle$ and $\langle H(h,t)\rangle$, as depicted in Fig. 6.2a, are small but mostly negative during this period and cause $\langle\theta_M\rangle$ to decrease according to (6.4), as shown in Fig. 6.3. Additionally, the mixed-layer depth $\langle h\rangle$ slightly increases because of the positive $\langle w_e\rangle$, as illustrated in Fig. 6.2b, which contributes again to an increase of $\Delta\theta$ according to (6.2). The rapid decrease of $\langle\Delta\theta\rangle$ during the mid-morning is caused by both the shallow $\langle h\rangle$ and increasingly strong $\langle H(0,t)\rangle$ and $\langle H(h,t)\rangle$ which cause $\langle\theta_M\rangle$ to increase and thus $\langle\Delta\theta\rangle$ to decrease rapidly, as (6.6) indicates.

The growth rate of $\langle h\rangle$ is relatively small during early morning
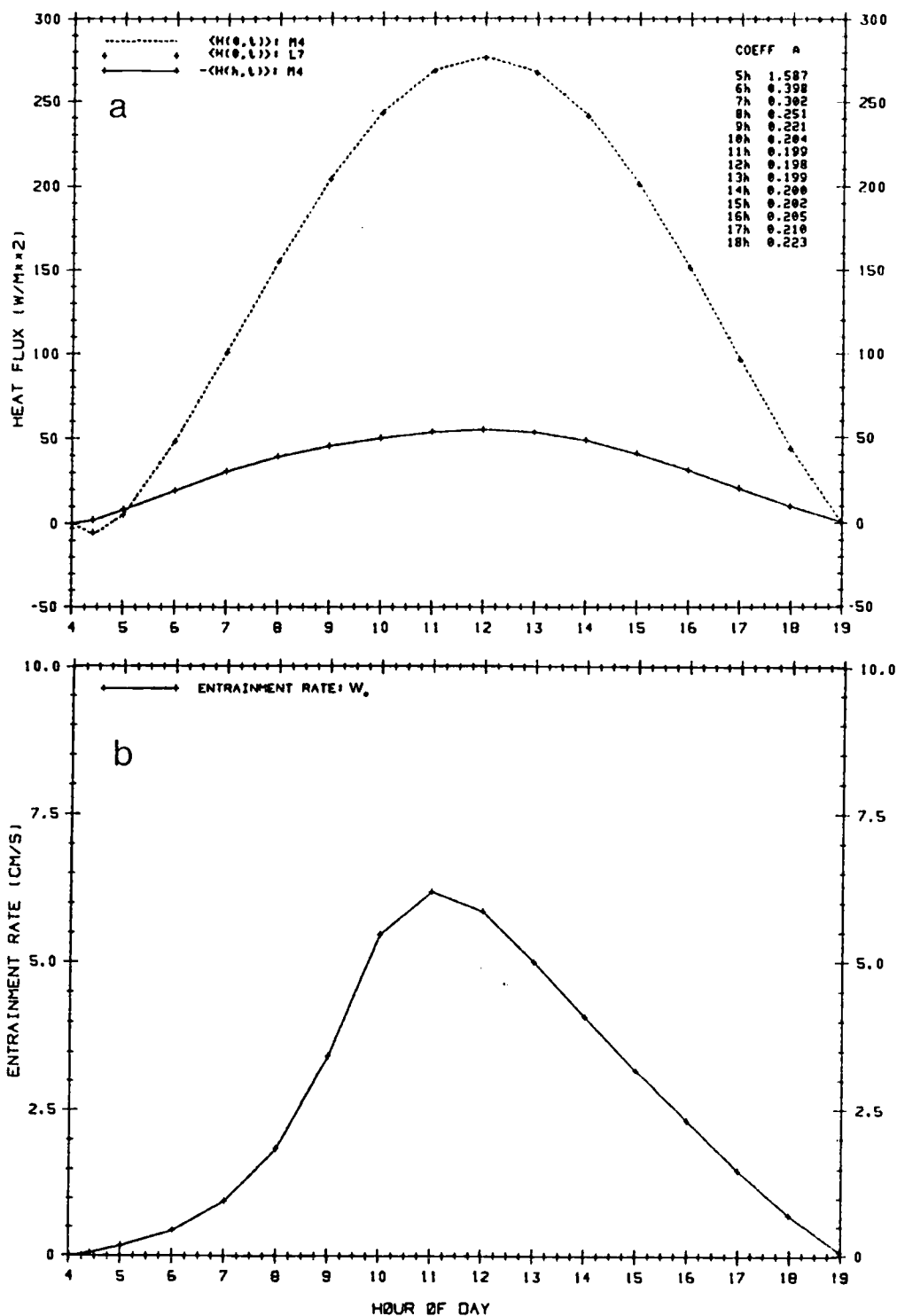
Fig. 6.2. (a): Domain-averaged surface sensible heat fluxes <H(0,t)> for M4 and L7 models, and entrainment heat flux at the mixed-layer top <H(h,t)> for M4 model as functions of time of day. Units are watts m^{-1}. Time is LST. Also shown is the coefficient A of (6.8) for M4. (b): Domain-averaged entrainment $<w_e>$ (cm s^{-1}) for M4.
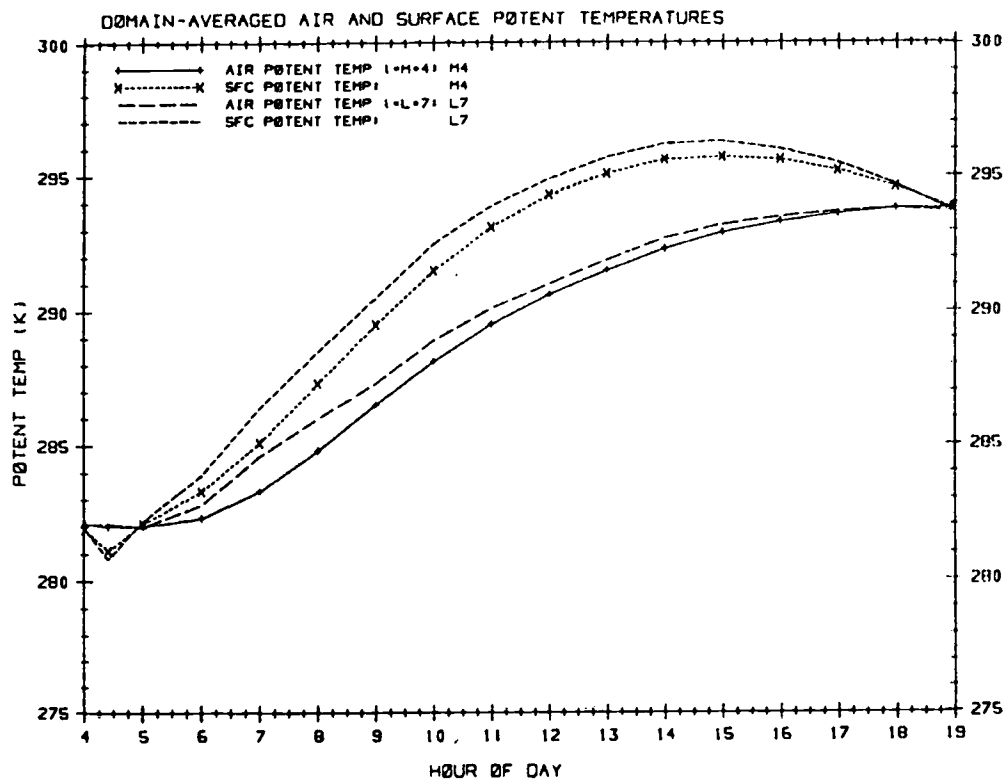
Fig. 6.3. Domain-averaged potential temperatures (K) of the mixed layer for M4 and of layer ℓ = 7 for L7 as functions of time of day. Also shown are the ground surface potential temperatures for M4 and L7.

hours, but becomes larger as $\langle w_e \rangle$ increases rapidly through late morning hours, as shown in Fig. 6.2b, and eventually balances in (6.6) with the negative effect of $\langle H(0,t) \rangle / h$ and $\langle H(h,t) \rangle / h$ on the growth rate of $\langle \Delta\theta \rangle$ at ~1100 when $\langle \Delta\theta \rangle$ attains its minimum. The height of the inversion $\langle h \rangle$ begins to increase rapidly after ~0800, well before $\langle \Delta\theta \rangle$ reaches its minimum, indicating that in M4-model results the significant entrainment process starts much earlier than when the inversion strength becomes minimum. In fact, $\langle w_e \rangle$ reaches its maximum at ~1100 when $\langle \Delta\theta \rangle$ attains its minimum. In other words, the transition from the period of the "morning transient" to that of the "morning convection" defined by Tennekes (1973) occurs well before the initial inversion has been "filled in." During the period of the "afternoon convection" that follows, $\langle h \rangle$ continues to deepen but at an increasingly slow rate, while $\langle \Delta\theta \rangle$ linearly increases very slightly during this period.

The mixed-layer depth has grown from $\langle h_0 \rangle$ = 289 m at 0500 to $\langle h \rangle$ = 850 m at 1100 so that $(\langle h_0 \rangle / \langle h \rangle)^\alpha = 1.5 \times 10^{-3}$ for A = 0.2 i.e., α = 6. Therefore, the influence of the initial inversion strength $\langle (\Delta\theta)_0 \rangle$ and depth $\langle h_0 \rangle$ virtually has vanished by this time, and the approximations (6.13) and (6.14), which make $\langle \Delta\theta \rangle$ proportional to ~γh, are valid during the afternoon convection period.

Comparing the evolution of $\langle h \rangle$ depicted in Fig. 6.1a with that of the mean boundary layer thickness deduced for the O'Neill data (Lettau and Davidson, 1953) and given in Fig. 1 of Carson (1973), it may be said that the development of $\langle h \rangle$ obtained from the M4 model qualitatively agrees with the observed data as far as its daytime behavior is concerned. It is noted that the shape of the entrain-

ment $\langle w_e \rangle$ shown in Fig. 6.2b with its peak in the late morning is also similar to that depicted in Fig. 9 of Carson (1973) obtained for the convection periods in his model.

In the M4 model $H(h,t)$ was computed using (4.23b) with w_e being calculated from Eq. (3.55) and $\Delta\theta$ determined by the procedure described in Section 4.1.4. The entrainment constant A between $\langle H(h,t) \rangle$ and $\langle H(0,t) \rangle$ computed using (6.8) is shown in Fig. 6.2a, which remains near 0.2 during most of the day, as the entrainment rate equation (3.55) dictates when the surface heating is strong. The laboratory experiments by Deardorff et al. (1980) suggest that the value of A is near 0.2, while Carson (1973) obtained 0.5 for the early afternoon by examining the O'Neill data.

To examine the effect of initial values $(\Delta\theta)_0$ and h_0 on the evolutions of $\Delta\theta$ and h, (6.11) and (6.12) have been solved itera- tively by using Newton's method. The values of $\langle h \rangle$ and $\langle \Delta\theta \rangle$ illus- trated in Fig. 6.1a were used as the values of h and $\Delta\theta$ at the starting times t_0 = 05, 08, 09, and 1100. The third term on the right side of (6.12) was integrated numerically using the linearly interpolated values of $\langle H(0,t) \rangle$ shown in Fig. 6.2a with also linear- ly interpolated values of A incorporated in the quadrature. The value of γ was set to a constant 0.005 K m^{-1}. Eq. (6.11) assumes that (6.8) holds true, while (6.12) involves no assumption. The results are shown in Fig. 6.4. It is seen that h and $\Delta\theta$ computed from (6.11) and (6.12) are very similar to $\langle h \rangle$ and $\langle \Delta\theta \rangle$ from the M4 model. In particular, the slow-growing behavior of h during the period of the morning transient followed by the rapid growth of h in the morning convection period is exhibited regardless of the initia-
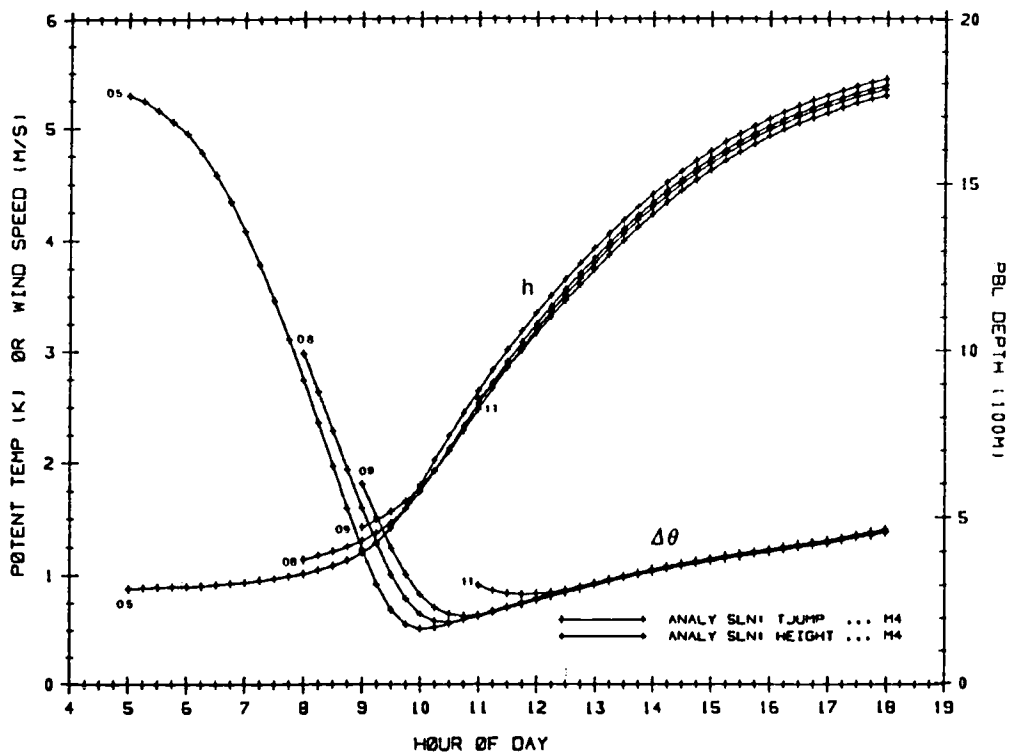
Fig. 6.4. Evolutions of h (100 m) and Δθ (K) computed using (6.11)
and (6.12). The number labeling a curve refers to the
designated starting time of the calculations.

tion time of the calculations. The inversion strength, on the other hand, decreases relatively rapidly during the morning transient period, reflecting a slower growth of h and a fast increase of $\langle H(0,t) \rangle$ and $\langle H(h,t) \rangle$. This behavior of $\langle h \rangle$ and $\langle \Delta\theta \rangle$ during the morning transient period could not be well explained by (6.13) and (6.14) which assumes $h_0 \ll h$ so that the effect of h_0 and $(\Delta\theta)_0$ on $\Delta\theta$ and hence h can be ignored. However, (6.13) and (6.14) should be also valid in the afternoon when $h_0 \ll h$ holds. It seems, on the other hand, that the assumption given by (6.8) has less effect on the behaviors of h and $\Delta\theta$ since the variation of A can be approximately accounted for by utilizing its hourly values in (6.11).

Therefore, it may be concluded that the evolution of $\langle h \rangle$ and $\langle \Delta\theta \rangle$ obtained from the M4-model run can be qualitatively explained by Tennekes' (1973) simple model in which nonzero $(h_0/h)^\alpha$ and $(\Delta\theta)_0$ are taken into account, although crude approximations have been made concerning the ratio between $\langle H(h,t) \rangle$ and $\langle H(0,t) \rangle$ and the potential temperature gradient aloft, γ.

Driedonks (1982), on the other hand, examined the sensitivity of h to variations in A and γ using Eqs. (6.13) and (6.14). He concluded that for $h \gg h_0$, a change in A from A = 0 to A = 0.2 will cause a change in h of about 20% at noon and that the same change in h occurs when A changes from 0.2 to 0.5. As for γ, an error of 0.001 K m^{-1} leads to a change in h of about 10% when a typical value of $\gamma = 0.005$ K m^{-1} is used. Therefore, we find that our findings given above are consistent with Driedonks' (1982) argument in that small variations in A and γ observed in the M4 results have minor effects on the behavior of h.

We now describe the evolution of $\langle h \rangle$ and $\langle \Delta\theta \rangle$ for the L7-model run illustrated in Fig. 6.1b. The depth of the nocturnal boundary layer which is assumed to occupy the lowest model layer was about 100 m everywhere before sunrise, and $\langle h \rangle$ stays steady until about 0800 at which time $\langle \Delta\theta \rangle$ attains its minimum, so that the description of the morning transient period by Tennekes (1973) also applies to the L7-model results. Therefore, the mixed-layer depth grows very little while the nocturnal boundary layer is being filled in, although a considerable amount of the downward heat flux $\langle H(h,t) \rangle$ exists during early-morning hours, as illustrated in Figs. 6.5a and b, at height $\langle h \rangle + \langle h_s \rangle$ which is located at half-level 6 + 1/2 of the L7 model. This is because in the L7 model the mixed-layer depth is diagnosed from the local Ricardson number Ri and the potential temperature gradient so that as long as Ri at the inversion base stays larger than a critical value $Ri_c = 1$ we chose in Section 3.3, h remains steady.

The development of $\langle h \rangle$ during the morning and afternoon convection periods somewhat deviates from the smooth behavior of $\langle h \rangle$ of the M4 model but is approximately linear in time until 1500 or so. The mixed-layer deepens from 97 m at 0500 and 1340 m at 1500, an increase of 1243 m, while the M4 model gives 291 m at 0500 to 1578 m at 1500, resulting in an increase of 1287 m. Considering the differences in procedures used in obtaining the mixed-layer depth in the two models, 4% difference in the estimates of $\langle h \rangle$ is rather small. The growth of $\langle h \rangle$ after 1500, however, diminishes noticeably with an increase of 114 m between 1500 and 1900, while the M4 model shows an increase of 223 m during the same period.
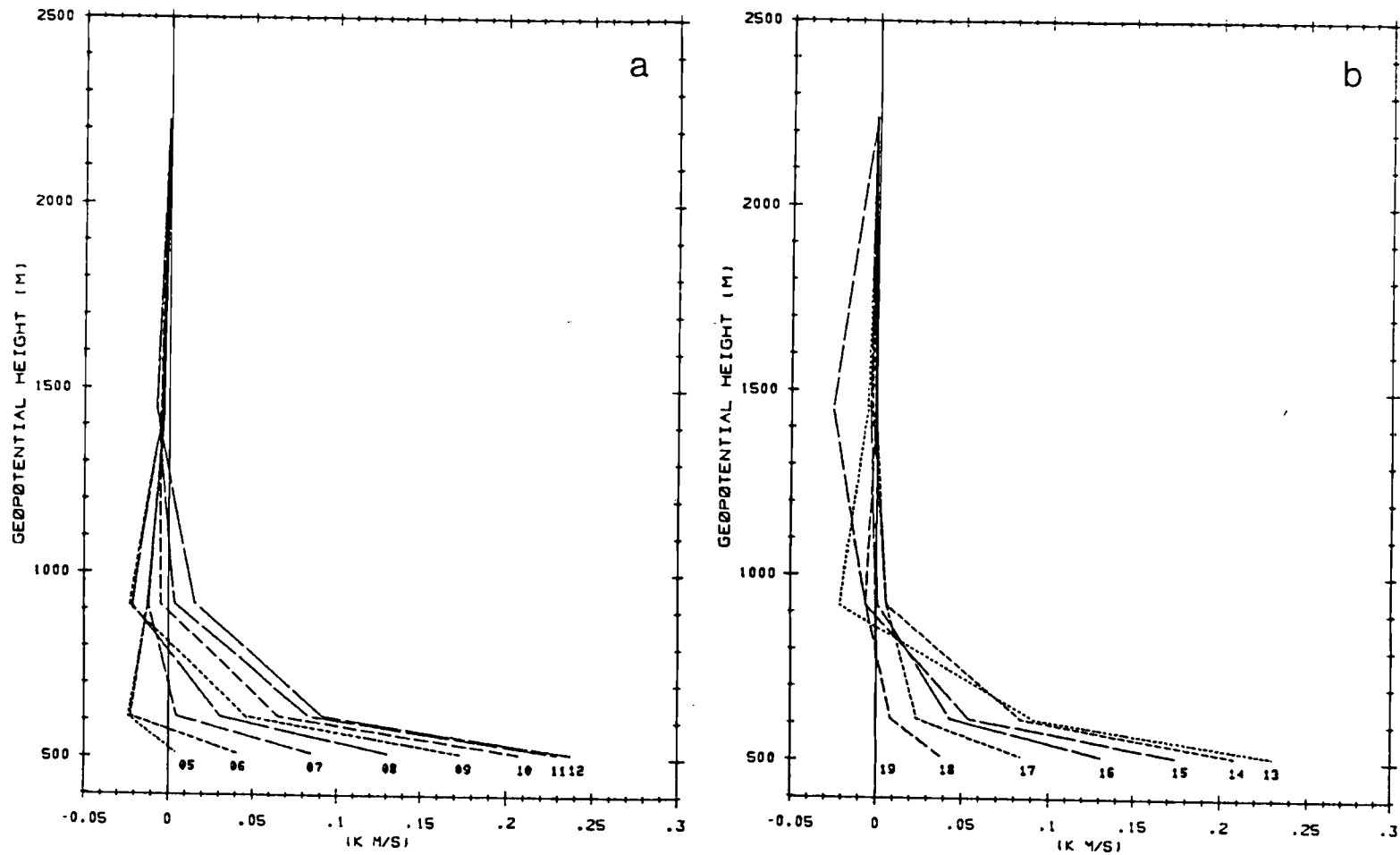
Fig. 6.5. Time evolutions of layer-averaged sensible heat flux for L7 computed at layer interfaces (half levels); (a): for 0500-1200 LST and (b): for 1300-1900 LST. Except for the surface heat flux which was obtained using (4.20), heat fluxes were computed using the eddy transfer coefficients K_M shown in Fig. 6.11. Units are K ms^{-1} (abscissa) and m (ordinate). The number labelling a curve refers to the time of day.

The evolution of <h> exhibited by the L7 model during the late afternoon convection period resembles that deduced for the O'Neill data and shown in Fig. 1 of Carson (1973), who described it as follows: the weakening thermals generated by the positive but decreasing surface heat flux are no longer able to maintain the thorough mixing throughout the established deep mixed layer or their penetration of the stable layer. Interfacial mixing has decayed and mechanical effects begin to dominate the evolution, and <h> remains steady or even begins to decrease. In the M4 model, on the other hand, <h> keeps increasing in the late afternoon as long as <H(0,t)> is positive, as indicated by (6.14), and the assumption that no subsidence exists makes an decrease of <h> impossible. However, considering the procedure used in the L7 model in estimating h with the aid of Ri's and gradients of θ, the agreement of the evolution of <h> from both models may be considered good.

The evolution of <Δθ> is smooth during the morning transient period, and the local minimum and maximum can be explained using the equations given earlier. At the beginning of the morning convection period, <Δθ> increases noticeably between 0800 and 0900, but after 0900 through 1200 its growth is small but smooth and linear in time. In the afternoon the development of <Δθ> is somewhat irregular but still mostly linear in time. <Δθ> increases from 0.48 K at 1100 to 1.10 K at 1900, an increase of 0.62 K, while the M4 model gives 0.91 K at 1100 and 1.45 K at 1900, an increase of 0.54 K. The procedure used in determining Δθ in the L7 model was discussed in Section 4.1.4, and it seems that the second format in (4.28a), which is equivalent to (6.13), is in effect during the

convection periods after 1100.

6.3 Evolution of Domain-Averaged Mixed-Layer Winds

Fig. 6.6a illustrates the hodographs of the domain-averaged mixed-layer winds for the M4 and L7 experiments. The mixed-layer wind for L7 is a mass-weighted vertical average of the winds below the mixed-layer top as determined by the procedure discussed in Section 3.3. It can be seen that the behaviors of the wind vectors of M4 and L7 are quite similar to each other and in both cases counterclockwise rotation of the hodograph is generated although the hodograph for L7 is not as smooth as that for M4. Observational evidence suggests that counterclockwise rotation of the winds, when observed diurnally in the Northern Hemisphere under certain physical circumstances, indeed occurs even though most of observed hodographs turn clockwise. For example, Fosberg and Schroeder (1966) found that the hodographs at some stations near the coast in central California showed a counterclockwise turning with time (see their Fig. 3). Staley (1959) also found that in the Columbia Basins in eastern Washington and Oregon, rotation of the wind vectors is partially counterclockwise (see his Fig. 3) at some stations near the mountain valleys, and Mass (1982) reported that in the lowlands of western Washington between the Coast Range and the Cascades the winds also turn counterclockwise on the western side of the basin. The hodograph shown in Fig. 6.7 has been deduced from the Wangara data used by Clarke (1974) which is composed of 40-day observations at height 44 m averaged by hour of day. The u component of the wind is always aligned with the direction of the geostrophic wind so that
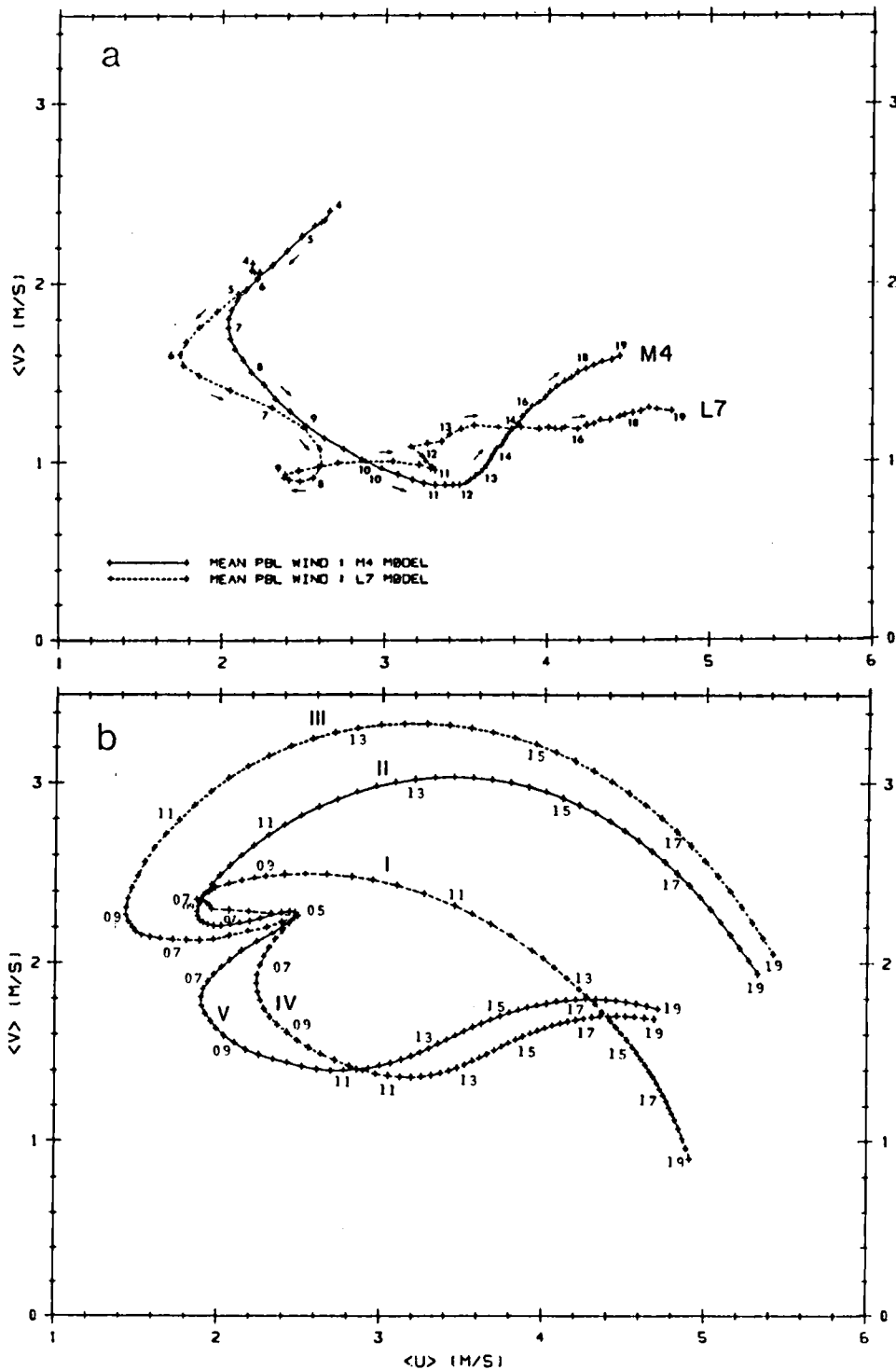
Fig. 6.6. (a): Hodographs of the domain-averaged mixed-layer winds for M4 and L7 experiments. Units are ms^{-1}. Numbers labeling the points refer to LST. (b): Hodographs of model results. Curve I: analytical solution (6.17) of (6.16); II: numerical solution of (6.16) with quadratic friction law; III: solution of (6.18); IV and V correspond to solutions of (6.19) and (6.20), respectively.
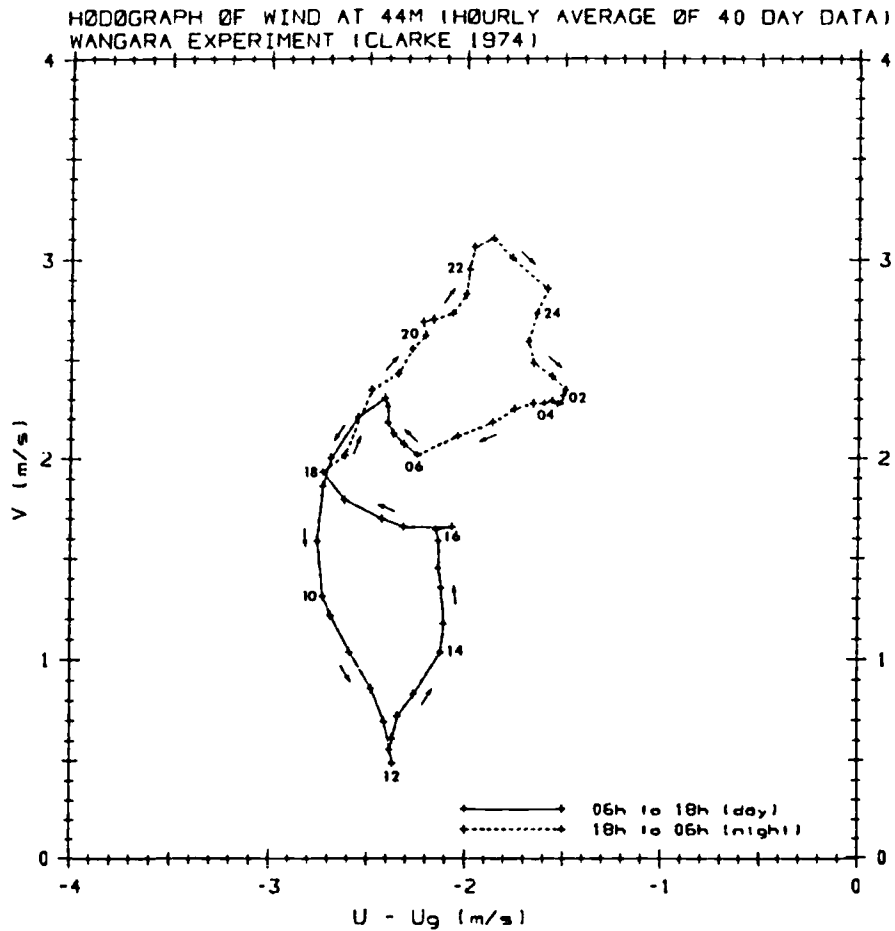
Fig. 6.7. Hodograph of Wangara data at height 44 m deduced from data
by Clarke (1974), transferred to the Northern Hemisphere.
Wind components are hourly averages of 40-day observations.
u components are aligned with the geostrophic wind. Units
are ms^{-1}. Numbers labeling the points refer to LST.

the v component of the geostrophic wind is zero. This hodograph, already transferred to the Northern Hemisphere, shows a counter-clockwise turning of the wind during daytime.

Theoretical studies on rotation of the wind hodographs, on the other hand, have been mostly concerned with the nocturnal jet and the sea breeze. Blackadar (1957) proposed a simple theory that attributed the formation of the nocturnal jet and its clockwise turning with time to an inertial oscillation induced by release of all frictional constraints near sunset. Buajitti and Blackader (1957) sought the cause of the diurnal wind-structure variations in the atmospheric boundary layer by adding the diurnally varying tur-bulent stresses to Blackadar's (1957) model. Again rotation of hodographs was always clockwise. Thorpe and Guymer (1977) also extended Blackadar's (1957) theory by considering a model with three slabs (layers). Included in their momentum equations (for horizon-tally homogeneous flow) were the mixed-layer depth and the parame-terized surface stress that were allowed to vary only at sunrise and sunset. Their model was further extended by Malcher and Kraus (1983) to examine the effects of entrainment processes, advection and large-scale pressure gradients on the variations of the low-level jet. Added also in their model were time-dependent sur-face stress and mixed-layer depth. They also found turning of the winds to be clockwise. Kusuda and Alpert (1983) performed an inves-tigation of counterclockwise rotation of the wind hodograph by using a two-dimensional, 10-level sea-breeze model with its lower boundary consisting of a steep mountain and an ocean surface and found that at the lee side of the mountain the hodographs partially turned

counterclockwise in the lowest levels during the hours from the
afternoon to the following morning. They also solved a linear model
analytically following Haurwitz (1947) to show that inclusion of a
thermal force in the counterclockwise sense generates clear
(complete) counterclockwise rotation of the wind. Their model,
however, applies only to the cases for which an inertial oscillation
can be ignored, contrary to Blackadar's (1957) and Thrope and
Guymer's (1977) studies in which an inertial oscillation played a
predominant role in rotation of wind vectors.

To understand the major mechanisms of partial counterclockwise
rotation of the hodographs shown in Fig. 6.6a, we utilize here the
simple slab model for daytime by Thorpe and Guymer (1977). The
equation of motion for horizontally homogeneous mixed-layer flow in
which the coordinates are rotated so that the x-direction is aligned
with the constant geostrophic wind is:

$$\frac{\partial \underset{\sim}{V}}{\partial t} + f\underset{\sim}{k} \times (\underset{\sim}{V} - \underset{\sim}{V}_g) = \frac{\partial \underset{\sim}{\tau}}{\partial z} \tag{6.15}$$

where the y component of $\underset{\sim}{V}_g$ is zero, and $\underset{\sim}{\tau}$ is the turbulent stress
in the mixed layer. The assumption of horizontal homogeneity thus
eliminates advection and (mesoscale) pressure gradient terms in
(6.15). If we assume that the stress decreases linearly with height
to zero at the top of the mixed-layer whose depth is h, i.e.,
$\underset{\sim}{\tau}_B = 0$ at z = h, (6.15) can be written as

$$\frac{\partial \underset{\sim}{V}}{\partial t} + f\underset{\sim}{k} \times (\underset{\sim}{V} - \underset{\sim}{V}_g) = -\frac{\underset{\sim}{\tau}_s}{h} \tag{6.16}$$

where the subscript s refers to the surface. If the surface stress τ_s is parameterized using Swinbank's (1970) hypothesis that the stress and velocity vectors are parallel, i.e., $\tau_s = k_s \underset{\sim}{V}$, where k_s is a constant, (6.16) can be solved explicitly using complex notation for the winds, $U = u + iv$:

$$U = \frac{f^2 U_g}{r^2 + f^2} + \frac{f U_g r}{r^2 + f^2} + U_0 \exp\{-(if + r)t\} \qquad (6.17)$$

where $r \equiv k_s/h$ is a constant, and U_0 is a complex constant determined from the initial conditions. In evaluating (6.17), the coefficient r obtained at every hour by setting r equal to a linearized friction coefficient $<C_D/h><V>$ (Anthes, 1980), where $V = |\underset{\sim}{V}|$ and $< >$ refers to the domain-averaged value of the M4 results, was interpolated linearly to give the values of r at 15-min intervals. The constant U_0 was evaluated using $<u>$ and $<v>$ at 0500, and U_g was set at 5 ms^{-1} and $f = 10^{-4}s^{-1}$. The solution thus obtained was plotted as Case (I) in Fig. 6.6b. It is noted that (6.17) is the solution of (6.16) with constant r, while the hodograph (I) in Fig. 6.6b was obtained using variable r in (6.17). We also note that the above hypothesis of the wind-stress parallelism in the boundary layer is not as good as the classical hypothesis that the stress and velocity shear are parallel, as shown by Carson and Smith (1973), and is only acceptable in the lowest levels of the boundary layer.

Eq. (6.16) with a quadratic law for surface stress, $\tau_s = C_D V \underset{\sim}{V}$, was next integrated numerically using the Euler backward (Matsuno) scheme with a 15-min time-step interval. Again

the values of $\langle C_D/h \rangle$ interpolated at 15-min intervals were fed in as the values of C_D/h on the right side of (6.16). The results are shown as Case (II) in Fig. 6.6b. Furthermore, the integration of (6.16) was repeated with "form drag" $\underset{\sim}{F}_D$ from M4 added to the right sides of (6.16). Form drag was computed according to the procedure described by DUH (1984). Thus, (6.16) now takes the following form:

$$\frac{\partial \underset{\sim}{V}}{\partial t} + f\underset{\sim}{k} \times (\underset{\sim}{V} - \underset{\sim}{V}_g) = - \frac{C_D V V}{h} - \frac{\underset{\sim}{F}_D}{h} \qquad (6.18)$$

where the components of form drag averaged over the domain are given by

$$(F_D)_x = \frac{1}{\langle \rho \rangle} \langle p_s \frac{\partial h_s}{\partial x} \rangle; \quad (F_D)_y = \frac{1}{\langle \rho \rangle} \langle p_s \frac{\partial h_s}{\partial y} \rangle$$

The solution of (6.18) using $(F_D)_x$ and $(F_D)_y$ obtained from M4 at 15-min intervals is illustrated as Case (III) in Fig. 6.6b.

We see that major features of the hodographs (I), (II) and (III) are quite similar: rotation of the wind hodographs is clockwise through the entire integration period in all cases, and it is therefore apparent that the behavior of the hodographs shown in Fig. 6.6a cannot be explained by the combined effects of the Coriolis force, the surface stress and form drag alone.

An assumption we have made in (6.16) and (6.18) is that the turbulent stress diminishes at the top of the mixed layer. If we now take into account the non-zero turbulent stress at the mixed-layer top $\underset{\sim}{\tau}_B$ while keeping the linearity assumption of the stress, we would need to modify (6.16) to:

$$\frac{\partial \underset{\sim}{V}}{\partial t} + f\underset{\sim}{k} \times (\underset{\sim}{V} - \underset{\sim}{V}_g) = \frac{\underset{\sim}{\tau}_B - \underset{\sim}{\tau}_s}{h} \qquad (6.19)$$

where the components of τ_B are $(\tau_x)_B = w_e(u_3 - u)$,

$(\tau_y)_B = w_e(v_3 - v)$, w_e is the entrainment rate, and u_3 and

v_3 are the components of the wind in the free atmosphere just above

the mixed-layer top. Since u_3 and v_3 are not computed in the simple

model we are using here, the domain-averaged wind components

$<u_{\ell=3}>$ and $<v_{\ell=3}>$ from M4 are utilized so that $(\tau_x)_B/h$ and

$(\tau_y)_B/h$ in (6.19) are replaced by $<w_e/h>[<u_3> - u]$ and

$<w_e/h>[<v_3> - v]$, respectively. The results of numerical

integration of (6.19) are plotted as Case (IV) in Fig. 6.6b.

Furthermore, adding form drag terms to (6.19) gives

$$\frac{\partial \underset{\sim}{V}}{\partial t} + f\underset{\sim}{k} \times (\underset{\sim}{V} - \underset{\sim}{V}_g) = \frac{\underset{\sim}{\tau}_B - \underset{\sim}{\tau}_S - \underset{\sim}{F}_D}{h} \qquad (6.20)$$

whose numerical solution is depicted as Case (V) in Fig. 6.6b. It

is apparent that the hodographs (IV) and (V) showing counterclock-

wise rotation are much closer to those shown in Fig. 6.6a. We have

found, therefore, that the momentum flux at the mixed-layer top

plays a predominant role in the diurnal variations of the

domain-averaged mixed-layer wind structure obtained from the M4 and

L7 experiments.

In Figs. 6.8 and 6.9, individual acceleration terms of (6.20)

corresponding to Case (V) in Fig. 6.6b are plotted. It can be noted

that the deceleration effect of the surface stress shown as (A) in

both Figs. 6.8a and b decreases nearly monotonically throughout the

day but in the afternoon it becomes nearly constant. The effect of

form drag terms (C) which is roughly in phase with that of (A) shows

a similar tendency, with its magnitude being about one-third of (A)
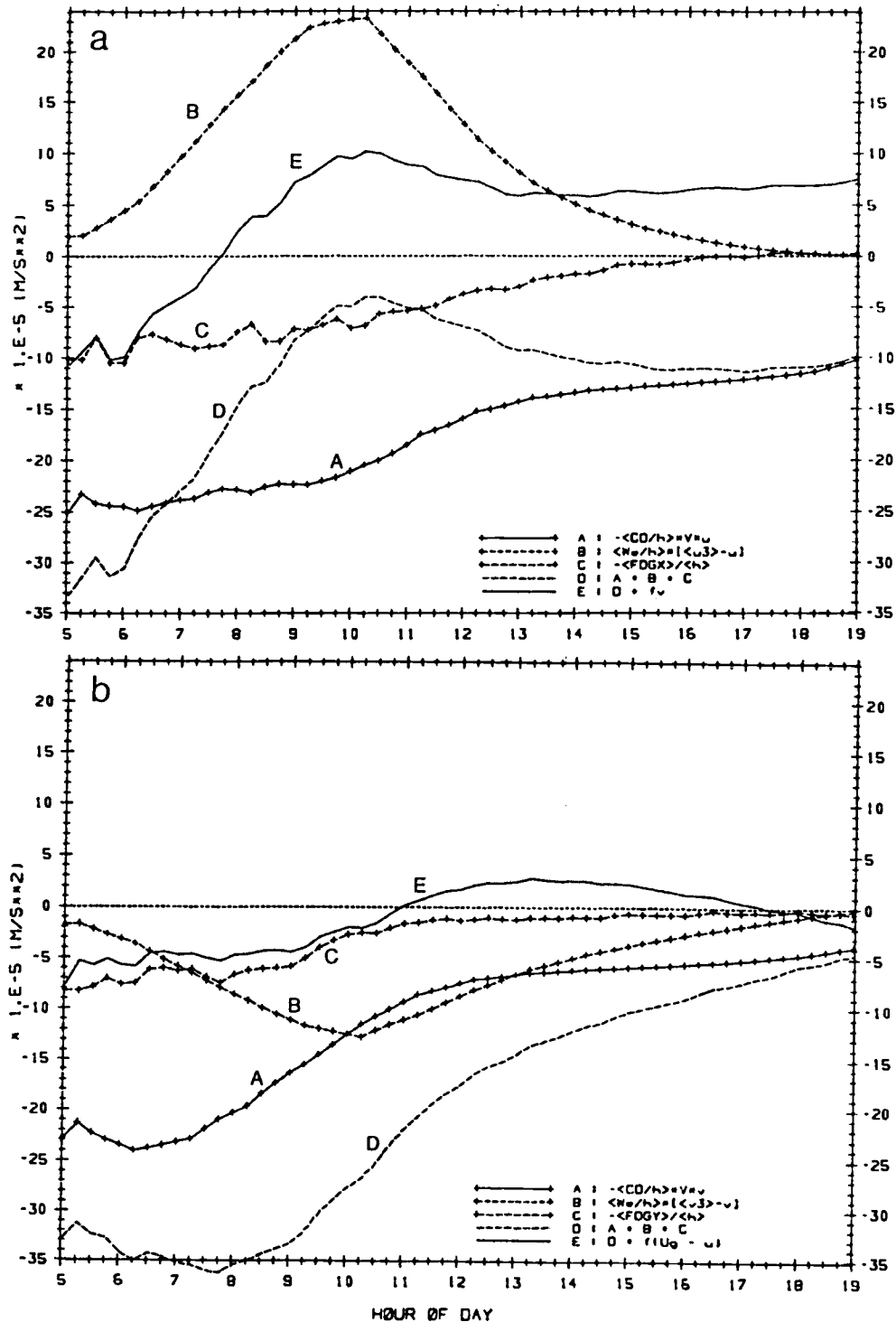
Fig. 6.8. (a): Time evolutions of acceleration terms in u-component of (6.20). Units are 10^{-5} ms^{-2}, time is LST. Curve A: $-\langle C_D/h\rangle|\underline{v}|u$; B: $\langle w_e/h\rangle(\langle u_3\rangle - u)$; C: $-\langle p_s \partial h_s/\partial x\rangle/(\langle\rho\rangle\langle h\rangle)$; D: sum of A, B and C; E: sum of D and fv. (b): As in (a) except for v-componemt of (6.20), and the curve E is now the sum of D and $f(U_g-u)$.
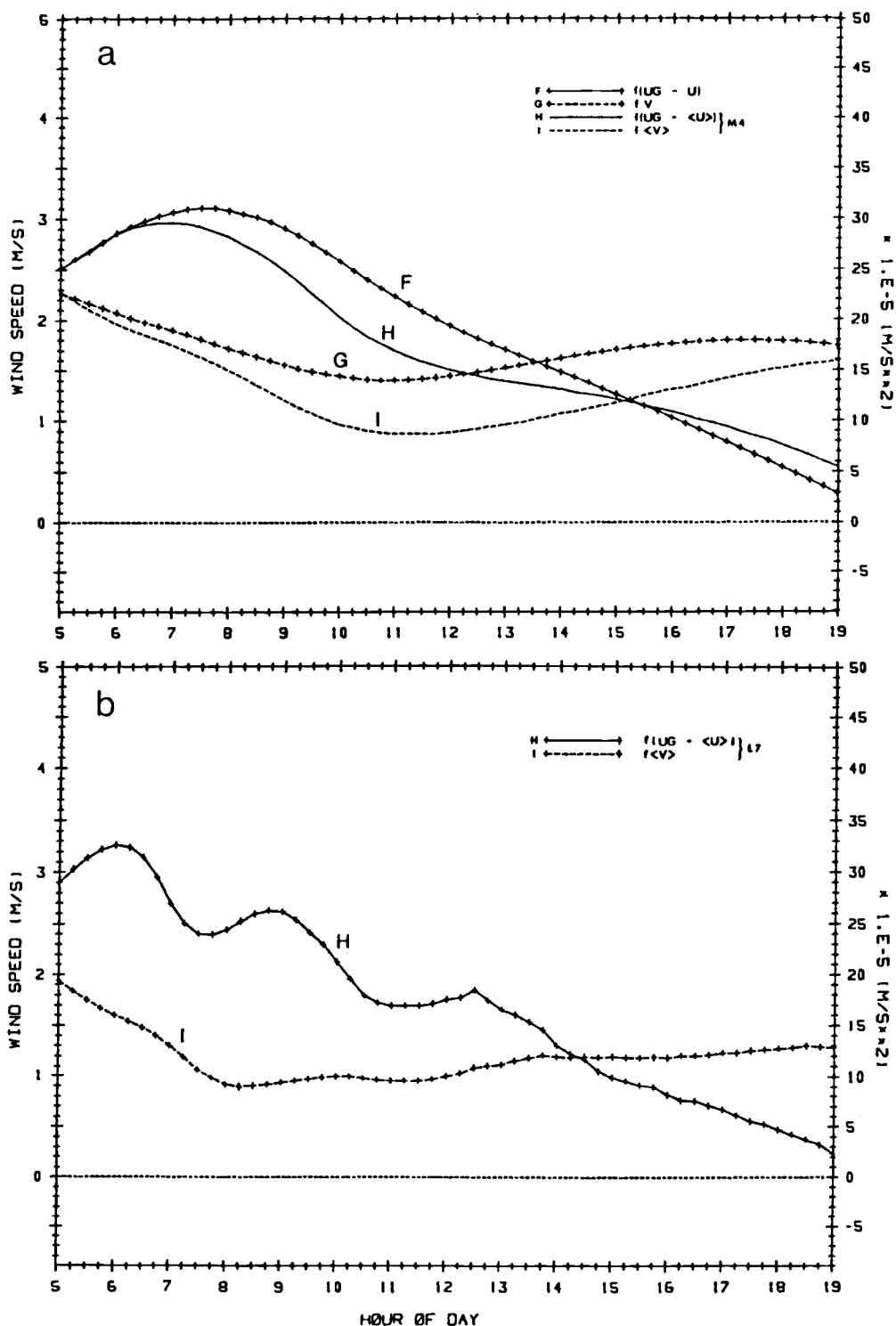
Fig. 6.9. (a): Evolutions of Coriolis force terms in (6.20). Curve F: $f(U_g-u)$; G: fv. Units are 10^{-5} ms^{-2} as shown on the right ordinate. Also illustrated are those obtained from M4; H: $f(U_g-<u_M>)$ and I: $f<v_M>$. The same curves can display geostrophic departures of wind components if f is removed. Units are ms^{-1} as shown on the left ordinate. (b): As in (a) except for layer 7 of L7 experiment.

during the morning hours. On the other hand, the entrainment effect at the top of the mixed layer (B) on the u component is positive (acceleration) throughout the day. It increases during the morning hours till ~1000 when its magnitude becomes comparable to that of the surface stress effect but with opposite sign, and decreases monotonically through the rest of the day, vanishing before sunset. The shape of (B) is similar to that of $\langle w_e \rangle$ shown in Fig. 6.2b but its peak is reached about one hour earlier than that of $\langle w_e \rangle$. The entrainment effect on the v component, on the other hand, is always negative (deceleration) and in opposite phase (180° difference) with that on the u component. It attains a maximum (negative) magnitude at ~1000, which is comparable to that of the stress effect but about one-half of the entrainment effect on the u component. The combined effects of these three terms (A)-(C) on individual components are illustrated as (D) in Figs. 6.8a and b. We find that these three terms alone decelerate both u and v in the context of (6.20).

If the Coriolis-force effect, which is shown in Fig. 6.9, is added we obtain the curves (E) in Figs. 6.8a and b. By comparing them with the hodograph (V) in Fig. 6.6b, we see that the combined acceleration effect (E) makes the u component decrease during early hours in the morning until ~0730, but from then on they make u increase, while the effect on v is a deceleration through the morning till ~1100, an acceleration between then and ~1730, and then again a deceleration after 1730. The hodograph (V) of Fig. 6.6b clearly shows the combined effect of the acceleration by making noticeable turns at around 0730, 1100 and 1730. In Figs. 6.9a and b the u- and v-components of the layer-averaged winds of the lowest

layers (and the Coriolis forces) are plotted for M4 and L7, respectively, and it can be seen that the results from the simple slab model in this section do not deviate too far from those of M4 and L7 as far as components of the wind are concerned, despite oversimplifications in the model used here.

We next examine the relative contributions of the Coriolis force and the turbulent stresses to turning of the domain-averaged mixed-layer winds. Following Burk and Staley (1979) and Kusuda and Alpert (1983) the equation for the local rate of change of the horizontal wind direction can be written as

$$\frac{\partial \alpha}{\partial t} = \frac{1}{V^2} \, \underset{\sim}{k} \cdot (\underset{\sim}{V} \times \frac{\partial \underset{\sim}{V}}{\partial t}) \tag{6.21}$$

where α is the angle between the wind vector and the positive direction of the x-axis. This expression shows that those forces that have a component normal to the wind vector contribute to the turning of the wind. We consider again horizontally homogeneous mixed-layer flow:

$$\frac{\partial \underset{\sim}{V}}{\partial t} = - f\underset{\sim}{k} \times (\underset{\sim}{V} - \underset{\sim}{V}_g) + \underset{\sim}{F} \tag{6.22}$$

where $\underset{\sim}{F}$ represents the frictional force. Substitution of (6.22) into (6.21) then yields

$$\frac{\partial \alpha}{\partial t} = - f + f \frac{\underset{\sim}{V} \cdot \underset{\sim}{V}_g}{V^2} + \frac{\underset{\sim}{k} \cdot \underset{\sim}{V} \times \underset{\sim}{F}}{V^2} \tag{6.23}$$

If we consider as $\underset{\sim}{F}$ the force due to the surface stress only, then we have as in Cases (I) or (II) above:

$$\underset{\sim}{F} = - \frac{\underset{\sim}{\tau}_s}{h} = - \frac{k_s \underset{\sim}{V}}{h} \quad \text{or} \quad - \frac{C_D V \underset{\sim}{V}}{h}$$

Therefore, it is clear from the third term on the right side of (6.23) that the surface stress contributes nothing explicitly to rotation of the wind vector, whether a linear or quadratic friction law is used. Thus we see that in Cases (I), (II) and (III) shown in Fig. 6.6b, α increases through midmorning because $\underset{\sim}{V}\cdot\underset{\sim}{V}_g/V^2 = (V_g/V)\cos\alpha > 1$, but from then on through the afternoon α decreases due to the fact that $V_g\cos\alpha < V$ and the winds turn clockwise because V increases monotonically with time. On the other hand, if we take into consideration the stress at the mixed-layer top $\underset{\sim}{\tau}_B = w_e(\underset{\sim}{V}_3-\underset{\sim}{V})$ we have

$$\frac{\underset{\sim}{k}\cdot\underset{\sim}{V}x\underset{\sim}{F}}{V^2} = \frac{\underset{\sim}{k}\cdot\underset{\sim}{V}x\underset{\sim}{V}_3}{V^2}\frac{w_e}{h} = \frac{[uv_3-u_3v]}{V^2}\frac{w_e}{h}$$

Here we omitted the domain-averaging symbol < > for simplicity. In general $\underset{\sim}{V}_3$ is not aligned with $\underset{\sim}{V}$ so that it gives non-zero contribution to rotation of the wind. It has been found for Case (IV) that the second term on the right side of (6.23), which is always positive, is larger than f between 0500 and 1750 with its maximum value being ~1.45f between ~1000 and 1100, whereas the third term is always negative, and attains a maximum magnitude which is ~1/2 of the second term, i.e., ~3/4f around 1000~1100. The sum of three terms is negative from 0500 to 1215 and from 1545 to 1900 so that α decreases during these periods and thus the wind vector turns clockwise, whereas between 1215 and 1545 the sum is positive, making α increase and thus causing counterclockwise rotation of the wind vector. It is noted that decreasing α does not necessarily mean a clockwise rotation of the hodograph and in fact

the hodograph itself turns counterclockwise through mid-afternoon.

Kusuda and Alpert (1983), on the other hand, examined the magnitudes of the various terms contributing to the rate of rotation including the advection and mesoscale pressure gradient terms for their 2-D model mentioned earlier. [For the complete equation for the rotation rate see Eq. (3) of Kusuda and Alpert (1983).] They concluded that the mesoscale pressure gradient term, the advection term, as well as the frictional force term, were important for the occurrence of partial counterclockwise rotation. We have found, however, that counterclockwise rotation of the domain-averaged mixed-layer winds from M4 and L7 can be mostly explained by the turbulent mixing of momentum at the mixed-layer top.

Corresponding to the hodograph shown in Fig. 6.6a of the mass-weighted vertical-mean mixed-layer winds for L7, the evolution of the layer-averaged winds for each of the lowest 5 layers for L7 is shown in Fig. 6.10. It is immediately noticed that only the hodograph for the lowest layer rotates counterclockwise. During early hours in the morning the model mixed layer consists of the lowest layer only, as determined by the given initial conditions. As the solar insolation becomes stronger it deepens and its domain-averaged top has penetrated into the layer above ($\ell = 6$) by 0630. The hodograph for $\ell = 6$ shows that the layer-averaged wind rapidly loses its u momentum between 0600 and 0900 by mixing with the low-momentum air in layer 7. Part of the u momentum of the layer-6 wind is transferred to the lower layer and accelerate the u component of the layer-7 wind. By 0930 layer 6 is completely within the mixed-layer, and we see that by noon the layer-averaged momentum
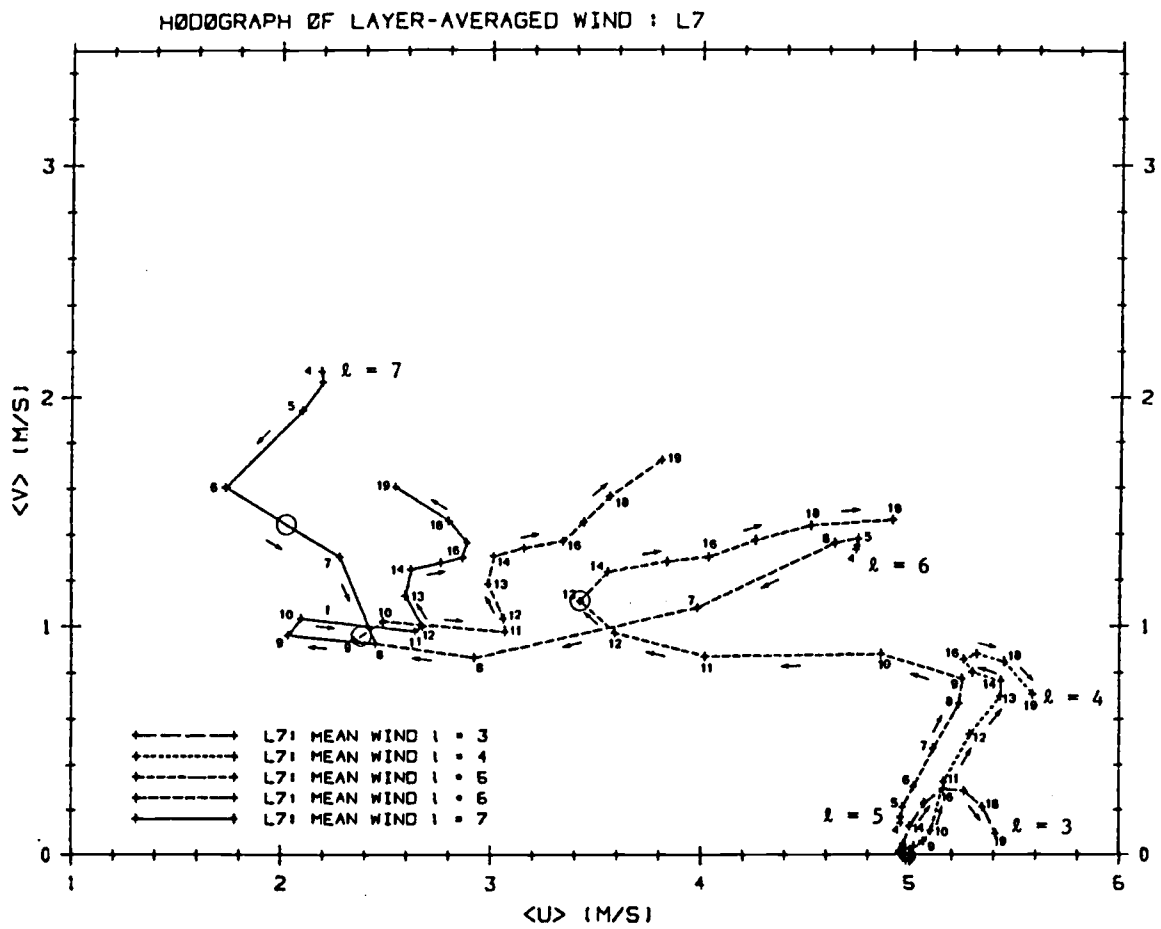
Fig.6.10. Hodographs of layer-averaged winds for the lowest 5 layers
of the L7 experiment. Units are ms^{-1}. Numbers labeling
the points refer to LST. The circles indicate the
estimated time when the mixed-layer top has completely
risen above a particular layer.

in the lowest three layers, which were clearly distinct from each other initially, has become well-mixed. The mixed-layer top further rises and reaches the lower boundary of layer 4 around 1300. Contrary to layers 5 and 6, however, the u components of layer 4 loses its momentum only slightly between 1300 and 1600. This may be understood if one considers the mass in each layer in terms of σ: $\delta\sigma_7 = 0.0204$, $\delta\sigma_6 = 0.0612$, $\delta\sigma_5 = 0.1021$, and $\delta\sigma_4 = 0.1428$ so that the layer $\ell = 4$ has more mass than that of the lower three layers combined. The domain-averaged mixed-layer top reaches ~2000 m above sea level at 1730 which is slightly lower than the domain-averaged interface level height between layers $\ell = 4$ and 3 so that the layer $\ell = 4$ remains partially above the mixed layer throughout the afternoon. This is because in the L7 model the turbulent diffusion coefficients K_M and K_H are functions of Ri, vertical wind shear and height, as given by (3.36), and the diminishing K_M and K_H in higher levels during mid- and late-afternoon can barely maintain the thorough mixing throughout the deepened mixed layer, and consequently, the mixed-layer top is unable to penetrate further into the stable layer. This is evidenced by the time evolution of the domain-averaged vertical heat flux depicted in Fig. 6.5 as well as that of the turbulent diffusion coefficient for momentum shown in Fig. 6.11. The diminishing growth rate of the mixed-layer depth is also evident in <h> shown in Fig. 6.1b.

It is noticed that after ~1400 the wind vectors in a layer within the mixed layer, particularly the u components, begin to depart again from those in neighboring layers and show an

LAYER-AVERAGED DIFFUSION COEFF Km :   HSAV = SI1 (M)
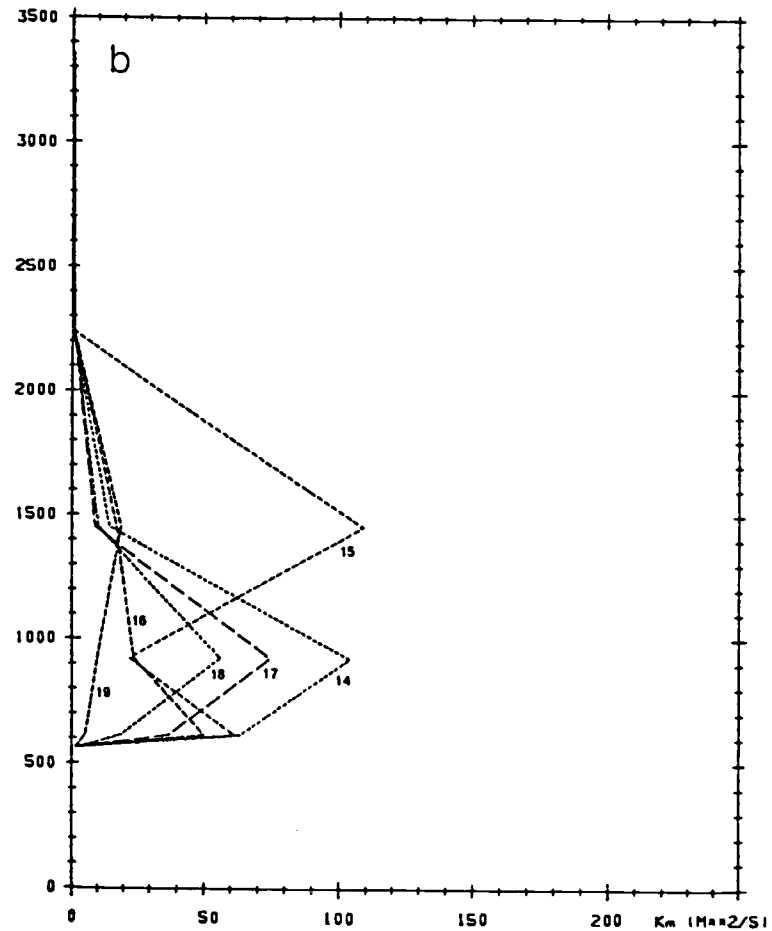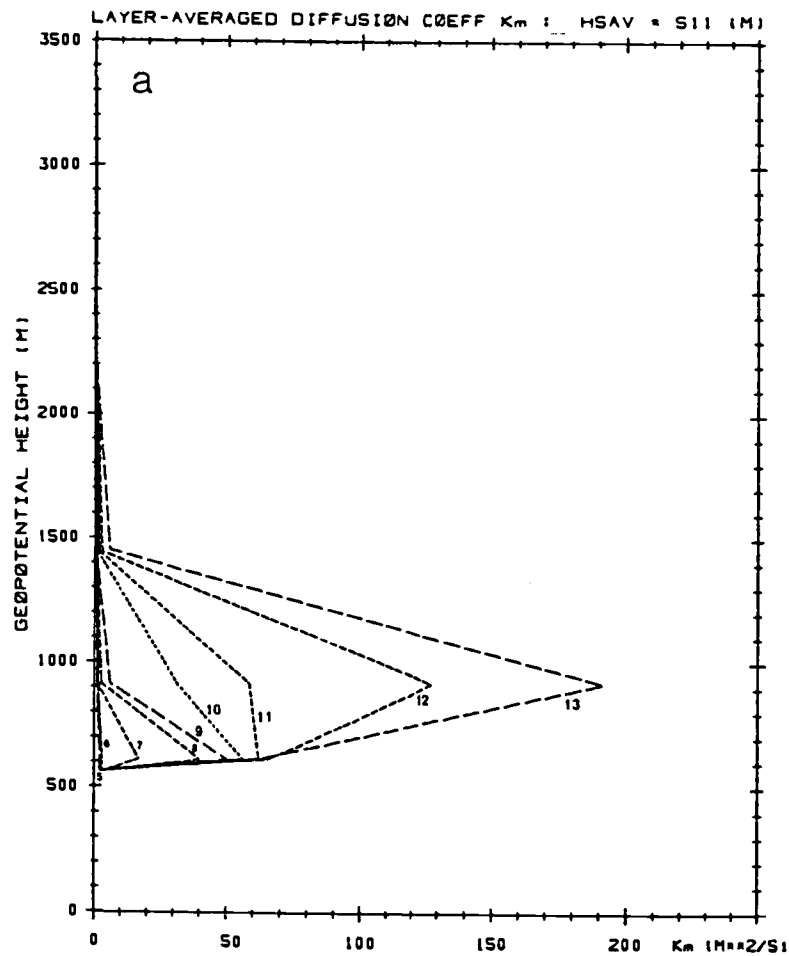
Fig. 6.11.   Time evolution of layer-averaged diffusion coefficient for
momentum K_M obtained at interface levels for L7 experiment.
Units are $m^2 s^{-1}$.   Numbers labeling individual curves refer
to LST.   (a): for 0500-1300 LST.   (b): for 1400-1900 LST.

Ekman-spiral-type turning with height, an observational example of which was illustrated, for example, by Brown (1970). On the other hand, the winds in layer 3, which is in the free atmosphere all the time and is not affected by the surface heat flux, are nearly geostrophic through the morning ($u_3 \simeq U_g$, $v_3 \simeq 0$) and shows smooth clockwise turning in the afternoon with small variations in magnitude.

We have thus found that although the hodograph of the mass-weighted vertical-mean mixed-layer wind for L7 resembles very much that for M4, only during the peak period of convective activities momentum at a given instant is vertically well-mixed and hence can be reasonably well expressed by a type of model in which a single layer represents the whole mixed layer, such as our M4 model. In particular, the evolution of the wind with height in the afternoon behaves much like an Ekman spiral, i.e., the v component increases monotonically with height and attains a maximum magnitude halfway up but then decreases to zero at the mixed-layer top, while the u component increases monotonically with height and reaches its maximum near the mixed-layer top. The corresponding profiles of vertical momentum fluxes illustrated in Figs. 6.12 and 6.13 show that the x component of the stress $-\overline{u'w'}$ is positive in the mixed layer and approaches zero near the mixed-layer top. On the other hand, the y component $-\overline{v'w'}$ starts out with a positive value in the surface layer, decreases in general to zero at some height below $\langle h + h_s \rangle$, reaches a maximum negative value and then increases with height to approach zero again near the mixed-layer top. The above behavior of the profiles of momentum fluxes agrees with a general
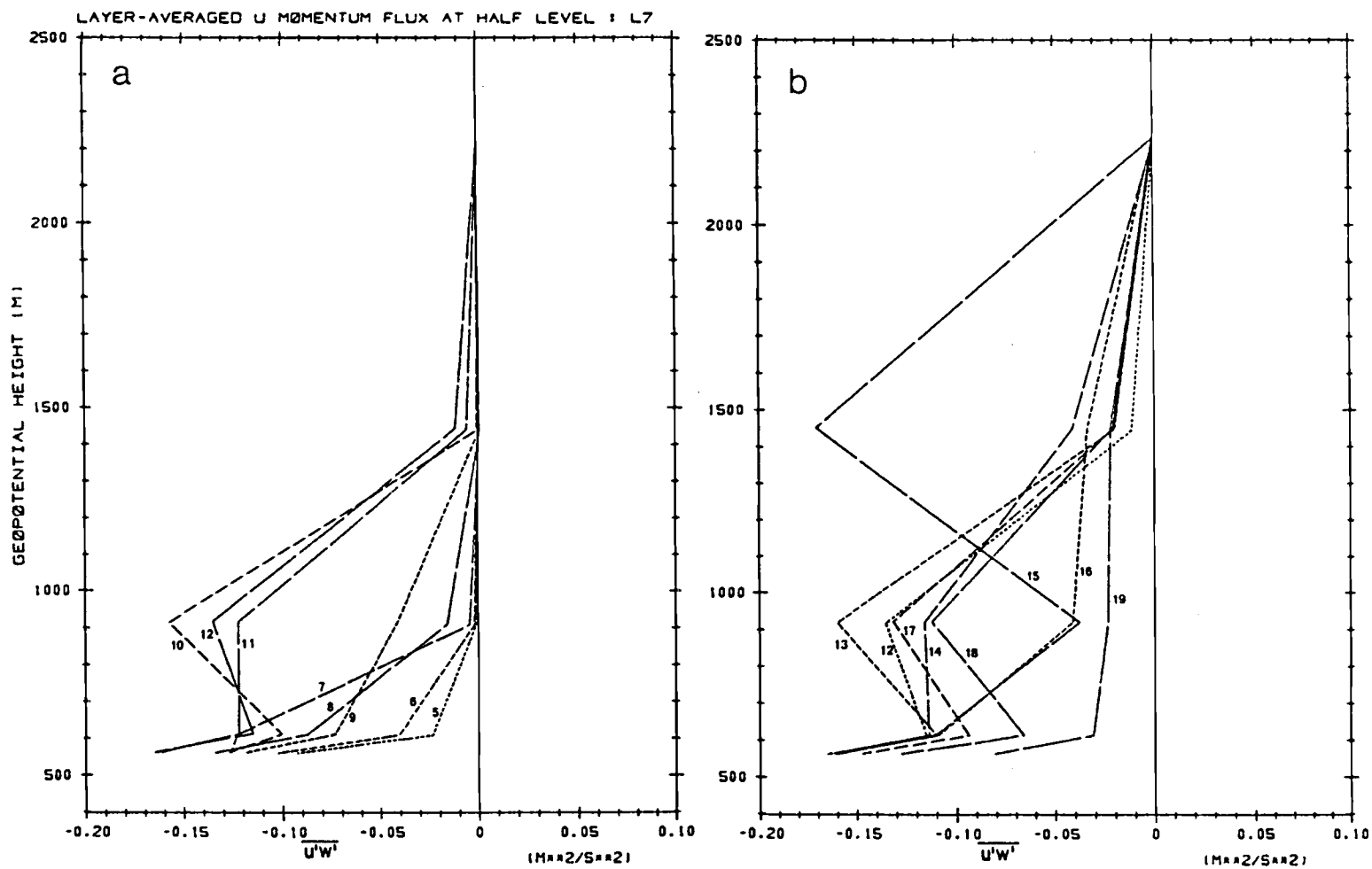
Fig. 6.12. Profiles of the layer-averaged u-momentum flux $\overline{u'w'}$ at layer-interface levels for L7. Units are m^2s^{-2}.
(a): for 0500-1200 LST. (b): for 1200-1900 LST.

LAYER-AVERAGED V MOMENTUM FLUX AT HALF LEVEL : L7

Fig. 6.13. As in Fig. 6.9 except for the v-momentum flux $\overline{v'w'}$.
(a): for 0500-1200 LST. (b): for 1200-1900 LST.

description of momentum given by Burk and Staley (1979) for the wind with an Ekman-type turning, and thus we see that the profiles of vertical momentum fluxes obtained for L7 are consistent with those of the winds.

In the M4 model the turbulent stress term in the momentum equation for the mixed layer has the same form as the right side of (6.19), and the wind structure of a whole column in the mixed layer is represented by a single wind vector. In the L7 model, on the other hand, we have used the turbulent diffusion coefficient K_M which is a function of the Richardson number, vertical wind shear and height. Therefore, stability and wind shear have effects on the vertical transport of momentum and the wind direction as illustrated by the hodographs in Fig. 6.10.

As another way of appreciating the differences between the M4 and L7 model results, the vertical distributions of the layer-averaged horizontal winds are plotted as functions of time along with $<h + h_s>$ in Figs. 6.14a and b. Arrows represent winds at a full-level height at which they originate. Westerly winds are indicated by arrows directed to the right parallel to the abscissa, while southerly winds are indicated by those directed upward parallel to the ordinate. These figures also show the major features of both model results discussed above as well as the basic difference in the vertical structure of the two models.

6.4 Mean Mixed-Layer Potential Temperatures

The domain-averaged potential temperatures of the lowest layer, $<\theta>$, and of the ground surface, $<\theta_s>$, have been shown in Fig. 6.3
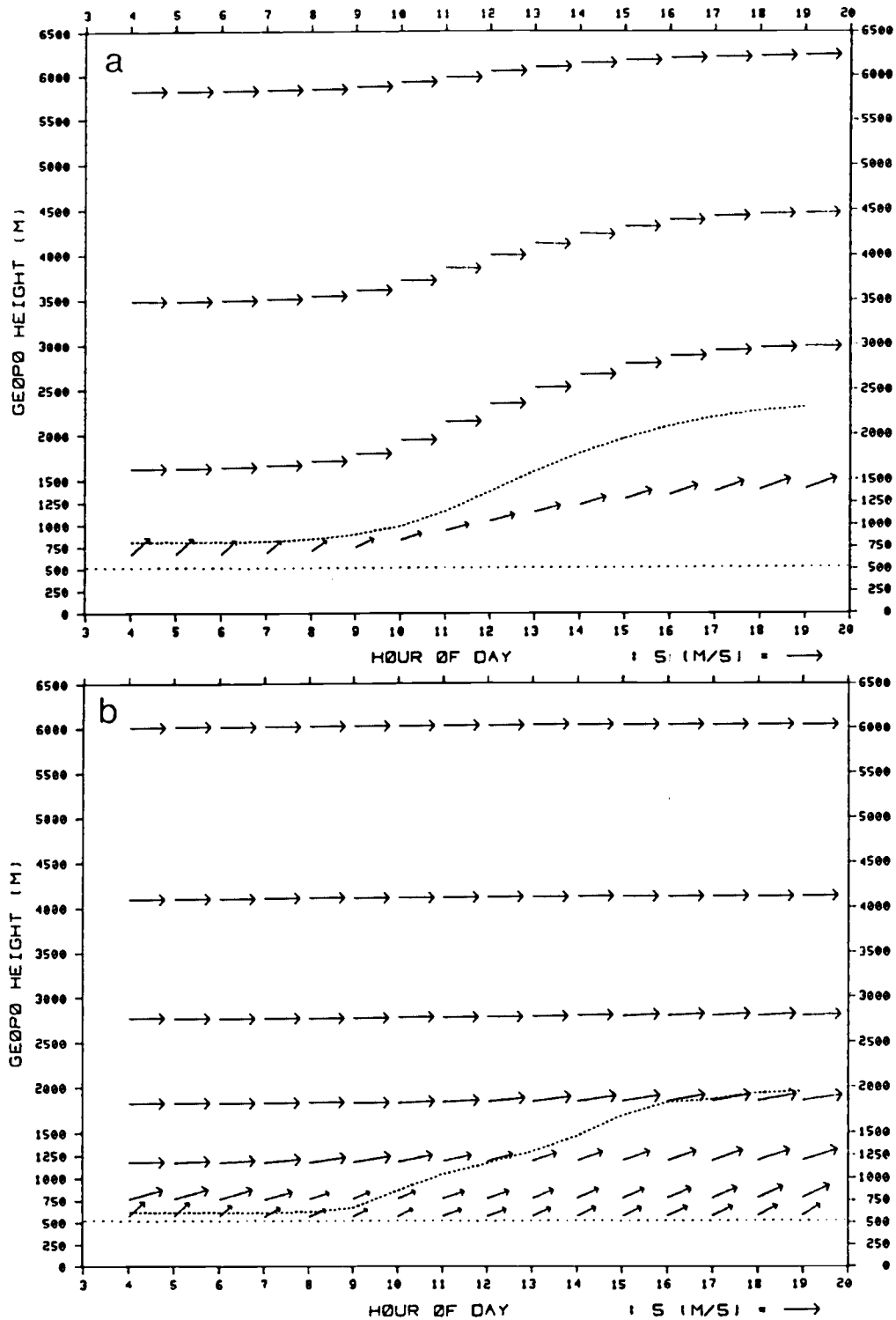
Fig. 6.14. Vertical distribution of layer-averaged horizontal winds as function of time of day for (a): M4 and (b): L7. Scale is shown in the lower right corner in units of ms^{-1}. $<h>+<h_S>$ is indicated by a fine dotted line, whereas $<h_S>$ is shown by a coarse dotted line in unit of m. See text.

for both M4 and L7 experiments. It is seen that both $<\theta_M>$ and $<\theta_S>$ for M4 are slightly higher than corresponding values for L7 for most of the day despite their starting out at nearly equal values in the early morning. We have found earlier that the domain-averaged sensible heat flux from the ground surface $<H(0,t)>$ is nearly equal for both experiments as illustrated in Fig. 6.2a, and also that the mixed-layer depth $<h>$ for M4 is about 200 m deeper than that for L7 in the early morning (Figs. 6.1a and b). It seems, therefore, that the temperature difference between the two model results is mostly governed by the initial thickness of the mixed layers to be warmed up with a given amount of surface sensible heat flux. As the solar insolation and $<H(0,t)>$ decrease in the afternoon, $\partial<\theta_M>/\partial t$ levels off but is still positive [see Eq. (6.4)], while $\partial<\theta_S>/\partial t$ becomes negative because the energy balance equation (3.53) requires smaller $<\theta_S> - <\theta_M>$ corresponding to the reduced solar insolation.

The evolution of the profile of the layer-averaged potential temperature for M4 is plotted in Fig. 6.15a, which has been produced by representing the mixed-layer temperature by a single value and combining with the diagnosed temperature jump $<\Delta\theta>$ at height $<h> + <h_S>$. We find that the results illustrated in Fig. 6.15a display exaggerated sharp inversion bases, but still correspond qualitatively to observed profiles from the O'Neill experiment (see, for example, Fig. 5 of Stull, 1973; Fig. 1 of Stull, 1976), or those from the Wangara experiment (see Fig. 1b of Deardorff, 1974).

On the other hand, the layer-averaged potential temperature profiles for L7 are depicted in Fig. 6.15b and have been obtained by
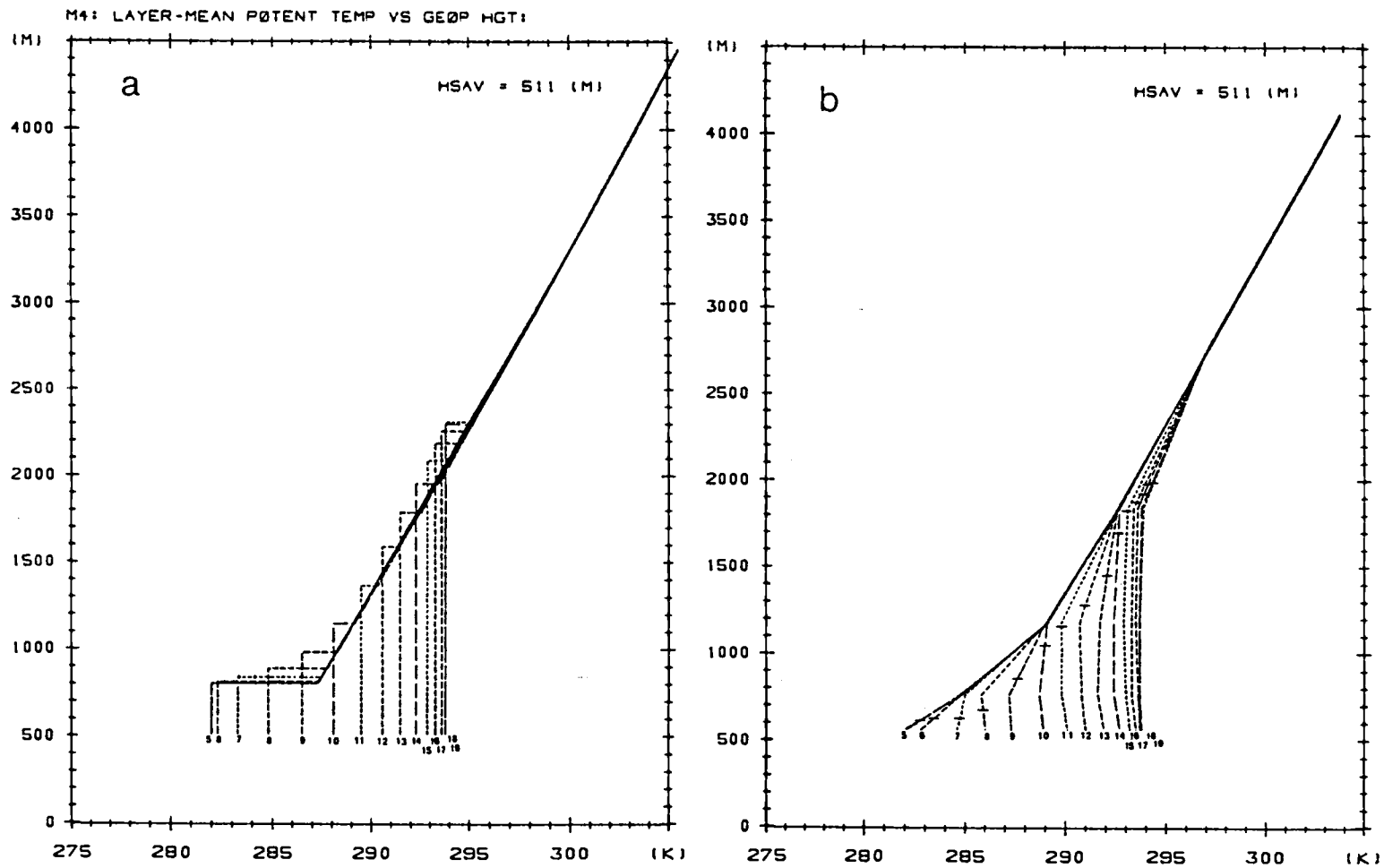
Fig. 6.15. (a): Evolutions of layer-averaged θ profile and Δθ for M4. (b): As in (a) except for L7 and <θ> only. Units are degree K, and time is LST. The lowest level at which <θ> is shown is <h_s>, but <$θ_s$> is not included. Horizontal bars in (b) indicate domain-averaged mixed-layer top (m) at each hour. See text.

linearly interpolating the values of $\langle\theta_\ell\rangle$ at full levels for
$\ell = 2, 3, \ldots, 7$, without taking into account $\langle h\rangle$ or $\langle\Delta\theta\rangle$ shown in
Fig. 6.1b. Therefore, the inversion base has been smeared and it is
difficult to locate it and measure the inversion strength. It is
noted that below the top of the mixed layer $\langle h\rangle + \langle h_s\rangle$, which is
marked by a horizontal bar, the individual profile is represented by
values at two to four levels after 0900 and crudely resembles a
typical observed structure shown, for example, by Melgarejo and
Deardorff (1974): the structure near the ground is superadiabatic
while near the top of the mixed layer it is slightly stable. We
also see that the evolution of the profiles for L7 is somewhat
similar to those of observed data, for instance, illustrated by
Chorley et al. (1975), or Lenschow et al. (1979), although no clear
inversion base is visible in the profile for L7.

As another way to appreciate the structure of the vertically
well-mixed potential temperature for L7, the evolution of individual
$\langle\theta_\ell\rangle$ for $\ell = 3, 4, \ldots, 7$ is depicted in Fig. 6.16. Thus,
comparing the profiles for M4 with those for L7 we may say that the
single-layer representation of the boundary layer in the M4 model
performs as well as the multi-level representation in the L7 model
as far as the layer-averaged potential temperature is concerned,
i.e., $\langle\theta\rangle$ is relatively well-mixed vertically compared to $\langle u\rangle$ or
$\langle v\rangle$, so that a single value of $\langle\theta\rangle$ can represent well that of a
whole column in the mixed layer.

The profiles of potential temperatures averaged at height z are
also illustrated in Figs. 6.17a and b for M4 and L7, respectively.
The potential temperatures at a given grid point were first linearly
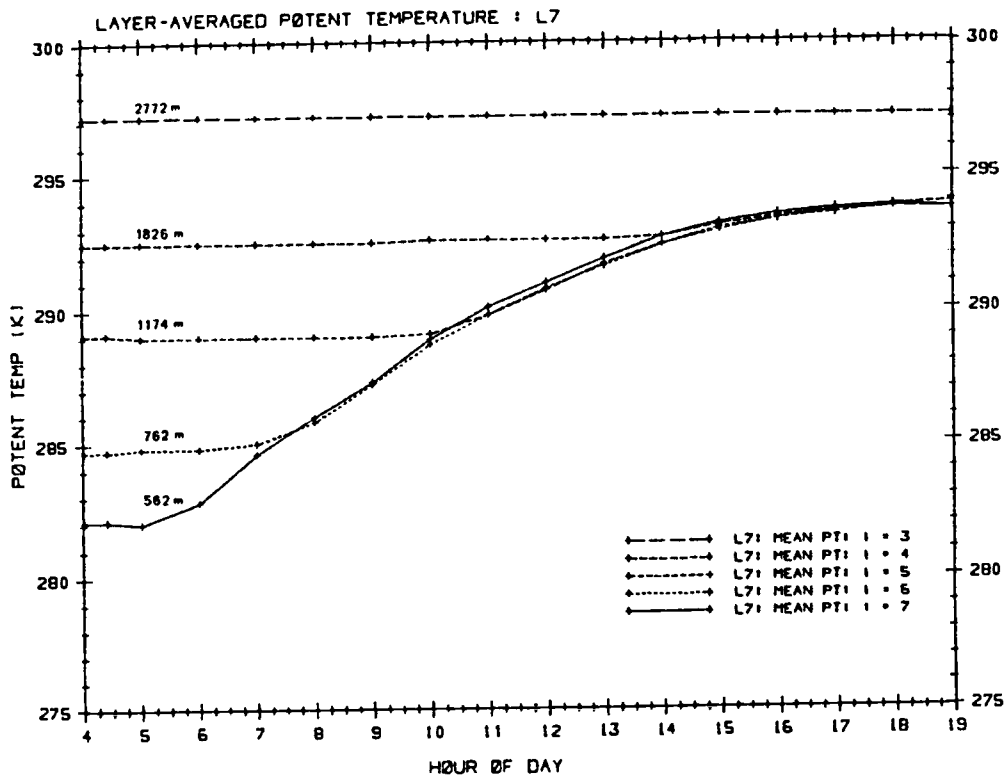
Fig. 6.16. Evolutions of layer-averaged θ for the lowest 5 layers for L7. Units are degree K, and time is LST. Approximate average layer heights of full levels are shown near individual curves.
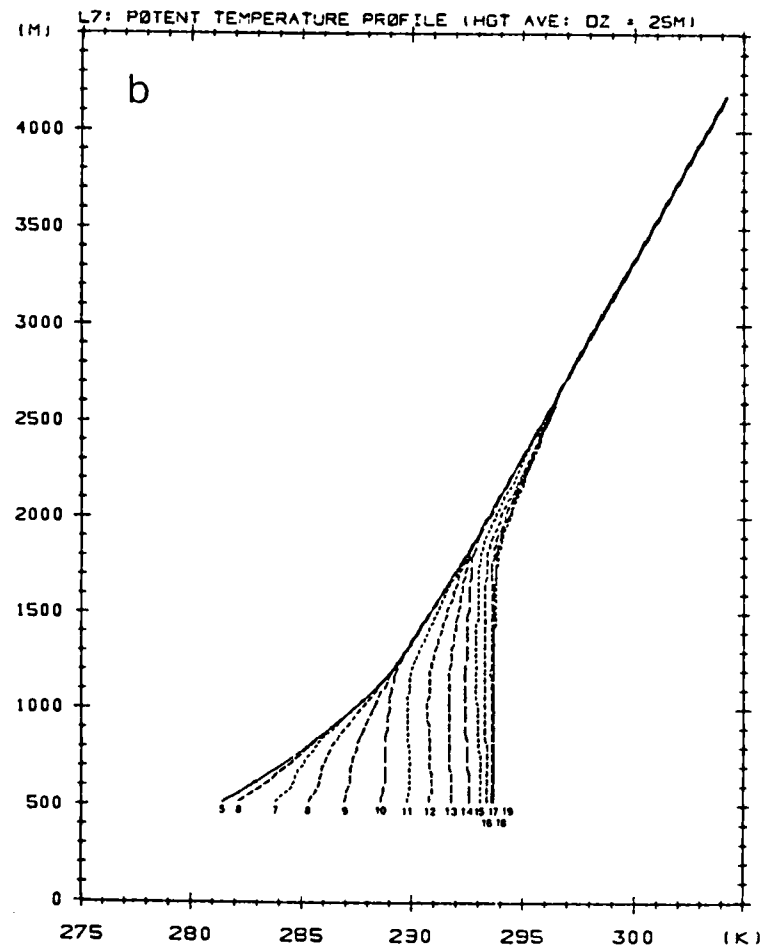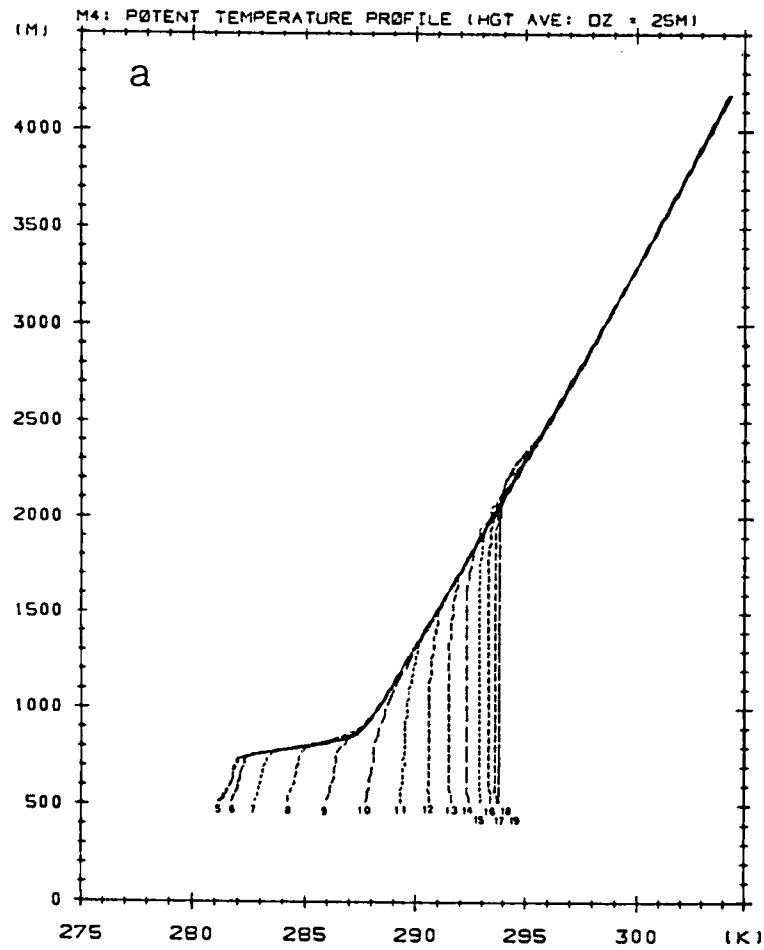
Fig. 6.17. Evolution of the profile of potential temperature $\langle\theta_z\rangle$ averaged at height z for (a): M4 and (b): L7. The lowest level at which $\langle\theta_z\rangle$ is shown is $\langle h_s\rangle$. See text.

interpolated to find the values at height z. This process was applied to all grid points and a domain average was taken to obtain the mean potential temperature $\langle\theta_z\rangle$ at height z. The process was repeated at descrete height $z + \Delta z$ starting with $z_{min} = \langle h_s\rangle$ and $\Delta z = 25$ m. These figures illustrate that at a height level below the highest hill (783 m above sea level), $\langle\theta_z\rangle$ tends to be smaller during the morning hours as z gets lower and closer to $\langle h_s\rangle$, due to the fact that within the lowest layer the initial potential temperature is a linear function of height [see Eq. (9.2)]. However, as the horizontal amomalies of θ diminish in the afternoon, as illustrated in Figs. 6.1a and b, $\langle\theta_z\rangle$ is seen to become vertically more uniform. The profiles shown in Fig. 6.17b rather resemble observed profiles obtained by Whiteman (1982) who analyzed the data collected in long but narrow mountain valleys in western Colorado. It is also noted that while the evolutions of two profiles for L7 in Figs. 6.15b and 6.17b are quite similar, the inversion strength $\langle\Delta\theta\rangle$ for M4, which is distinctively displayed in Fig. 6.15a, has been smeared in Fig. 6.17a, thus making the profiles from M4 and L7 more resemble each other. However, in the vicinity of the probable inversion base, the evolution of the afternoon profiles for M4 in Fig. 6.17a looks much more realistic than that for L7 in Figs. 6.15b and 6.17b. This is due to the fact that in the L7 profiles we ignored the discontinuity and linearly interpolated θ_ℓ predicted at levels whose intervals are rather coarse.

6.5 Horizontal Wind Velocities

The horizontal wind vector fields for the mixed layer of M4 are shown in Fig. 6.18 for the period between 0500 and 1900 at 2-hour intervals. The length of the arrow which originates at an "h" point is proportional to the speed of the wind whose x- and y-components at a given "h" point were obtained by averaging its adjacent u's and v's. The contour lines indicate the terrain elevation relative to the mean height of 511 m.

Shortly after sunrise the wind field at 0500 is somewhat similar to the steady flow pattern we obtained in the earlier experiments without the horizontal variations of the mixed-layer potential temperature θ_M or entrainment w_e (see Fig. 4 of Han et al., 1982). The winds are generally stronger over the hills and weaker over the lower terrain, and the flow is considerably deflected over the primary hill. Pockets of the weak winds occur upwind over the southwestern slope of the primary peak at the edge of the basin and over the eastern slope of the secondary hill. In particular, the former intensifies during the early-morning hours through 0900 and persists through midday while remaining approximately at the same location. After its initial decrease the overall wind speed begins to increase and wind vectors become more uniform after 0800, while the diversion of the flow diminishes markedly in the afternoon. The flow direction becomes most westerly around 1100 after which it begins to turn somewhat northwards again, the behavior that we have noticed in the domain-averaged u and v given in Fig. 6.6a. Shown in Fig. 6.19, on the other hand, are the horizontal wind vector fields for the lowest layer ℓ = 7 of L7. It
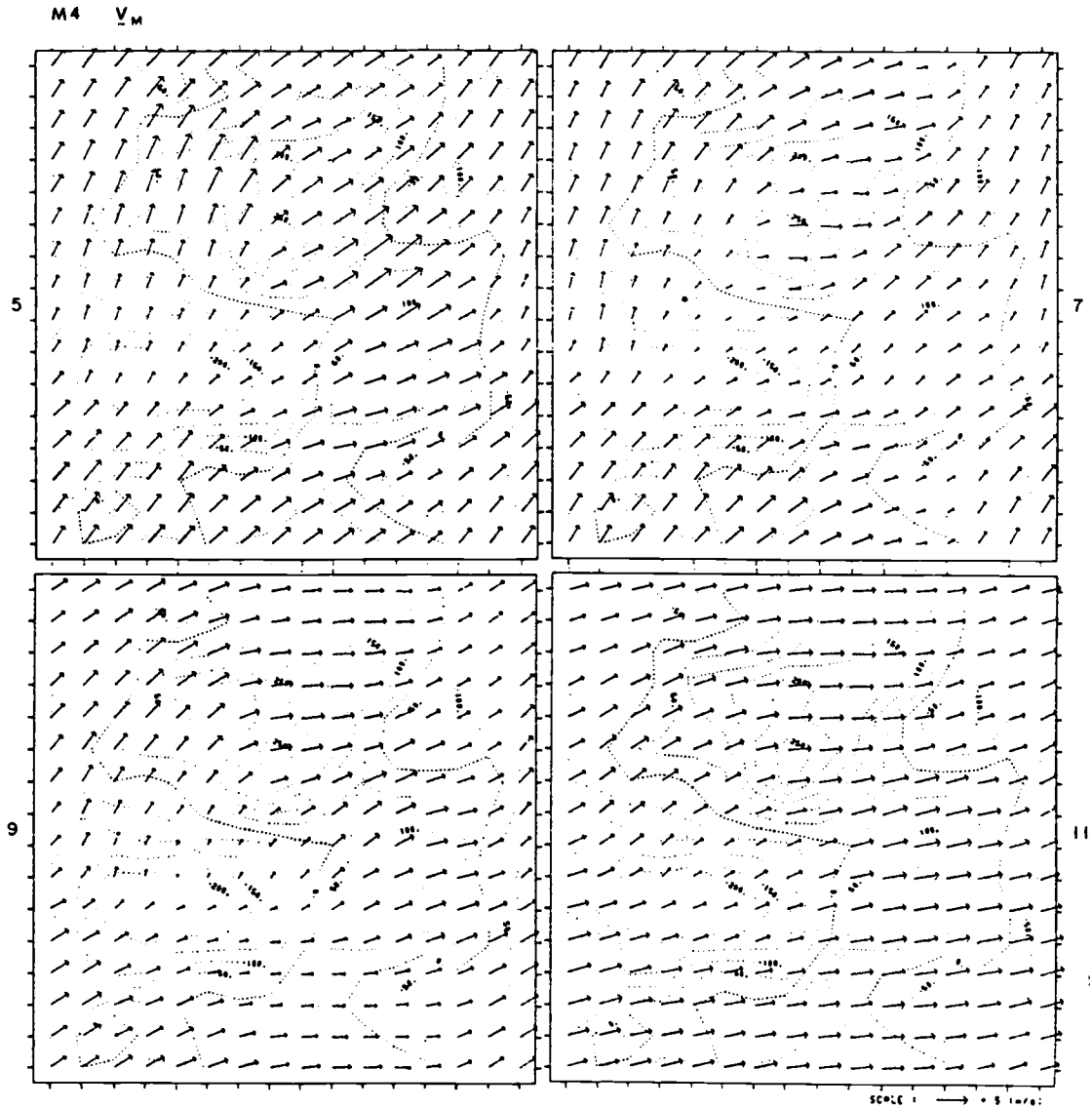
Fig. 6.18a. Horizontal wind fields of the mixed layer for M4 at 05, 07, 09 and 1100 LST. The wind vectors originate at "h" points and the length of the arrow is proportional to the wind speed. The scale is shown in the bottom right corner of the figure. The contour lines indicate the terrain elevation relative to the mean height of 511 m above sea level.

M4 $\underline{V}_M$
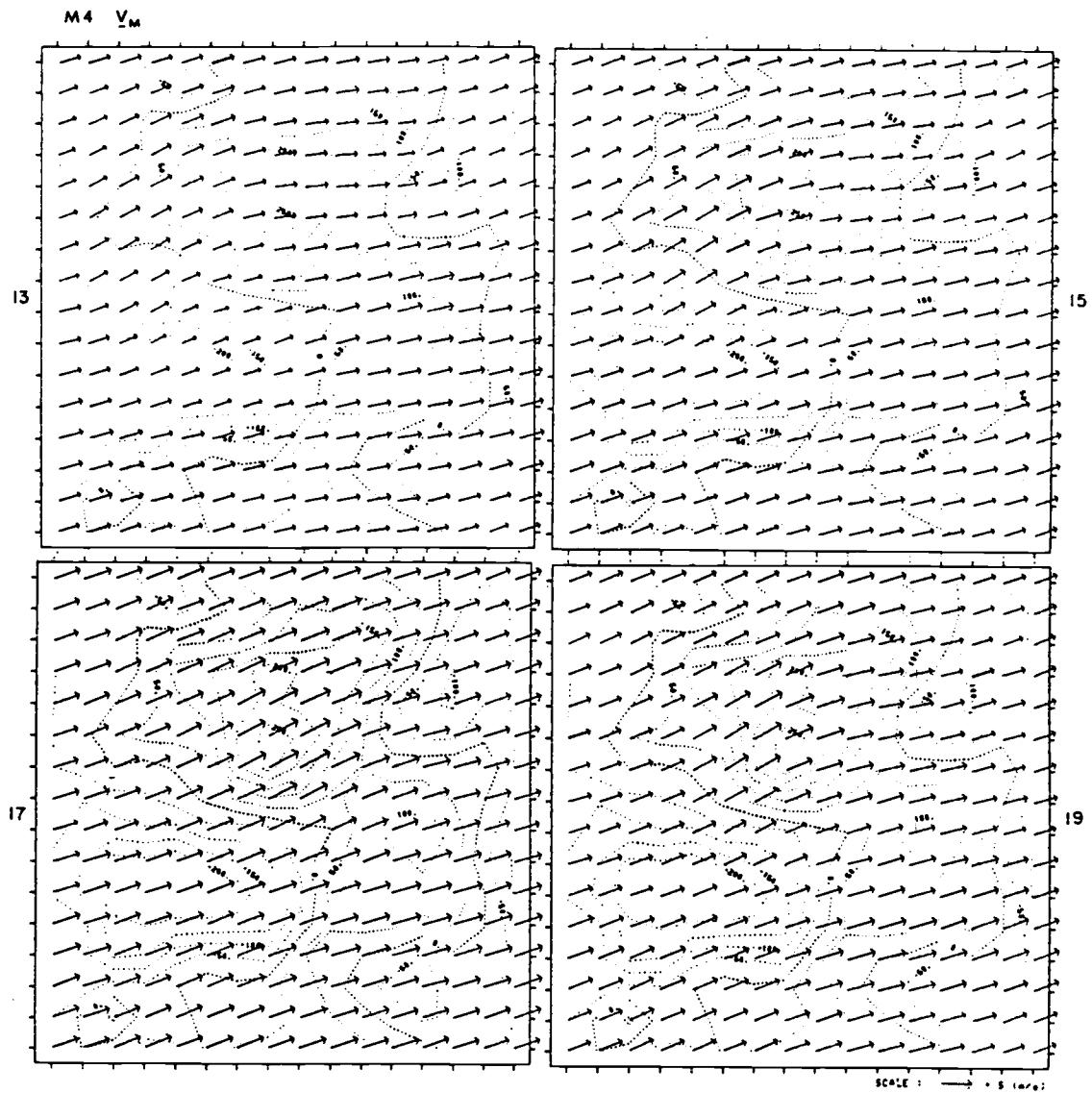
Fig. 6.18b. As in Fig. 6.18a except for 13, 15, 17 and 1900 LST.
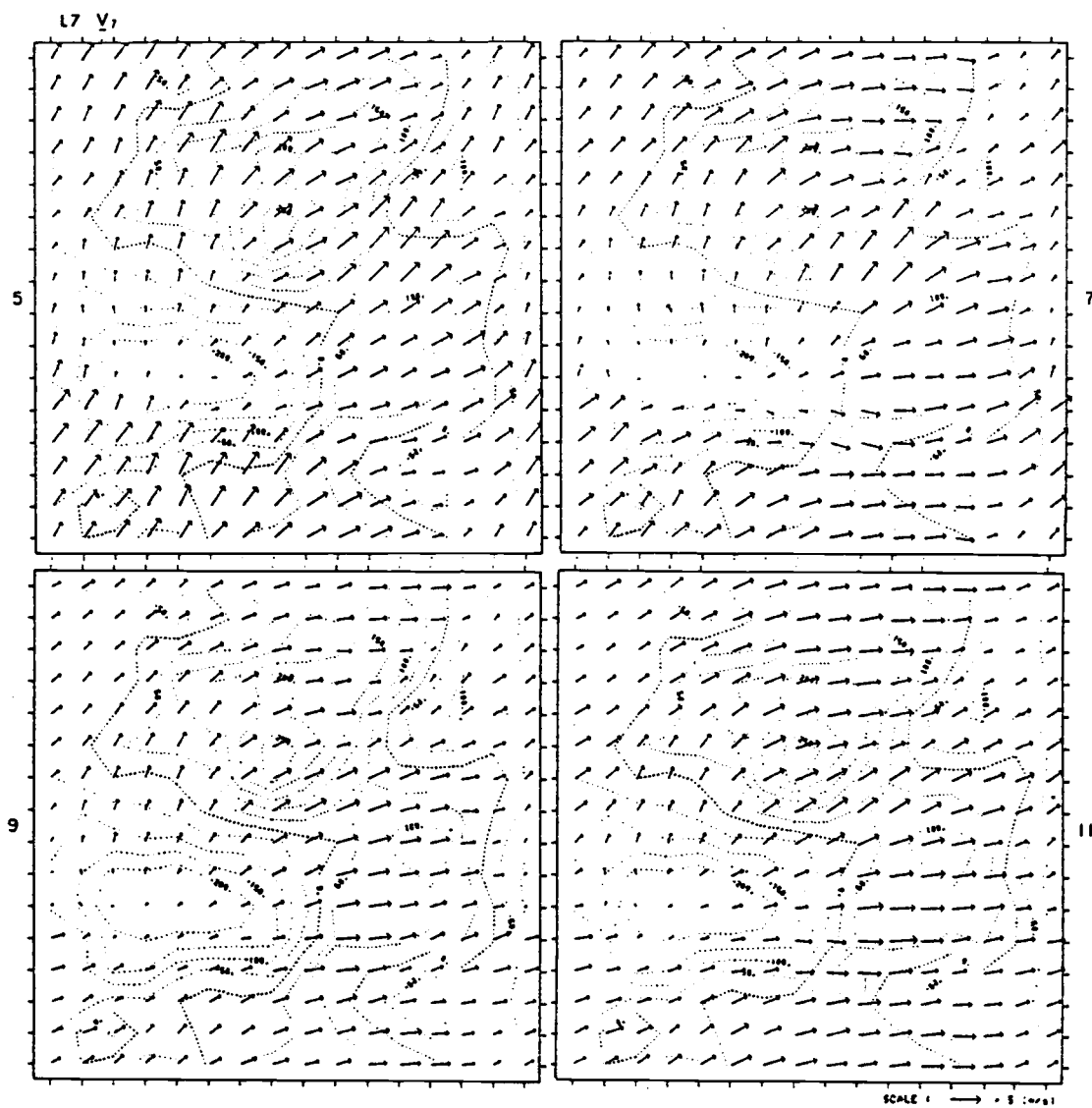
Fig. 6.19a. Horizontal wind fields for layer 7 of L7 at 05, 07, 09 and 1100 LST. Otherwise, as in Fig. 6.18a.

L7 V₇
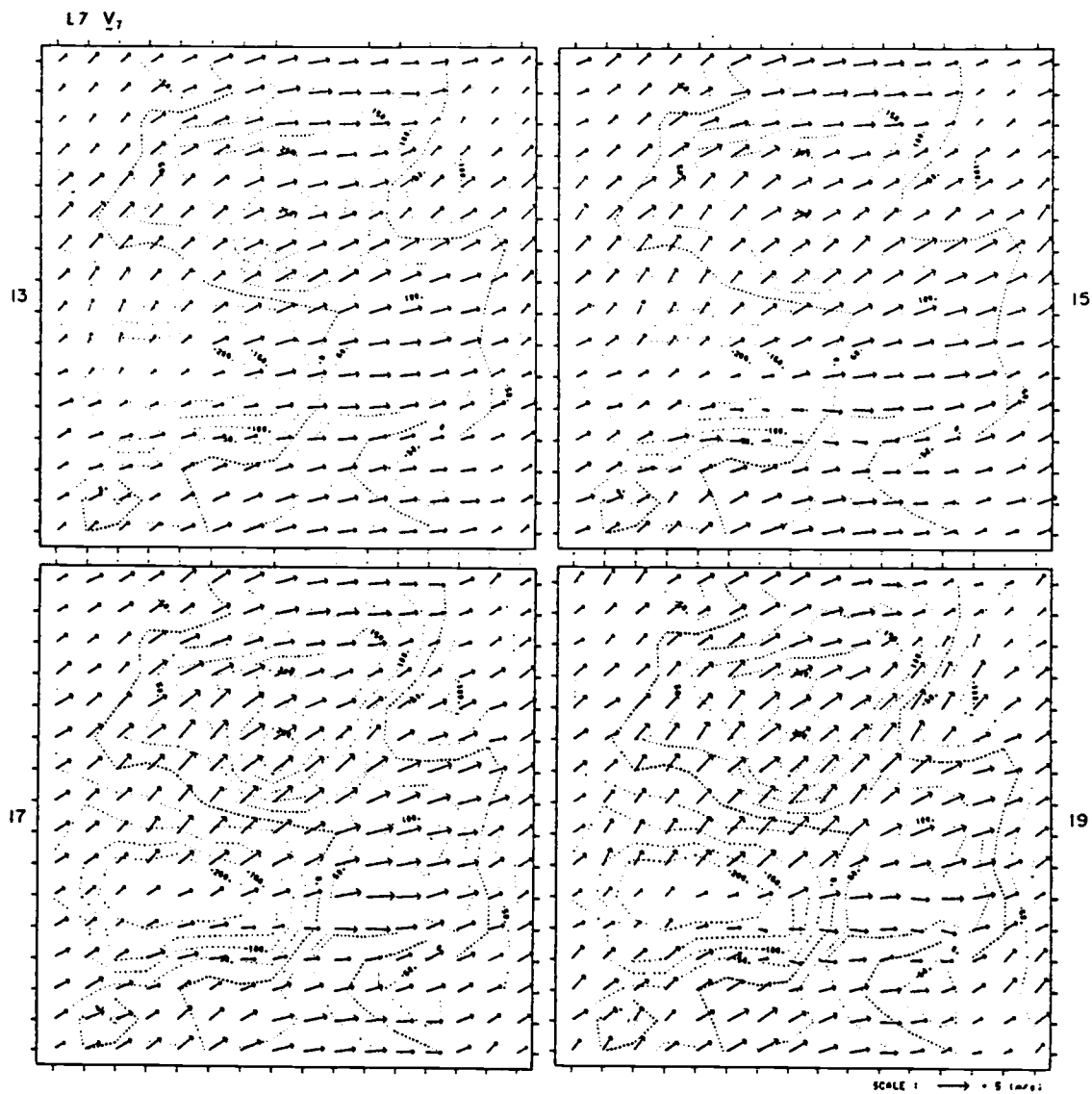
Fig. 6.19b.   Horizontal wind fields for layer 7 of L7 at 13, 15, 17
and 1900 LST.   Otherwise, as in Fig. 6.18a.

is noted that the layer is about 100 m thick and is centered about 50 m above the ground surface throughout the day, while the thickness of the mixed layer in the M4 model varies with time. The level at which the mixed-layer variables in M4 are predicted therefore generally climbs higher as the integrations progress (see Fig. 6.14a). The wind-vector field of the lowest layer of L7 at 0500 is similar to that of the M4 results except that the primary weak-wind pocket is now situated at the middle of the primary basin with its smaller wind speed (1.9 ms^{-1} for M4 and 0.7 ms^{-1} for L7). The weak winds are now also visible in the minor basins in the north- and south-east corners of the domain. The primary weak-wind pocket, which seems to intensify through midmorning, remains within the basin until about 1400 when it begins to drift southeastwards. Contrary to the M4 results, the weak-wind pockets are visible throughout the day with the minimum speed still being 1.3 ms^{-1} (vs. 3.2 ms^{-1} of M4) even at 1500, while at the same time the deflection of the winds around the hills also remains evident. Thus, the flow pattern established in the early morning is approximately maintained throughout the day, indicating that the overall flow pattern in the lowest layer of L7 is mostly dictated by the terrain irregularities and their correlation with early-morning temperatures.

The wind vector fields for the layer $\ell = 6$ of L7 are presented in Fig. 6.20. In this layer, which is about 300 m thick, the wind field at 0500 predicted at height around 250 m above the ground is much less deflected around the hills than that for the layer $\ell = 7$ due to the fact that the layer is still in the free atmosphere. The
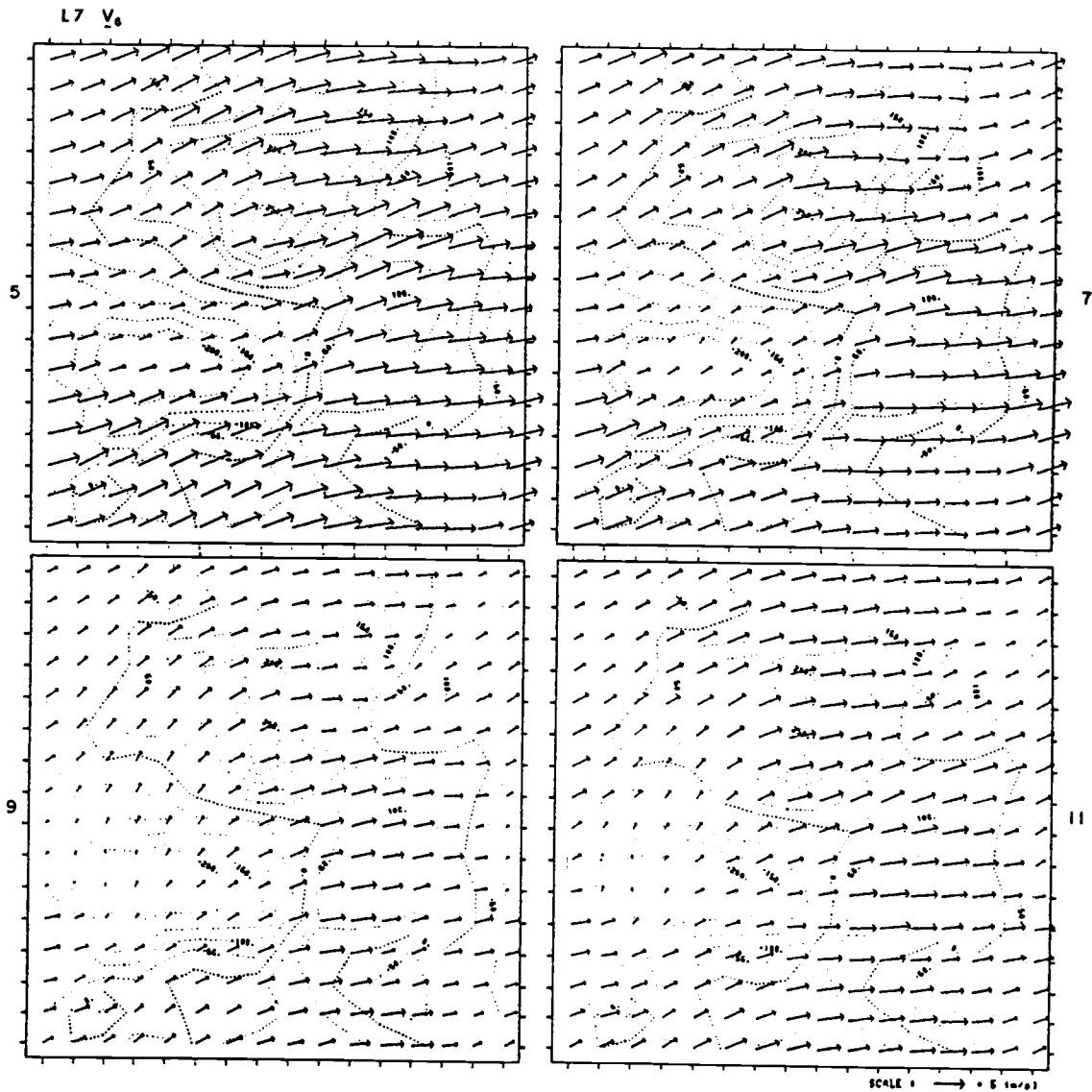
Fig. 6.20a. As in Fig. 6.19a except for layer 6 of L7.

L7 $\underline{V}_6$
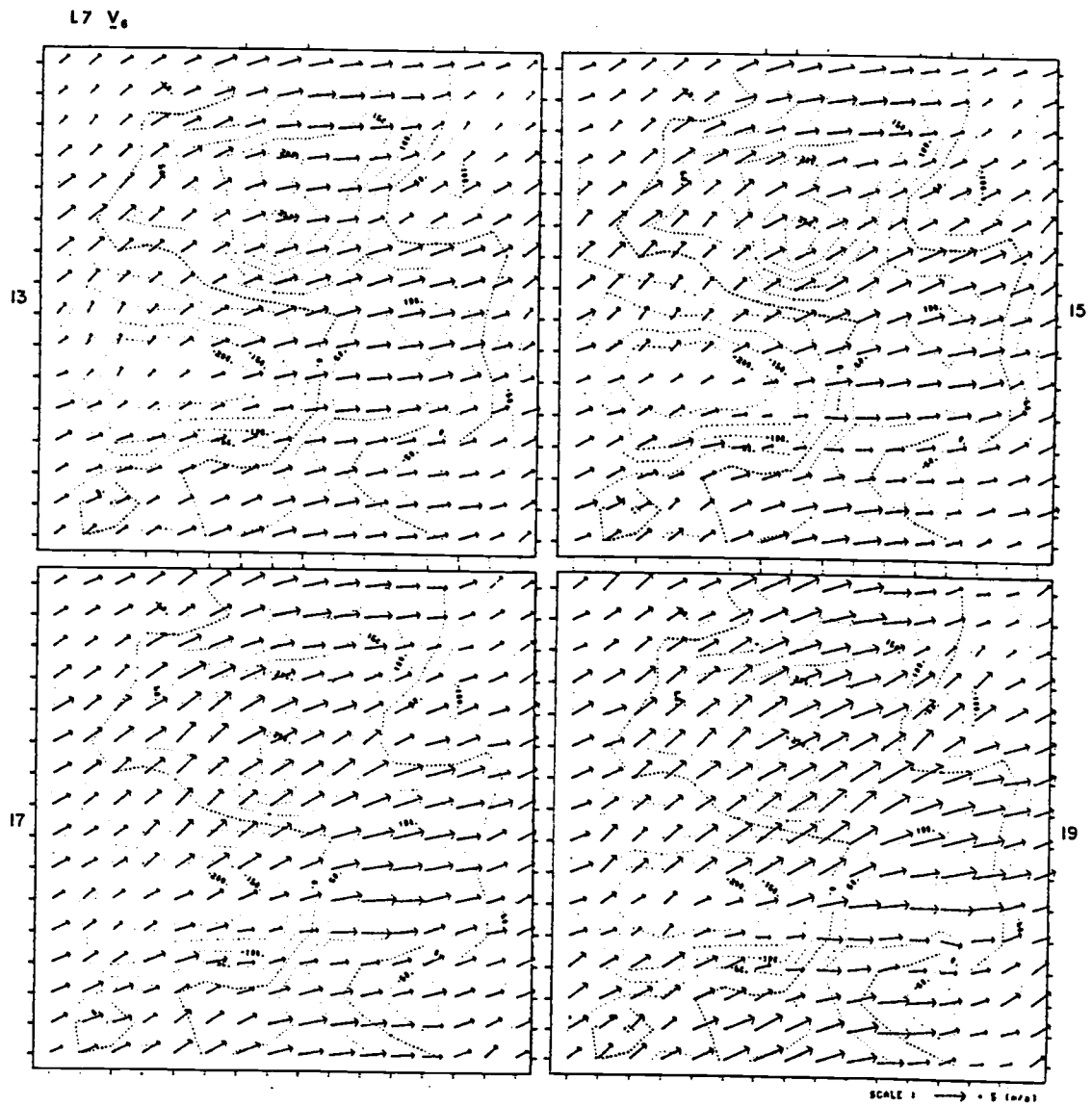
Fig. 6.20b. As in Fig. 6.19b except for layer 6 of L7.

wind is more westerly with its speed mostly over 5 ms^{-1} over the mountains. A pocket of weak winds again appears over the northern edge of the primary basin. We notice that by 0700 the overall wind speed has more or less uniformly weakened while the flow pattern itself remains approximately the same. By 0900 the wind field has closely resembled that for the layer ℓ = 7 in direction and magnitude of individual wind vectors, with intensified weak-wind pockets on the leeward slopes of the hills. The above behavior of the wind vector field for the layer ℓ = 6 is consistent with the earlier statement on the domain-averaged hodographs that by 0630 the mixed layer has grown into the layer ℓ = 6 and by 0930 the latter has been mostly within the mixed layer. From 1100 on the overall flow pattern is virtually indistinguishable from that for the layer ℓ = 7, although we noted the differences in the layer-averaged hodographs shown in Fig. 6.10.

The wind vector fields for the layer ℓ = 5 are next shown in Fig. 6.21. The full level ℓ = 5 lies at approximately 950 m above sea level over the primary basin and 1400 m over the highest hill, with the layer being about 530 m thick. Thus this layer is located above the height level of the primary hilltop where the influence of the terrain irregularities are expected to be much less compared to those on the lower layers. The wind vector field, which consists of the supergeostrophic westerlies through the morning, displays marked weakening in speed over the basins at 1100, indicating that the mixed-layer top has penetrated into this layer by this time. By 1300 this layer is on average within the mixed layer, and the overall flow field closely resembles those for the lower layers for

L7 $\underline{V}_5$

SCALE : ⟶ = 5 (m/s)
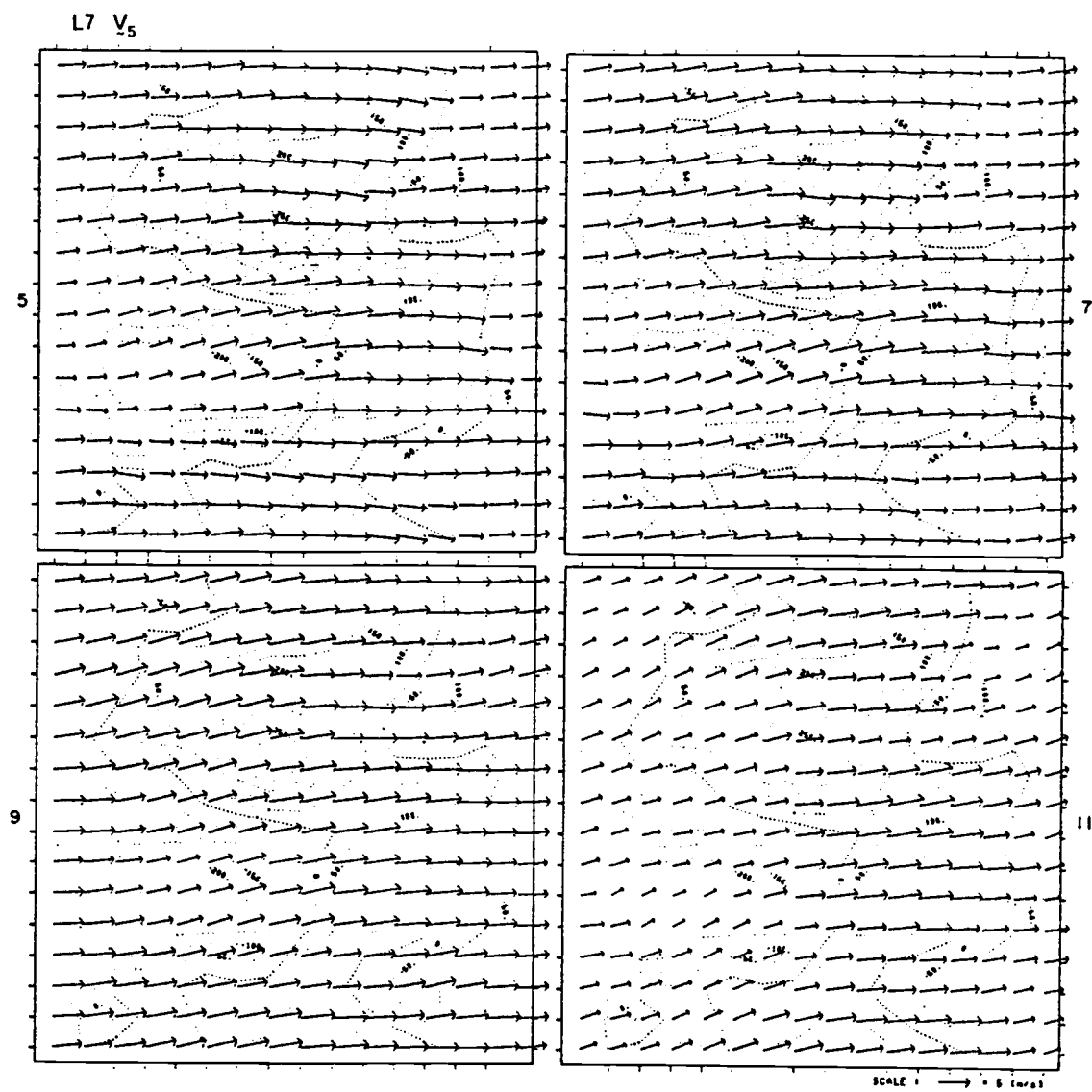
Fig. 6.21a. As in Fig. 6.19a except for layer 5 of L7.

L7 V₅
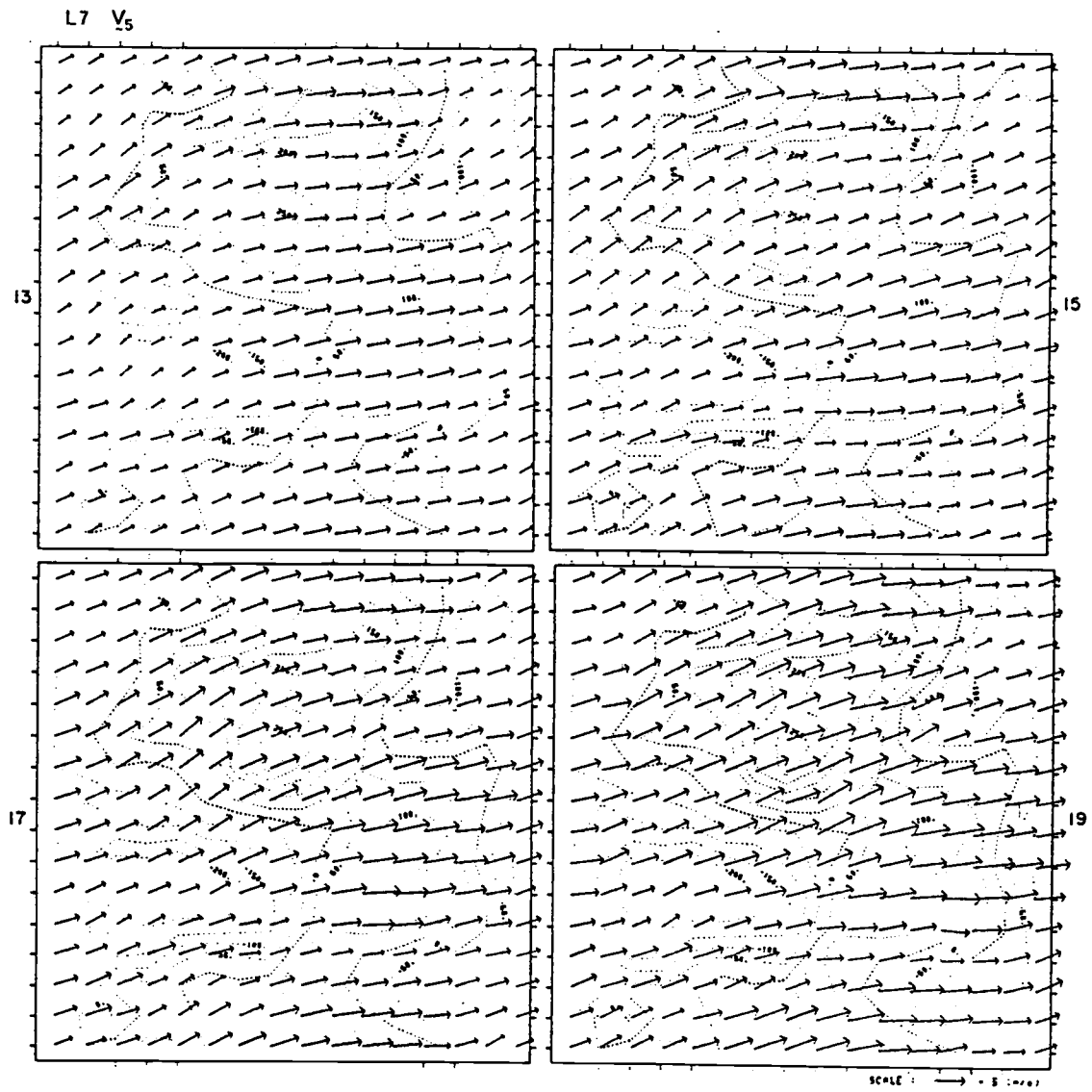
Fig. 6.21b. As in Fig. 6.19b except for layer 5 of L7.

the rest of the day, with the regions of weak winds being visible
even at 1700 and 1900, as in the case of the lower layers. In the
layer ℓ = 4 (not shown), which mostly remains above the influence of
surface heating, winds are uniformly westerly for most of the time.
Only after 1500 do noticeable perturbations appear in the wind
directions over the lower lands.

The wind vector fields for L7, which represent mass-weighted
vertical averages within the mixed layer, are illustrated in
Fig. 6.22. As may be expected from the domain-averaged hodograph
shown in Fig. 6.6a, they are very much similar to those of the M4
model shown in Fig. 6.18. In the vertically-averaged fields,
however, weak-wind pockets in the north- and south-east corners of
the domain are more visible and the deflection of the flow around
the hills is also more evident during the early-morning hours due to
the shallower mixed layer assumed before sunrise. By midday,
however, the overall flow pattern has become more uniform and
virtually indistinguishable from that of M4, although in the L7
results the weak-wind spot over the southern edge of the primary
basin persists through the day and the flows are spatially less
uniform even in the late afternoon.

6.6 Weak-Wind Pockets

We have noticed in the wind vector fields of both models that
pockets of weak winds persisted in the basins and valleys through
the mid-afternoon. The descriptions for the weak-wind pockets given
in a previous study of terrain-induced mesoscale motions in a
heated, growing mixed layer (DUH, 1984) are generally valid and

L7 $\underline{V}_{VA}$
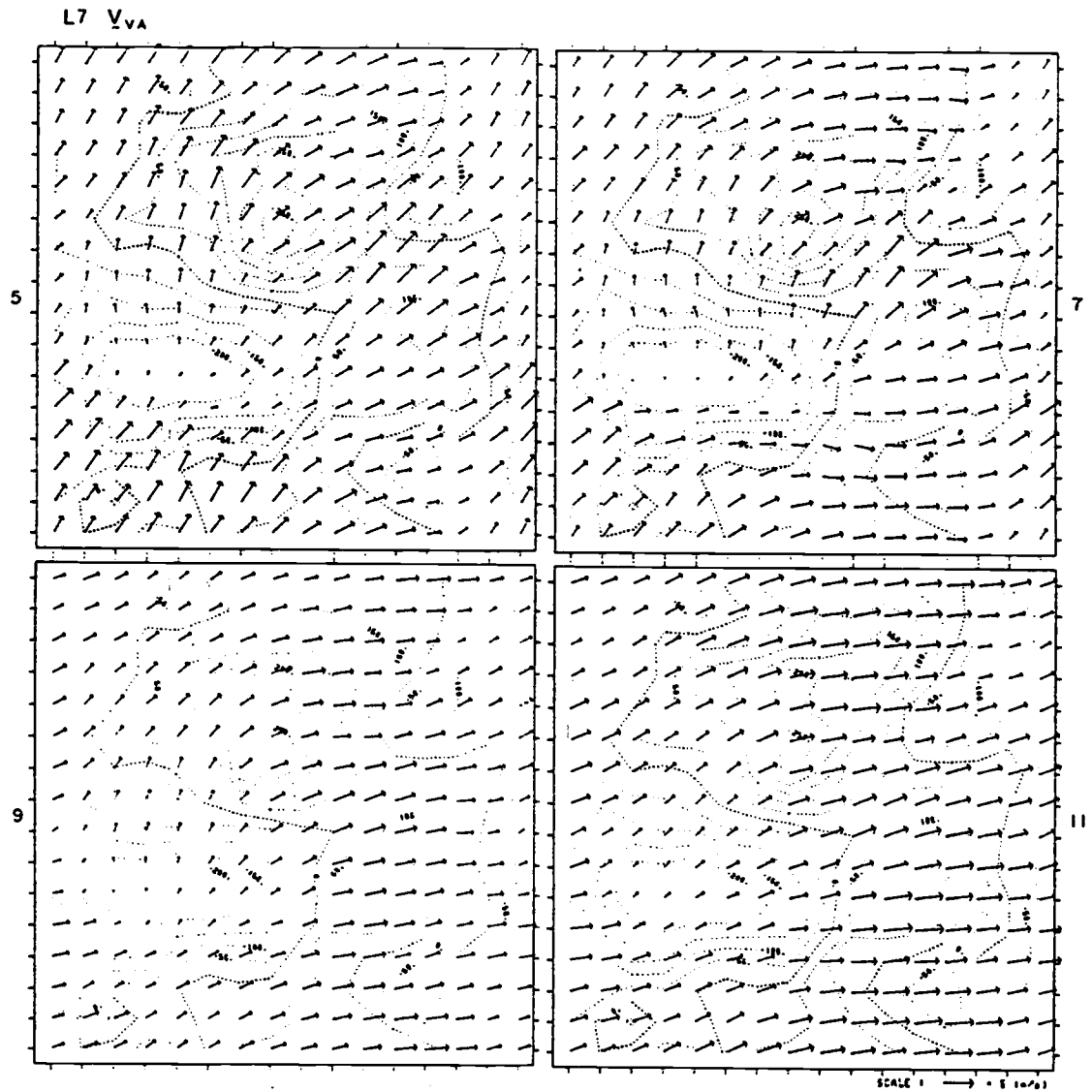
Fig. 6.22a. Mass-weighted vertical-average fields of horizontal mixed-layer winds for L7 at 05, 07, 09 and 1100 LST.

L7 $\underline{V}_{VA}$
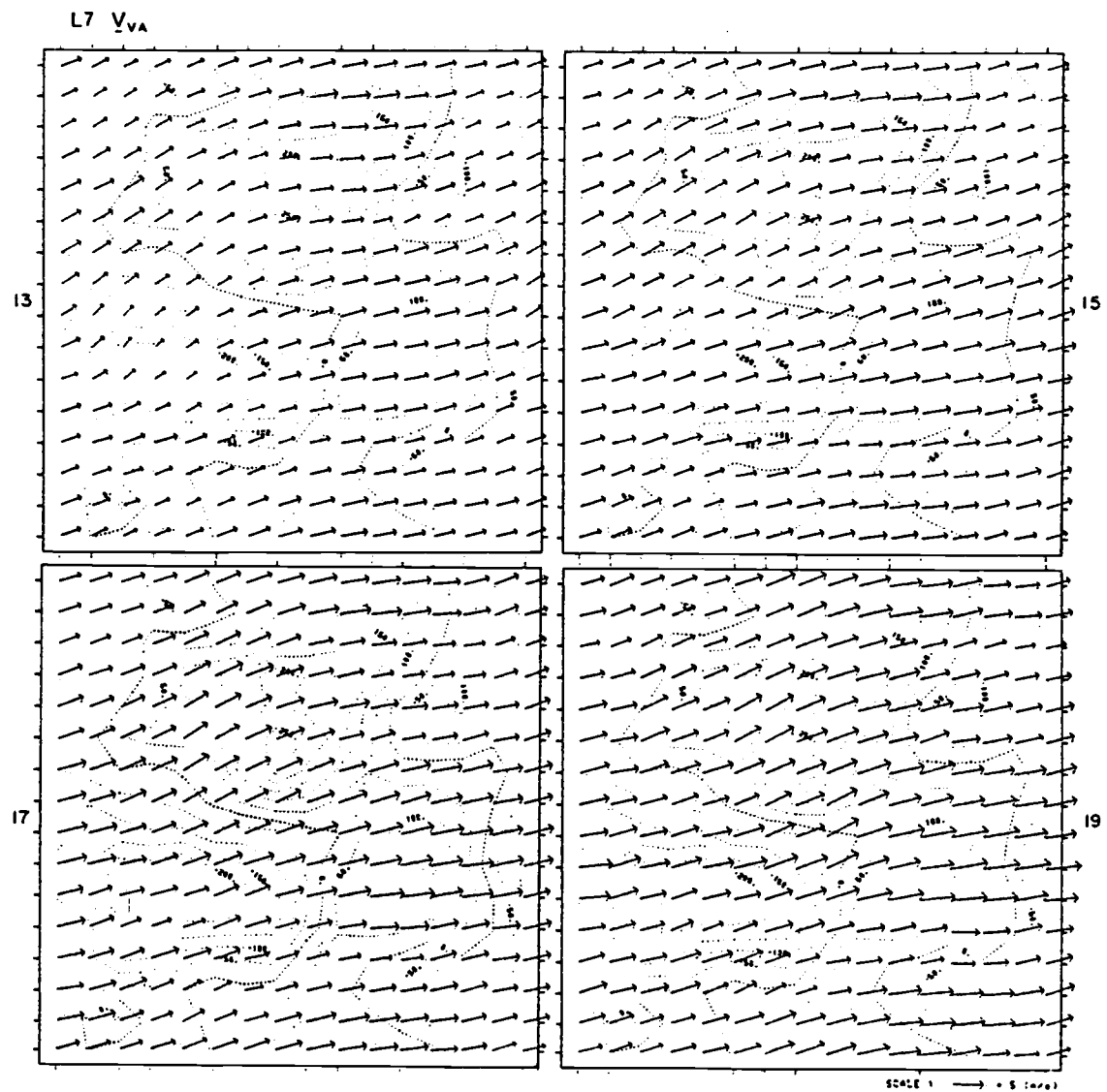
Fig. 6.22b. As in Fig. 6.22a except for 13, 15, 17 and 1900 LST.

apply to our current results. We attempt here to explain in more detail the wind vector fields described in the previous section, particularly the persistent weak wind regions, by utilizing the momentum equation for the 2-layer mesoscale model of the well-mixed PBL developed by Keyser and Anthes (1977), an extension of which has lead to the present M4 model.

By assuming vertically homogeneous profiles of potential temperature and horizontal wind velocity within the PBL under conditions of strong surface heating, Keyser and Anthes (1977) derived the following expression, in ordinary coordinates, for the horizontal velocity $\underset{\sim}{V}$:

$$\frac{D\underset{\sim}{V}}{Dt} = - f\underset{\sim}{k} \times [\underset{\sim}{V} - \underset{\sim}{V}_g(h_T)] - \overline{\frac{1}{\rho}\nabla p}^z + \overline{\frac{1}{\rho}\frac{\partial \underset{\sim}{\tau}}{\partial z}}^z \qquad (6.24)$$

where $\overline{(\ )}^z = (1/h) \int_{h_s}^{h+h_s} (\ )dz$ is the vertical-averaging operator, applied to eliminate the height dependence of the variables, and

$$-\overline{\frac{1}{\rho}\nabla p}^z = \frac{g(h_T - h - h_s)}{2\theta_M} [\nabla\theta(h_T) + \nabla\theta^+ - \gamma\nabla(h + h_s)]$$
$$(I)$$

$$-g [\frac{\theta^+ - \theta_M}{\theta^+}] \nabla(h + h_s) + \frac{gh}{2\theta_M}\nabla\theta_M; \qquad (6.25)$$
$$(II) \qquad\qquad (III)$$

$$\overline{\frac{1}{\rho}\frac{\partial \underset{\sim}{\tau}}{\partial z}}^z = \frac{\underset{\sim}{\tau}^-/\rho - \underset{\sim}{\tau}_s/\rho}{h} \qquad (6.26)$$

with h_T being the height at which the mesoscale perturbations in potential temperature produced by surface heating or topography are assumed to vanish, θ^+ the potential temperature at the height just

above the inversion base, γ the lapse rate of θ in the free atmosphere, and $\underset{\sim}{\tau}^-/\rho$ and $\underset{\sim}{\tau}_s/\rho$ are the turbulent stresses given by Eqs. (4.33) and (4.32), respectively. The determination of h_T is arbitrary, since there is no firm physical basis for predicting it, and as Anthes et al. (1980) pointed out, when $h_T - h - h_s$ becomes larger as the surface heating intensifies, small errors in the temperature structure can lead to significant erroneous acceleration in the mixed-layer wind. We apply here to our results for M4 the following expression for h_T used by Anthes et al. (1980):

$$h_T = \max \begin{cases} 2(h+h_s)_{max} - <h+h_s> \\ (h+h_s)_{max} + 1000 \text{ m.} \end{cases}$$

Under the assumption that h_T is proportional to the depth of the perturbation induced in the $h + h_s$ field, we thus examine the effects of the individual forcing terms in Eqs. (6.24)-(6.26) on the mixed-layer wind vector field. We also assume that $\nabla\theta(h_T)$ is negligible, $u_g(h_T) = 5$ ms^{-1}, $v_g(h_T) = 0$, and $\gamma = 0.005$ K m^{-1} = constant. We choose for the present purpose the wind vector field at 0800 shown in Fig. 6.23a as being representative of the wind patterns in the early morning hours during which the temporal variations seem to be minimal.

The baroclinic effect in the mixed layer [term (III) in (6.25)] is shown in Fig. 6.23b, while Fig. 6.23c illustrates the effect of the horizontal gradient of the mixed-layer height combined with the discontinuity of θ at this height [see term (II)], and the resulting effect of these two terms is depicted in Fig. 6.23d. The fields of

Fig. 6.23. Vector fields of various forcing terms in Eqs. (6.25) and (6.26). Unless otherwise specified, figures were obtained using the M4 results for the mixed layer at 0800 LST, and the arrow length equivalent to one grid-interval length corresponds to $5 \times 10^{-4} ms^{-2}$. Also shown are the fields of $\underset{\sim}{V}_M$, C_D, and h at 0800 LST.

(a): Horizontal winds of the mixed layer. The scale of the arrows is 5 ms^{-1}/grid-length interval.

(b): Baroclinic term (III) in (6.25). The scale of the arrows is $10^{-3}ms^{-2}$/grid-interval length.

(c): Forcing term (II) due to the horizontal gradient of $h + h_s$ in (6.25). The scale is as in (b).

(d): Forcing resulting from the sum of the terms (II) and (III) in (6.25).

(e): Forcing term (I) due to the upper-layer effect in (6.25).

(f): Total pressure-gradient forcing represented by the sum of the terms (I), (II) and (III) in (6.25).

(g): Forcing $-\mathcal{I}_s/\rho h$ due to surface stress in (6.26).

(h): Forcing $\mathcal{I}-/\rho h$ due to momentum entrainment in (6.26).

(i): Field of C_D. The contours are drawn at 2×10^{-3} intervals. Shaded areas denote below-average values.

(j): Field of h. The contour is drawn at 100 m intervals. Shaded areas denote below-average values.

(k): Turbulent stress given by (6.26), i.e., the sum of (g) and (h).

(l): Coriolis forcing given by the 1st term on the right side of (6.24).

(m): Forcing resulting from the sum of turbulent stress (k) and Coriolis effect (l).

(n): Total forcing (f) + (k) + (l) represented by the right side of (6.24).

(o): As in (m) except for 1500 LST instead of 0800 LST. The scale of the arrows is $2.5 \times 10^{-4}ms^{-2}$/grid-interval length.

(p): Combined forcing due to the Coriolis effect and the turbulent stress represented by the 1st and 3rd terms on the right side of (6.24), computed for layer 7 of the L7 model at 1700 LST. The scale of the arrows is $10^{-3}ms^{-2}$/ grid-interval length.
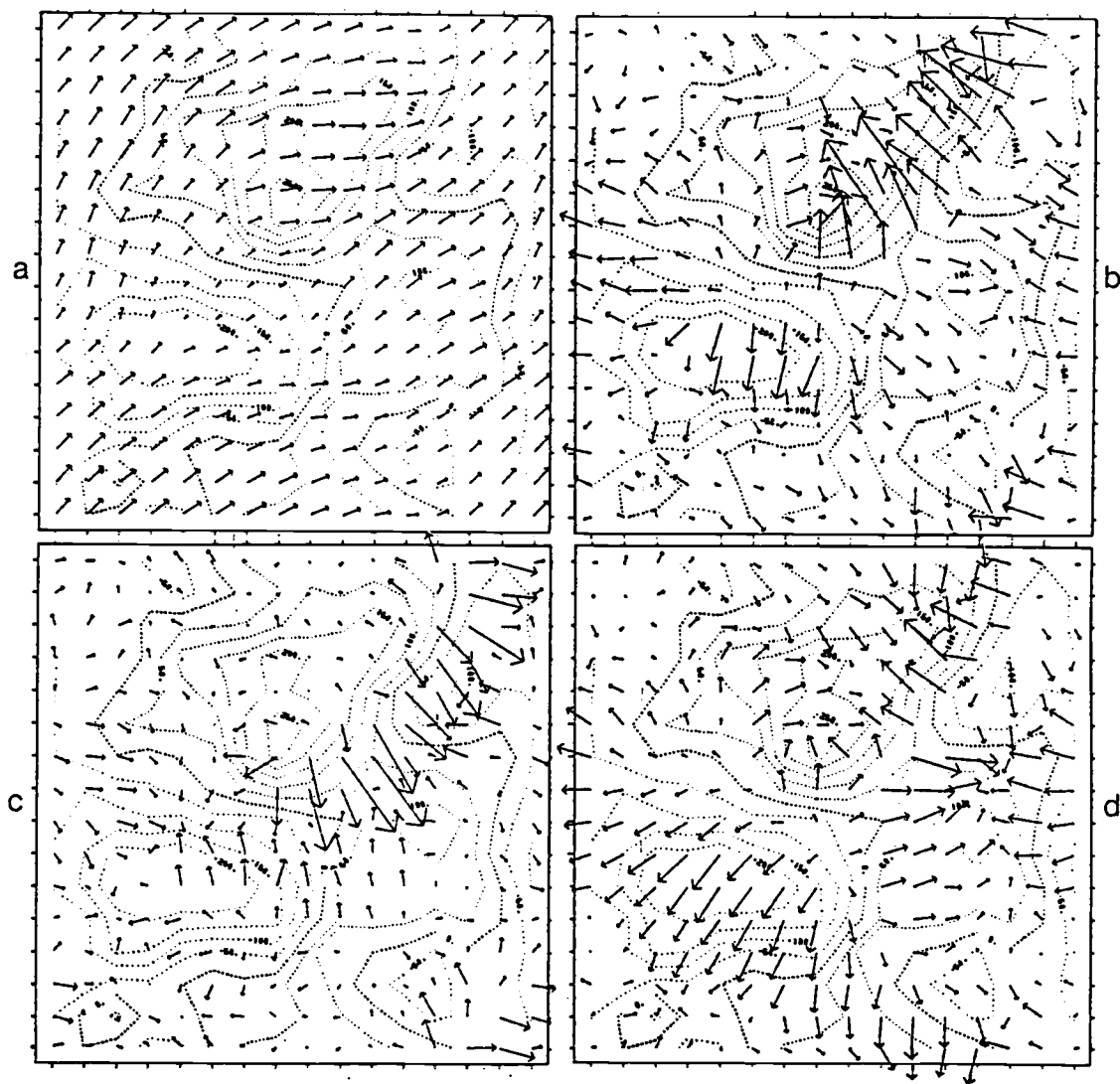
Fig. 6.23. Continued.
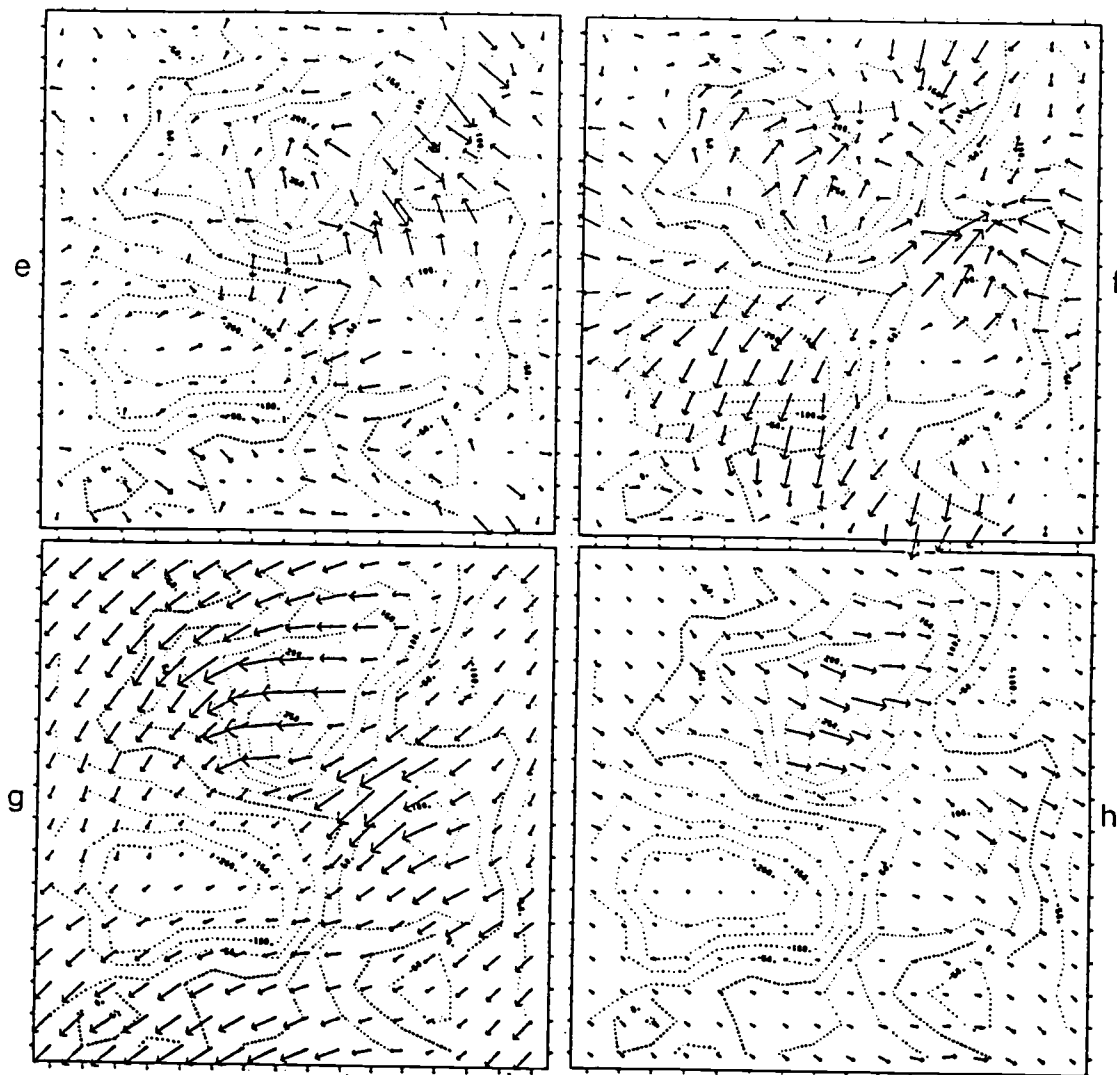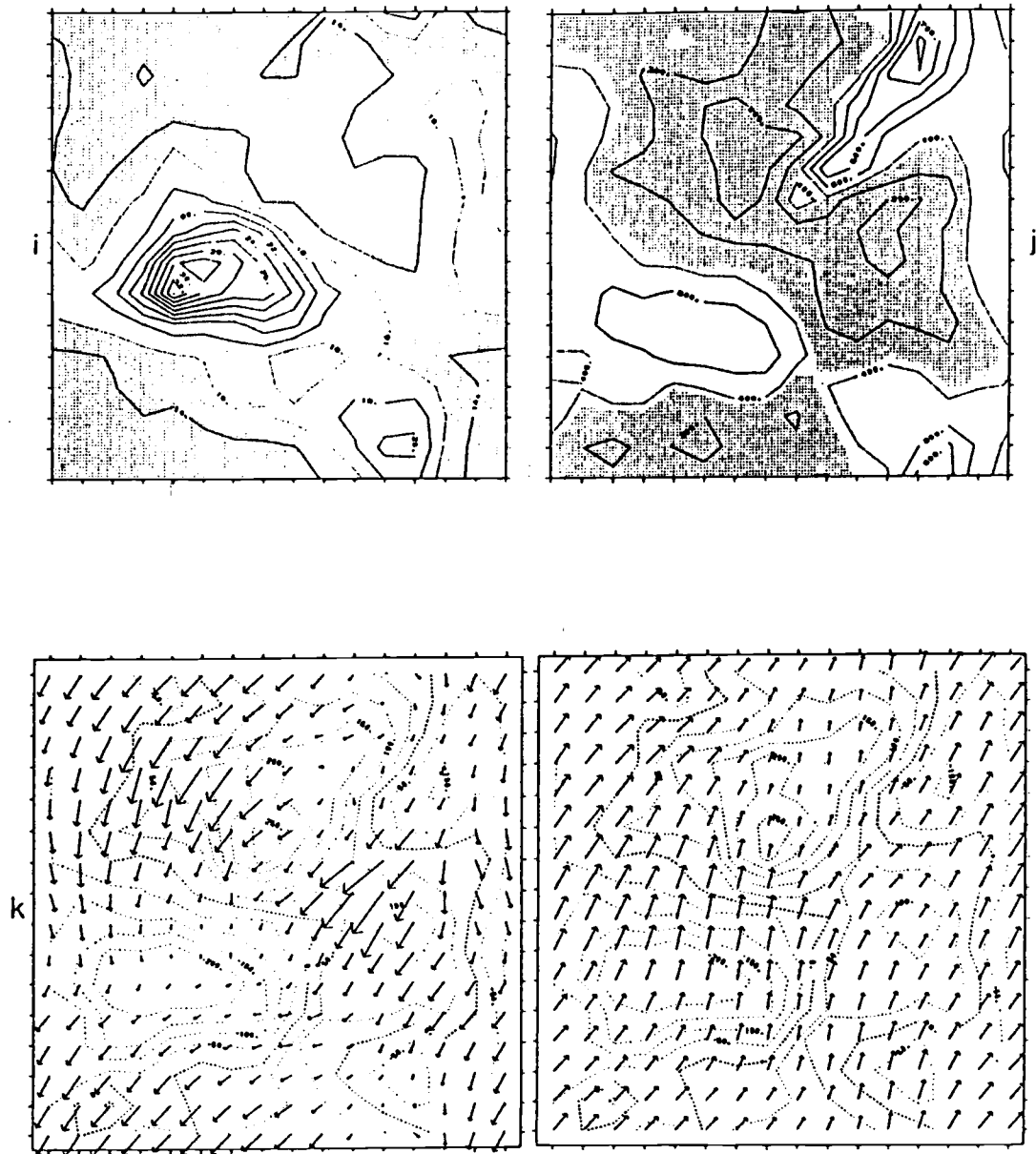
Fig. 6.23. Continued.
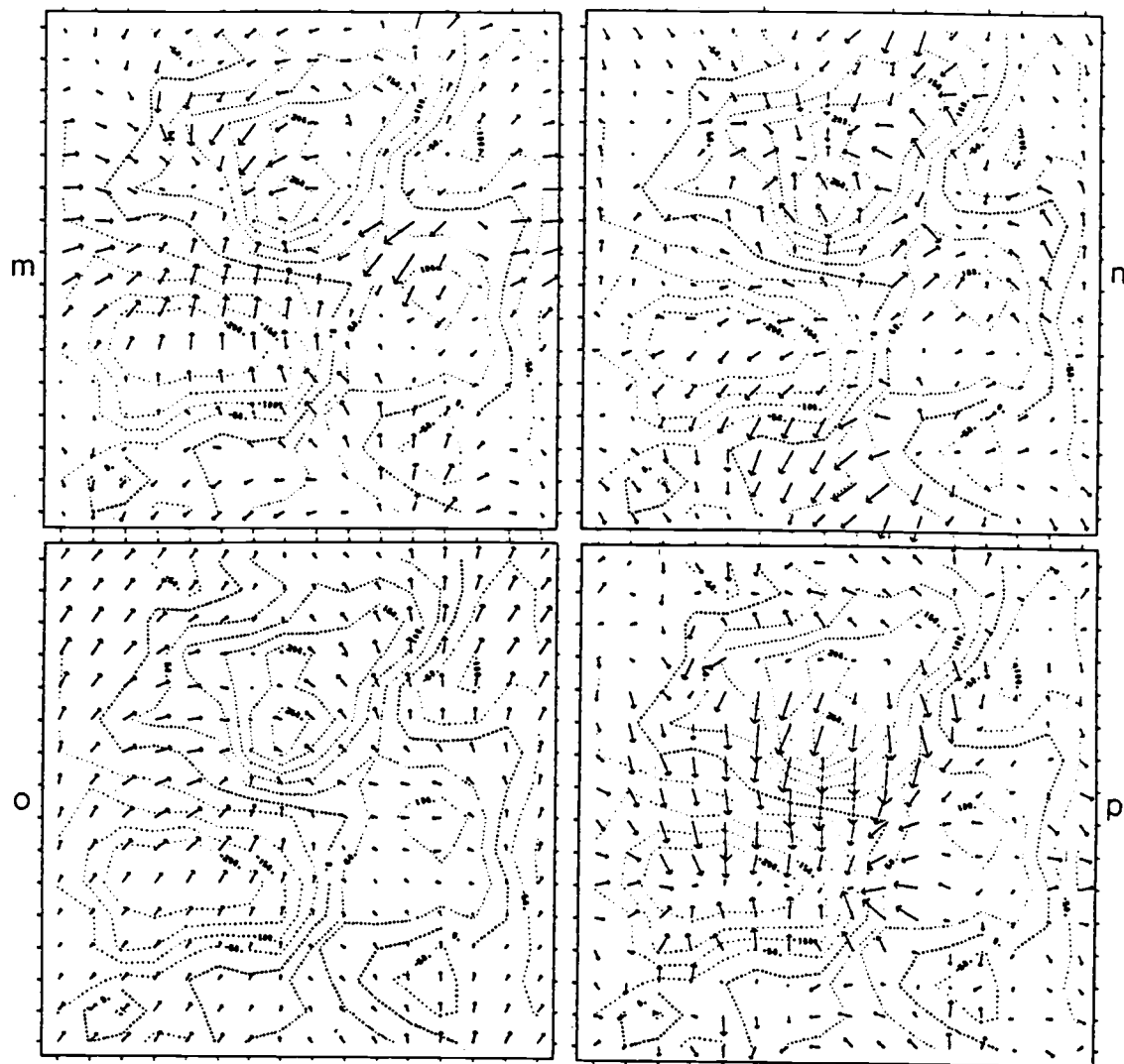
Fig. 6.23.   Continued.

Fig. 6.23. Continued.

θ_M, $\theta^+ - \theta_M$ and $h + h_S$ are depicted in Figs. 6.24, 6.35 and 6.37, respectively. It is seen that in general the height effect [term (II)] and the baroclinic effect [term (III)] oppose each other: the former has relatively greater accelerating effects on air parcels where the wind vectors are smaller, whereas the latter is more consistent with the wind vector field. Particularly, in the regions of weak winds, the decelerating effect of spatial θ_M variation is markedly larger so as to overcome the accelerating force due to height variation, resulting in the forcing vector pattern depicted in Fig. 6.23d which shows greater decelerating effect in these regions. We notice that individual effects of these opposing terms are very large along the slopes of the primary hill facing the southeast and extending toward the northeast, but the combined force is greatly reduced, with the temperature effect generally overcoming the height effect. The force due to baroclinity above the mixed-layer top [term (I)], shown in Fig. 6.23e, is considerably smaller than either of the two terms discussed above (note the differences in scale). Although uncertainty of h_T makes the influence of the term (I) less reliable, the depth of the upper layer $h_T - h - h_S$ is still relatively shallow and spatially uniform at 0800, thereby making the upper-layer effect secondary in the combined pressure gradient force of three terms depicted in Fig. 6.23f. Term (I) generally has a greater accelerating effect on air parcels where winds are weak. However, the major features of the baroclinic term (III) prevail in the vector field of the total pressure-gradient force given by Eq. (6.25). This seems to explain the major weak-wind regions,

although rather strong accelerating effects over northern slopes of both primary and secondary hilltops are somewhat inconsistent with the wind vector field.

We next examine the forcing vector fields due to the stress term given by Eq. (6.26). The forcing fields due to surface stress and entrainment at the mixed-layer top are shown in Figs. 6.23g and h, respectively. The bulk transfer coefficient C_D for momentum at 0800 depicted in Fig. 6.23i is rather uniform over the hills and is in the range of $10\text{-}15 \times 10^{-3}$ while in the northern edge of the primary basin the values are much larger, ranging up to 34×10^{-3}. The field of h at 0800 is also depicted in Fig. 6.23j, which shows shallower depth over the hills. Thus, combining C_D, $\underset{\sim}{V}$ and h, we obtain the field of forcing vectors $C_D|\underset{\sim}{V}|\underset{\sim}{V}/h$ which are anti-parallel to the wind vectors, as illustrated in Fig. 6.23g. The decelerating effect of C_D is much stronger over the hills, but is very small in the regions of weak winds, which, therefore, are not explained by the surface-stress effect. On the other hand, the forcing field due to the momentum entrainment depicted in Fig. 6.23h, which is equivalent to the turbulent stress at the top of the mixed-layer, shows that it generally accelerates mixed-layer air parcels eastwards with a small component directed southward over the hills where w_e itself is larger (see Fig. 6.36), while in the areas of lower elevations its effect is negligible. The resulting forcing vector fields due to these stresses is illustrated in Fig. 6.23k, which shows the influence of w_e that accelerates air parcels mostly eastwards, but is not quite sufficient to overcome the stronger surface drag force.

The remaining force in Eq. (6.24) exerted on air parcels is the Coriolis force $-f\underline{k} \times [\underline{V}-\underline{V}_g(h_T)]$, shown in Fig. 6.23l. Adding this force to that due to stresses yields Fig. 6.23m, which indicates that the resulting force accelerates air parcels north- and north-eastwards in the regions of weak winds. We notice that over the mountains the decelerating force due to stresses becomes very diffuse except over the northwestern slopes of the major hills. Finally, combining Fig. 6.23f with Fig. 6.23m, we obtain the total-forcing vector field shown in Fig. 6.23n, represented by the right side of (6.24). Although it shows somewhat diminished correlations to the wind vector field, there are still positive correlations in general between the regions of weak winds and the stronger decelerating force. The stronger accelerating force on the north- and north-western slopes of the major hills seen in Fig. 6.23f is now counterbalanced by stresses, making the total forcing field more consistent with the wind vector field. On the other hand, the total forcing field excluding the baroclinic effect of the upper layer [term (I) in Eq. (6.25)] (not shown) exhibits higher correlations with the wind vector field, indicating that uncertainty involved in determining h_T may have contaminated the vector field of the total forcing exerted on air parcels.

In summary, we have found that baroclinity in the mixed layer is the most dominant effect in maintaining the regions of weak winds seen in the early morning hours when surface heating is still moderate and thus the mixed layer is shallow and its top relatively smooth. The entrainment forcing peaks at about 1000 when w_e is near its maximum value but h is still small: it is generally

stronger over the hills and weaker over the basins, and when combined with the surface stress, a forcing pattern similar to that at 0800 results. However, the entrainment effect alone is not strong enough to overcome the surface drag effect even during its peak period. It rapidly weakens as h deepens, almost vanishing by 1500, while the effect of surface stress is still evident throughout the afternoon (see Fig. 6.8a). Since the wind vector fields in the late afternoon are remarkably uniform in magnitude and direction, we may assume that in the regions of weak winds there must be an accelerating force working on air parcels throughout the afternoon. If we posturate that the baroclinic and height effects described earlier should weaken as horizontal perturbations of $h + h_s$ and θ_M diminish in the afternoon, then the combined forcing-vector field due to C_D, w_e, and f, should largely dictate the flow patterns in the mixed layer, as shown in Fig. 6.23o for 1500 LST, particularly over the regions of weak winds. Thus, the wind speeds become spatially less and less varied through late afternoon. This combined effect due to turbulent stresses, Coriolis and large-scale pressure gradient forces is evident through the late afternoon. However, the so-called Ekman balance between the stress and Coriolis terms has never been attained for broader regions other than the areas over and to the south of the secondary hill, indicating that the local pressure gradient force is still a major factor, especially over the lower lands, in determining the flow patterns.

It is not feasible to apply Keyer and Anthes' mixed-layer model to examine the wind vector fields for L7 shown in Figs. 6.19-22 because the assumption of the well-mixed boundary layer is not

implied in design of the L7 model. However, as in the case of M4, the effect of baroclinity in the lowest layer seems to play a major part in intensifying and maintaining the weak-wind pockets during the morning hours. Contrary to the M4 results, these regions of weak winds are still evident even in the late afternoon, not only in the lowest layer but also even in the layer $\ell = 5$. However, we expect that the slight spatial anomalies still seen in the late-afternoon temperature fields depicted in Figs. 6.30-32 play a minor role in determining the flow patterns. Steadiness of the overall flow patterns throughout the day in the layers $\ell = 6$ and 7 suggests that the topographic effect must also be a major factor in determining the flow patterns in the lower layers which are within the mixed layer. The vector fields of the combined forcing of turbulent stresses at the surface and at the layer interface given by Eq. (4.38) for $\ell+1/2 = 6+1/2$, together with the Coriolis effect, have been plotted for the lowest layer of L7. We have found that the forcing vector field at 1700 depicted in Fig. 6.23p is a typical pattern that persists throughout the afternoon. It shows a strong decelerating force directed southwards over the southern slope of the primary hill as well as a northward-accelerating force over the southern edge of the primary basin. The forcing due to the surface stress is much stronger than that in the case of M4 because of small thickness of the layer $\ell = 7$, which consequently makes the effect of the Coriolis force almost negligible. By comparing Fig. 6.23p with its M4 counterpart in Fig. 6.23o, we find that the combined effects of the above three forcing terms in the late afternoon are nearly opposite in these two models, although the magnitudes are much

different. Since the forcing vector pattern in Fig. 6.23o is
apparently inconsistent with the flow pattern in Fig. 6.19 the
pressure-gradient force must be working on air parcels so as to
counterbalance the effect of turbulent stress and maintain more or
less the steady flow pattern throughout the day. An inspection of
the potential temperature fields suggests that the baroclinic effect
is counterbalancing the stress effect, but it is not certain whether
the baroclinity is strong enough to be a dominant part of the
pressure gradient force in the late afternoon. In the σ-coordinate
system, however, it is rather difficult to deduce what causes $-\nabla_p\phi$
given by (2.33) to counterbalance the stress in the lowest layer of
the L7 model without term-by-term analyses. It is, therefore, only
suggested that in addition to the $\theta_{\ell=7}$ anomaly the fields of
$\phi_{\ell=7}$ and p_S are such that $-\nabla_p\phi$ is positive partly due to the
terrain irregularities and counterbalances the stress effect through
the afternoon.

6.7 Evolution of Potential Temperatures

The fields of the mixed-layer potential temperature θ_M for M4
are shown in Fig. 6.24 at 2-hour intervals beginning at 0500. A
fraction of the cold air pool initially located in the primary basin
is seen to be gradually advected through the mountain pass between
two major hills during the morning hours. However, the major
portion of the relatively cold air persists until after 1500 when it
finally moves out of the major basin toward east over the secondary
hill. The mixed layer still maintains 1 K or so of the spatial
variation of θ_M over the domain even in the late afternoon.
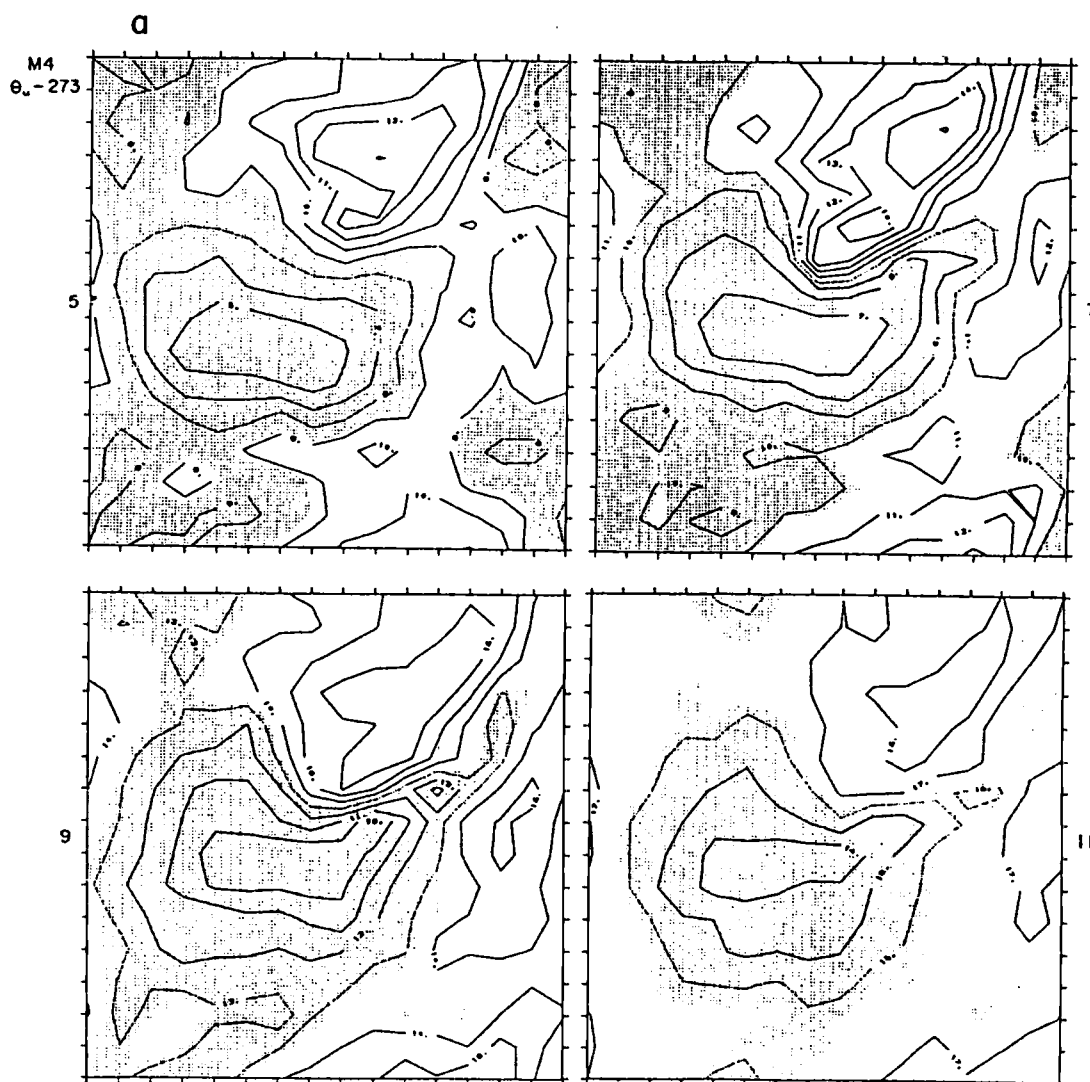
Fig. 6.24. Fields of θ-273 (K) for the mixed layer of M4. Shaded areas denote below-average values. (a): At 05, 07, 09 and 1100 LST. The contour interval is 1 K. (b): At 13, 15, 17 and 1900 LST. The contour interval is 0.5 K.

184
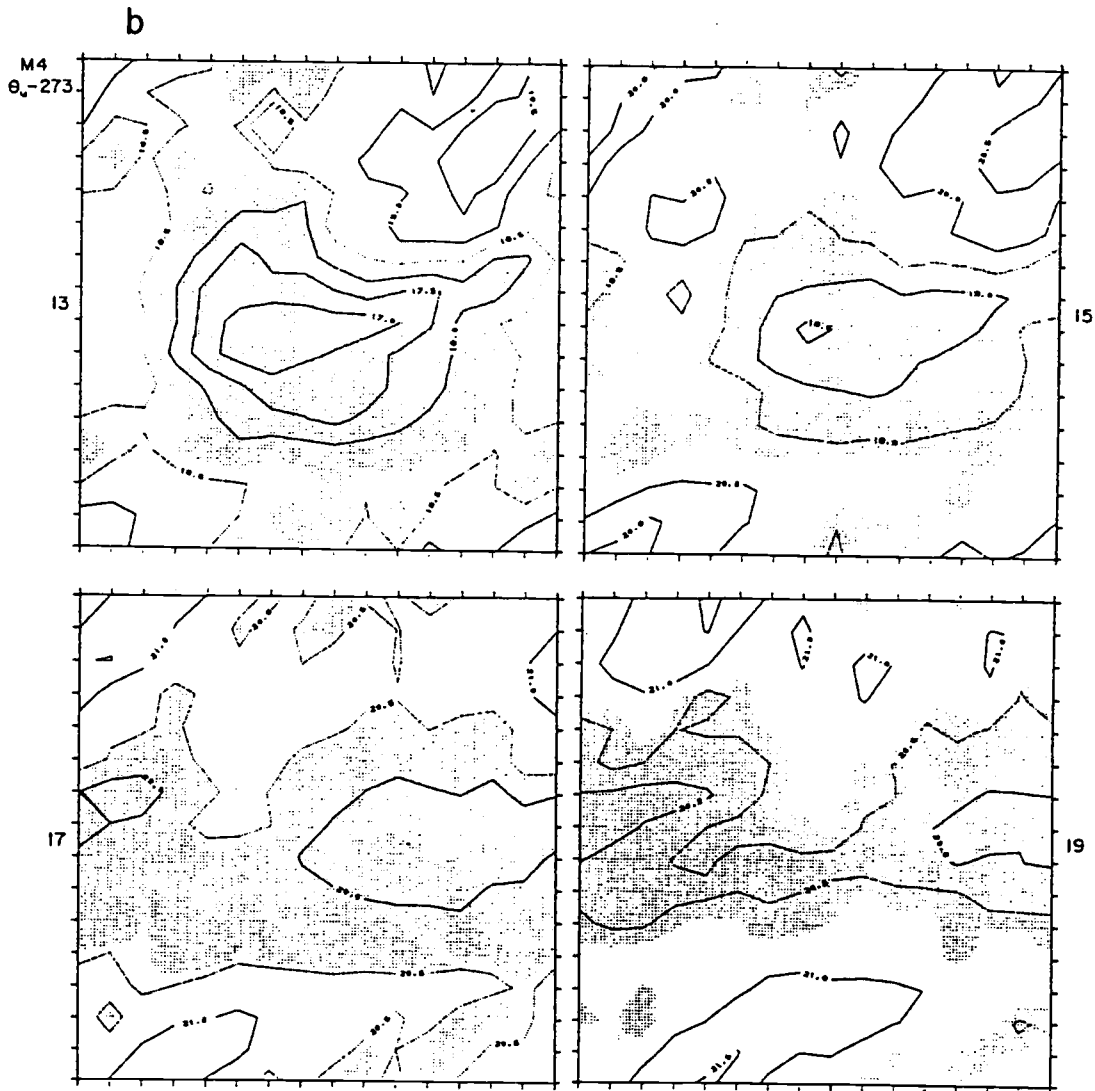
Fig. 6.24. Continued.

Warmer air initially existent over the mountains also persists until after 1500 when it is finally advected eastwards. The spatial temperature difference of 8 K existent at 0500 between the primary hilltop and the basin reduces to 1 K by 1900, indicating that cool air in the basin has warmed up much faster than that over the hilltop.

In a previous study (DUH, 1984) a description of the evolution of the horizontal root-mean-square variability of θ_M, $\delta\theta_M = \langle(\theta_M - \langle\theta_M\rangle)^2\rangle^{1/2}$, shown in Fig. 6.1 was presented, in which a weak buildup of $\delta\theta_M$ until 0800 was associated with a lesser surface heat flux over the cool anomaly (see Fig. 6.33) whose depth is relatively large. Shown in Figs. 6.25-27 are the fields of the effective heating rate due to:

(i) the direct surface heat flux, together with the entrainment heat flux which is on average about 20 - 25% of the former during the daytime (see Fig. 6.2a), $(H_S + w_e\Delta\theta)/h$;

(ii) the horizontal advection of θ_M, $-\underline{V}_M\cdot\nabla\theta_M$; and

(iii) the sum of the above two effects.

We notice, for example, in Fig. 6.25d, that at 0700 the spatial difference in warming rate due to (i) between the higher terrain and the basin is much greater than the spatial variation of surface heating shown in Fig. 6.33 suggests. This is because of the greater mixed-layer depth h over the basin early in the morning, as Fig. 6.28 illustrates, which would deter the decrease of $\delta\theta_M$. However, the advective effect of θ_M illustrated in Fig. 6.25e for 0700 greatly compensates the effect of direct turbulent heating over the hills by bringing in colder air from the lower terrain
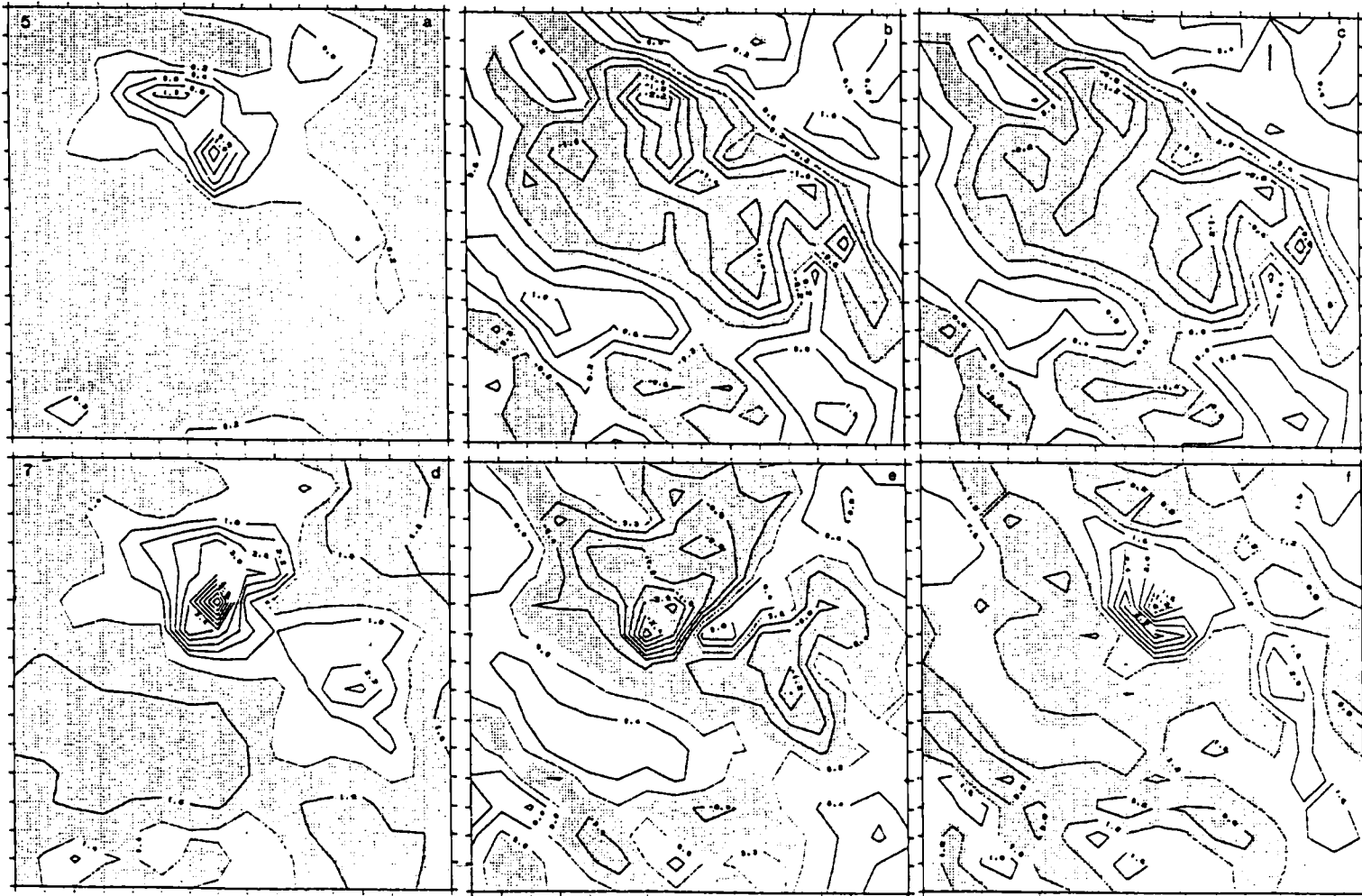
Fig. 6.25. Fields of effective heating rates (K/hr) of mixed layer of M4 due to i): direct surface and entrainment heat fluxes (left column); ii): horizontal advection of θ_M (middle); and iii): sum of i) and ii) (right). Contour interval is 0.4 (K/hr). Shade areas denote below-average values. Top row is for 05 and bottom row is fo 0700 LST.
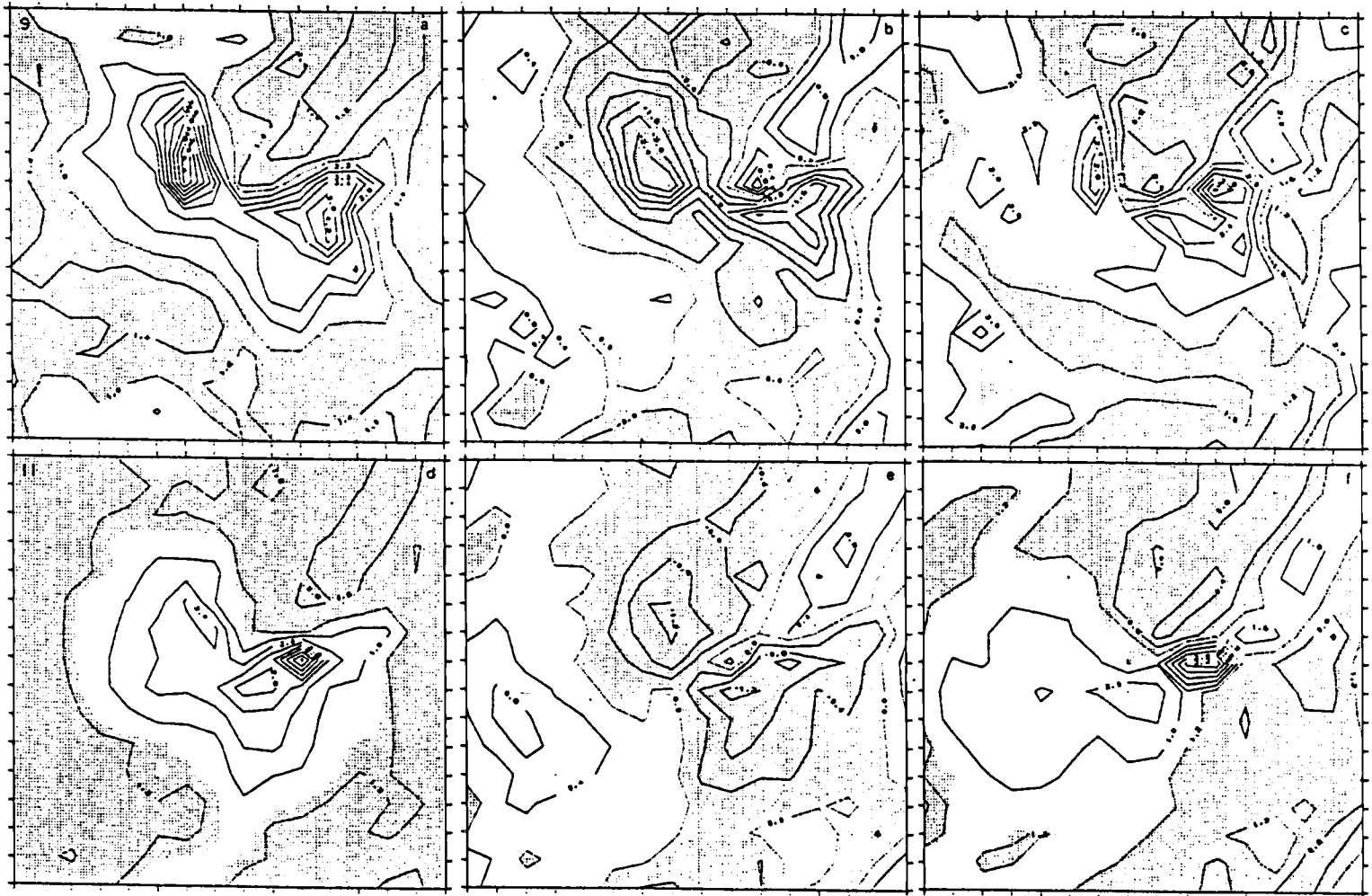
Fig. 6.26. As in Fig. 6.25 except for 0900 (top) and 1100 LST (bottom).
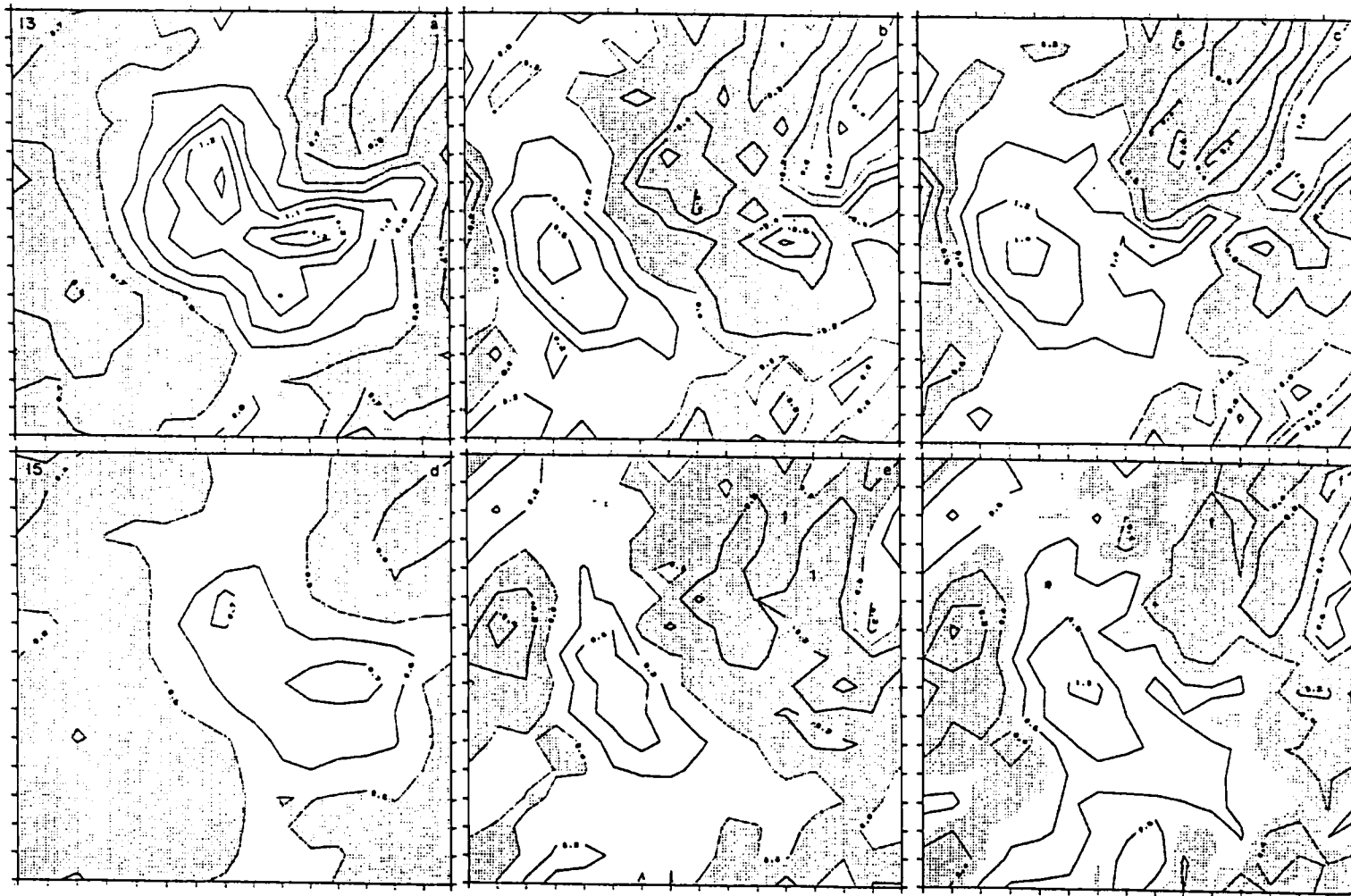
Fig. 6.27. As in Fig. 6.25 except for 1300 (top row) and 1500 LST (bottom). Contour interval is 0.1 (K/hr) for left column, 0.2 (K/hr) for middle and right columns.
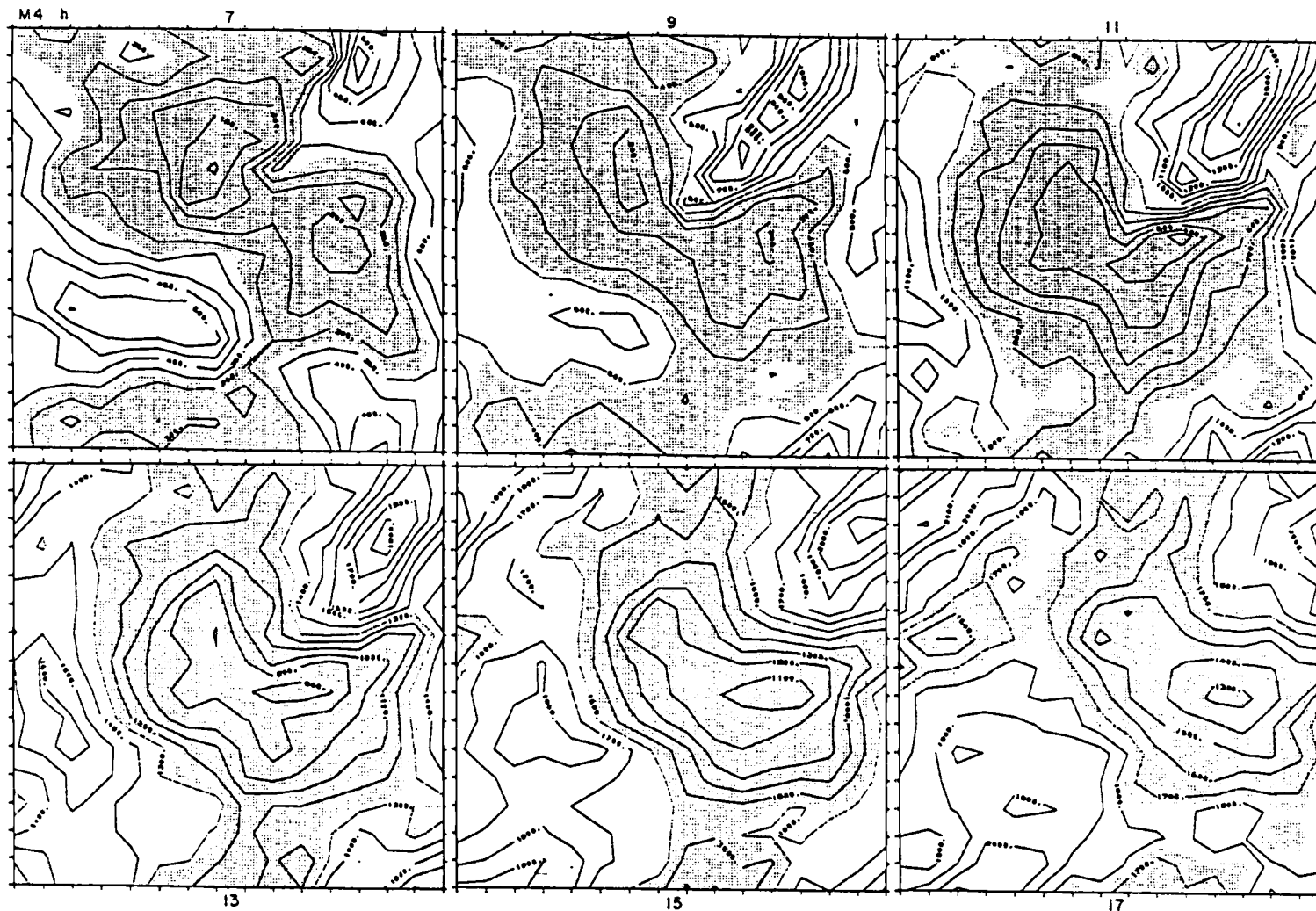
Fig. 6.28. Fields of the mixed-layer depth h (m) for M4 at designated hours. The contour interval is 50 m for 0500, and 100 m for all other hours. Shaded areas denote below-average values.

upstream. The resulting sum of these two nearly opposing effects, equivalent to $\partial\theta_M/\partial t$ to a first approximation, is depicted in Fig. 6.25f for 0700. It shows variations smaller in magnitude but more scattered in space than the surface-heating effect alone. However, the effect of a greater direct surface heating rate over the major hills is still evident, which tends to oppose the decrease of $\delta\theta_M$. The spatial perturbations of the heating rate become most pronounced at 0800 [0.7 to 6.5 K hr^{-1} for (i), -3.2 to 1.2 K hr^{-1} for (ii), and -0.3 to 3.5 K hr^{-1} for (iii)]. In this sense the most intense transition seems to occur at around 0800 as far as θ_M is concerned.

After 0900 the effective heating-rate pattern which will persist through midafternoon begins to emerge (Fig. 6.26c). The relatively strong direct surface-heating effect due to both the stronger surface heating and smaller h exists over the pass between two major hilltops (Figs. 6.26a and d). Furthermore, the advective heating over the lower terrain, particularly along the valley in the northeastern corner of the domain and over the western part of the primary basin, together with the strong advective cooling over the hills (Figs. 6.26b and e), results in a faster warming in the valley and over the southwestern slopes of the basin (Figs. 6.26c and f). This helps a rapid erosion of the cold air tongue extending northeastwards from the basin as well as warming of colder air in the north- and south-western corners of the domain. Comparing the effective heating-rate patterns from 0900 on (Figs. 6.26-27) with the corresponding fields of θ_M (Fig. 6.24) we find a strong negative correlation between them, i.e., where θ_M is relatively

smaller the effective heating rate is greater, thus helping reduce $\delta\theta_M$ with time.

In our previous study mentioned earlier it was stated that the initially negative correlation between θ_M and h vanished by midmorning as the pattern of entrainment w_e (Fig. 6.36) caused h to grow rapidly in the region of warmer mixed-layer air and smaller discontinuity $\Delta\theta$ at the mixed-layer top (Fig. 6.35), and that after 0900 the cool-air region was thus associated with smaller h. Since the fields of surface heating shown in Fig. 6.33 vary spatially at most 10 - 15%, we see that during midday the regions of smaller h are strongly associated with those of larger heating rate due to direct surface flux (Figs. 6.26d, 6.27a, and 6.28). However, without the advective cooling effect θ_M would have been much higher over the major hilltops and their upwind slopes, while without the advective warming effect the mixed-layer air would have been much cooler over the western region of the primary basin and in the valley in the northeast corner of the domain (Figs. 6.26e and 6.27b).

By inspecting the fields of θ_M and h during midmorning, we find that in general where h is relatively small the magnitude of $\nabla\theta_M$ is relatively large, particularly along the upwind slopes of the primary hill as well as the pass between two major hills. This is indicated by the evolution of the correlation coefficient between h and $-\underaccent{\sim}{V}_M \cdot \nabla\theta_M$ shown in Fig. 6.34b (curve I). It seems that the cool-air pool in the primary basin has been pushed upslope halfway against the windward slopes, but short of clearing over them. Rapid increases of θ_M and h through late morning occur over downwind

sides of the major hills, while on the upwind slopes they are increasing little. This has created horizontal patterns of θ_M and h such that where h is small the magnitude of $\nabla\theta_M$ is large, which has resulted in a high negative correlation between the heating-rate pattern due to advection and that due to direct surface flux (curve M in Fig. 6.34b). As the horizontal variations of θ_M, h and wind speeds become smaller in the afternoon, so do those of $-\underset{\sim}{V}_M \cdot \nabla\theta_M$ and the heating rate due to direct surface flux, thus making the negative correlation between the effects of the θ_M advection and direct surface heat flux less pronounced.

The effect of the θ_M advection on the warming rate is in a strong negative correlation with that of direct surface heating but is somewhat secondary to the latter between 0700 and 0900 in shaping the patterns of the effective heating rate. It, however, begins to play an increasingly dominant role, as seen in Figs. 6.26-27, when the warming rate due to direct surface heating begins to taper off after reaching its maximum at around 0900. Therefore, in addition to the negative feedback effect between θ_M and h that tends after 0900 to warm faster the region of thinner h associated with cooler air, we find that the effect of the θ_M advection tends to spatially compensate the effect of direct surface heating on the warming rate and thus plays a major role in determining the time evolution as well as spatial variations of θ_M. The fields of the warming rate which accounts for both effects are shown in the right figures of Fig. 6.25-27. They are seen to have stronger negative correlations with the θ_M fields than those of the direct turbulent-heating alone. Particularly, the faster warming of the

western region of the primary basin and the valley in the northeast corner of the domain could not have been attained without considering the advective effect of θ_M.

On the other hand, in their study of observed data obtained in shallow valleys in northeastern Colorado, Lenschow et al. (1979) have emphasized the importance of the advective effect on a rapid transition in temperature, relative humidity and wind speed of the morning boundary layer over terrain of variable elevation whose scale and slope are on order of 10 km and 1×10^{-2}, respectively. They have found that the local surface heating is not sufficient to account for the observed temperature rise, and suggested that as surface heating begins the colder valley air becomes less stably stratified and increasingly turbulent, and eventually the shear stress at the top of the boundary layer becomes large enough to pull the cold air out of the valley, to be replaced by the deeper, warmer mixed layer advected into the valley from the upstream slopes and plateaus, consequently breaking up the early-morning stable layer.

As far as the evolution of θ_M is concerned, our results for M4 presented here are consistent with the above observational study in that the advective effect was found to be important. However, as described earlier, we have found that the turbulent stress at the mixed-layer top expressed in terms of w_e in the M4 model is not sufficient to pull the cold air out of the depressions and consequently dissolve the stable layer. The scales of the terrain used in our experiments are on order of several tens of kilometers, the slopes on order of 5×10^{-3}, but the spatial resolutions of the grids, are rather coarse, and the model does not seem to be able to

resolve the detailed transitions in the early-morning boundary layer as observed by Lenschow et al. (1979).

On the other hand, Whiteman (1982) who analyzed the data obtained in narrow but long valleys on the western slopes of the Rockies in western Colorado has reported that in the majority of observed cases he studied the nocturnal inversion layers are destroyed by two processes: the continuous upward growth of a warming convective boundary layer from the valley floor by entrainment of warmer air from above and the continuous descent of the top of the nocturnal temperature inversion. This subsidence is caused by the removal of mass from the base and sides of the stably stratified cool pool by the upslope flows that develop in the convective boundary layers over sidewalls. It causes the elevated inversion to sink deeper into the valley and to warm adiabatically, and results in a decrease in the growth rate of the convective layer. The vertical potential temperature gradient within the nocturnal stable layers Whiteman (1982) analyzed was 0.0295 K m^{-1} on average, while their average depth was 604 m. Above this stable core was a neutral stability layer, above which the free atmosphere characterized by more stable temperature structure existed.

On the contrary, the potential temperature structure used in our M4 experiment initially consisted of a shallow mixed layer capped by an interfacial entrainment layer with infinitesimal thickness which is characterized by an abrupt θ discontinuity. Above this layer the free atmosphere was assumed to exist with a stable θ lapse rate, but no neutral layer was assumed above the inversion. In the L7 experiment we assumed the initial mixed layer

consisted of the layer ℓ = 7 which was characterized by a relatively large increase in θ between full levels ℓ = 6 and 7. Above the lowest layer the assumptions were as in the M4 model. Additionally, no upslope flows were generated due to mainly gentle slopes of the hills used in our model topography and to uniform large-scale geostrophic forcing imposed as well as coarse grid resolutions used. Consequently, Whiteman's (1982) mechanism for subsidence of the mixed-layer top was not apparent. Therefore, it is again difficult to compare our results to analyses of observed data by Whiteman.

The advective effect on the time rate of change of θ_M greatly varies from one grid point to another, depending on the local conditions. Nevertheless, we attempt here to find some general effects of advection on θ_M by examining relationships among heating rates, θ_M and h at several selected "sites" (grid points) in the domain. Time evolutions of these quantities in the primary basin represented by grid points (3,6), (4,6), (5,6) and (3,5) (see Fig. 5.1) are shown in Figs. 6.29a and b. We note that in the early morning when the surface heat flux is still weak relatively strong advective warming, shown in the middle panels, exists at sites selected upwind of cool air. In general, warm advection increases θ_M in the basin, as seen in the bottom panels, while cold advection reduces θ_M over the higher terrain. Therefore, the advective effect tends to redistribute sensible heat so as to make horizontal gradients of θ_M decrease. However, this advective warming itself is not sufficient to wipe out the capping inversion. By ~0800 the warming rate due to direct surface heating has become
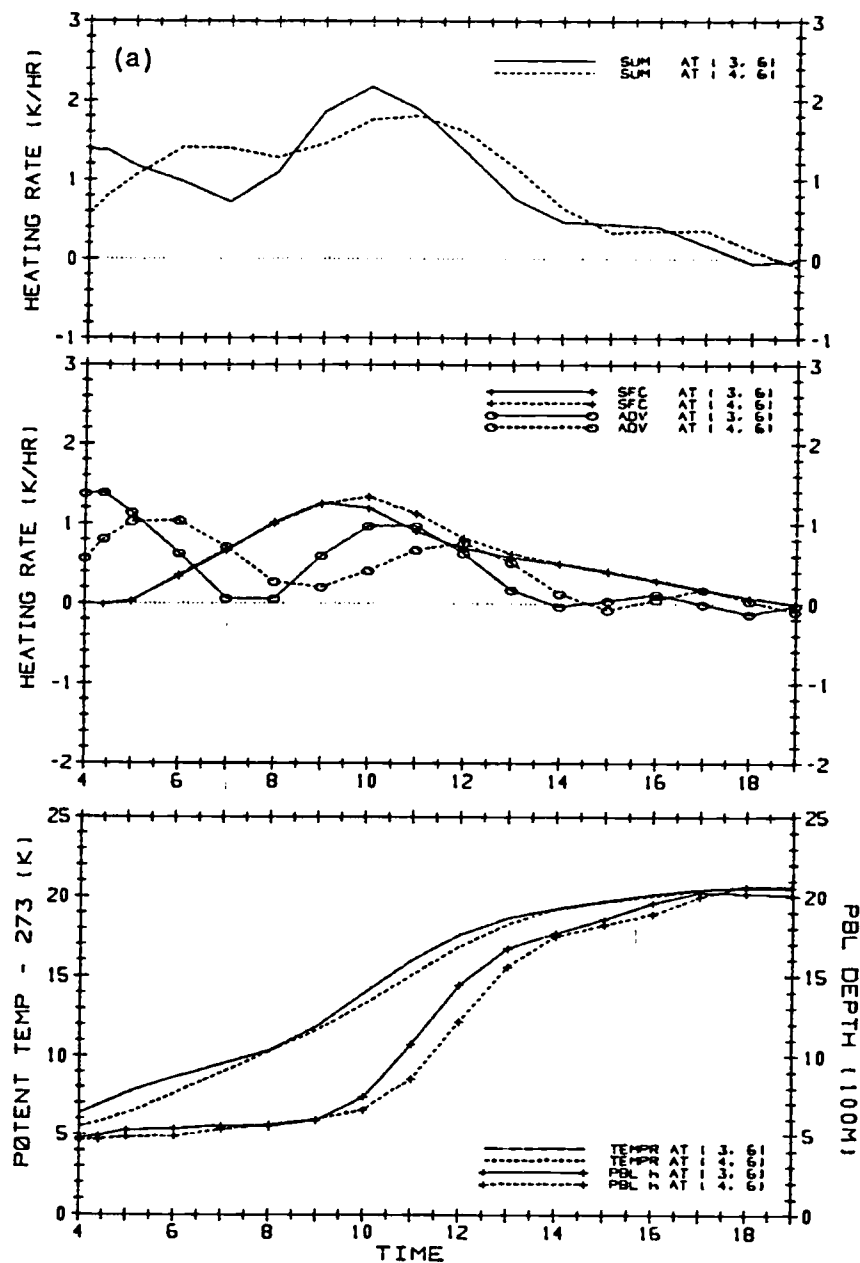
Fig. 6.29a.   Evolution of the heating rate (K/hr) of the mixed layer
for M4 at grid points (3,6) and (4,6) in the primary
basin, due to (i): direct surface heat flux (SFC) and
(ii): advection (ADV), both shown in the middle panel,
and (iii): the sum of (i) and (ii) (SUM) in the top
panel. Evolutions of θ_M − 273 (K) and h (100 m) are
also shown in the bottom panel.
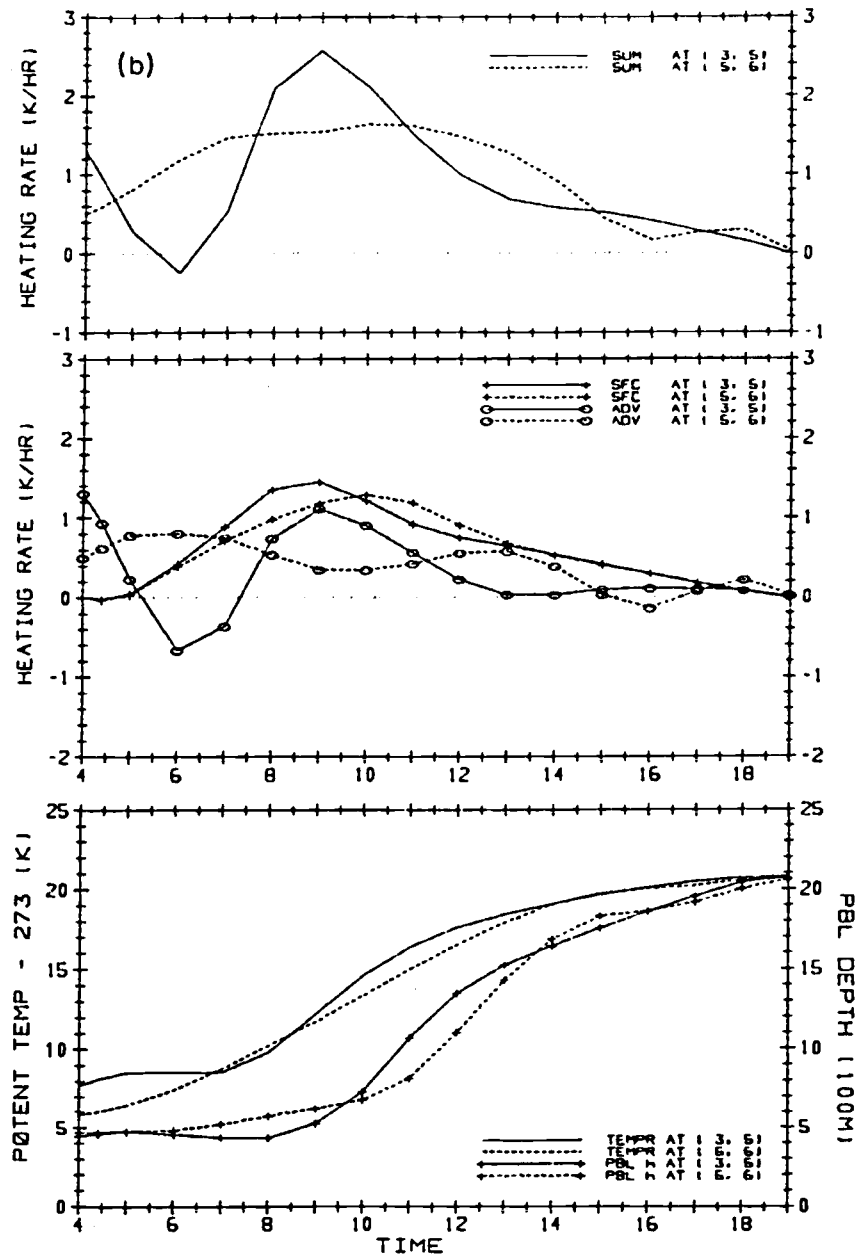
Fig. 6.29b. As in Fig. 6.29a except for grid points (3,5) and (5,6) in the primary basin.

dominant and, due to the difference in h rather than the solar insolation itself, differential heating of the mixed layer occurs, resulting in a faster increase of θ_M over the higher ground where h is relatively small and a slower increase of θ_M in the basin where generally h is relatively large. This in turn brings about a temporary increase in local horizontal gradients of θ_M again and hence of advection of θ_M.

It seems that in general the maximum of warming rate attributed to direct surface heat flux, which occurs in the midmorning, precedes a local maximum of warm advection. An increase in wind speed after 0900 should also contribute to a local maximum of warm advection during midday. As the total heating rate, shown in the top panels, becomes larger, θ_M increases rapidly in the early-morning mixed layer, causing a rapid increase in w_e and hence in h during midday. Reduced horizontal gradients of θ_M in the mid-afternoon results in a diminished advection of θ_M, while deepened h makes the effect of surface heat flux become nearly negligible. Thus, warming rates decrease and the increases of θ_M as well as h are minimal after mid-afternoon.

In Fig. 6.29c the evolutions of heating rates are depicted for grid point (10,13) situated at about 30 km northeast of the primary hilltop, representing the region of higher θ_M in the morning, and for point (9,8) in the coolest-air region, located about 30 km south of the same hilltop. At the latter point where the initial gradients of θ_M are relatively large, advection continuously brings in cool air, causing θ_M to attain a minimum at around 0600, while its horizontal gradients there are being reduced. It is noted
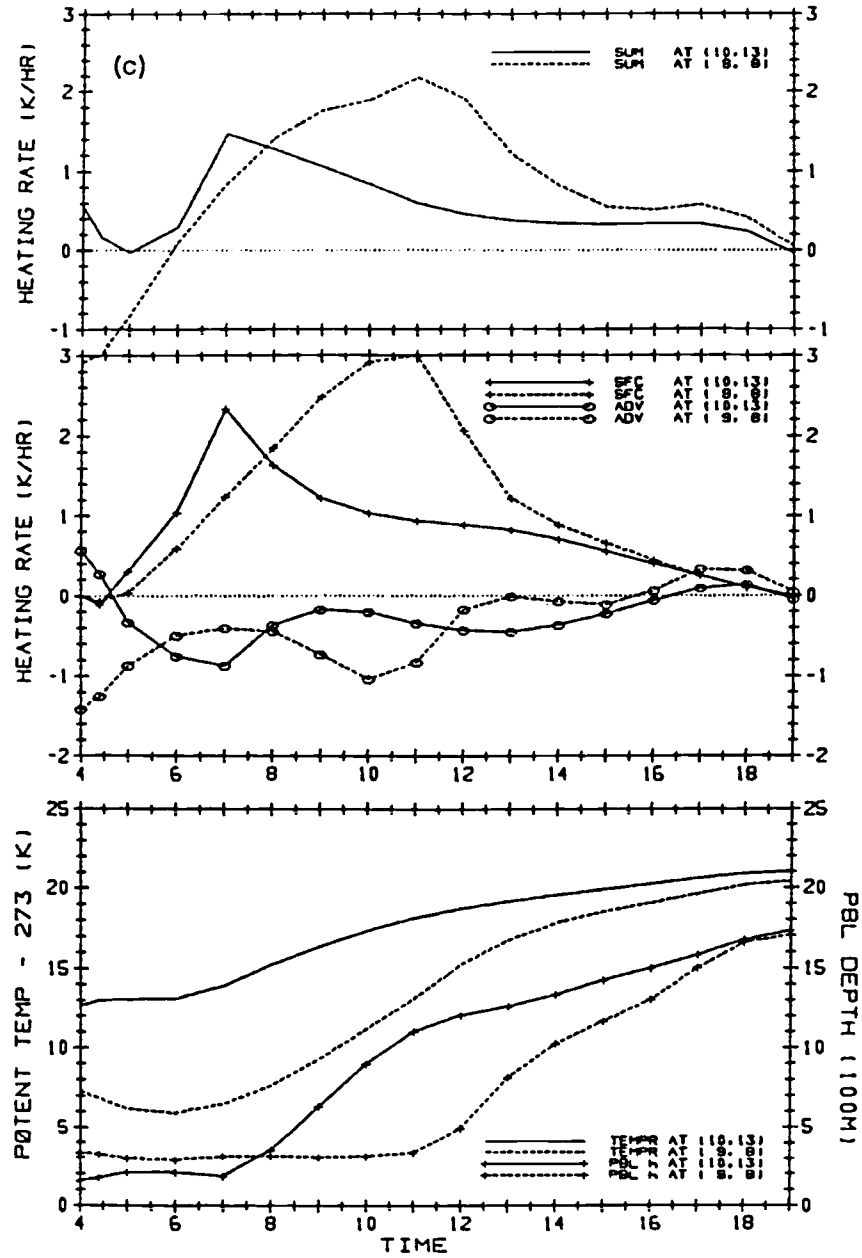
Fig. 6.29c. As in Fig. 6.29a except for grid points (10,13) and (9,8) in the warmer and cooler spots, respectively.

that a pocket of weak winds which intensifies through midmorning is located slightly upstream of the coldest region where point (9,8) is situated, which helps reduce the intensity of the cold advection. Cooling there due to advection again increases and peaks at 1000, due to the increased local gradients of θ_M to the north and to the east of this point created by spatial differences in the effective heating rates. Despite a relatively large total heating rate which warms cooler air rapidly, a larger value of $\Delta\theta$ at height $h + h_s$ associated with the lower θ_M during the early morning hours causes h to stay at about the same depth until after 1100 when the mixed layer of medium depth (initially) is finally filled in. At grid point (10,13) the effect of advection is also mostly cooling throughout the day. The difference is that at (10,13) the initially higher θ_M and shallower h cause h to grow faster earlier in the morning, resulting in a smaller warming rate attributed to direct surface flux and hence a slower increase of θ_M from midday on. Thus, the difference in θ_M between the warmest and coolest regions has become less than 1 K at the end of the day.

Illustrated in Fig. 6.29d are the evolutions of the same quantities near hilltops. We notice that while the warming rate due to direct surface heat flux is very large during the midmorning, advective cooling is also strong due to cooler air in the basin, carried up from upstream, helping θ_M increase modestly even during the peak period of direct surface heat-flux effect. It is noted that while θ_M is increasing rather rapidly, h deceases slightly during the midmorning at these points, and also at point (7,11) near sunset, which must be caused by mass flux divergence.
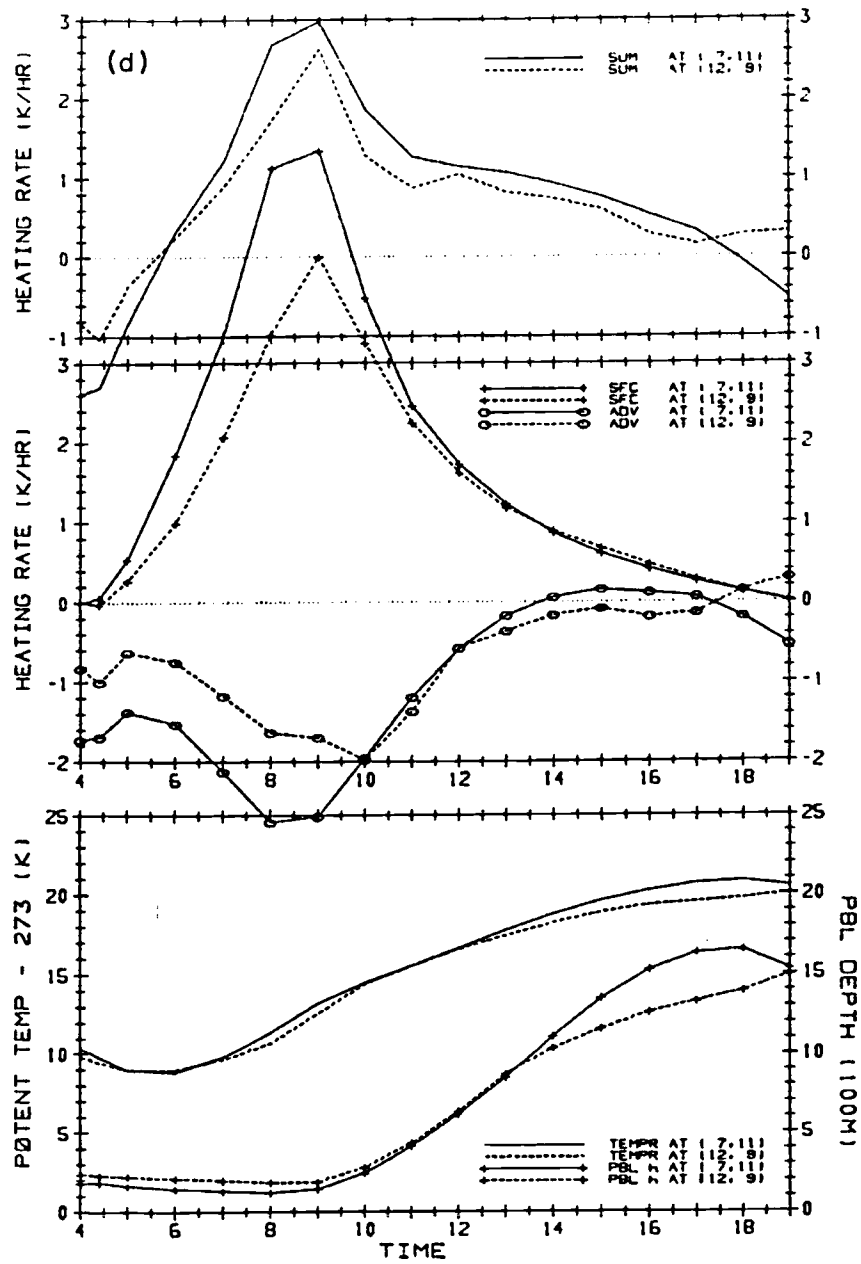
Fig. 6.29d. As in Fig. 6.29a except for grid points (7,11) and (12,9) near major hilltops.

Examples of a sharp increase in θ_M during the early morning of the present study are depicted in the bottom panel of Fig. 6.29e. Similar results have been reported in the field studies by Banta and Cotton (1981) who examined the data obtained in South Park, a relatively flat, wide valley in the Colorado Rockies, and Lenschow et al. (1979) as mentioned earlier. The initial drop in θ_M at (11,10) is caused by strong cold advection resulting from cool valley air being forced up the slope in response to increased instability and pressure gradient forcing generated by solar insolation, despite substantial warming effect due to direct H_S [see the middle panel for (11,10)]. The relatively large warm advection that follows, whose peak coincides with or is preceded by that of the warming effect due to direct surface flux, results in rapid warming of the shallow mixed layer during the midmorning hours.

The cases in which large warming due to advection contributes to a increase of θ_M as much as the effect of direct surface heat flux are illustrated in Figs. 6.29b and f for points (3,5) and (13,12), respectively. These points are located in the southwestern corners of the primary basin and the valley in the northeast corner of the domain, respectively. In both cases, as in most other cases we have examined, warm advection of θ_M during the early morning hours is not sufficient to wipe out the capping inversion, and a second "wave" of advective warming is needed to trigger a rapid increase of θ_M and hence of h in the regions of lower elevation. This "wave" seems to be generated by spatial differential heating of the mixed-layer air. On the other hand, a period of approximately
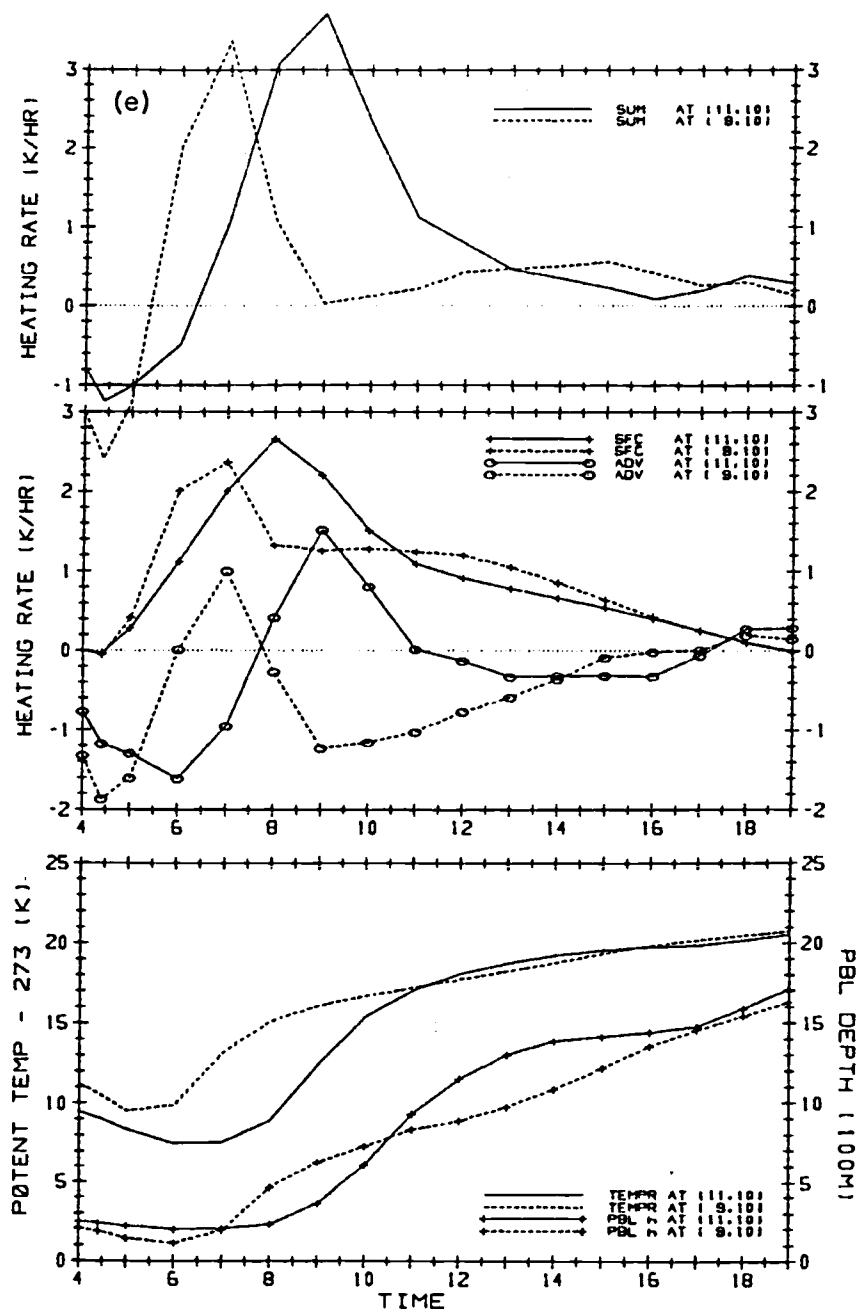
Fig. 6.29e. As in Fig. 6.29a except for grid points (9,10) and (11,10) where sharp increases in θ are seen in the morning.
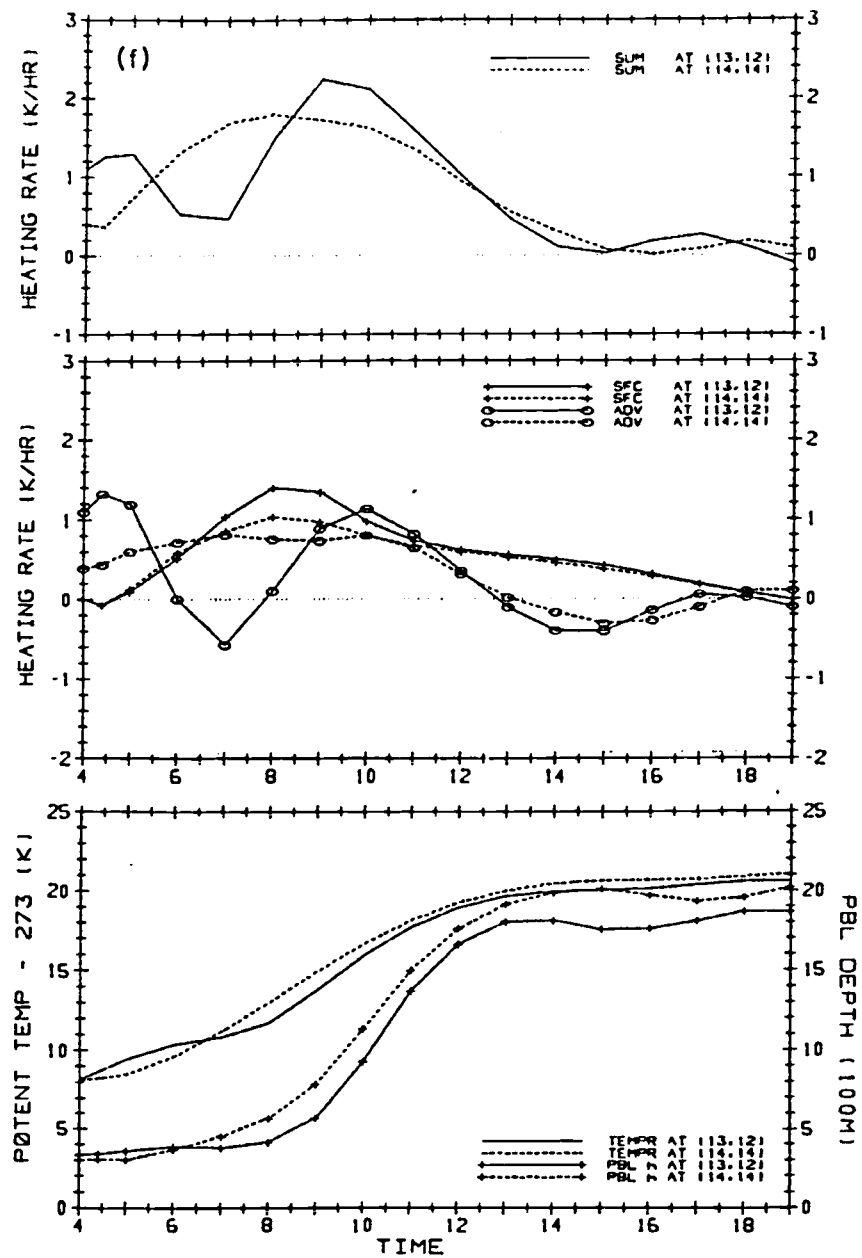
Fig. 6.29f. As in Fig. 6.29a except for grid points (13,12) and (14,14) on the downwind side of the primary hill.

6.5 hrs detected in the wavy patterns of advective heating rates at many points might be associated with the gravity waves generated by initial imbalance in pressure-gradient and the Coriolis-force fields. However, it is thought that an explanation given earlier seems more feasible.

On the other hand, the effects of advective warming further downstream in the interior regions of lower elevation are more uniform and fluctuate less throughout the day, as shown in Fig. 6.29b and f for points (5,6) and (14,14), respectively. This causes the increase of θ_M and h to be more gradual and smooth.

We will next discuss the evolutions of θ obtained from the L7 experiment. The fields of θ for the layer $\ell = 7$ of L7 are illustrated in Fig. 6.30. By comparing them with those for the mixed layer of M4 in Fig. 6.24, we notice that the spatial distributions of θ are in general quite similar in both cases. However, the region of the coldest air in the early morning in L7 is now concentrated at the western edge, instead of the northeast corner, of the primary basin, and right over the weak-wind pocket. The cool-air pool remains in the bottom of the basin during the morning, and slightly downwind of the region of weak winds during midday, but it is less influenced by advective effects than in the case of M4 even in the late afternoon. The domain-averaged θ for the lowest layer of L7 is slightly higher than that of M4 for most of the day. This is because in the M4 model the whole depth h of the mixed layer, which gradually increases with time, is assumed to warm up uniformly, while in the case of L7 the thickness of the layer $\ell = 7$ remains approximately uniform (~100 m) through which

Fig. 6.30a. Fields of θ - 273 (k) for layer 7 of L7 at designated hours. The contour interval is 1 K for 05 and 07, and 0.5 K for 09 and 1100 LST.
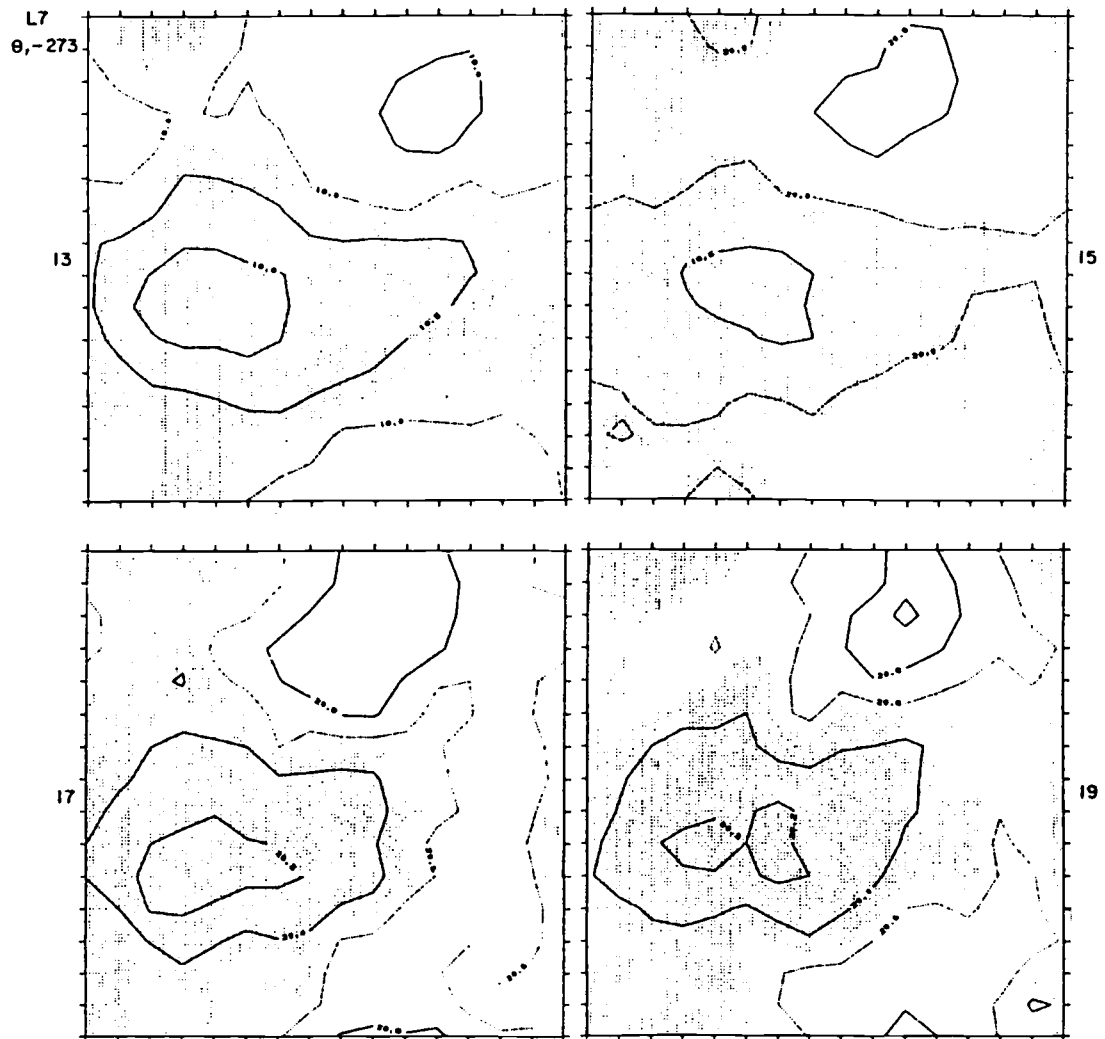
Fig. 6.30b. As in Fig. 6.30a except that the contour interval is
             0.5 K for 13 and 15, and 0.2 K for 17 and 1900 LST.

sensible heat from the ground surface must be transported upward by turbulent diffusion. The fields of θ for the layer $\ell = 6$ of L7, shown in Fig. 6.31, closely resemble those for the lowest layer except during the early morning (before 0900) when this layer is still in the free atmosphere. This indicates that θ is vertically well-mixed in the lowest two layers after ~0900. The evolution of the θ field in the layer $\ell = 5$ is quite similar to that of the layer $\ell = 6$. Consequently, the fields of the vertical mass-weighted average of θ below the diagnosed mixed-layer top, $h + h_s$, as depicted in Fig. 6.32, are virtually identical to those of the lowest layer before 0900, and from 0900 on they greatly resemble those for both layers $\ell = 6$ and 7.

6.8 Surface Sensible Heat Flux

The fields of the surface sensible heat flux H_s for L7 are shown in Figs. 6.33a and b, which are found to be nearly identical to those for M4 (not shown). As in a previous study (DUH, 1984), we find that the spatial variations in H_s are positively correlated with those in wind speed $|\underline{V}_7|$, as depicted in Fig. 6.33c for 1100, while a strong negative correlation exists between $|\underline{V}_7|$ and $\theta_s - \theta_{\ell=7}$, where θ_s is the ground-surface potential temperature. This result is demanded by the surface energy balance. This negative correlation in turn results in variations of the bulk Richardson number Ri_B [Eq. (3.14)] in the lowest layer which are positively correlated with variations in $\theta_s - \theta_{\ell=7}$. The bulk heat transfer coefficient C_H, which is a function of Ri_B, then reflects the stability of air near the ground surface, as shown in Fig. 6.33c,
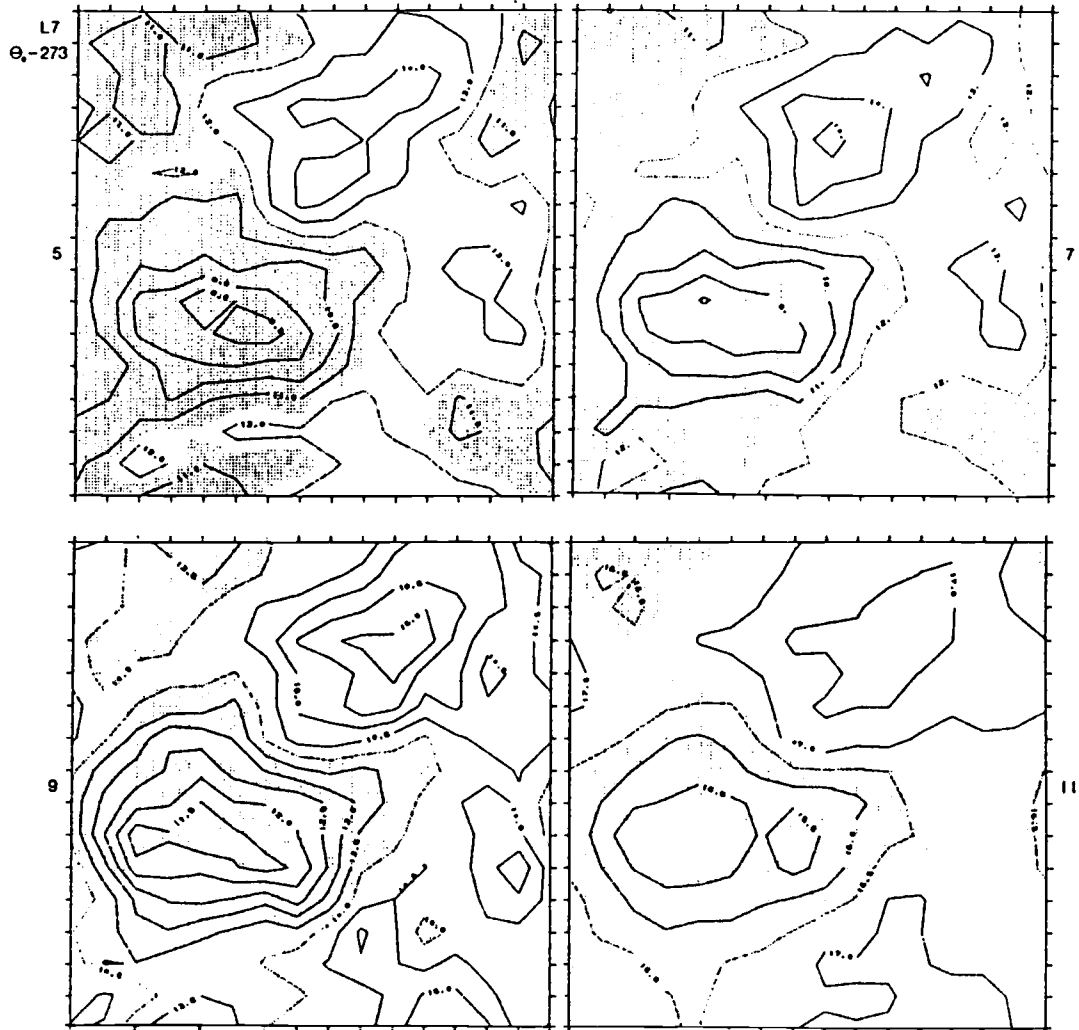
Fig. 6.31a. Fields of θ-273 (K) for layer 6 of L7 at designated hours. The contour interval is 1 K for 05 and 07, and 0.5 K for 09 and 1100 LST.
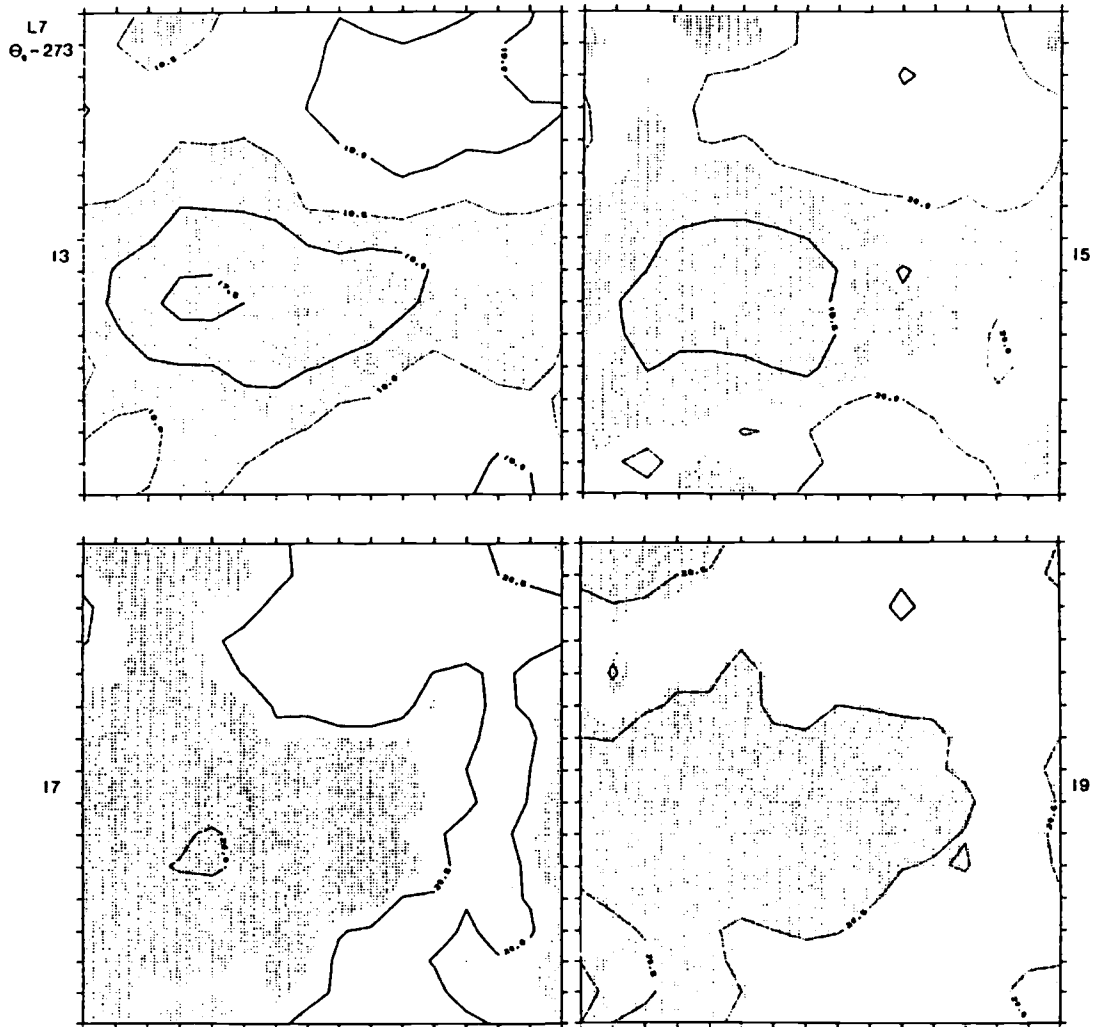
Fig. 6.31b. As in Fig. 6.31a except   that the contour interval is
0.5 K for all hours.
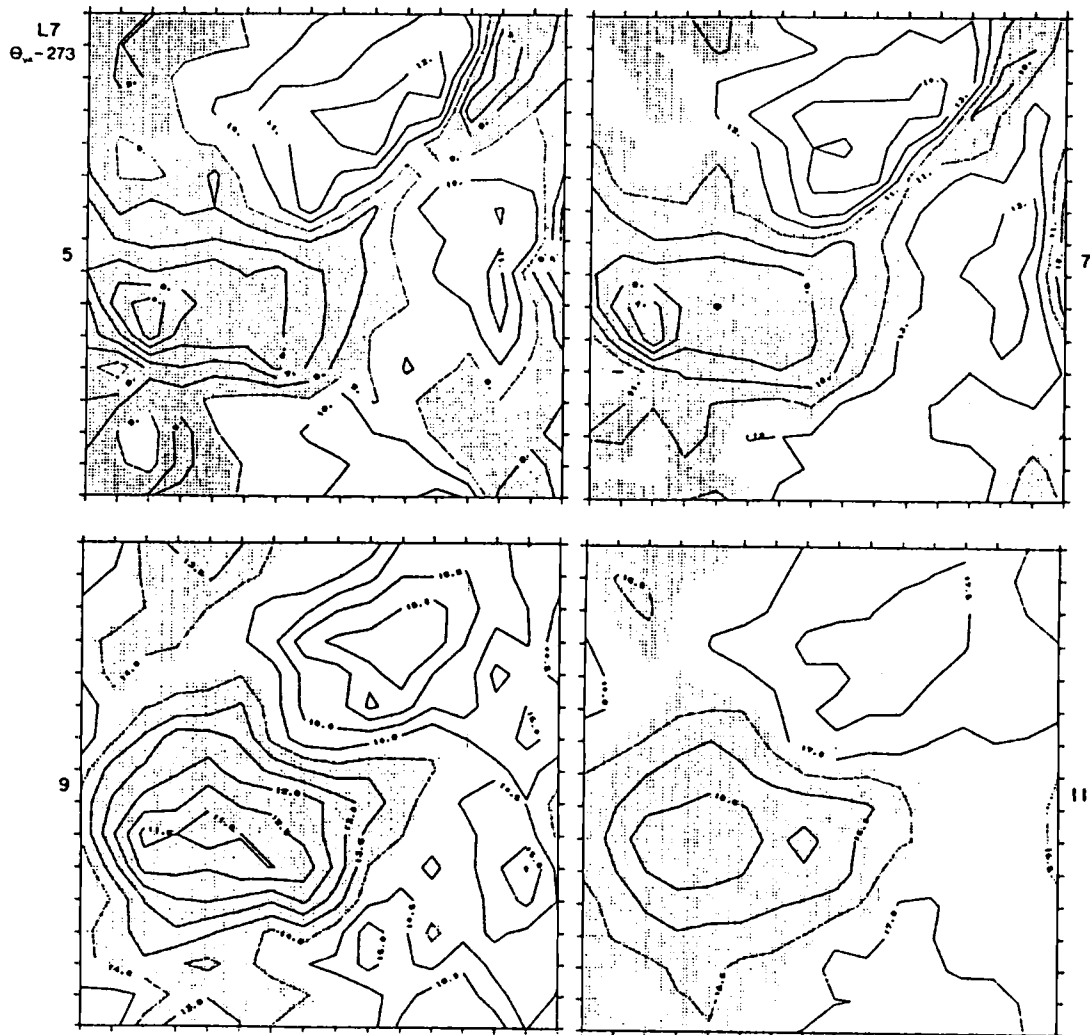
Fig. 6.32a. Fields of the vertically averaged mixed-layer θ-273 (K) for L7 at designated hours. The contour interval is 1 K for 05 and 07, and 0.5 K for 09 and 1100 LST.
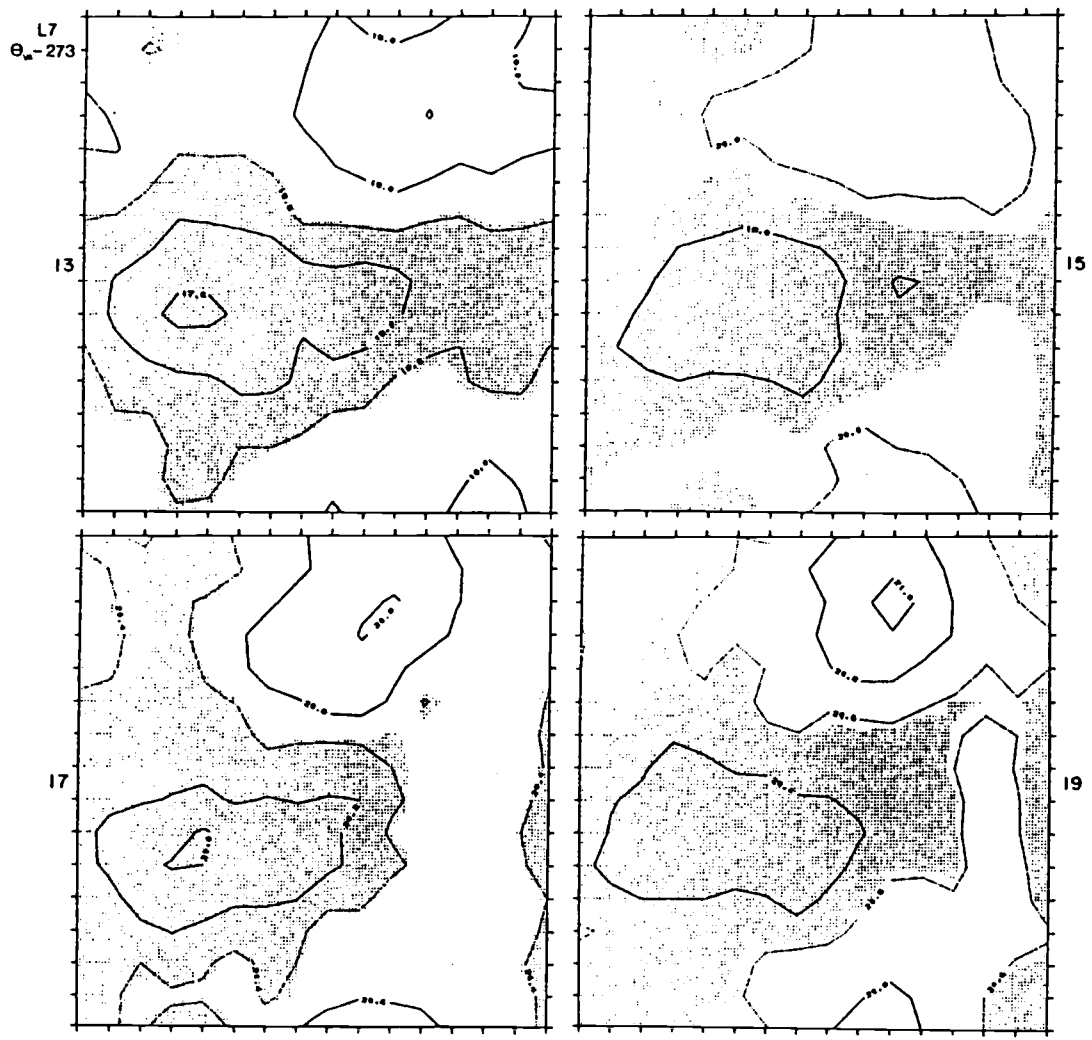
Fig. 6.32b. As in Fig. 6.32a except that the contour interval is
0.5 K for all hours.
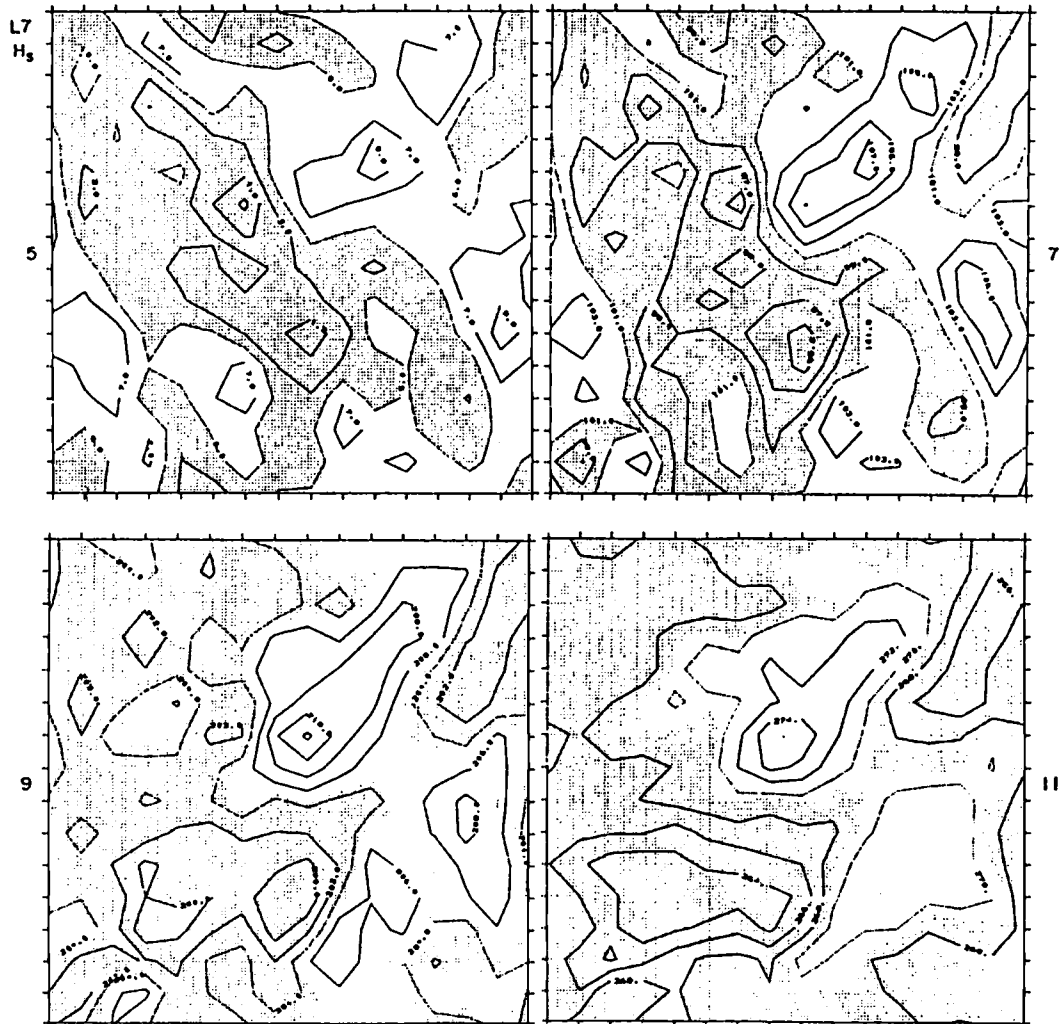
Fig. 6.33a. Fields of surface heat flux H_s for L7 at 05, 07, 09 and 1100 LST. The contour interval is watts m^{-2}. Shaded areas denote below-average values.

Fig. 6.33b. As in Fig. 6.33b except for 13, 15, 17 and 1900 LST.
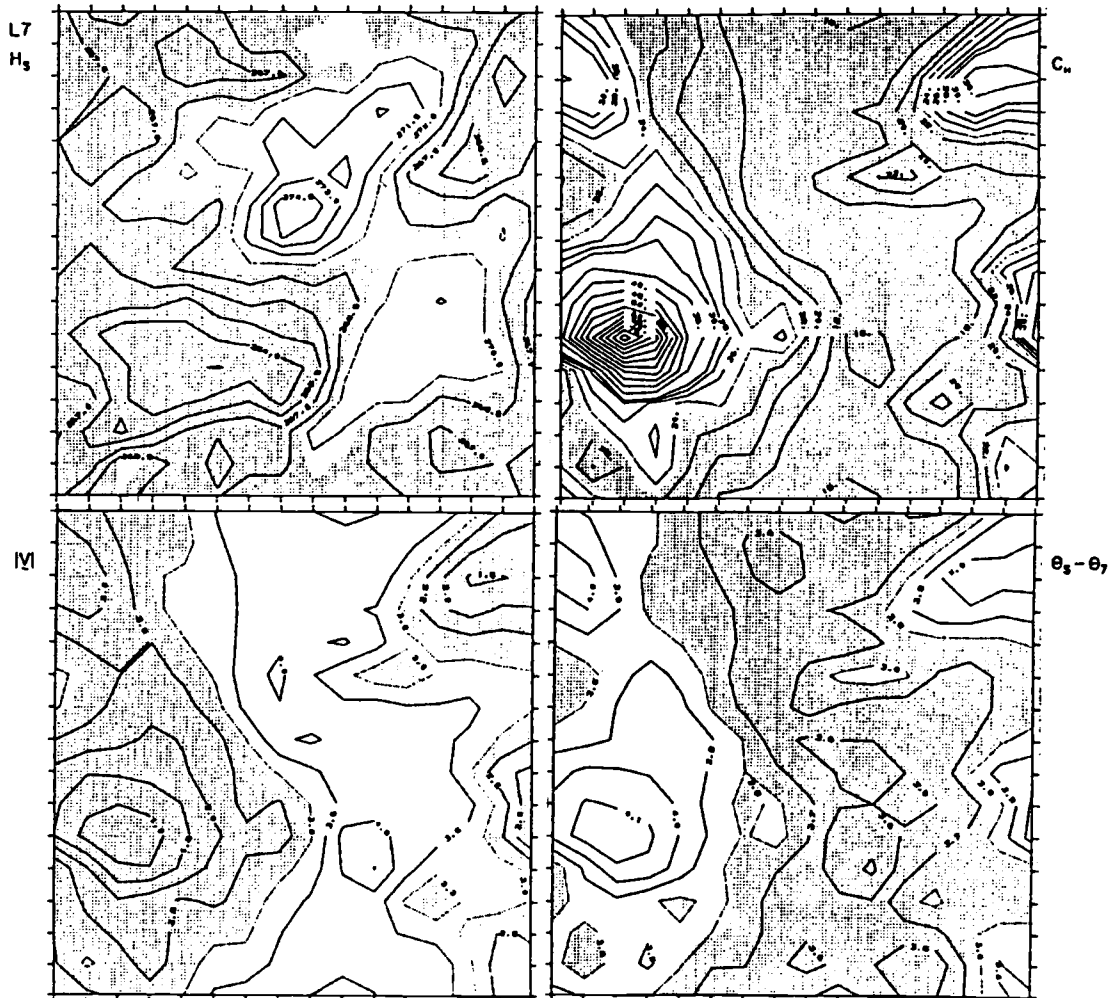
Fig. 6.33c. Fields of H_s, C_H, $|\underset{\sim}{V}_{\ell=7}|$, $\theta_s - \theta_7$ for L7 at 1100 LST. The contour intervals and units are 1.5 (watts m^{-2}) for H_s; 2 ($\times 10^{-3}$) for C_H below 30 and 5 ($\times 10^{-3}$) above 30; 0.5 (ms^{-1}) for $|\underset{\sim}{V}_{\ell=7}|$, and 0.1 (K) for $\theta_s - \theta_7$.

and indicates a strong positive correlation with $\theta_S - \theta_{\ell=7}$. The perturbations in wind speed are then responsible for the small spatial variations of H_S. H_S is generally smaller over the lower elevations and larger over the higher terrain, but these spatial variations are found to be much smaller compared to those obtained in our previous study (see Fig. 10 of DUH, 1984) in which a constant C_H was used. This is because the negative correlation between variable C_H and $|\underset{\sim}{V}_7|$ tends to reduce the spatial variation of the quantity $C_H|\underset{\sim}{V}_7|$, and thus reduces the spatial variation of H_S computed using the formula given by Eq. (4.20). Unlike in the case with constant C_H, the fields of $\theta_{\ell=7}$ then do not reflect this small variations in H_S; rather they are more strongly associated with spatial variations of h and with advective effects.

6.9 Fields of $h + h_S$, w_e and $\Delta\theta$

A description of w_e and $\Delta\theta$ has been given in DUH (1984), which also applies to the results for M4 presented here. The relationships among various quantities are best expressed in the form of correlation coefficients among them, as plotted in Fig. 6.34a. The fields of the discontinuity $\Delta\theta$ at the mixed-layer top is depicted in Fig. 6.35 for M4. A high negative correlation between $\Delta\theta$ and θ_M during the morning results from $\Delta\theta$ initially being the difference between the relatively uniform value of θ^+ just above the mixed-layer top and the much more variable θ_M. This uniform θ^+ is caused by the relatively smooth mixed-layer top $h + h_S$, as presented in Fig. 6.37, and horizontally nearly uniform θ aloft. Therefore, as shown in Fig. 6.36, the entrainment rate
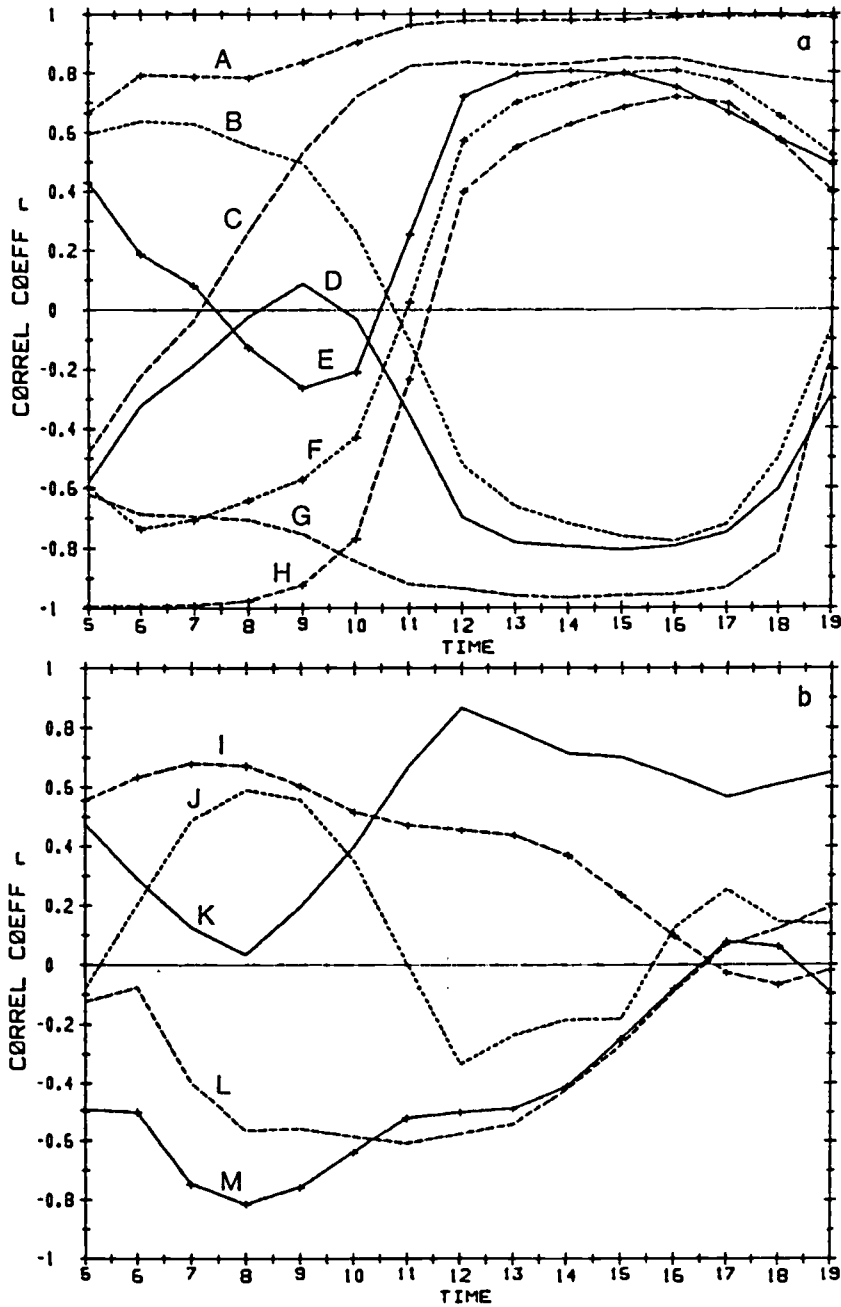
Fig. 6.34. Evolutions of correlation coefficients among various quantities. "*" is used below to indicate correlation. Figure (a) shows (A): θ_M * h + h_s, (B): w_e * h + h_s, (C): θ_M * h, (D): w_e * h, (E): $\Delta\theta$ * h, (F): $\Delta\theta$ * h + h_s, (G): $\Delta\theta$ * w_e, (H): $\Delta\theta$ * θ_M. Figure (b) illustrates (I): $-V_M \cdot \nabla\theta_M$ * h, (J): $\delta h/\delta t$ * w_e, (K): $-\nabla \cdot (hV_M)$ * $\delta h/\delta t$, (L): $-\nabla \cdot (hV_M)$ * w_e, (M): $-V_M \cdot \nabla\theta_M$ * $-\delta H/\delta z$.
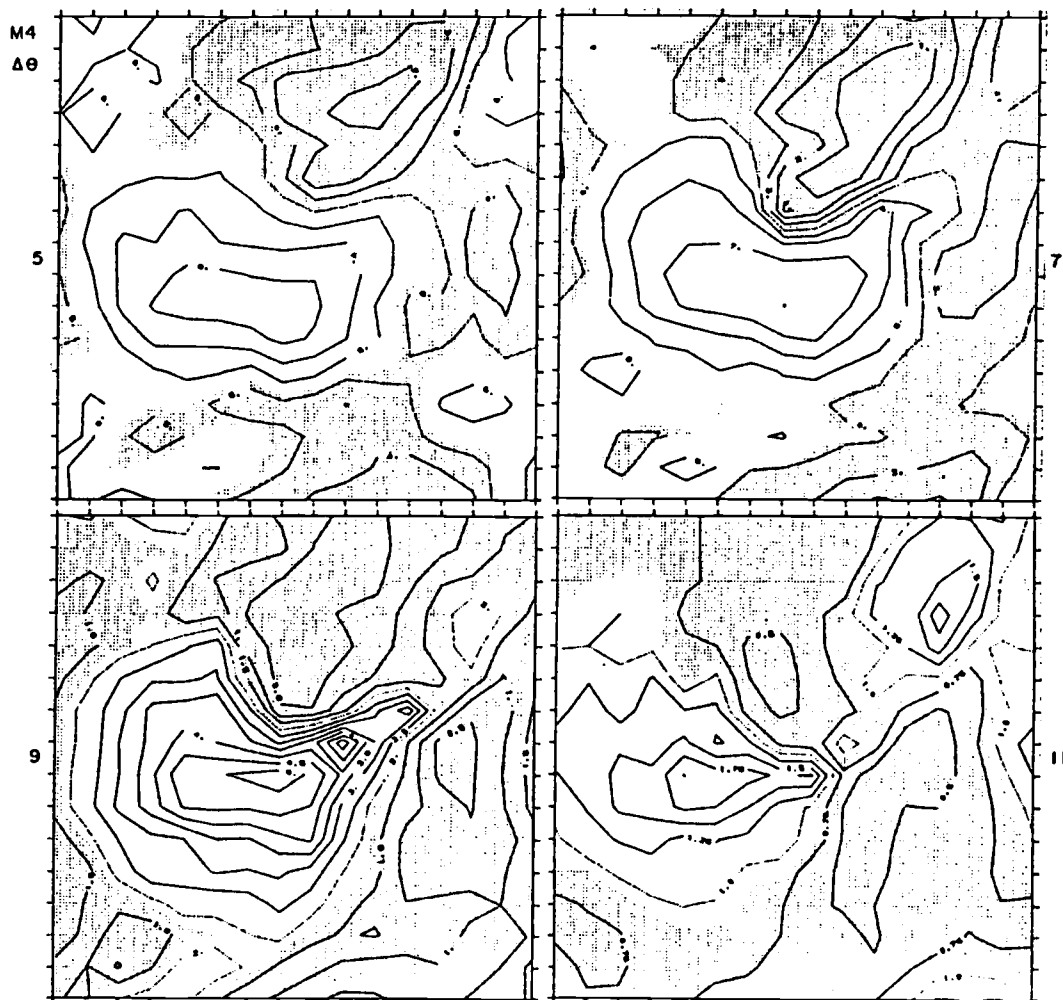
Fig. 6.35a. Fields of potential temperature discontinuity Δθ (K) at the mixed-layer top for M4 at 05, 07, 09 and 1100 LST. Shaded areas denote below-average values. The contour interval is 1 K for 05 and 07, 0.5 K for 09, and 0.25 K for 1100 LST.
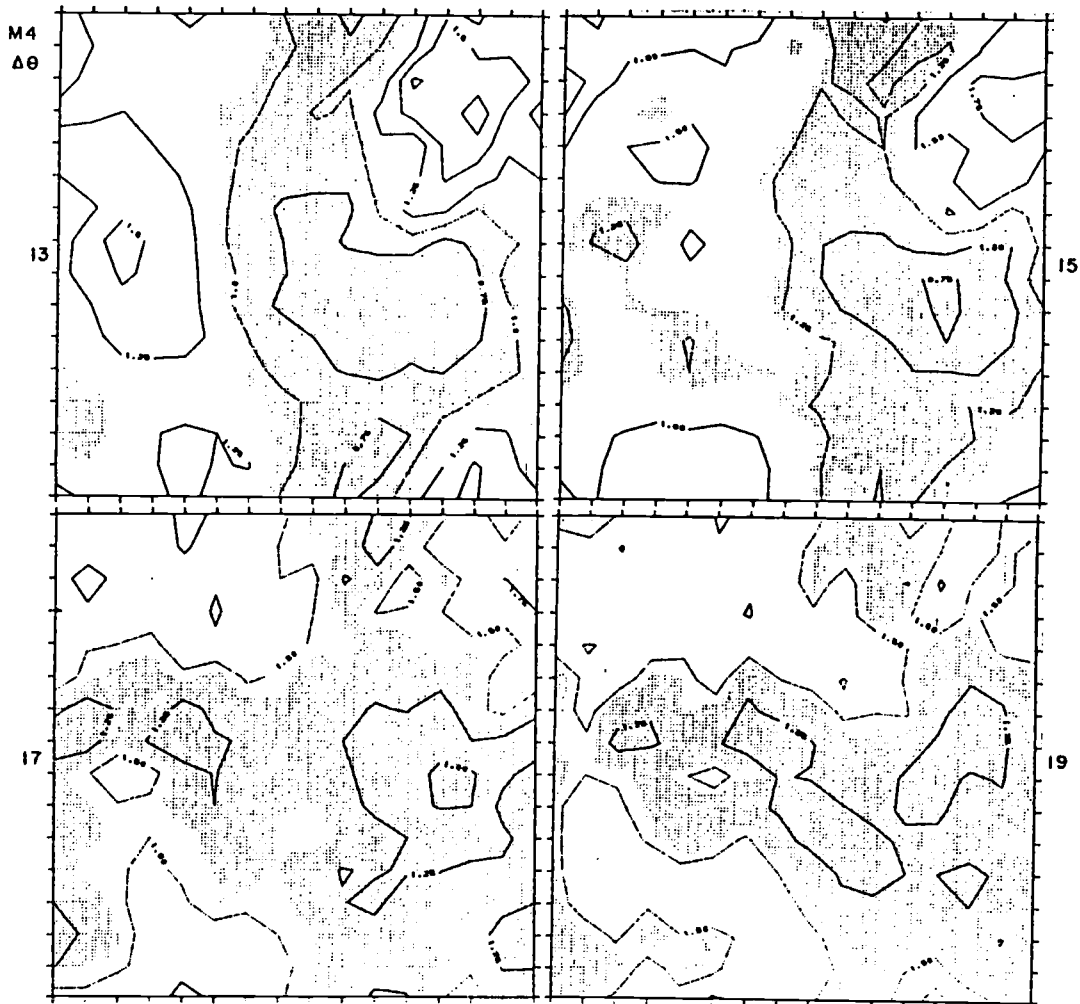
Fig. 6.35b. As in Fig. 6.35a except for 13, 15, 17 and 1900 LST. The contour interval is 0.25 K for all hours.
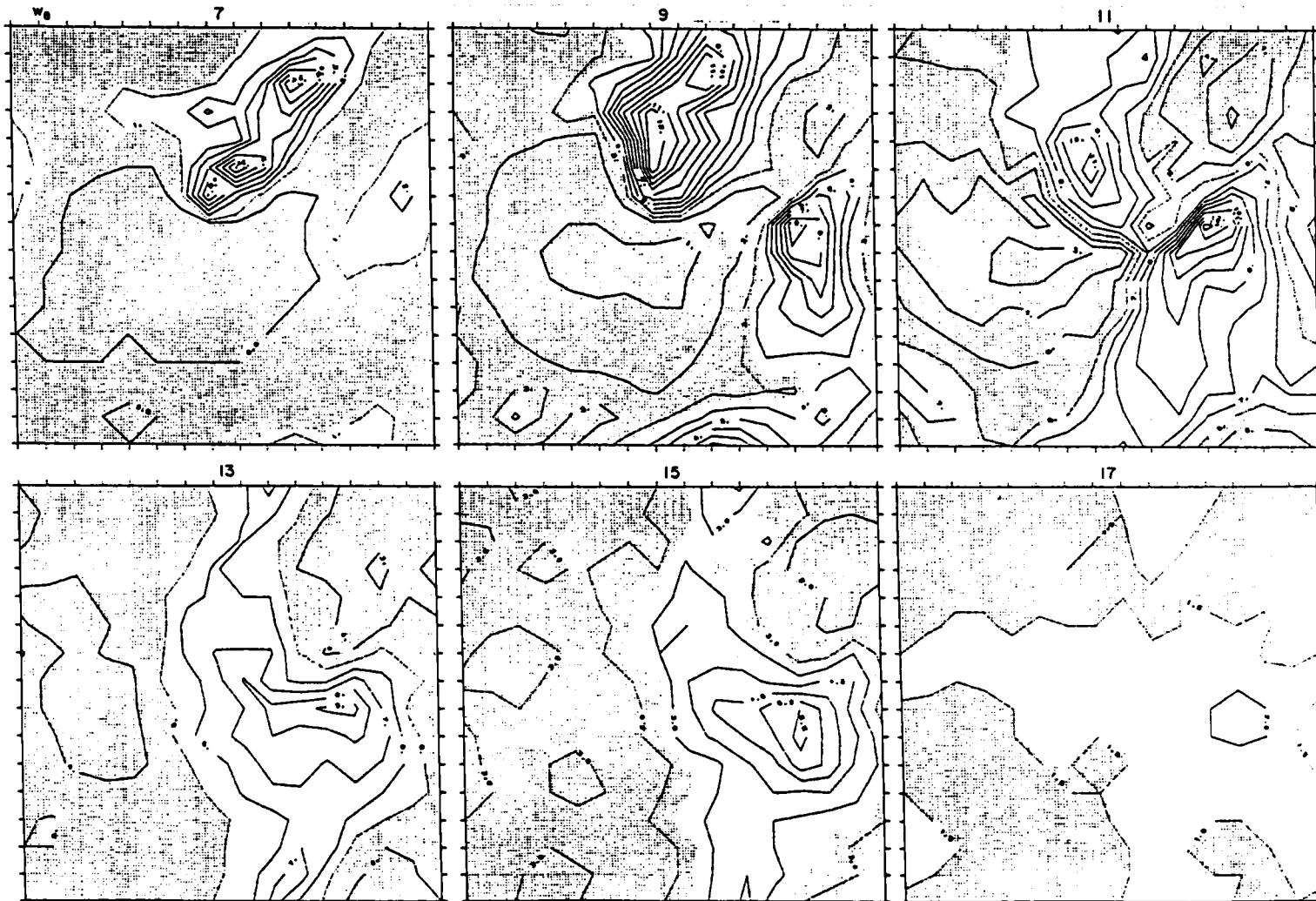
Fig. 6.36. Fields of entrainment rate w_e (cm s^{-1}) for M4 at designated hours. Shaded areas denote below-average values. The contour interval is 1 cm s^{-1} for 07, 09, 1100 LST, and 0.5 cm s^{-1} for 15 and 1700 LST.
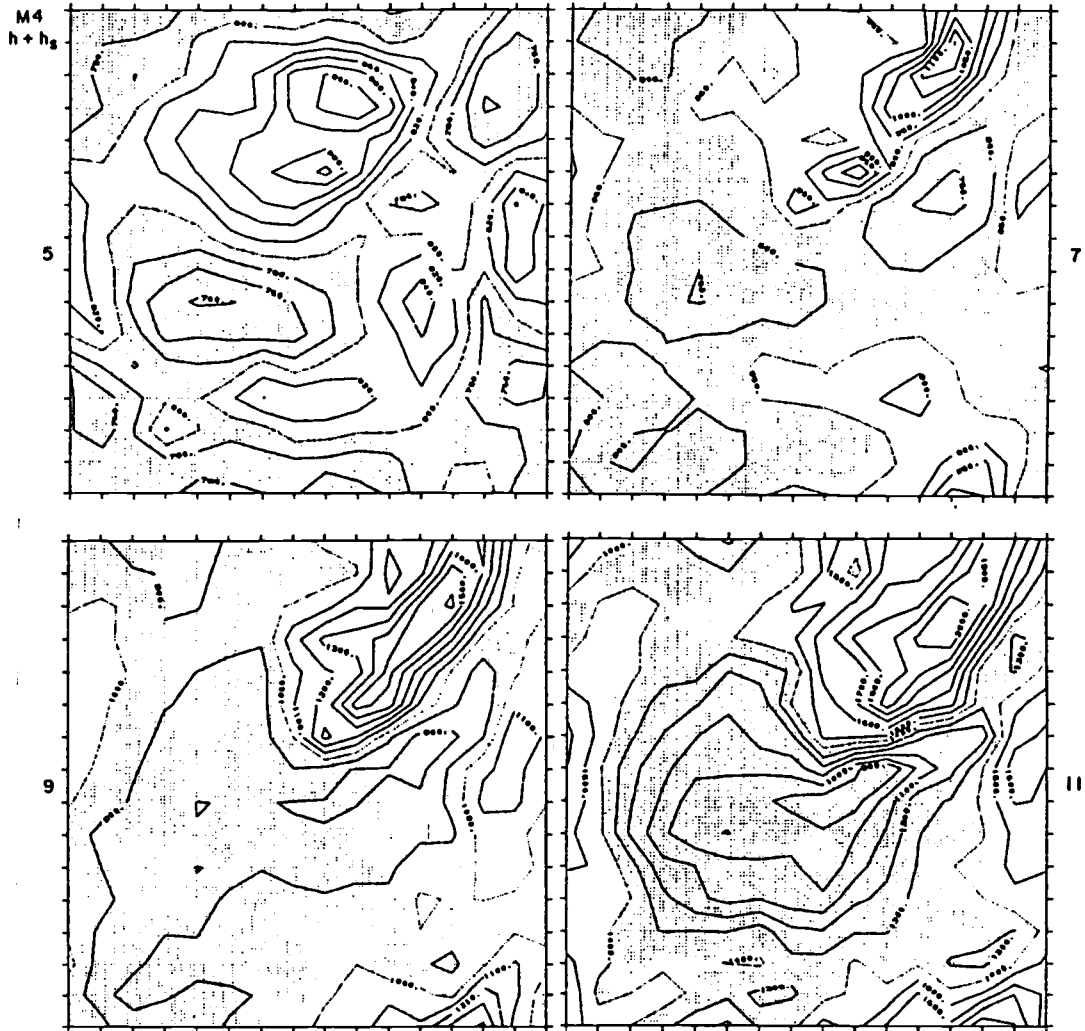
Fig. 6.37a. Fields of the mixed-layer top height h + h$_s$ (m) for M4 at 05, 07, 09 and 1100 LST. Shaded areas denote below-average values. The contour interval is 20 m for 05, 50 m for 07, and 100 m for 09 and 1100 LST.
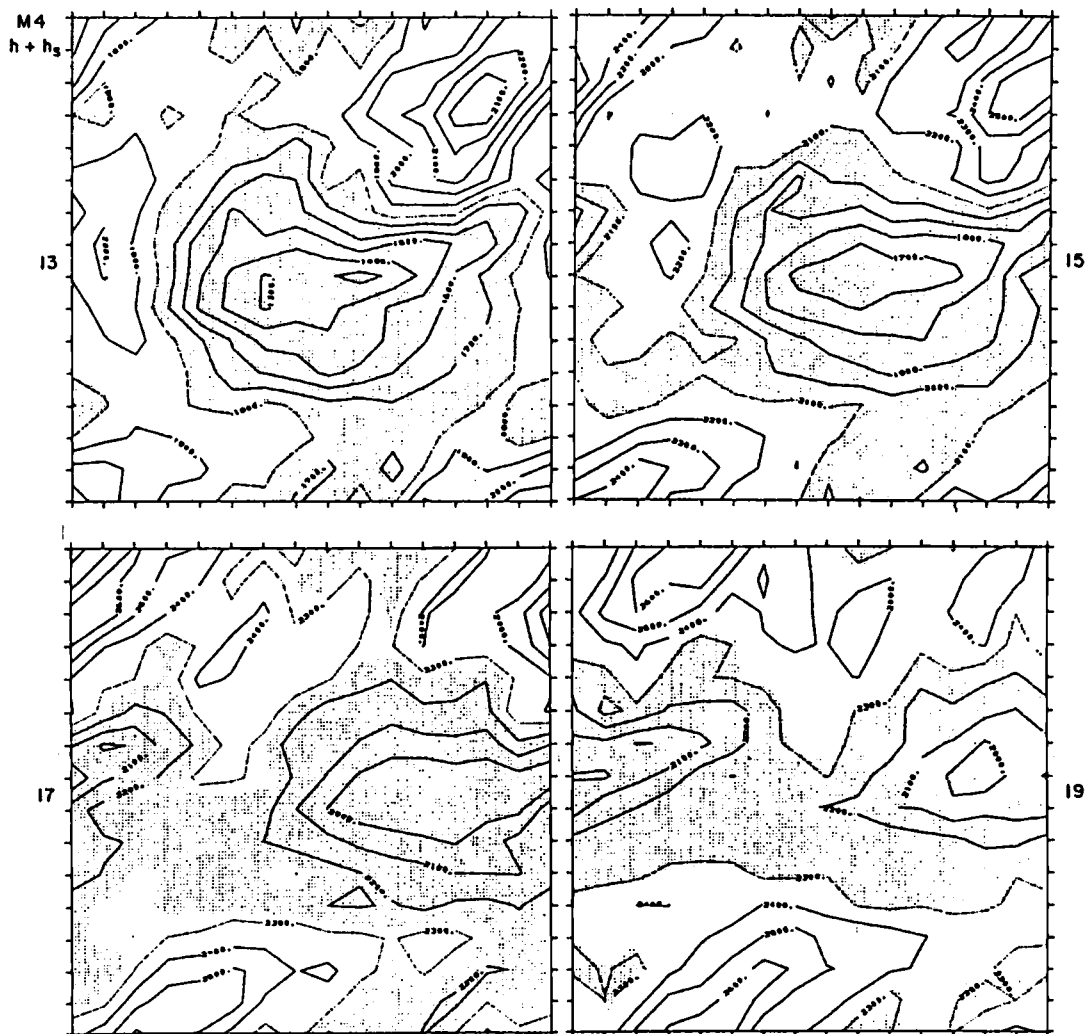
Fig. 6.37b. As in Fig. 6.37a except for 13, 15, 17 and 1900 LST.
The contour interval is 100 m for all hours.

w_e during the morning is much greater over the elevated terrain where θ_M is larger and h smaller than at the lower elevations where θ_M is smaller and h deeper (for the fields of h, see Fig. 3.28). This results in a faster increase of $h + h_s$ over the higher terrain. Hence, the initially negative correlation between h and θ_M has reversed to become a high positive correlation by ~0900. In the process the regions of smaller h have become associated with those of larger horizontal gradients of θ_M between 0700 and 0900, so as to cause a higher positive correlation between the areas of smaller h and stronger advective cooling, and hence a strong positive correlation between heating rate due to direct H_s and advective cooling.

The field of $h + h_s$, which was in general positively correlated with θ_M at 0500, is also positively correlated with w_e during early morning. Thus, a faster increase of $h + h_s$ results where θ_M is larger. However, this positive correlation between $h + h_s$ and w_e has reversed to become a negative one by 1100; as h and hence $h + h_s$ increases and the horizontal variation of θ_M becomes smaller, the spatial variation of $\Delta\theta$ now mainly results from irregularities of $h + h_s$ and relatively uniform fields of θ_M. Therefore, the areas of larger $h + h_s$, although θ_M is also relatively large there, have become associated with those of larger $\Delta\theta$. Hence, the areas of larger $h + h_s$ have become associated with smaller w_e after 1100. This contributes to a reduction of spatial irregularities of $h + h_s$ in the late afternoon.

On the other hand, the initially strong positive correlation

·between h and $\Delta\theta$ has quickly diminished to become negative by 0800. This is because deeper h has become associated with greater θ_M as h grows rapidly, while where θ_M is greater $\Delta\theta$ is still smaller at this time. After 1100 this negative correlation reverses itself to become positive again because now the areas of larger θ_M are associated with those of larger $\Delta\theta$, while θ_M and h are highly positively correlated. The correlation between h and w_e is approximately a mirror image of that between h and $\Delta\theta$ because w_e and $\Delta\theta$ are highly negatively correlated.

It is seen that the pattern of $h + h_S$ as well as of h established by 1100 persists until late afternoon while being translated slowly eastwards. It is therefore likely that in addition to the direct effect of w_e the influence of mass flux convergence expressed as the first term on the right side of Eq. (6.1a), in which the advective effect on h is implied, must play a major role in shaping the patterns of $h + h_S$, particularly over the leeward sides of the major hills where the flows seem to converge during the morning hours.

The overall patterns of $h + h_S$ for L7, shown in Fig. 6.38, resemble fairly well those for M4 between 0900 and 1500, during which H_S (and hence the turbulent vertical mixing within the mixed layer) is most strong, considering that totally different procedures have been used to obtain h for these two models (see Section 3.3). Although the fields of $h + h_S$ for L7 are spatially less smooth owing to the coarse vertical-grid resolution which could cause wide fluctuation of estimated Ri and potential temperature profiles, their qualitatively fair agreement indicates that the scheme used in
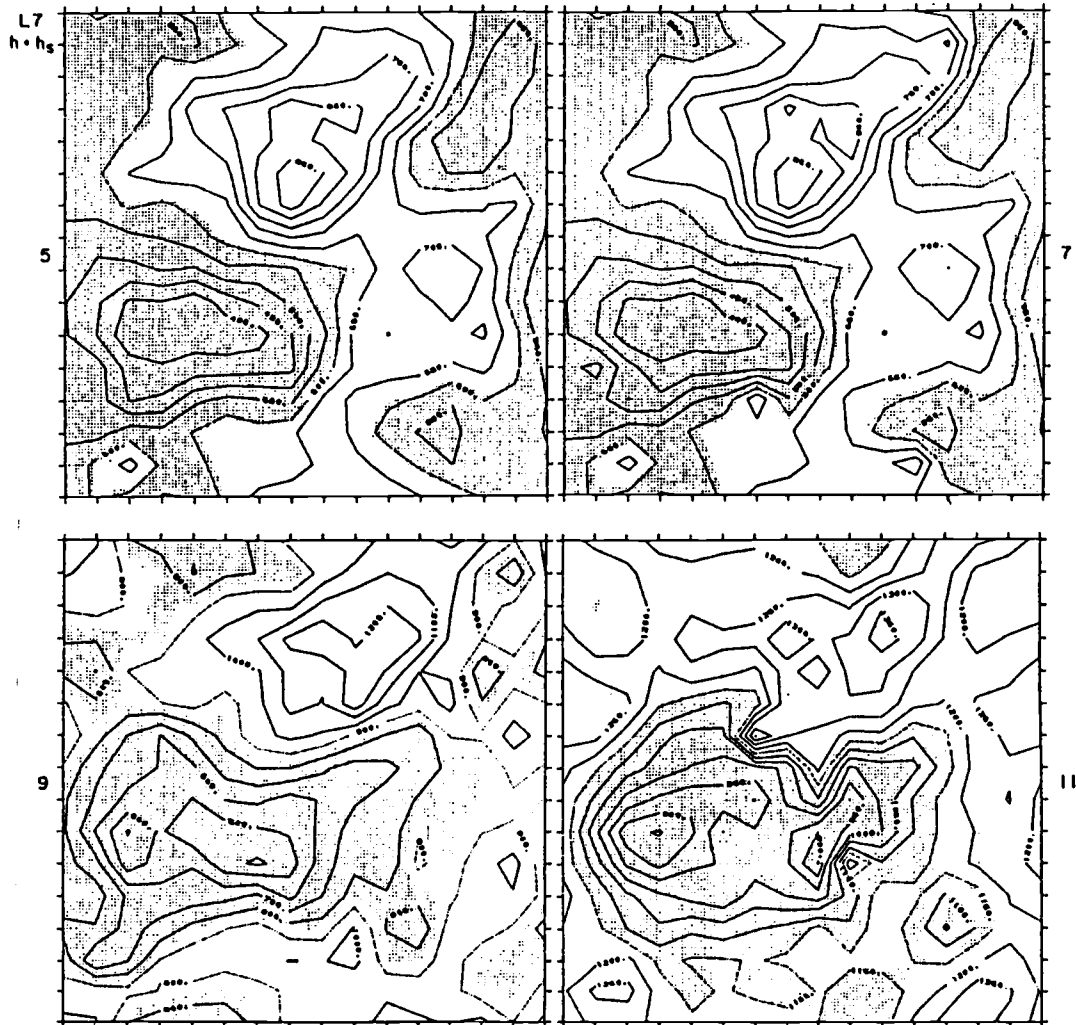
Fig. 6.38a. As in Fig. 6.37a except for L7. The contour interval is
50 m for 05, 07 and 1100 LST, and 100 m for 0900 LST.
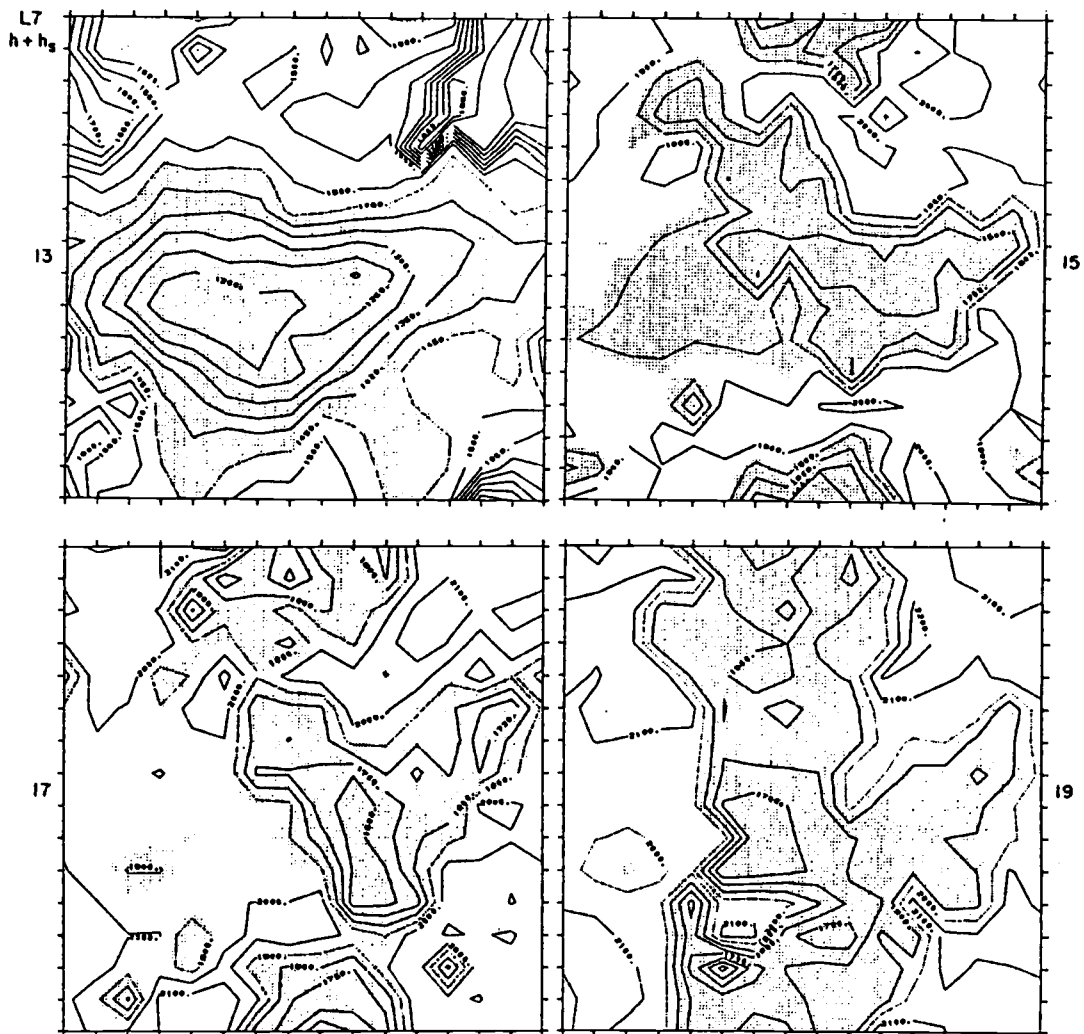
Fig. 6.38b. As in Fig. 6.37b except for L7. The contour interval is
50 m for 13, 100 m for 15, 17 and 1900 LST.

the L7 model is a reasonable alternative to a direct and explicit prediction of h when the latter is not feasible in a model such as our L7 model.

6.10 Regions of Mass Flux Convergence

The occurrence of a region of convergence to the downwind side of mountains has been described by, for example, Banta (1984) who studied observed data obtained in South Park, a broad, relatively flat basin in the Colorado Rocky Mountains. He suggested that the convergence zone occurs at the upwind edge of a cool air pool in a mountain valley, and is an important mechanism for the initiation of mountain-generated cumulus clouds. In this section we examine the horizontal evolution of mass flux convergence for M4 as computed using the form $-\nabla \cdot (h\underline{V}_M)$ given in (6.1a) as a first approximation to the corresponding term in Eq. (2.20a). The fields of $-\nabla \cdot (h\underline{V}_M)$ are depicted in Fig. 6.39. Correlation coefficients between terms in Eq. (6.1a) are also plotted in Fig. 6.34b.

We see in Fig. 6.34b that from early to midmorning w_e is a dominant factor in shaping the patterns of $h + h_s$ (curves J and K), while the influence of $-\nabla \cdot (h\underline{V}_M)$ decreases as w_e intensifies. However, the correlation of w_e with $\partial h / \partial t$ declines after 0800 and becomes negative after 1100 and stays so until 1500, while the effect of $-\nabla \cdot (h\underline{V}_M)$ increases steadily after 0800 and is strongly in positive correlation with $\partial h / \partial t$ throughout the afternoon. The correlation between w_e and $-\nabla \cdot (h\underline{V}_M)$ are negative for most of the day, i.e., where entrainment is strong mass flux divergence is also strong. Therefore, the negative correlation of
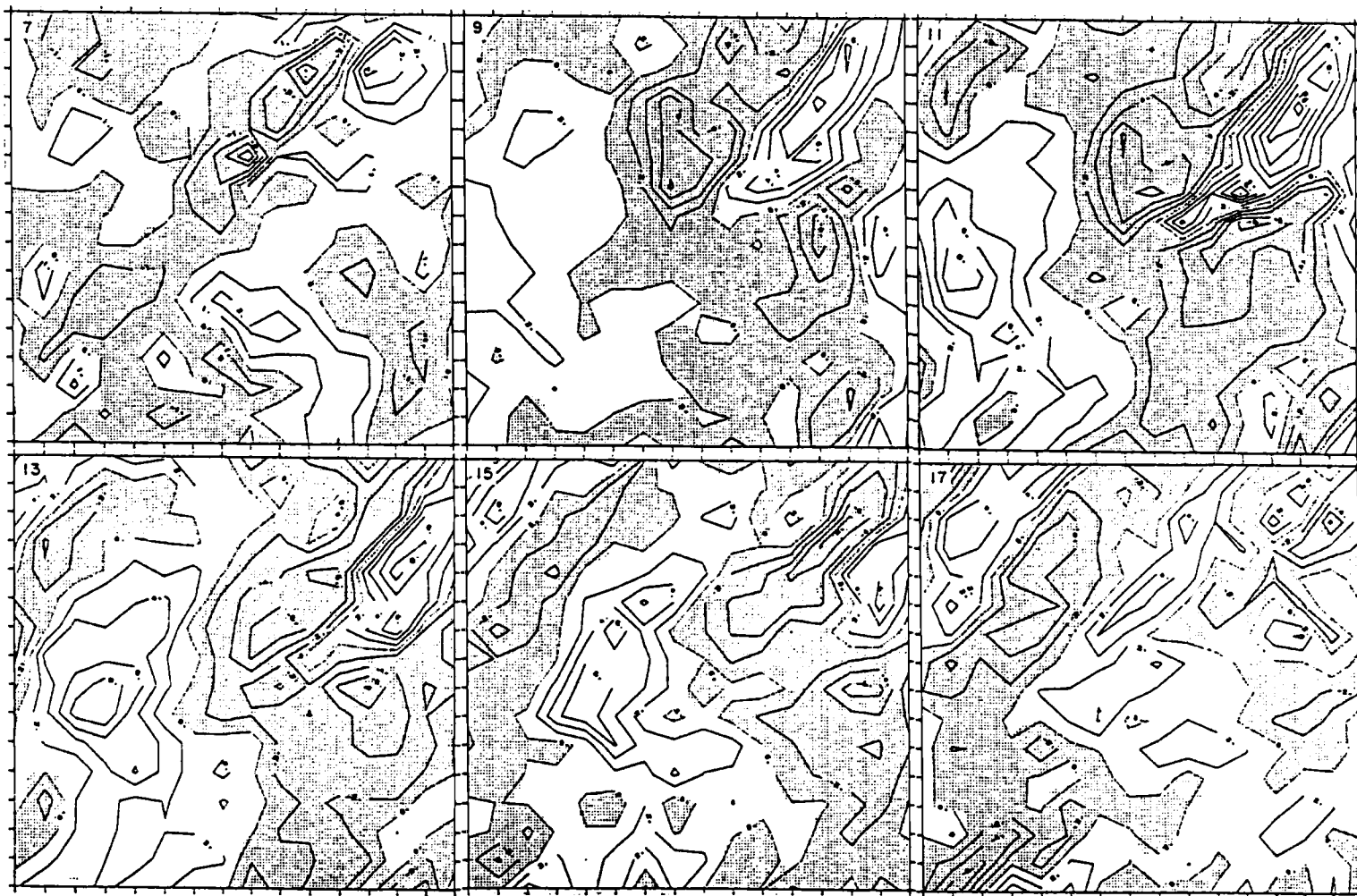
Fig. 6.39. Fields of mass flux convergence $-\nabla \cdot (h V_M)$ for the mixed layer of M4 at designated hours. The unit is 10^{-8}cm s^{-1}, the contour interval is 1 for 07 and 2 for other hours. Shaded areas denote below-average values.

w_e with $\partial h/\partial t$ after 1100 suggests that the overall spatial irregularities of $h + h_s$ should become less pronounced during the afternoon as far as the effect of w_e is concerned.

In Fig. 6.39 the regions of relatively strong mass flux convergence are seen to have developed by 0900 over the downwind slopes of major hills. This is a consequence of higher $h + h_s$ caused by larger w_e over the ridgetop to the west of a convergence zone, enhanced by the resulting spatial deceleration of $\underline{V}_M$ as air flows down the leeward slopes. However, the overall pattern of $h + h_s$ is still dictated by that of w_e at this hour. By early afternoon $h + h_s$ has become highest in the areas east of the regions where w_e is relatively strong but slightly west of the regions where mass flux convergence is strongest, i.e., over the leeward slopes of the primary ridge and the secondary hill. Meanwhile, the overall patterns of $h + h_s$ and $-\nabla \cdot (h\underline{V}_M)$ are seen to shift gradually eastwards, while the correlation between $-\nabla \cdot (h\underline{V}_M)$ and $\partial h/\partial t$ is strongly positive and peaks at 1200. On the other hand, the patterns of w_e and $\partial h/\partial t$ have become negatively correlated after 1100. Particularly, w_e is relatively small in the northeast corner of the domain where $h + h_s$ is largest. This suggests that mass flux convergence is playing an equally important role in shaping patterns of $h + h_s$ during midday. It is noted that there are spots where h may be decreasing owing to local dominance of mass flux divergence in the afternoon, such as at grid points (7,11) and (14,14) shown in the bottom panels of Figs. 6.29d and f, respectively.

6.11 Cross Sections of Potential Temperature

In this section the evolution of the mixed-layer structure as revealed by cross sections of potential temperature is presented. Shown in Fig. 6.40 are the vertical cross sections of θ for M4 along the diagonal line segment "A" connecting the grid points (1,3) and (14,1) on the west and north boundaries, respectively (see Fig. 5.1). Since we have used the cyclic lateral boundary conditions, the part of the cross section connecting points (14,1) and (1,3) on the south and east boundaries, respectively, shows up on the right end of each figure. For the vertical coordinate pressure (mb) in a log scale is used. The cross sections are shown up to 700 mb since above this level there are little appreciable perturbations in θ. The horizontal distance between two grid points is 14.1 km, and the solid curve near the bottom of the figure indicates the height level of the ground surface. Potential temperatures are shown in units of θ - 273 K. The mixed-layer top, which is also indicated by a solid curve, is located where approximately horizontal isentropes in the free atmosphere turn downward to the ground surface. Since we assumed that θ_M is vertically well-mixed in M4, isentropes are vertical in the mixed layer. In the free atmosphere θ was interpolated linearly in P [see Eq. (2.25)], while at the top of the mixed-layer the discontinuity $\Delta\theta$ was taken into account. The plane of the cross section approximately passes through the regions of weak winds and cool air, and through the peak of the primary hill as well as its ridgetop extending downwind toward the northeast. The terrain slopes are approximately 0.01 and 0.003 on the windward and leeward slopes of

Fig. 6.40. Vertical cross sections of θ - 273 (K) for M4 along the
line segment "A" in Fig. 5.1 at designated hours.
Isentropes are drawn at 0.5 K intervals. The numbers
along the abscissa denote the grid indices along the
x-axis in Fig. 5.1, and the grid interval is 14.1 km.
The solid curve closest to the abscissa indicates the
round surface height h_s. $h + h_s$ is also shown by a
solid curve above the ground surface. The letters "W"
and "K" denote the warmer and cooler regions, respectively.
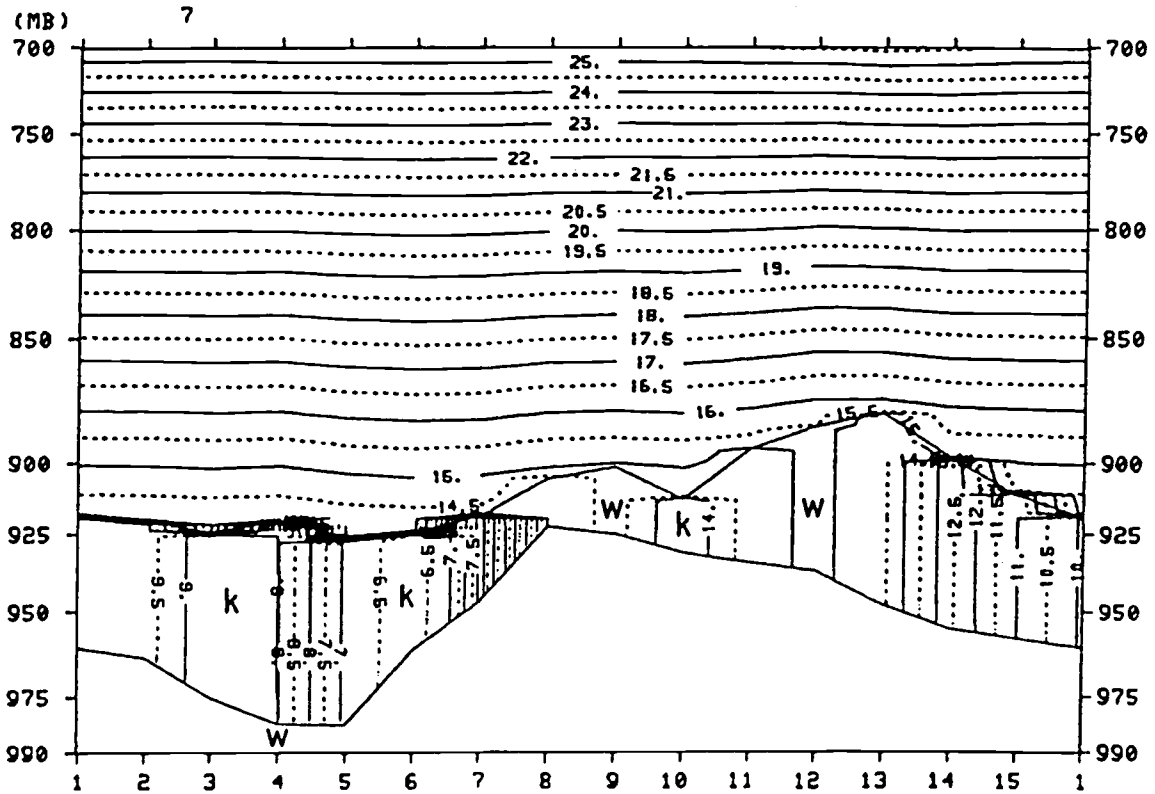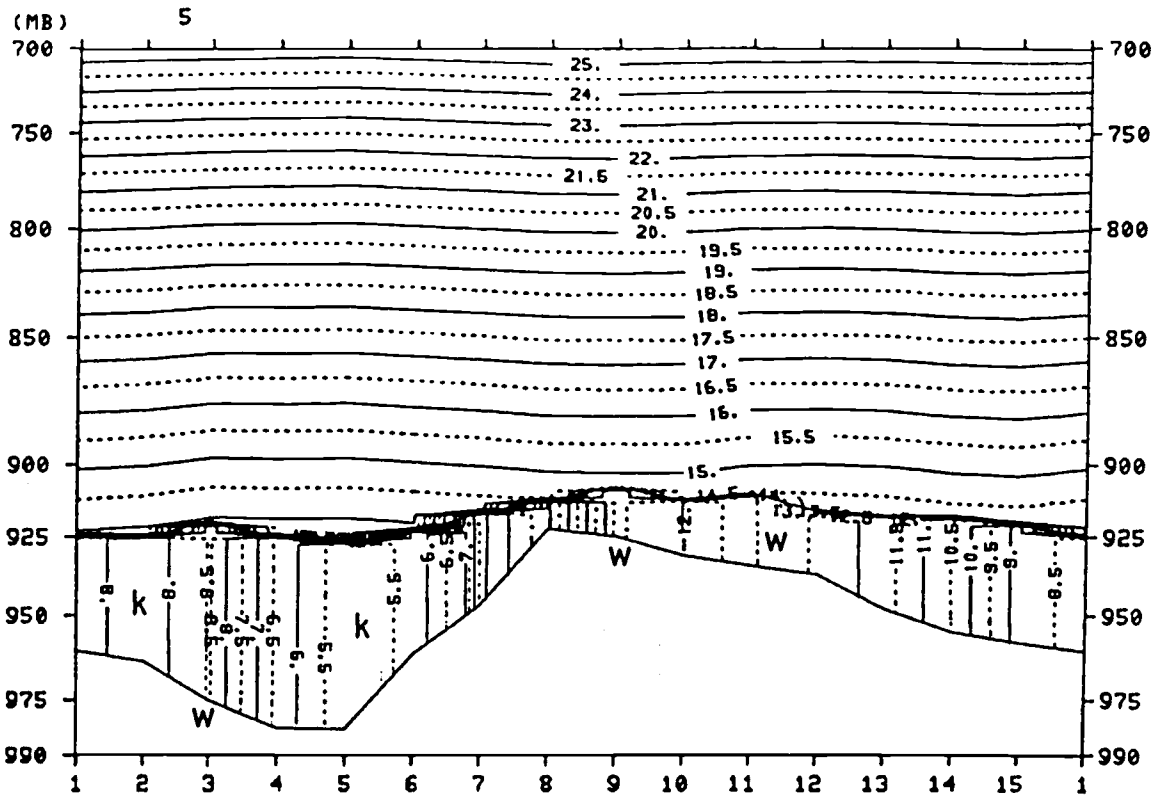
Fig. 6.40. Continued.
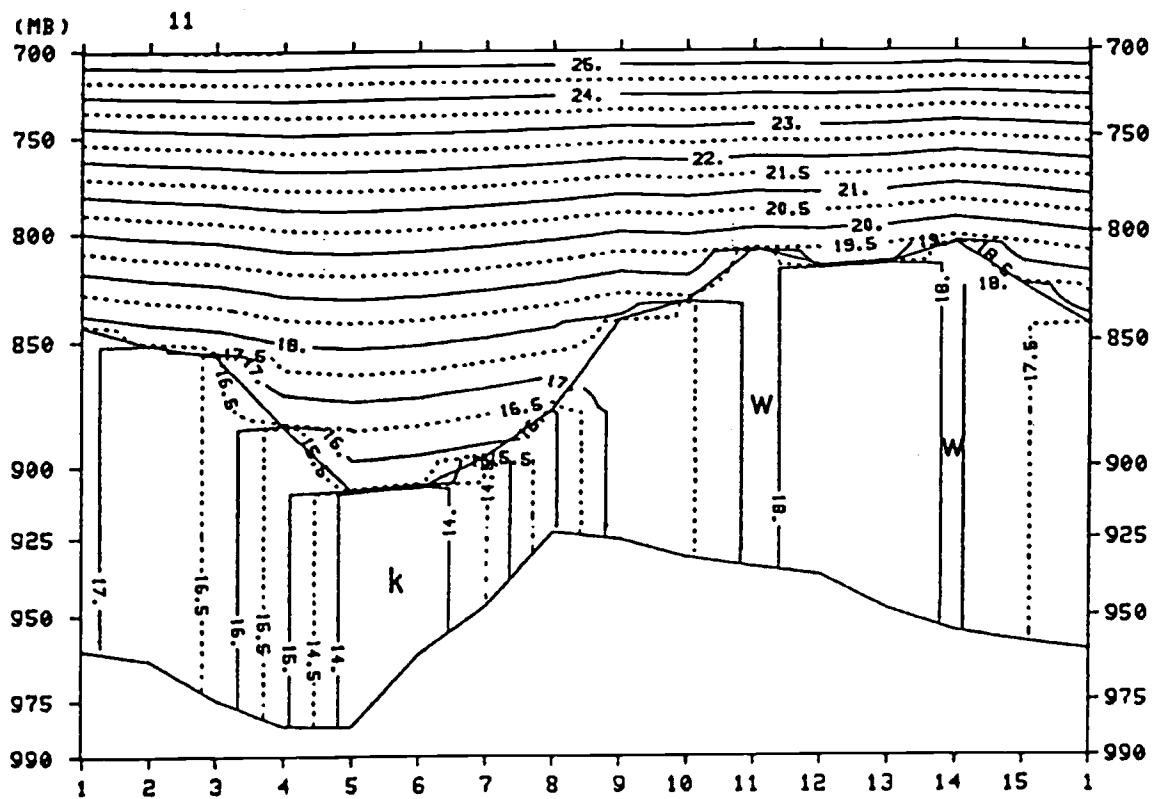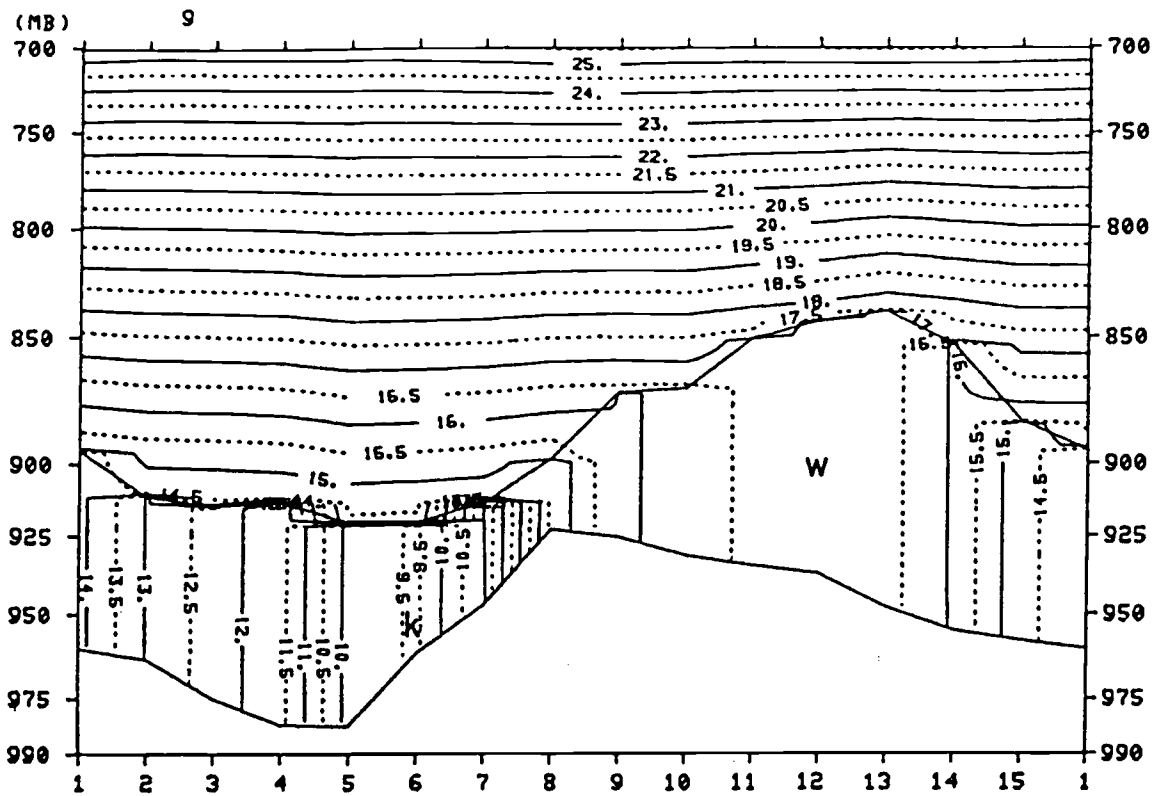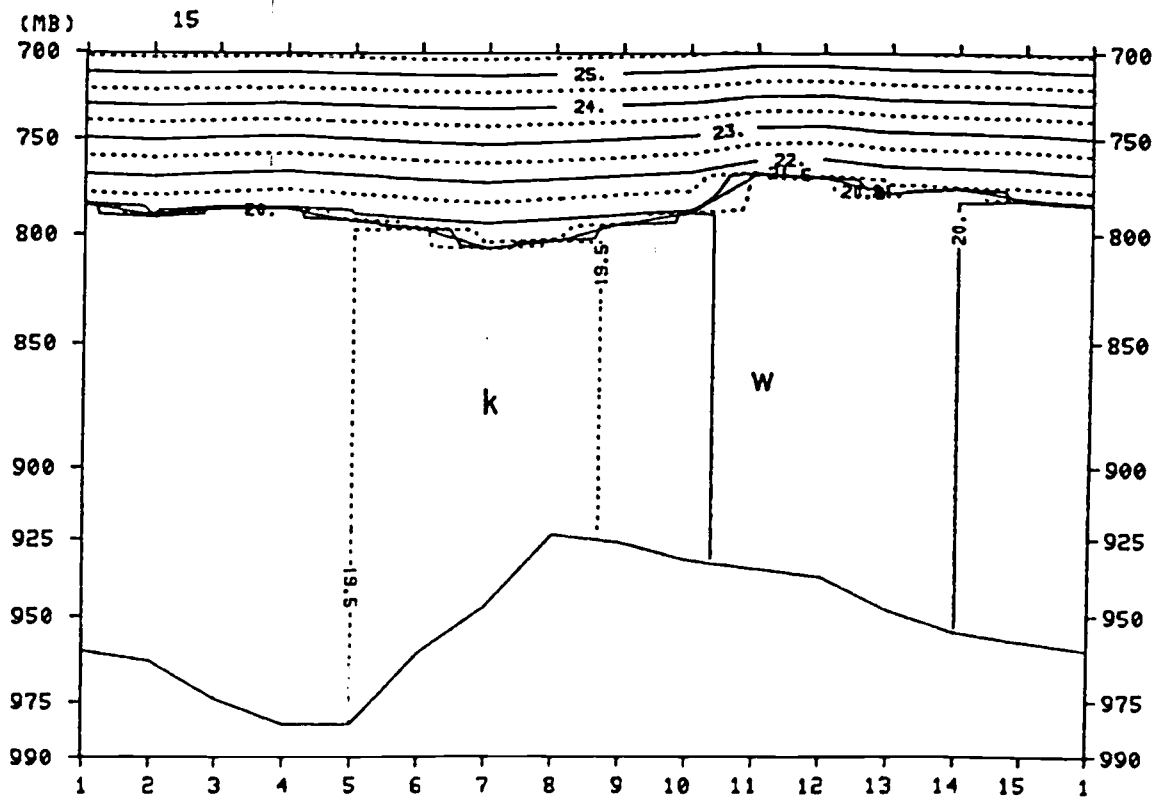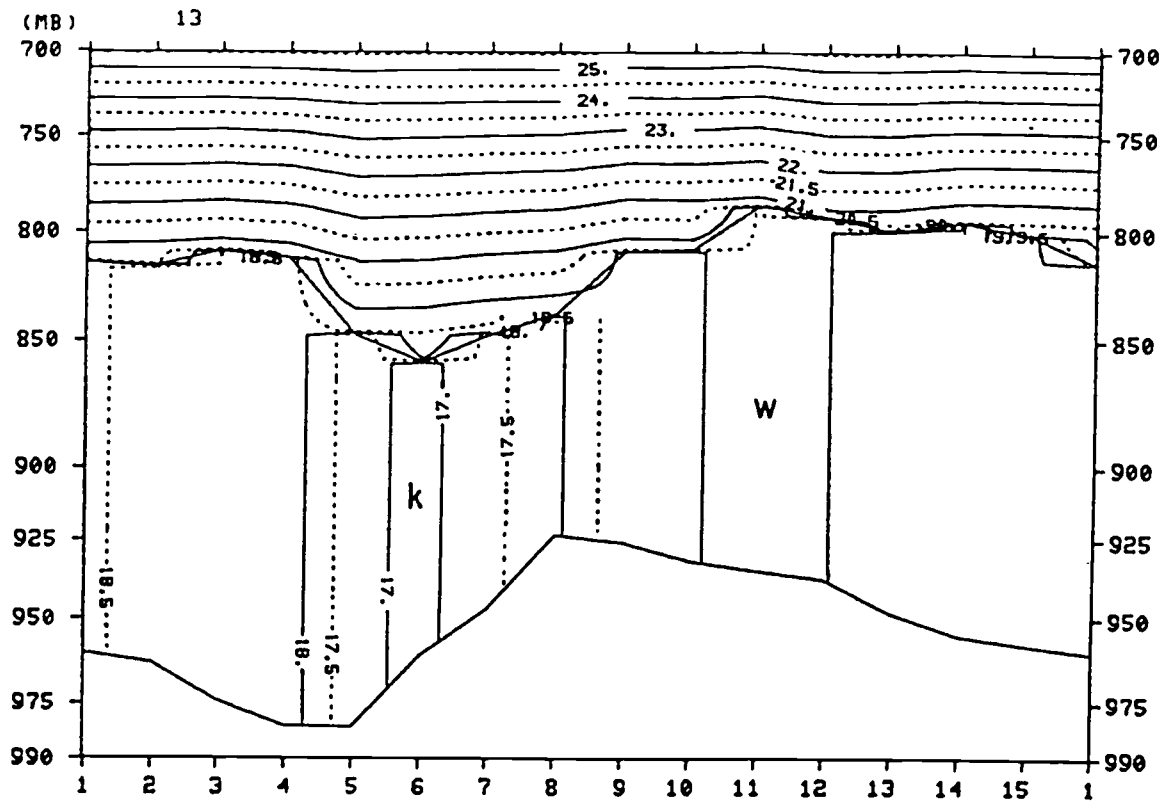
Fig. 6.40. Continued.

Fig. 6.40. Continued.

the primary hill, respectively.

Shortly after sunrise at 0500, isentropes in the mixed layer, whose top is rather flat, clearly show negative correlation of h with θ_M, as illustrated in Fig. 6.40. By 0700 the mixed layer has grown into the free atmosphere in the region of the leeward slope of the hill where θ_M is warmest and h smallest, and warmer air entrained from above has helped diminish the concentration of isentropes there, while the effect of $-\nabla \cdot (h \underline{V}_M)$ on the growth rate of h is still minimal at this moment (see curve K in Fig. 6.34b). It is noted that the direction of $\underline{V}_M$ on the plane of the cross section is not always parallel to it temporally or spatially. The cool-air pool is seen to be pushed upslope against the upwind slope of the hill and a large concentration of isentropes has developed near the hilltop where h is smallest. This gives an indication that the mechanism proposed by Lenschow et al. (1979) is playing a role in the M4 model in breakup of the early-morning stable layer: that as solar heating increases and the stability decreases, the downward turbulent momentum transport becomes larger at the top of the boundary layer and eventually the stress divergence becomes sufficient to accelerate the cold valley air and pull it out of the valley, to be replaced by the deeper, warmer mixed layer generated upwind. The intensification of the shear stress at the mixed-layer top for M4 was discussed in Section 6.6, although we found that this stress alone is not quite sufficient to overcome the negative stress at the ground surface.

As solar heating intensifies, the negative correlation between h and θ_M reverses to become a positive one by 0800 over the

downwind of the ridge, with areas of deep h being associated with those of smaller $\Delta\theta$ (curves C and E in Fig. 6.34a). By 0900 the mixed layer has began to grow over the west end of the basin where the effect of mass flux convergence has become visible, whereas in the areas of cool air the growth of h is still minimal, particularly on the upwind slope near the hilltop where $\Delta\theta$ is large. By this time isentrope packing has diminished over the ridge where h has become deeper than over the depression. It is noted that although h has grown rapidly over the ridge, mass flux divergence has been occurring throughout the day over most of the area downwind of the ridge in the cross section, as illustrated in Fig. 6.39. This indicates that w_e must be mostly responsible for the fast rise of h + h_s, which is consistent with the fields of w_e shown in Fig. 6.36.

Due to strong mass flux convergence as well as relatively large w_e, h over the windward slope of the basin at the left end of the cross section has grown as deep as that over the ridge between 0900 and 1100. There deeper h begins to be associated with larger $\Delta\theta$ again owing to diminishing horizontal variations of θ_M and horizontally rather uniform θ aloft. This has reduced w_e and hence the growth of h due to w_e (curves E and J in Figs. 5.34a and b, respectively). However, h in the cool-air pool still has not grown much; in addition to smaller w_e due to smaller θ_M and greater $\Delta\theta$, there has been mass flux divergence in this area all morning where wind speeds increase upslope, thus further reducing the growth rate of h.

Between 1100 and 1300 h has deepened rapidly in the cool-air

pool because the early-morning stable layer has finally warmed enough to make w_e relatively large over the upwind slope near the hilltop, while mass flux convergence over the leeward slope of the secondary hill at both left and right ends of the cross section has become increasingly strong. On the other hand, over the ridge east of the primary peak, both stronger mass flux divergence and smaller w_e due to the already high $h + h_s$ (which tends to cause larger $\Delta\theta$) are deterring the growth of h. As this trend continues through midafternoon, variations of $h + h_s$ have become negligible while perturbations of θ_M have diminished to ~0.5 K by 1500, partly helped by the advective effect.

Cross sections of θ for L7 are next depicted in Fig. 6.41 on the same vertical plane. Since there is no distinct mixed-layer defined in the L7 model, θ has been linearly interpolated in P without considering the height level of the diagnosed mixed-layer top. At 0500 the early-morning stable layer is still confined within the lowest model layer consisting of air about 100 m thick along the ground surface, and isentropes tend to slant into the ground, reflecting the initial distribution of $\theta_{\ell=7}$. We notice weak mountain-lee-wave-like patterns in the free atmosphere whose lines of constant phase tilt westward with height, which were not as evident in the cross sections of θ for M4. At 0700 the mixed layer is still approximately of uniform depth, but the pattern of isentropes is now more similar to that for M4, particularly over the downwind side of the ridge where turbulent mixing of warm air into the mixed layer from above is most vigorous. The height of the mixed-layer top, estimated by following the kinks of θ in the
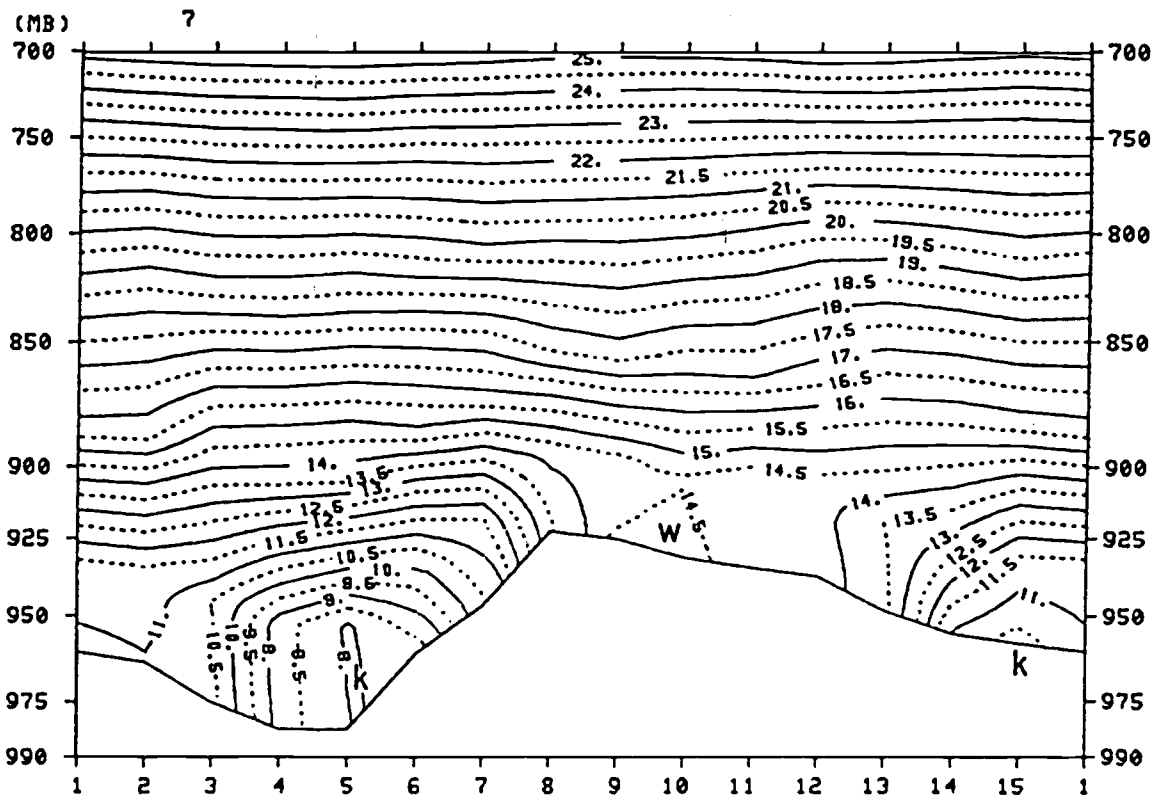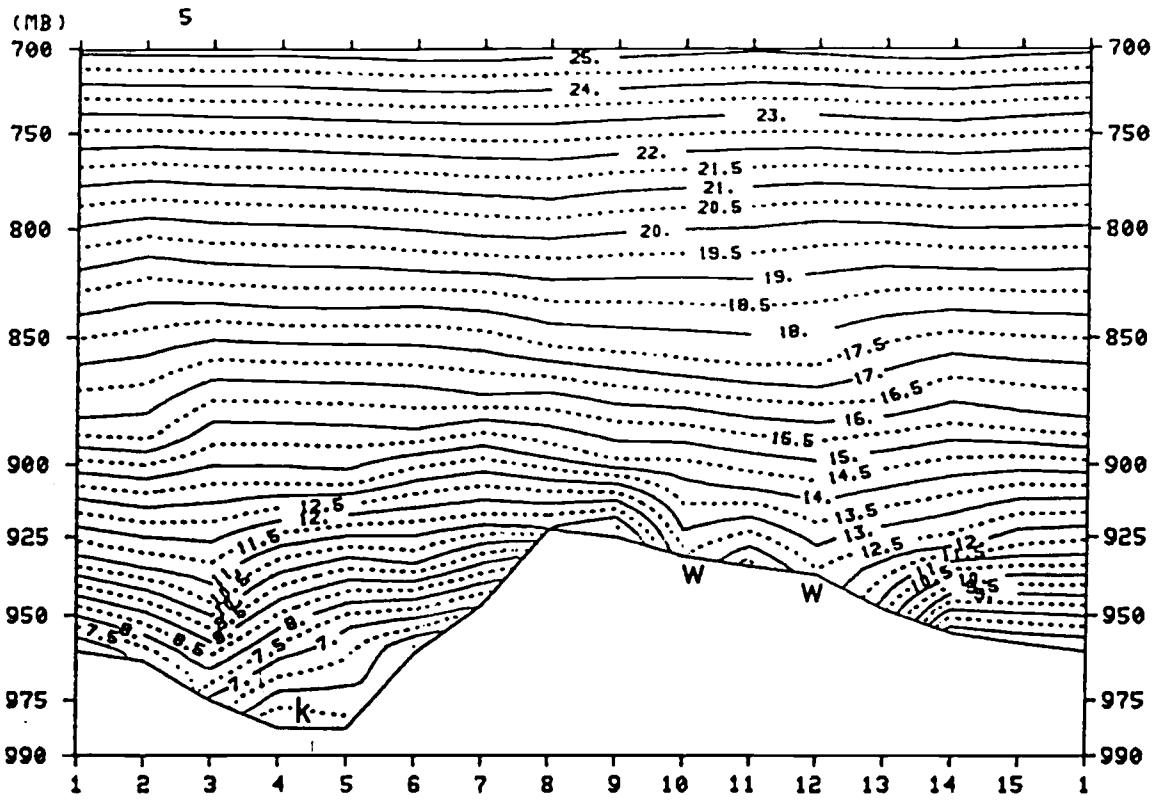
Fig. 6.41. As in Fig. 6.40 except for L7. The estimated h + h_s is not indicated in this case.
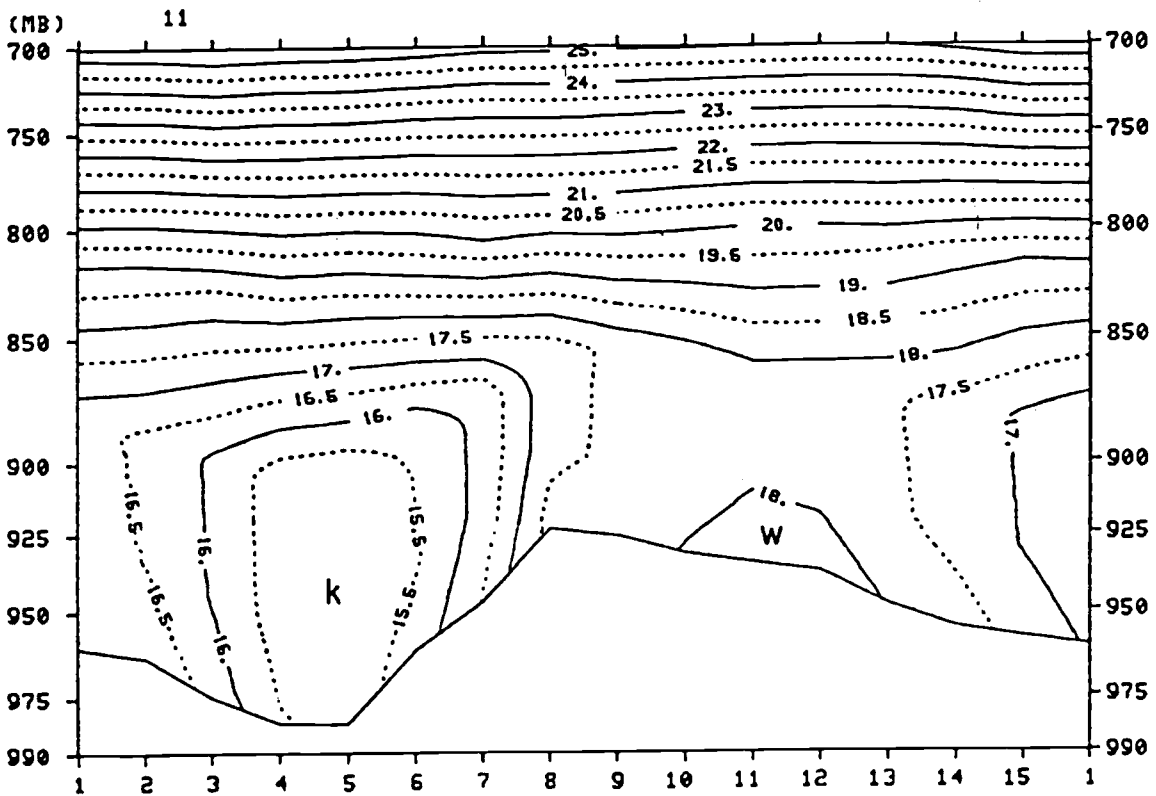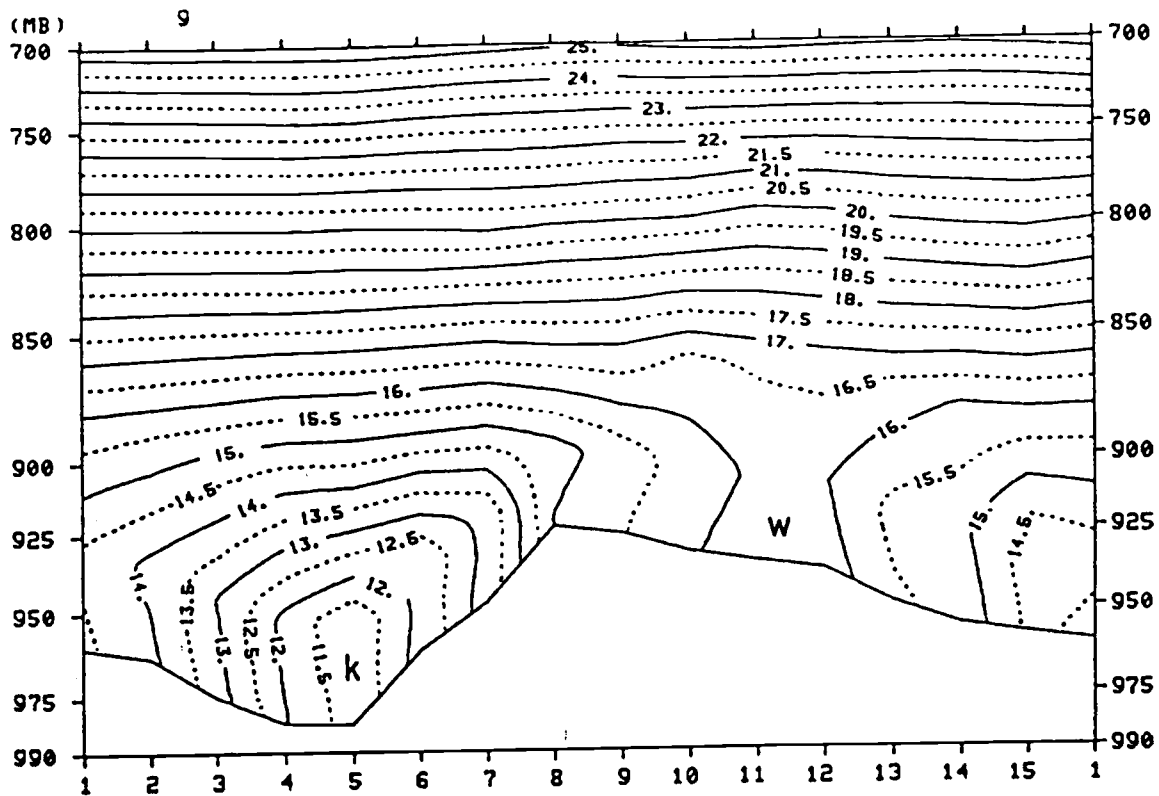
Fig. 6.41. Continued.
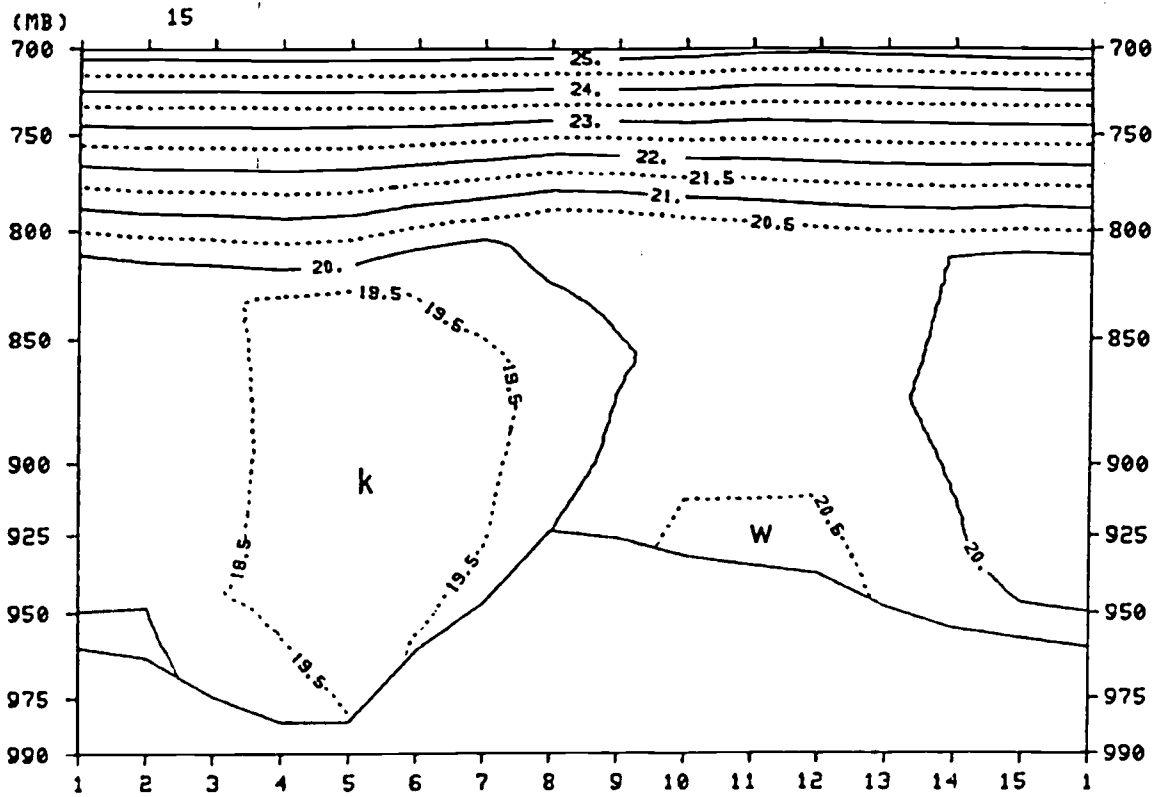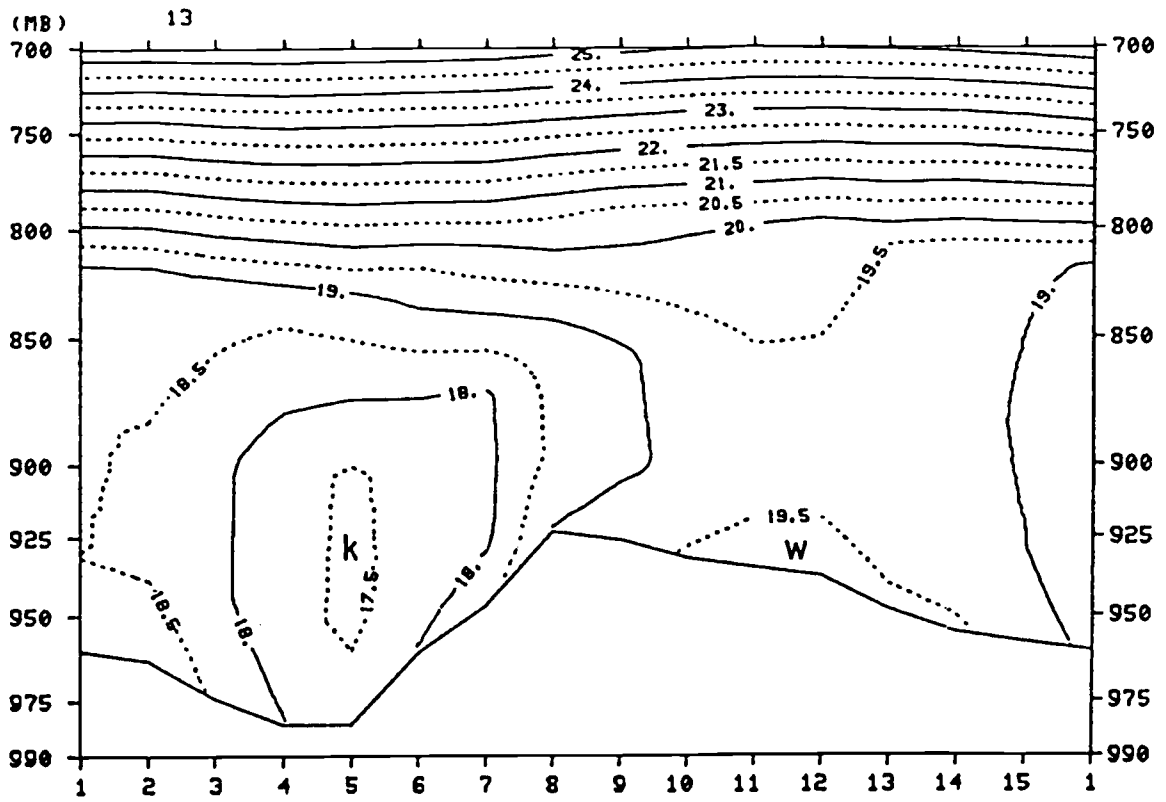
Fig. 6.41. Continued.

computer-produced cross section, does not necessarily agree to that obtained by the procedure for L7 described earlier because in the latter the stability of air in terms of Richardson number Ri has additionally been taken into account. In the cross section at 0900 we notice that by this hour the mixed-layer air in the depression has become warmer than that of M4 due to the shallower depth of the layer. Also note that the cool-air pool stays in the lowest region of the basin, contrary to the case of M4 in which the cold pool was pushed halfway upslope and stayed there through the morning. The estimated height of the mixed-layer top is still lower than that of M4, but a rapid growth of h is evident over the ridge halfway downstream from the hilltop, as in the case of M4 (see Fig. 6.41 at 1100).

At 1100 isentropes in the mixed layer for L7 are quite similar to those of M4. Although h disagrees quantitatively, overall tendencies of the growth of h are quite similar in both models: the growth rate of h is smallest on the upwind slope near the hilltop, while it is largest in the region of the ridge midway downstream from the hilltop.

By 1300 the packing of isentropes over the ridge has been wiped out, while over the basin ~1 K of the θ anomaly remains in the mixed layer, much like in the case of M4. After another 2 hours at 1500 isentropes have virtually vanished, with only ~0.5 K of horizontal gradients of θ detected, which was also the case in the M4 results. Although the overall fields of the diagnosed h + h_s depicted in Fig. 6.34 are less smooth than those of M4 due to increasing irregularities of Ri caused by diminishing turbulent heat

flux reaching the established mixed-layer top from the ground surface, the estimated $h + h_s$ in the cross section has become more uniform and approximately parallel to that of M4 by 1500, with the difference being ~200 m on average.

A cross section of p velocity in units of 10^{-3}mb s^{-1}, taken on the same plane used for those of θ, is presented in Fig. 6.42 for L7 at 1300. Comparing it with the corresponding θ structure given in Fig. 6.41, we note that at this hour a well-organized upward motion, whose vertical extent approximately corresponds to the mixed-layer top, is occurring downstream of the ridge where mass flux convergence is likely to be strong, while an equally well-organized downward motion is seen in the area of cold-air pool. We have found, however, that generally the fields of p velocity are highly variable in both space and time, and it is often difficult to relate them with other fields such as those of θ.

Similarly, the vertical structure of the horizontal winds at 1300 on the same plane is next shown in Figs. 6.43a and b for M4 and L7, respectively. The arrow originates at the height of full level in each layer (see Fig. 2.1), with its length proportional to the wind speed and with directions of west and south winds parallel to the x- and y-axis, respectively. In the M4 model, the wind is assumed to be vertically uniform in the mixed layer and is represented by the arrow closest to the ground surface at each grid point. In the L7 model, on the other hand, the mixed-layer top at 1300 is located above the upper boundary of the layer $\ell = 5$ and there is an indication that it has grown into the layer above ($\ell = 4$) over the middle region of the leeward slope, as the corres-
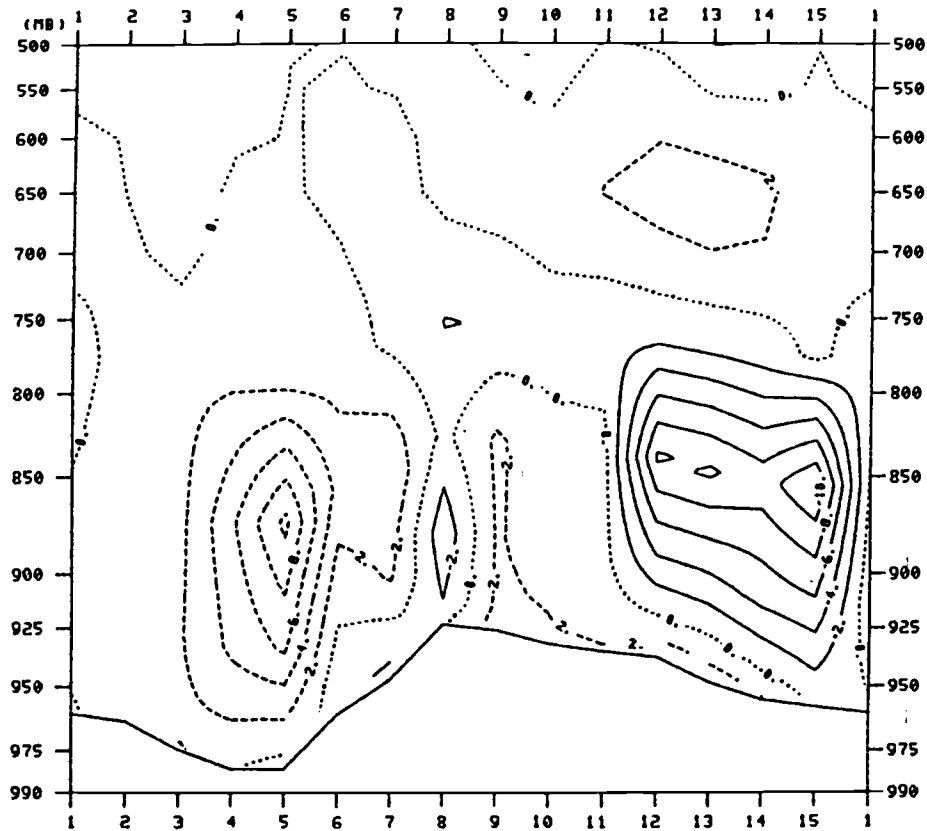
Fig. 6.42. Vertical cross section of p-velocity for L7 at 1300 along the line segment "A". The unit is 10-3 mb s^{-1}, and the contour interval is 2. The solid and broken contours indicate negative and positive p-velocities, respectively. The ground surface and the abscissa are as in Fig. 6.40.
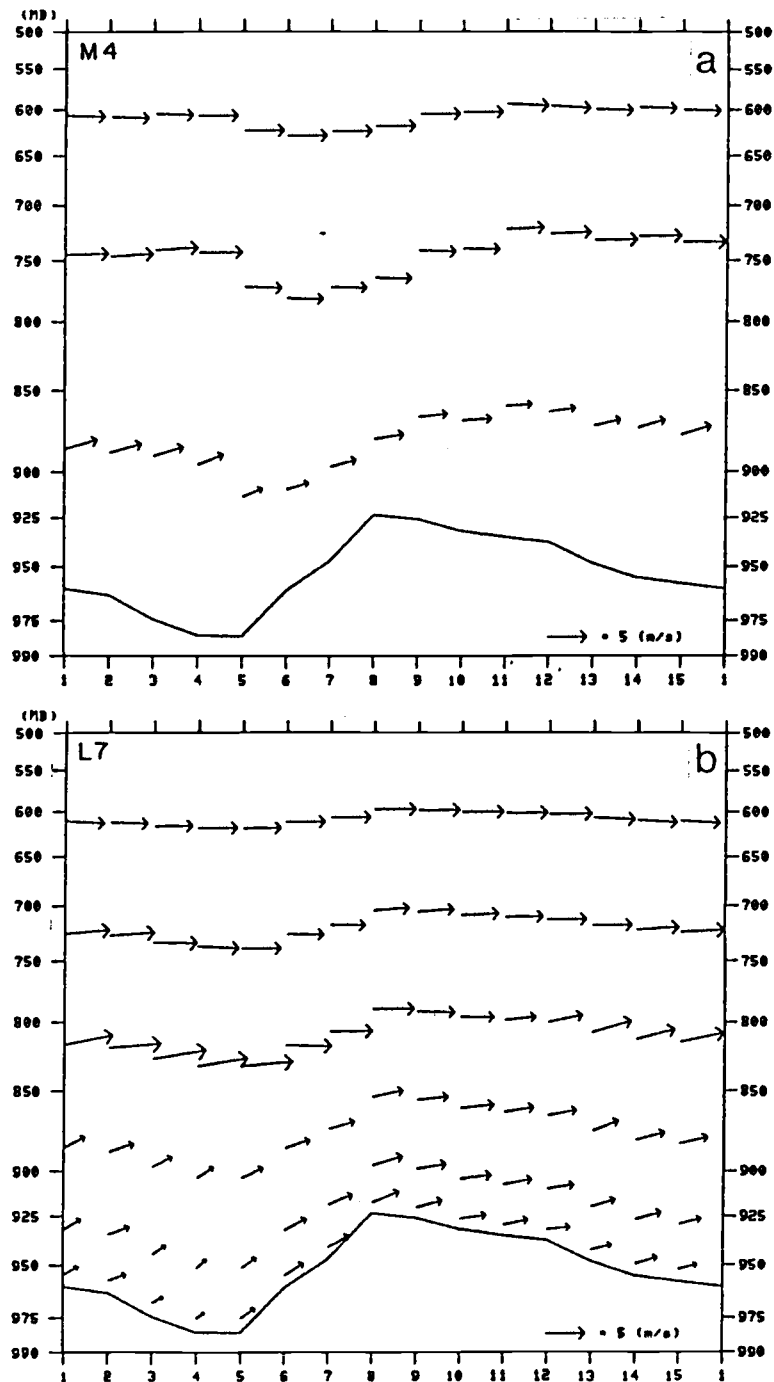
Fig. 6.43. Vertical cross sections of the horizontal winds at 1300 along the line segment "A". (a): for M4, and (b) for L7. The description of wind vectors given in Fig. 6.14 also applies here. The ground surface and the abscissa are as in Fig. 6.40.

ponding cross section of θ in Fig. 6.41 also indicates. Therefore, the profile of the mixed-layer winds is represented by 3 or 4 vectors at a given grid point.

We earlier found that at 1300 the layer-averaged momentum in the lowest three layers of L7 is in general vertically well-mixed (see Fig. 6.10), and also that the evolutions of the domain-averaged mixed-layer wind vectors for both models are very similar to each other for most of the day (Fig. 6.6a). However, we still detect, as illustrated in Fig. 6.43, some vertical variations of wind vectors within the mixed layer for L7, which were assumed negligible in the M4 model.

Observed examples of wind structure are given by, for example, Whiteman (1982) who found by studying the data collected in long but narrow mountain valleys in western Colorado that vertical wind structure within the mixed layer over horizontally inhomogeneous terrain is much more variable than temperature structure. Hodographs at grid point (3,5) in the west end of the basin on the plane of the same cross section, shown in Fig. 6.44 for the lowest 4 layers of L7, illustrate an example of large vertical variability of wind structure with time. Therefore, representing the wind structure for a whole column of the mixed layer by a single wind vector, as in the case of M4, may not be appropriate, depending on the objectives of a particular model.

In order to obtain a better understanding of interrelationships between the effects of entrainment and mass flux convergence on the growth of $h + h_s$, an additional set of cross sections of θ for M4 are presented in Fig. 6.45. The plane of the cross section is taken
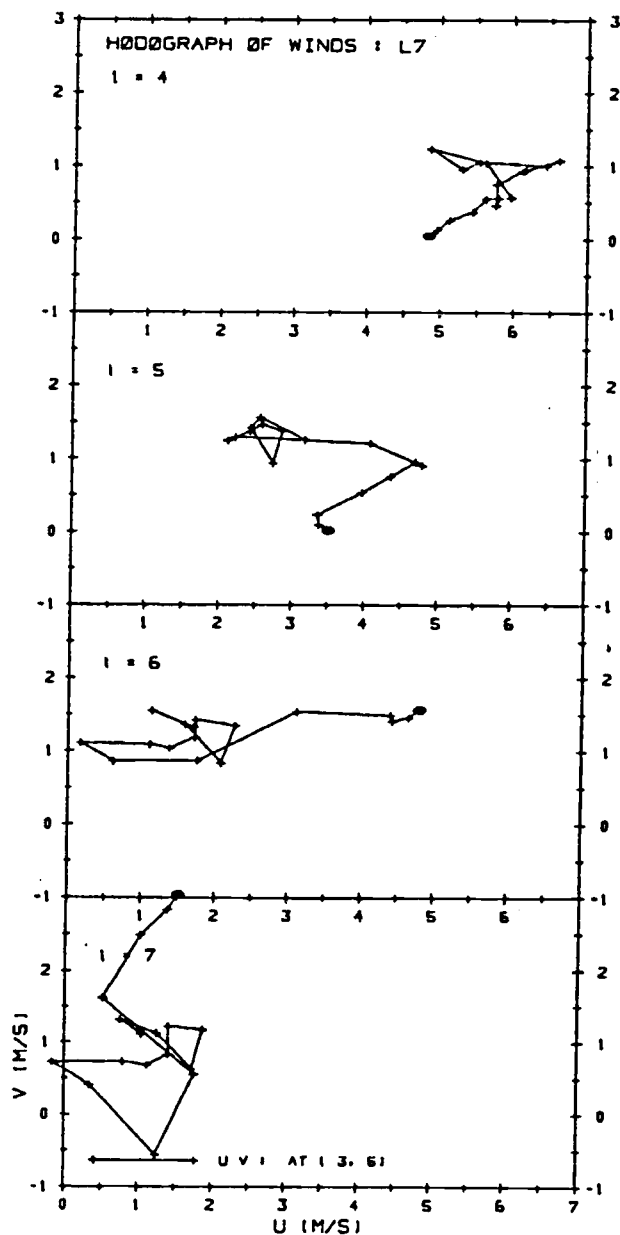
Fig. 6.44. Hodographs of the horizontal winds (ms^{-1}) at grid point
(3,5) between 0400 - 1900 LST for layers 4 to 7 of L7.
The position of the vector head at 0400 LST is indicated by
⊕. Each + mark corresponds to an hourly position of the
vector head except that there is an extra + for 0425 LST.
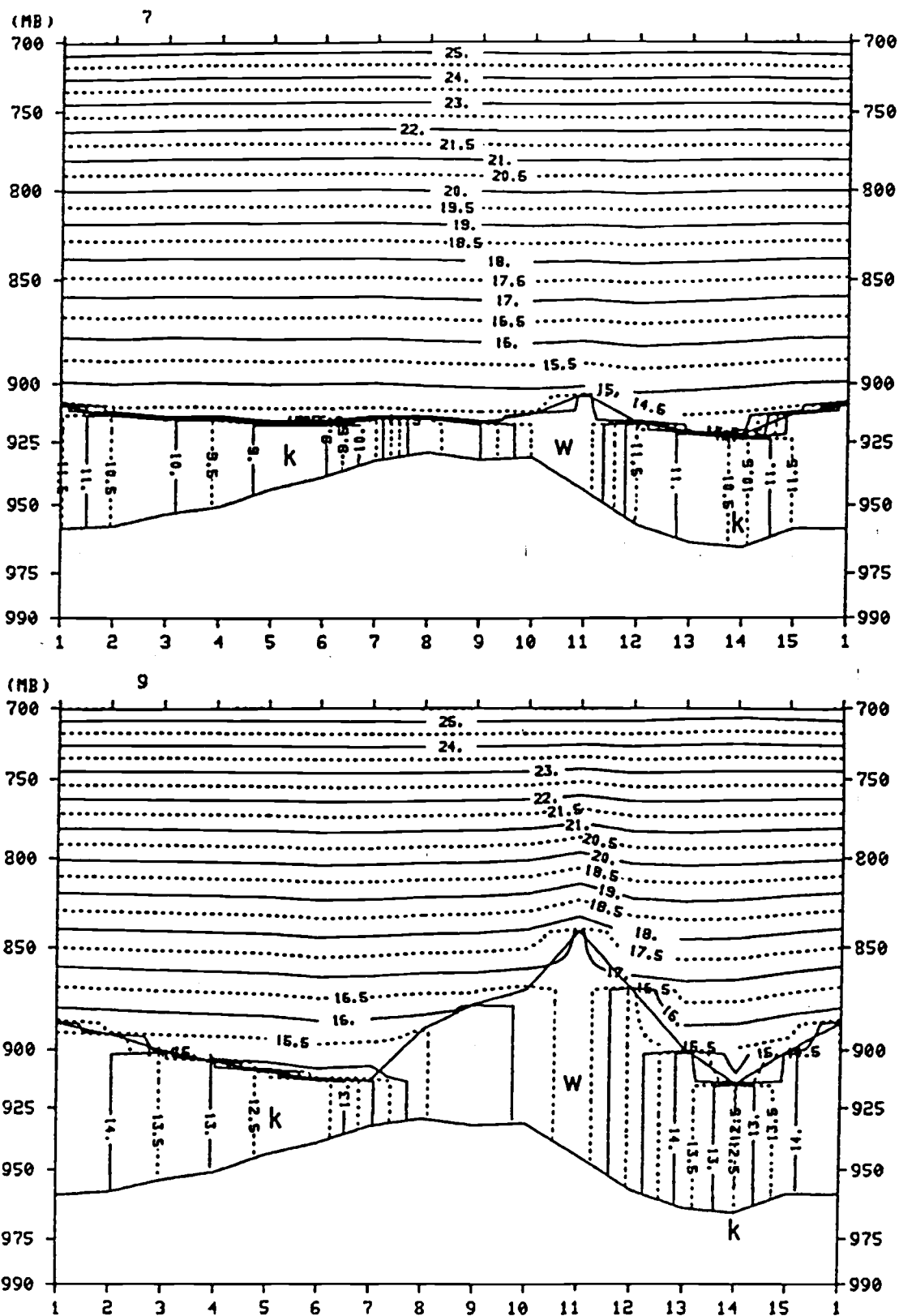
Fig. 6.45. As in Fig. 6.40 except cross sections for M4 are taken along the line "B" in Fig. 5.1. The grid interval is 10 km.
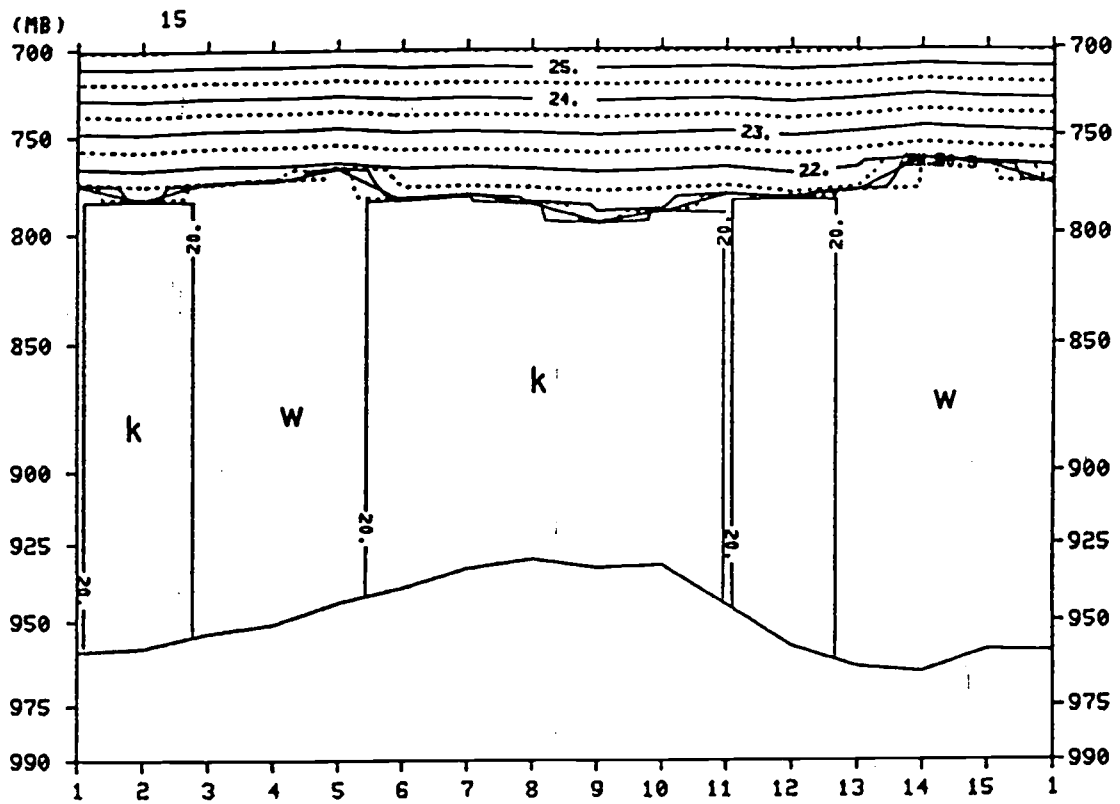
Fig. 6.45. Continued.

Fig. 6.45. Continued.

along the east-west line segment marked "B" in Fig. 5.1, connecting grid points (1,13) on both the east and west lateral boundaries. It crosses the ridgetop north of the primary hilltop where w_e is generally large during midmorning and the valley downwind of the ridge where mass flux convergence is strong. The mixed-layer winds are generally parallel to or directed into this plane at a small angle. The grid interval in this case is 10 km, and the terrain slopes are -0.004 and 0.01 on the windward- and leeward slopes of the peak, respectively.

Rapid growth of h between 0700 and 0900 at grid point (11,13) on the leeward slope of the ridge is apparently caused by large w_e occurring there, as seen in Fig. 6.36, where the effect of mass flux is weak during this period. On the other hand, at the lowest point in the valley (14,13) mass flux convergence is relatively strong, but small w_e prevents h from growing more rapidly. Between 0800 and 1100 w_e weakens and stays relatively small on the downwind slope, but mass flux convergence is now very strong (Fig. 6.39), resulting in a rapid growth of h there (Fig. 6.45 at 1100). Over the valley during midday w_e continues to be smaller, while mass flux convergence is strong and now mostly responsible for rapid growth of h over the lowest elevation in the valley.

It is noted that the center of convergence, as well as the location of the highest $h + h_S$, gradually drifts eastwards at a speed of -1.5 ms^{-1} through the afternoon, which is smaller than that of u_M or $u_{\ell=3}$ in this region. It seems that relatively large w_e occurring right over the ridge top during this period helps deter eastward translation of the peak of $h + h_S$ and the

region of mass flux convergence by generating a relatively fast growth of h upwind of the region of strong mass-flux convergence.

In Fig. 6.46, the corresponding cross sections of θ for L7 are depicted. As in the case of M4, breakup of the early-morning stable layer starts on the east edge of the ridgetop, and deepening of the mixed layer seems to propagate downstream over the the slope and valley. Although it is difficult to locate the most probable position of the mixed-layer top in this case, general agreement of overall mixed-layer structure in both models is again fairly good in terms of distributions of θ and $h + h_s$.

Banta (1984) constructed idealized cross sections of the θ field in the morning boundary layer in order to describe its evolution on a typical dry day in a valley downstream of a ridge by analyzing data obtained in South Park, a broad, relatively flat basin in the Colorado Rockies (Banta and Cotton, 1981). We find that cross sections of θ constructed from the results of our numerical models and presented in this section favorably compare to those of Banta (1984). He argued that the convectively mixed boundary layer grows at the higher elevations before it appears at the lower terrain mostly because at the higher elevations the early-morning inversion layer is generally shallower compared to that in the valley through which the convection has to penetrate vertically before a deep convective mixed layer forms. However, he fails to mention the importance of the inversion strength in determining the growth rate of h. In fact, the cross sections of θ in Fig. 6.40 clearly show that the growth of h in the early morning is slowest on the upwind slope where the depth of the mixed layer is
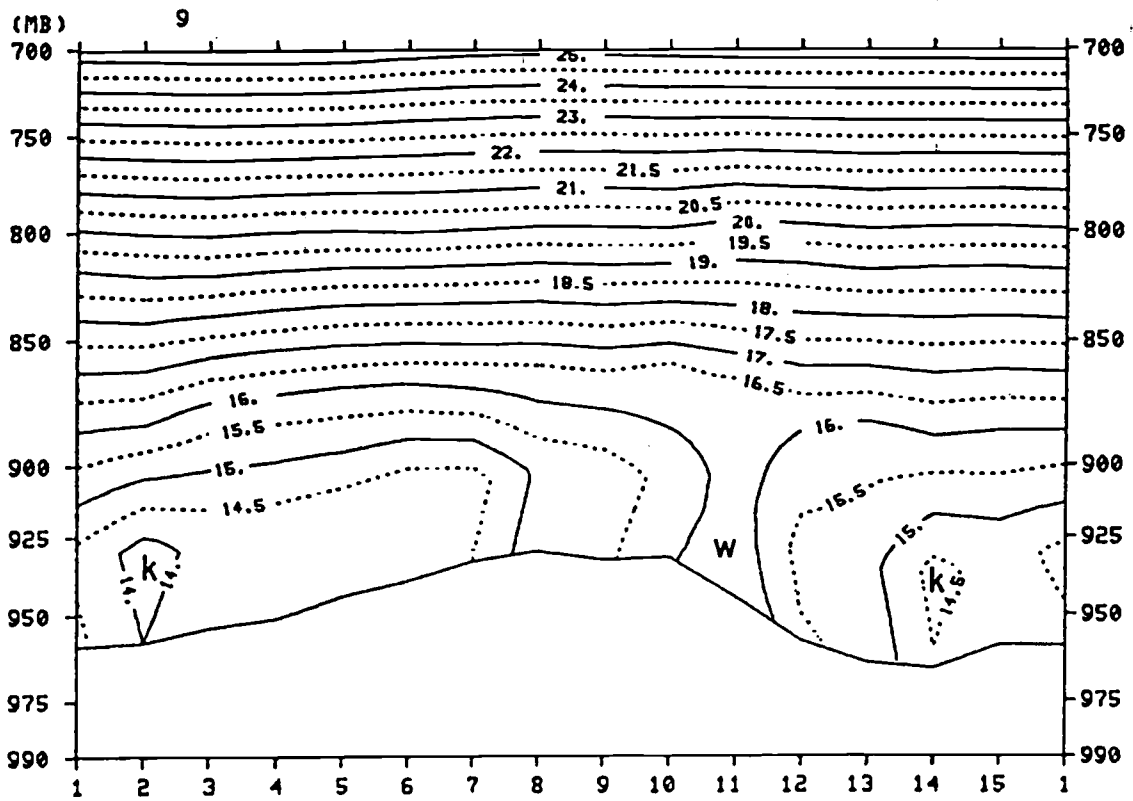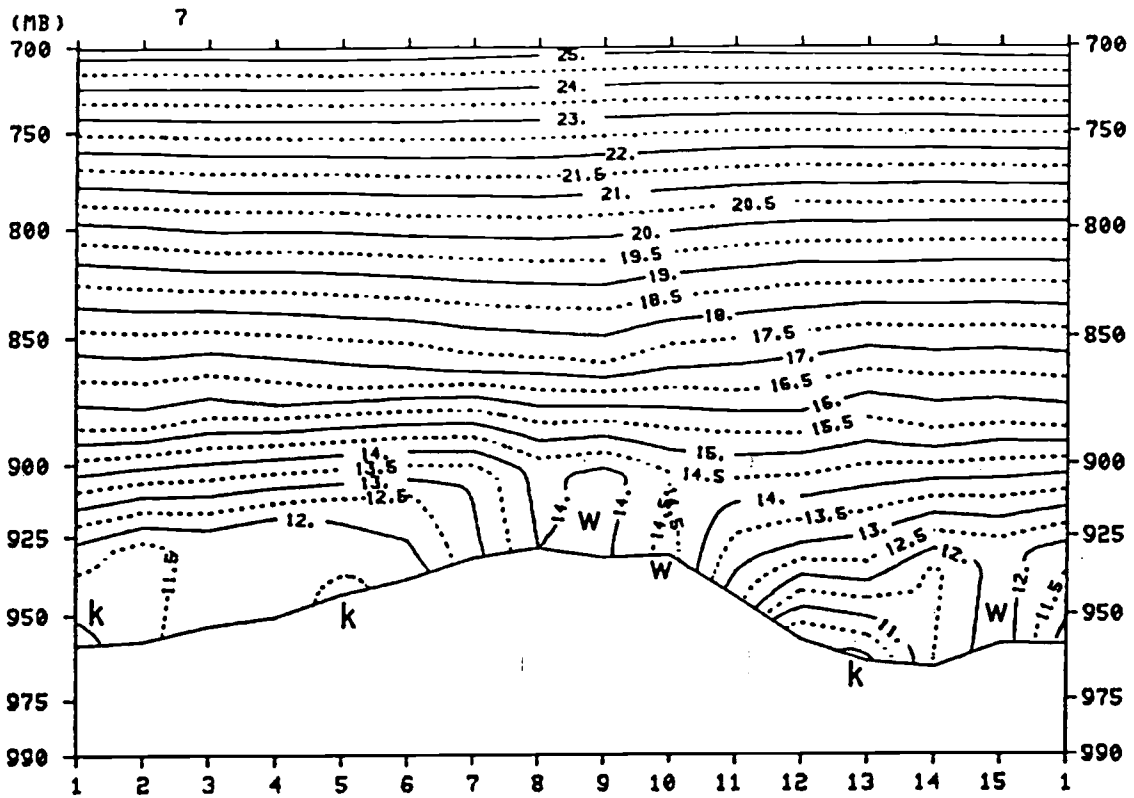
Fig. 6.46. As in Fig. 6.45 except for L7.
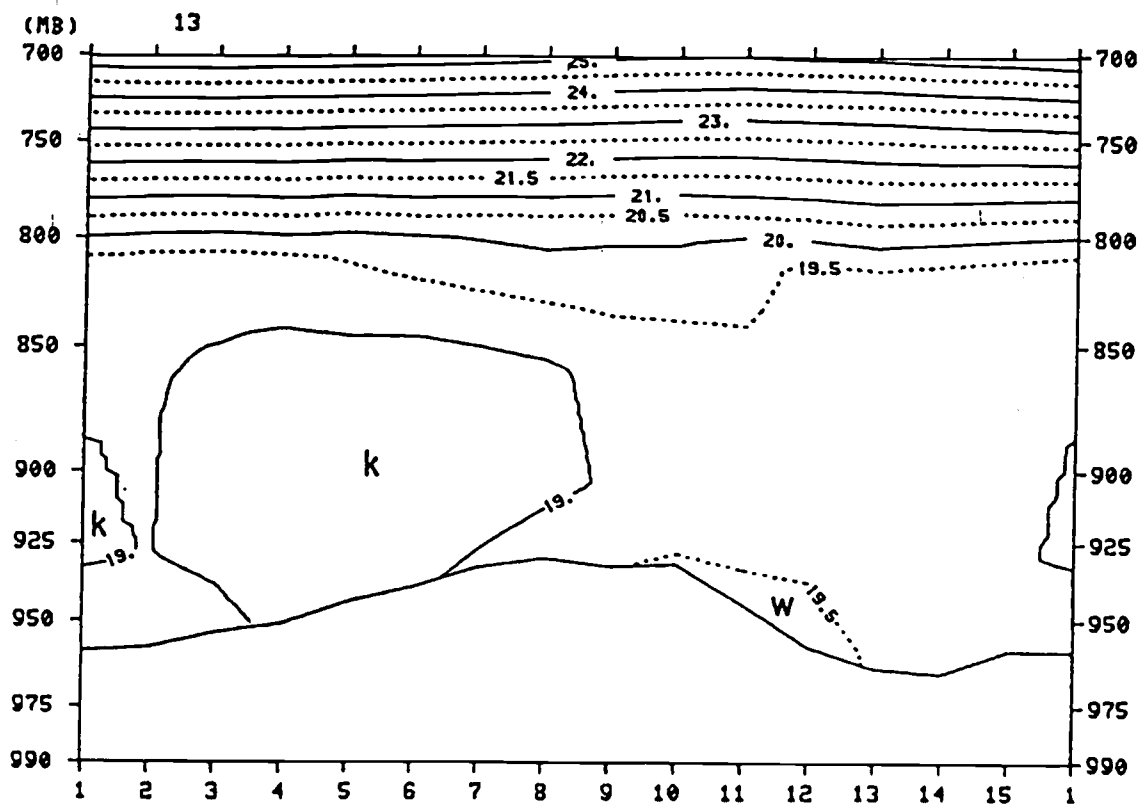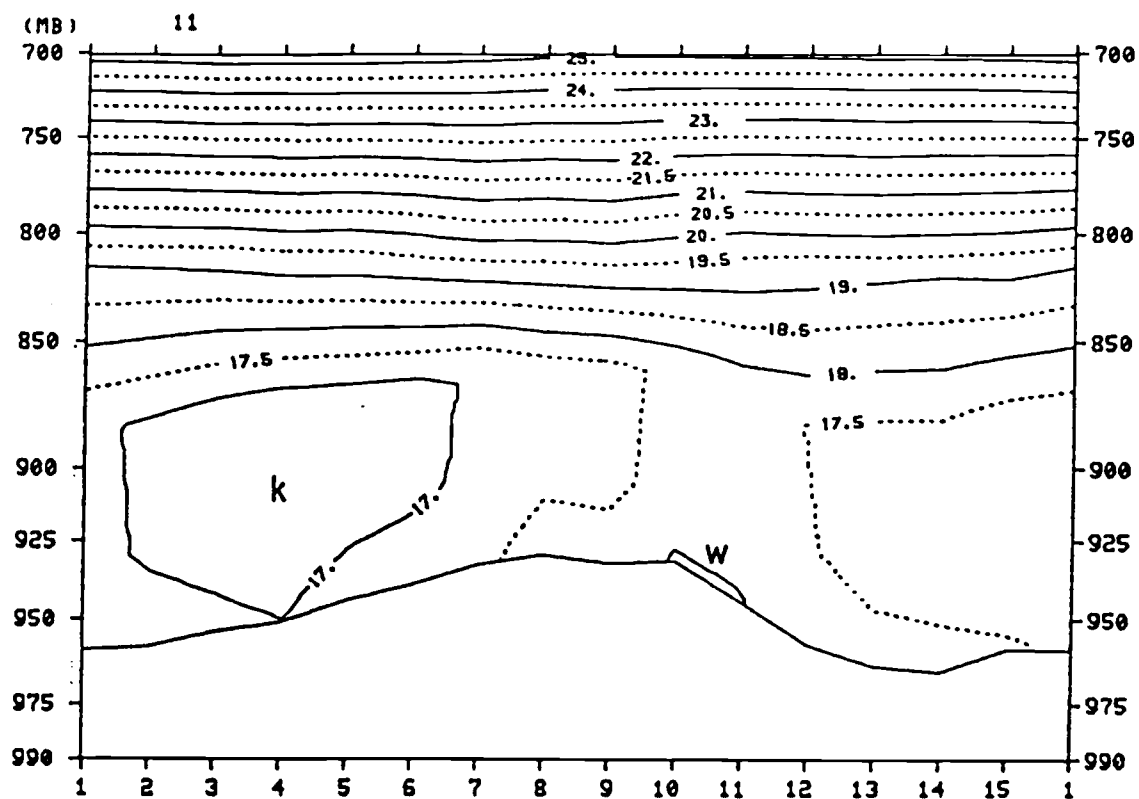
Fig. 4.46.   Continued.
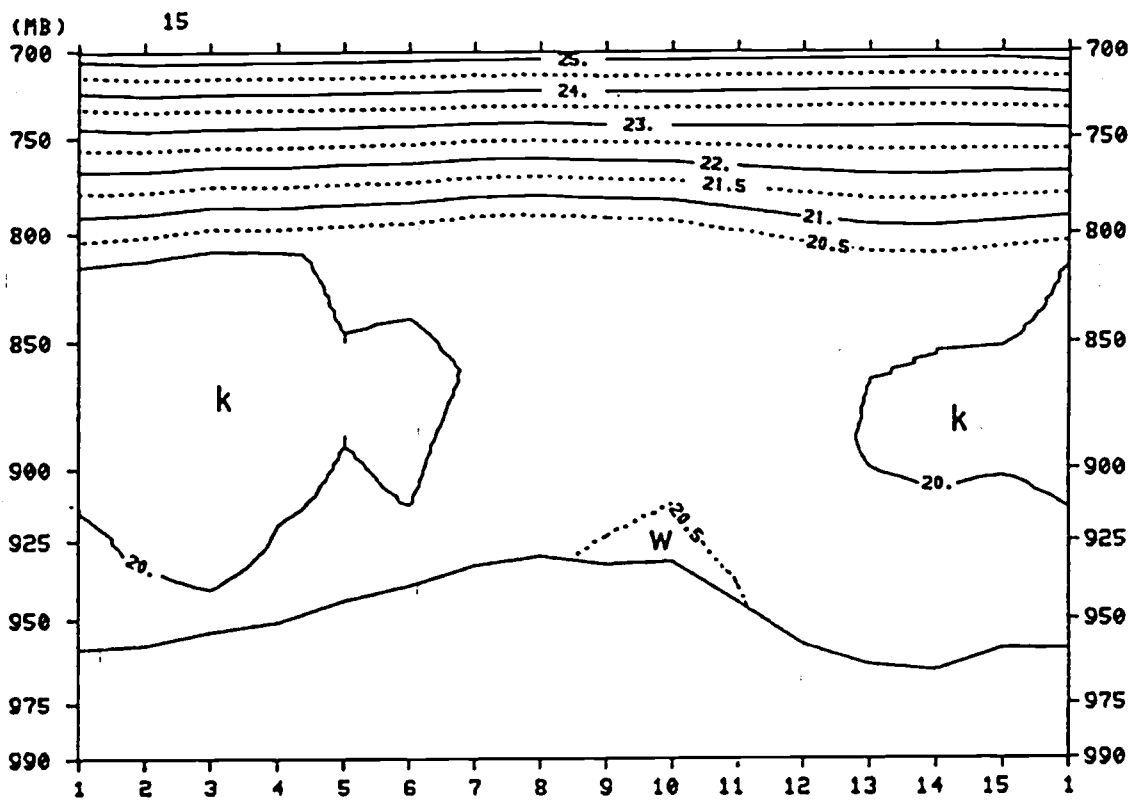
Fig. 4.46. Continued.

smallest. He also postulated that entrainment, which we have found to play a major role, is a factor contributing to the process. Therefore, he concluded, the horizontal extent of the cold-air pool shrinks by propagating down the slope as surface heating persists. At the same time, the shallow convective mixed layer that has formed along the underside of the cold pool grows in depth and erodes the pool from below.

Furthermore, the formation of the mass-convergence region was explained by Banta (1984) as follows: on the east-facing slope such as the downwind slope of the primary ridge in our model topography, upslope winds with an easterly component, which may be generated within the shallow convective mixed layer during the morning hours, meet with convectively-mixed winds with a westerly component, blowing down from the direction of the ridgetop, thereby forming a line of convergence to the lee of the ridge that propagates down the slope. He asserted that this low-level mass convergence and the formation of updrafts above the convergence zone are processes which are important in cloud initiation.

Due to gentle slopes of the hills in our topography, as explained by Lenschow et al. (1979), as well as the coarse grid intervals employed and uniform large-scale geostrophic forcing imposed, upslope winds on the leeward slope as described above were not generated in our model results. We notice, however, that there was an appreciable slowdown of winds in the lowest layer of L7 during the morning hours in the valley downwind of the primary ridge, indicating that the above-mentioned process that generates upslope winds was probably be in progress during midmorning.

Cross sections of the vertical θ shown in Fig. 6.45 are consistent with analyses of observed data by Banta (1984) in that the mixed layer grows most rapidly over the leeward slope near the ridgetop during the early-morning hours. Interpreted in terms of $-\nabla\cdot(h\underline{V}_M)$ in (6.1a), this large spatial gradient of h results in a region of strong horizontal mass flux convergence over the middle slope further downstream of the ridgetop. This convergence is further enhanced by the resulting spatial deceleration of the winds over the same region. Thus, growth of h becomes most rapid in this region during midmorning. The region of the highest growth rate of h, which is by 1000 mostly due to mass flux convergence, propagates downwind over the leeward slope through late morning, resulting in an expansion of the region of deep mixed layer, covering the areas from the ridgetop to the entire leeward slope and valley by early afternoon where horizontal gradients of θ have diminished. Thus, we may conclude that despite drawbacks mentioned earlier in each model, the formation of the regions of convergence and accompanying updrafts to the lee of a ridge on a typical clear dry day, processes which are likely to be important in cloud initiation that may lead to precipitation, seems to be simulated using the M4 model as well as the L7 model.

The evolution of vertical wind structure at grid point (14,13) located in the valley, along with the mixed-layer height, is also illustrated in Fig. 6.47. The evolution of $\underline{V}$ for L7 shown in Fig. 6.47b is quite similar to observed examples given by Whiteman (1982) who found close interrelationships between wind- and temperature-structure evolutions, and by Banta and Cotton (1981) as
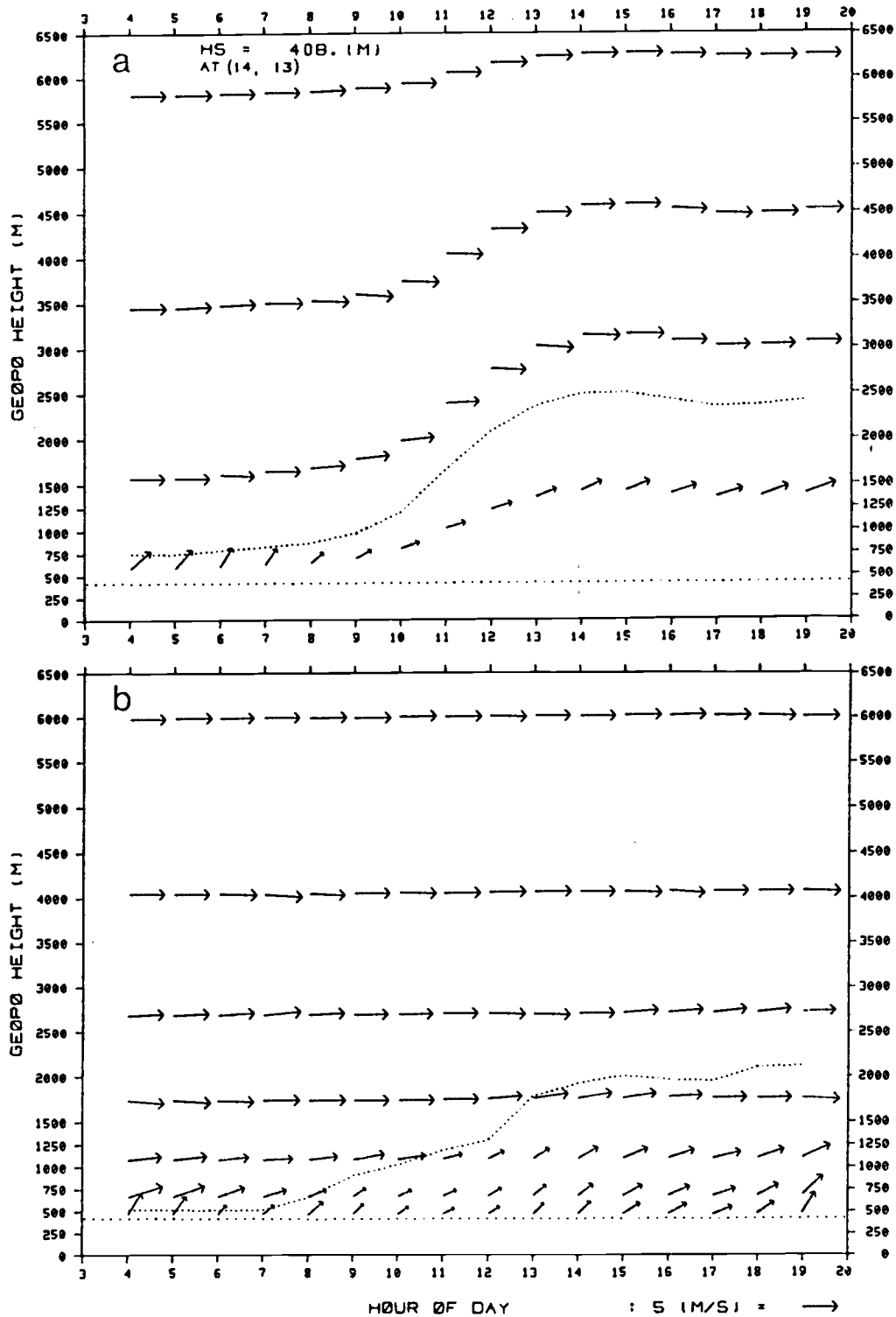
Fig. 6.47. Evolutions of the vertical profile of the horizontal winds at grid point (14,13). (a): for M4, and (b): for L7. The description of the wind vector given in Fig.6.14 also applies here. h + h_S and h_S are indicated by fine and coarse dotted lines, respectively.

mentioned earlier. We notice again vertical perturbations in the mixed-layer wind structure for L7, and the effect of turbulent mixing of momentum within the mixed layer during the period of strong heating is clearly seen.

7. SUMMARY AND CONCLUSIONS

7.1 Review of Model Results

The influence of irregular terrain on the evolution of the daytime planetary boundary layer (PBL) structure and meso-β scale dry circulations has been studied by using two three-dimensional hydrostatic σ-coordinate models which employ different approaches to the PBL parameterization.

The 4-layer model (M4 model) utilizes the bulk-layer approach which assumes vertically well-mixed PBL quantities, while the 7-layer model (L7 model) adopts the eddy-diffusivity approach (K-theory). In the M4 model, both the PBL top and the earth's surface are treated as coordinate surfaces by introducing a modified σ-coordinate. Thus, the depth of the PBL and the fluxes at the PBL top can be obtained directly by making use of an entrainment equation.

In both models a potential enstrophy and energy conserving scheme has been adopted for horizontal finite differencing. A test of the differencing scheme has been performed using the shallow-water system, which has demonstrated advantages of employing such a scheme. Additionally, an adiabatic reference atmosphere has been incorporated in order to reduce the truncation errors in pressure gradient force terms in vicinity of steep hills. A simple test clearly showed the effectiveness of utilizing the reference atmosphere. The ground surface temperature was diagnosed using the energy balance equation. A linear relationship between the ground heat flux at the surface and the net radiation was deduced from

observed data, and utilized in both models.

Integrations have been performed under the conditions of a typical, dry and sunny summer day in mid-latitudes with moderate prevailing westerly winds blowing over gently sloping idealized hills in a domain of 150 km on a side. The initial field of potential temperature in the assumed PBL or mixed layer of each model was proportional to the deviation of the ground surface height h_S from its average $<h_S>$. Cyclic lateral boundary conditions were employed and the grid interval was 10 km.

Tennekes' (1973) simple one-point mixed-layer model relating the PBL depth h to the inversion strength $\Delta\theta$ and the surface sensible heat flux was able to qualitatively describe the daytime evolutions of the domain-averaged values $<h>$ and $<\Delta\theta>$ from the M4 results. The development of $<h>$ and $<\Delta\theta>$ from the L7 results was also qualitatively similar to those of M4.

The evolutions of domain-averaged vectors of the mixed-layer winds of M4 and the vertical-mean PBL winds of L7 closely resembled each other. In both cases counterclockwise rotation of the hodograph with time of day was observed. Experiments using a simple slab model revealed that the combined effects of the surface stress and the large-scale pressure gradient and Coriolis forces alone could not explain this behavior of the hodographs. It was found that only when the non-zero momentum flux at the mixed-layer top was taken into account, the wind hodograph from the simple model showed counterclockwise rotation which resembled those of the M4 and L7 experiments. This demonstrates the importance of momentum-flux

transport through the PBL top in determining the overall behavior of the winds in the PBL.

However, the hodographs of the area-mean winds for individual layers of L7 showed that momentum in the PBL is vertically thoroughly mixed only during the peak period of convective activities. Thus, the influence of stability and wind shear within the boundary layer on the vertical transport of momentum, which was absent in the PBL parameterization scheme in the M4 model, was demonstrated.

The domain-averaged potential temperature $\langle\theta\rangle$ within the PBL of L7 displayed vertically quite well-mixed profiles compared to those of momentum, and fairly well resembled typical observed profiles. The evolutions of $\langle\theta\rangle$ for the PBL from both experiments were also similar, suggesting the bulk-layer approach should perform as well as the eddy diffusivity approach as far as the daytime $\langle\theta\rangle$ in the PBL is concerned, although their detailed vertical structures cannot be resolved by the former approach.

The regions of weak winds that persisted through the early afternoon in the mixed-layer flow patterns of M4 were attributed largely to the baroclinic effect of horizontal variations in the mixed-layer potential temperature θ_M which overcome the generally opposing effect associated with perturbations of the mixed-layer top height. The decelerating effect of the surface drag was found to be much smaller over the weak-wind spots. The influence of a relatively large drag coefficient in these regions was offset by the effect of generally larger h, resulting in a much smaller decelerating effect of surface drag in the weak-wind regions.

Turbulent stresses at the mixed-layer top associated with entrainment, which generally had an accelerating effect on mixed-layer air parcels of M4, were quite significant and could not be ignored, as is often the case in simple models. However, they were not sufficient to overcome stronger surface-drag effects and pull the cold air out of the valleys, leading to breakup of the early-morning boundary layer, as was the case in Lenschow et al.'s (1979) observational study.

The channeling effect and the regions of weak winds evident in the early-morning mixed-layer flow patterns of M4 markedly diminished and the flows become very uniform as h deepened. By contrast, these features were visible throughout the day in the flow fields of the lowest layers within the PBL of L7. The horizontal fields of vertical-mean PBL winds of L7, however, corresponded quite well to those of the M4 mixed layer even in the afternoon.

The combined effect of large-scale pressure-gradient and Coriolis forces and turbulent stresses seemed to be largely responsible for restoring uniform flow patterns in the deep afternoon PBL of M4. However, the so-called Ekman balance among these forces was not attained in broader areas of the domain. Relative steadiness of the overall low-level flow patterns of L7 indicated that the local pressure gradient force associated with terrain irregularities was likely to be more important than in the case of M4 in the behavior of the afternoon flows near the ground.

Thus, significant differences in the flow patterns of the two models, including the locations of weak-wind pockets, suggested that if an accurate knowledge of spatial variations in wind patterns near

the ground, say, 50 m above the ground, is essential, the multi-layer approach should be more desirable.

The effect of horizontal θ advection has been found to be very important in reducing spatial anomalies of θ existent in the early-morning mixed layer of M4. The advective effect tended to be positive (negative) where the warming rate associated with direct surface heat flux was small (large), thus playing a key role in determining the development of the θ_M patterns. The warm advection of θ_M into the valleys just after sunrise was found in general to be significant but not quite sufficient to wipe out the early morning inversion, and a second "wave" of advective warming was needed to prompt rapid increases of θ_M and h in the lower elevations. Therefore, ignoring the advective effect in prediction of θ_M, as is often the case in simple models, would seriously affect the representativeness of the calculated values in hilly regions.

The horizontal fields of θ in the lowest layers in the PBL of L7 resembled fairly well those of θ_M of M4 in pattern and magnitude. However, some discrepancies were found, as in the case of wind fields, in the locations of coolest and warmest regions. It seemed that these locations in the L7 results were less influenced by advective effects than in the case of M4 even in the late afternoon. This may be again attributed to the effect of irregular terrain on the air near the surface. The patterns of θ in the individual layers below the diagnosed PBL top of L7 were quite similar to each other, indicating the vertically well-mixed nature of θ. Consequently, the fields of the vertical-mean θ in the PBL

greatly resembled those of M4, although some shifts in the locations of extremes were detected.

The field of surface heat flux H_S was found to be negatively correlated with that of variable bulk transfer coefficient for sensible heat, C_H, but positively correlated with the pattern of wind speeds in the lowest layer, as was the case in which a constant C_H was used. Horizontal perturbations in the fields of H_S were significantly smaller than in the cases with a constant C_H, which resulted from a compensating effect between C_H and wind speed that entered in the aerodynamic formulation of H_S. The fields of H_S from the two experiments remarkably resembled each other, the cause of which is yet to be investigated. The influence of gentle slopes in the model terrain accounted for in the calculations of radiation at the surface seemed minor (DUH, 1984).

The overall patterns of the mixed-layer top, $h + h_S$, in the case of M4 during the morning hours, were mostly dictated by those of entrainment w_e. In the afternoon, however, the regions of relatively strong mass-flux convergence that developed over the downwind slopes of major hills were found to have a dominant influence on the development of the $h + h_S$ fields. The patterns of $h + h_S$ from the L7 experiment qualitatively corresponded fairly well to those of M4 during most of the daytime. This agreement was rather remarkable considering the totally different procedures used in the two models. Thus it may be said that the diagnostic procedure used in L7 to determine h utilizing both the local Richardson number and gradient of θ offered a reasonable alternative to directly predicting h, at least in our experiments.

Examination of the vertical cross sections of θ for M4 on a plane in the general direction of the morning wind clearly revealed the interrelationships among θ_M, $\Delta\theta$, h, w_e and mass-flux convergence. The fast growth of h over the leeward slope of the primary hill during midmorning was mostly associated with larger w_e there, while the noticeably slow growth of h over the upwind slope near the hilltop was caused by both larger $\Delta\theta$ (hence smaller w_e) resulting from cooler air and strong mass-flux divergence occurring there. Reduced perturbations in $h + h_S$ fields in the afternoon were promoted by the positive correlation between $\Delta\theta$ and h, along with the increased influence of mass-flux convergence.

The cross sections of θ for L7 on the same plane revealed that despite the differences in their initial structures the evolutions of the boundary layers of the two models qualitatively corresponded to each other remarkably well, in terms of h- and θ-structures. Thus, the similarity of apparent effects of subgrid-scale processes parameterized by the two different approaches seemed to be well demonstrated. A noticeable difference was the locations of the cool-air pool in the cross sections - in the case of M4 it was pushed halfway up the windward slope of the hill, while in the L7 results it stayed in the bottom of the upwind basin.

The wind structures within the PBL of L7 as revealed by the cross section also indicated that the assumption of vertically well-mixed momentum at a given location seemed feasible during the peak period of surface heating. The wind cross sections, however, seemed generally consistent with Whiteman's (1982) assertion that although there are close interrelationships between the wind- and

θ-structure evolutions, observed structures of winds over inhomogeneous terrain are much more variable than the θ-structures.

Another set of the cross sections of θ was obtained to examine the interrelationships between entrainment, mass-flux convergence and the growth of h. It seemed the patterns of w_e and mass-flux convergence in the case of M4 cooperated in generating a region of the highest $h + h_S$ in the early afternoon in the area downwind of the ridge where w_e was relatively strong but slightly upwind of the area in the valley of strongest mass-flux convergence.

The development of the PBL structure in these cross sections compared favorably to that of Banta (1984) who constructed by analyzing observed data idealized cross sections of the θ fields in the morning PBL to describe its evolution in a valley downstream of a ridge. According to Banta, a region of mass convergence and accompanying updrafts on the downwind slope of a mountain forms where upslope winds generated within the shallow morning mixed layer meet with convectively-mixed winds blowing down from the hilltop. In our experiments, however, due to uniformly imposed large-scale pressure-gradient forcing, upslope winds on the leeward slopes were not present in either experiments. However, an appreciable slowdown of low-level winds blowing down the leeward slope during the morning hours suggested that the above-mentioned process was probably in progress.

We may thus conclude that despite drawbacks inherent in either model, the formation of a region of mass-flux convergence and accompanying updrafts to the lee of a ridge, processes which are likely to be important in cloud initiation that may lead to

precipitation, seemed to be simulated using the M4 model as well as the L7 model.

7.2 Suggestions for Future Studies

We have found in this research that the overall agreement between the results from the M4 and L7 models is fairly good and some of meso-β scale features were realized under simple conditions specified for the experiments. However, it does not guarantee the models' capability of simulating correctly various mesoscale phenomena under different conditions. The models must be tested against observed data and their performances evaluated in order to be useful in real applications. For this purpose, many of the features that will be discussed below in this section need to be implemented.

Inclusion of detrainment processes at the mixed-layer top of the M4 model, which would enable the model to deal with late-afternoon and nighttime situations, is needed in order that meaningful integrations longer than one daytime period can be carried out and the results can be compared to those of the L7 model. Incorporation of basic processes dealing with moisture is also essential in the future versions of either model. This would be particularly useful in simulations of processes that may lead to terrain-induced convection associated with a mass convergence zone on the lee of a mountain.

The apparent insensitivity of surface heat flux H_S to variations of wind speed in the lowest layer in either model should be checked against observed data. Moreover, in the M4 model wind

speeds used in the aerodynamic formulation of H_S was calculated at the height level which grew as high as 1 km above the surface. The vertically well-mixed assumption of momentum through such a great depth is less likely to be valid even during the peak period of turbulent mixing, and it seems necessary to find a way to obtain the values of resolvable variables near the surface. To some extent, such consideration should also be applied to potential temperature of air used in the calculations of H_S.

The earth's surface temperature also seems to require an improved treatment for better predictions of H_S. The use of a predictive form of the energy balance equation should be considered, along with a more realistic specification of the horizontally variable roughness parameter in terms of vegetation and surface type over a real terrain. Implementation of a simple soil-air model should also be included in the long-range development plan for a mesoscale model.

Both the M4 and L7 models currently assume cyclic lateral boundary conditions on east-west as well as north-south boundaries. In reality, such infinite repetition of the identical topographic features has limited real application. Therefore, open boundary conditions such as those proposed by Ross and Orlanski (1982), which use the "C" grid, should be implemented. It is also suggested that an expanded model domain be used so that phenomena of larger scale which would influence mesoscale features of our interest can be treated. The current models can accommodate phenomena of wavelengths only up to ~200 km.

Although it seemed that perturbations reaching the free surface

of the model atmosphere placed at 400 mb in the current experiments
were small, the importance of pressure adjustment aloft for the
boundary-layer structure was demonstrated by Anthes et al. (1980).
Therefore, it would be desirable to use a deeper model atmosphere,
along with the possible adoption of a non-reflective top boundary
condition, such as that presented by Klemp and Duran (1982), in
future versions.

One of the most serious shortcomings of the M4 model is that it
seems unable to deal with situations in which the mixed-layer top is
intercepted by a mountain top. An example illustrating this
situation is the early-morning boundary layer capped by a flat
inversion which forms in mountainous regions under calm conditions.
This difficulty severely limits the scope of realistic applications
of the M4 model to situations in which either the boundary layer is
relatively deep or terrain irregularities are relatively small. In
order to overcome this deficiency the flux parameterization scheme
at the mixed-layer top must be modified so as to prevent
hydraulic-jump-like phenomena from occurring. Modifications of the
finite-difference scheme should be also useful for this purpose.

As a way to obtain values of resolvable quantities near the
surface needed for calculations of surface fluxes in the M4 model,
it is suggested to study the feasibility of developing a "hybrid"
model in which the mixed layer in the M4 model is further divided
into several layers while all the other features of M4 are
retained. Below the top of the boundary layer in this model,
however, the use of the eddy-difusivity approach is needed to
describe the flux exchanges between layers as in the L7 model. The

thickness of individual layers still increases as the boundary layer grows in height, but the vertical structure of the latter can be expected to be resolved as well as in the L7 model while maintaining an advantage of the M4 model that the height of the boundary-layer top can be explicitly obtained. The basic vertical differencing scheme of this hybrid model has already been developed and further testing of the model properties is needed before assessing the usefulness of adopting this approach in mesoscale modeling.

REFERENCES

Allard, H., and J. Derome, 1974: The adjustment of the wind field to small scale topography in a numerical weather prediction model. Atmosphere, 12, 106-117.

Andre, A. C., 1982: Parameterization schemes for the planetary boundary layer - A review and some general remarks. Workshop on the Planetary Boundary Layer Parameterization, European Centre for Medium-Range Weather Forecasts, 15-34, 260 pp.

Anthes, R. A., 1980: Boundary layers in numerical weather prediction. Workshop on the Planetary Boundary Layer, Wyngaad, Ed., Amer. Meteor. Soc., Boston, 247-279, 322 pp.

Anthes, R. A., and T. T. Warner, 1974: Prediction of mesoscale flows over complex terrain, Tech. Rep., ECOM-5532, U.S. Army Electronics Command, White Sands Missile Range, New Mexico, 101 pp.

Anthes, R. A., and T. T. Warner, 1978: Development of hydrodynamic model suitable for air pollution and other meso-meteorological studies. Mon. Wea. Rev., 106, 1045-1078.

Anthes, R. A., Seaman, N. L., and Warner, T. T., 1980: Comparisons of numerical simulations of the planetary boundary layer by a mixed-layer and multi-level model. Mon. Wea. Rev., 108, 365-376.

Atwater, M. A., and P. Brown, Jr., 1974: Numerical calculation of the latitudinal variation of solar radiation for an atmosphere of varying opacity. J. Appl. Meteor., 13, 289-297.

Arakawa, A., 1966: Computational design for long-term numerical integration of the equation of fluid motion. Part I. J. Comput. Phys., 1, 119-143.

Arakawa, A., 1972: Design of the UCLA general circulation model. Tech. Rept. No. 7, Dept. of Meteorology, Univ. of Calif., Los Angeles, 116 pp.

Arakawa, A., and V. R. Lamb, 1977: Computational design of the basic dynamical process of the UCLA general circulation model. Methods in Computational Physics, Vol. 17, Academic Press, 173-265.

Arakawa, A., and V. R. Lamb, 1981: A potential enstrophy and energy conserving scheme for the shallow water equations. Mon. Wea. Rev., 109, 18-36.

Arakawa, A., and M. J. Suarez, 1983: Vertical differencing of the primitive equations in sigma coordinates. J. Mon. Wea. Rev., 111, 34-45.

Arya, S. P. S., and A. Sundararajan, 1976: An assessment of proposed similarity theories for the atmospheric boundary layer. Bound.-Layer Meteor., 10, 149-166.

Baker, E. H., and T. L. Baxter, 1975: A note on the computation of atmospheric surface layer fluxes for use in numerical modeling. J. Appl. Meteor., 14, 620-622.

Banta, R. M., 1984: Daytime boundary-layer evolution over mountainous terrain. Part I: Observation of the dry circulations. Mon. Wea. Rev., 112, 340-356.

Banta, R. M., and W. R. Cotton, 1981: An analysis of the structure of local wind systems in a broad mountain basin. J. Appl. Meteor., 20, 1255-1266.

Bhumralkar, C. M., 1975: Numerical experiments on the computation of ground surface temperature in an atmospheric general circulation model. J. Appl. Meteor., 14, 1246-1258.

Bhumralkar, C. M., 1976: Parameterization of the planetary boundary layer in atmospheric general circulation models. Rev. Geophys. Space Phys., 14, 2, 215-226.

Blackadar, A. K., 1957: Boundary layer wind maxima and their significance for the growth of nocturnal inversions. Bull. Amer. Met. Soc., 38, 283-290.

Blackadar, A. K., 1962: The vertical distribution of wind and turbulent exchange in a neutral atmosphere. J. Geophys. Res., 67, 3095-3102.

Blackadar, A. K., 1979: High-resolution models of the planetary boundary layer. Advances in Environmental Science and Engineering, Vol. 1, Gordon and Breach Science Publishers, 51-85.

Bongeault, P., 1983: A non-reflective upper boundary condition for limited-height hydrostatic models. Mon. Wea. Rev., 111, 420-429.

Bornstein, R. D., 1975: The two-dimensional URBMET urban boundary layer model. J. Appl. Meteor., 14, 1459-1477.

Brown, R. A., 1970: A secondary flow model for the planetary boundary layer. J. Atmos. Sci., 27, 742-757.

Brutsaert, W., 1982: Vertical flux of moisture and heat at a bare soil surface. Land Surface Processes in Atmospheric General Circulation Models, Cambridge Univ. Press, 115-168, 560 pp.

Buajitti, K., and A. K. Blackadar, 1957: Theoretical studies of diurnal wind-structure variations in the planetary layer. Quart. J. Roy. Meteor. Soc., 83, 486-500.

Burk, S. D., and D. O. Staley, 1979: Comments "On the rotation rate of the direction of the sea and land breezes." J. Atmos. Sci., 36, 369-371.

Busch, N. E., S. W. Chang and R. A. Anthes, 1976: A multi-level model of the planetary boundary layer for use with mesoscale dynamic models. J. Appl. Meteor., 15, 909-919.

Businger, J. A., J. C. Wyngaard, Y. Izumi and E. F. Bradly, 1971: Flux profile relationships in the atmospheric surface layer. J. Atmos. Sci., 28, 181-189.

Businger, J. A., 1973: Turbulent transfer in the atmospheric surface layer. Workshop in Micrometeorology, American Meteorological Society, 67-100, 392pp.

Burridge, D. M., 1980: Some aspects of large-scale numerical modelling of the atmosphere. Proc. Seminar 1979, Vol. 2, Dynamical Meteorology and Numerical Weather Prediction, European Centre for Medium-Range Weather Forecasts, 3-78, 260 pp.

Camerlengo, A. L., and J. J. O'Brien, 1980: Open boundary conditions in rotating fluid. J. Comput. Phys., 35, 12-35.

Camuffo, D. and A. Bernardi, 1982: An observational study of heat fluxes and their relationships with net radiation. Bound.-Layer Meteor., 23, 359-368.

Carpenter, K. M., 1979: An experimental forecast using a nonhydrostatic mesoscale model. Quart. J. Roy. Meteor. Soc., 105, 629-655.

Carson, D. J., 1973: The development of a dry inversion-capped convectively unstable boundary layer. Quart. J. Roy. Meteor. Soc., 99, 450-467.

Carson, D. J., and F. B. Smith, 1973: The Leipzig wind profile and the boundary layer wind-stress relationship. Quart. J. Roy. Meteor. Soc., 99, 171-177.

Carson, D. J., and P. J. R. Richards, 1978: Modelling surface turbulent fluxes in stable conditions. Bound.-Layer Meteor., 14, 67-81.

Chang, S. W., 1981: Test of a planetary boundary-layer parameterization based on a generalized similarity theory in tropical cyclone models. Mon. Wea. Rev., 109, 843-853.

Chorley, L. G., S. J. Caughey and C. J. Readings, 1975: The development of the atmospheric boundary layer: Three case studies. Meteor. Mag., 104, 349-360.

Clark, T. L., and R. Gall, 1982: Three-dimensional numerical model simulations of airflow over mountainous terrain: a comparison with observations. Mon. Wea. Rev., 110, 766-791.

Clarke, R. H., 1974: Attempts to simulate the diurnal course of meteorological variables in the boundary layer. Izv. Atmos. Ocean. Phys., 10, 600-612.

Clarke, R. H., A. J. Dyer, R. R. Brook, D. G. Reid and A. J. Troup, 1971: The Wangara experiment: Boundary layer data. Tech. Paper, No. 19, CSIRO Australia, Division of Meteorological Physics.

Corby, G. A., A. Gilchrist and R. L. Newson, 1972: A general circulation model of the atmosphere suitable for long period integrations. Quart. J. Roy. Meteor. Soc., 98, 809-832.

Cullen, M. J. P., 1977: The application of finite element methods to the primitive equations of fluid motion. Finite Elements in Water Resources. Gary, Pinder and Brebbia, Eds., Pentech Press, London (pp. 4.231-4.246).

Deardorff, J. W., 1966: The countergradient heat flux in the lower atmosphere and in the laboratory. J. Atmos. Sci., 23, 503-506.

Deardorff, J. W., 1968: Dependence of air-sea transfer coefficients on bulk stability. J. Geophys. Res., 73, 2549-2557.

Deardorff, J. W., 1972: Parameterization of planetary boundary layer for use in general circulation models. Mon. Wea. Rev., 100, 93-106.

Deardorff, J. W., 1973: An explanation of anomalously large Reynolds stresses within the convective planetary boundary layer. J. Atmos. Sci., 30, 1070-1076.

Deardorff, J. W., 1974: Three-dimensional study of the height and mean structure of a heated planetary boundary layer. Bound.-Layer Meteor., 7, 81-106.

Deardorff, J. W., 1978: Efficient prediction of ground surface temperature and moisture, with inclusion of a layer of vegetation. J. Geophys. Res., 83, No. C4, 1889-1903.

Deardorff, J. W., G. E. Willis and B. H. Stockton, 1980: Laboratory study of the entrainment zone of a convectively mixed layer. J. Fluid Mech., 100, 41-64.

Deardorff, J. W., K. Ueyoshi and Y-J. Han, 1984: Numerical study of terrain-induced mesoscale motions and hydrostatic form drag in a heated, growing mixed layer. J. Atmos. Sci., 41, 1420-1441.

Deaven, D. G., 1976: A solution for boundary problems in isentropic coordinate models. J. Atmos. Sci., 33, 1702-1713.

DeHeer-Amissah, A., U. Hogstrom and A. S. Smedman-Hogstrom, 1981: Calculation of sensible and latent heat fluxes, and surface resistance from profile data. Bound.-Layer Meteor., 20, 35-49.

Driedonks, A. G. M., 1982: Sensitivity analysis of the equations for a convective mixed layer. Bound.-Layer Meteor., 22, 475-480.

Driedonks, A. G. M., and H. Tennekes, 1981: Parameterization of the atmospheric boundary layer in large-scale models. Bull. Amer. Met. Soc., 62, 594-598.

Dyer, A. J., 1974: A review of flux-profile relationships. Bound.-Layer Meteor., 7, 363-372.

Dyer, A. J., and B. B. Hicks, 1970: Flux-gradient relationships in the constant flux layer. Quart. J. Roy. Meteor. Soc., 96, 715-721.

ECMWF, 1982: Workshop on Planetary Boundary Layer Parameterization. 25-27 Nov. 1981. European Centre for Medium Range Weather Forecasts. 1-13, 260 pp.

Fairweather, G., and I. M. Navon, 1980: A linear ADI method for the shallow-water equations. J. Comput. Phys., 37, 1-18.

Fjortoft, R., 1953: On the changes in the spectral distribution of kinetic energy for two-dimensional, nondivergent flow. Tellus, 5, 225-230.

Fosberg, M. A., and M. J. Schroeder, 1966: Marine air penetration in central California. J. Appl. Meteor., 5, 573-589.

Fuchs, M., and A. Hadas, 1972: The heat flux density in a non-homogeneous bare loessial soil. Bound.-Layer Meteor., 3, 191-200.

Gadd, A. J., and J. F. Keers, 1970: Surface exchanges of sensible and latent heat in a 10-level model atmosphere. Quart. J. Roy. Meteor. Soc., 96, 297-308.

Gates, W. L., E. S. Batten, A. B. Kahle and A. B. Nelson, 1971: A documentation of the Mintz-Arakawa two-level atmospheric general circulation model. Rep. R-877-ARPA, The Rand Corporation, Santa Monica, Calif., 408 pp.

Garrett, J. R., 1978: Flux profile relations above tall vegetation. Quart. J. Roy. Meteor. Soc., 104, 199-211.

Gary, J. M., 1973: Estimate of truncation error in transformed coordinate, primitive equation atmospheric models. J. Atmos. Sci., 30, 223-233.

Gerrity, J. P., R. D. McPherson and P. D. Polger, 1972: On the efficient reduction of truncation error in numerical weather prediction model. Mon. Wea. Rev., 100, 637-643.

Ghan, S. J., J. W. Lingaas, M. E. Schlesinger, R. L. Mobley and W. L. Gates, 1982: A documentation of the OSU two-level atmospheric general circulation model. Report No. 35, Oregon State University, Corvallis, Oregon.

Gustafsson, B., 1971: An alternating direction implicit method for solving the shallow-water equation. J. Comput. Phys., 7, 239-254.

Grammeltvedt, A., 1969: A survey of finite difference schemes for a bartropic fluid. Mon. Wea. Rev., 97, 384-404.

Han, Y.-J., K. Ueyoshi and J. W. Deardorff, 1982: Numerical study of terrain-induced mesoscale motions in a mixed layer. J. Atmos. Sci., 39, 2464-2476.

Haurwitz, B., 1947: Comments on the sea-breeze circulation. J. Meteor., 4, 1-8.

Hicks, B. B., 1976: Wind profile relationship from the "Wangara" experiment. Quart. J. Roy. Meteor. Soc., 102, 535-551.

Hocevar, A., and J. D. Martsolf, 1971: Temperature distribution under radiation frost conditions in a central Pennsylvania valley. Agric. Meteor., 8, 371-383.

Hollingsworth, A., P. Kallberg, V. Renner and D. M. Burridge, 1983: An internal symmetric computational instability. J. Quart. Met. Soc., 109, 417-428.

Houghton, D. D., and E. Isaacson, 1970: Mountain winds. Studies in numerical analysis, 2, SIAM Publi., Philadelphia, 21-52.

Houghton, D. D., and A. Kasahara, 1968: Nonlinear shallow fluid over an isolated ridge. Commu. Pure Appl. Math., 21, 1-23.

Idso, S. B., J. K. Aase and R. D. Jackson, 1975: Net radiation-soil heat flux relations as influenced by soil water content variations. Bound.-Layer Meteor., 9, 113-122.

Isaacson, E., and H. B. Keller, 1966: Analysis of numerical methods. Wiley, New York, 541 pp.

Janjic, Z. I., 1977: Pressure gradient force and advection scheme used for forecasting with steep and small scale topography, Contr. Atmos. Phys., 50, 186-199.

Kalnay de Rivas, E., 1972: On the use of nonuniform grids in finite-difference equations. J. Comp. Phys., 10, 202-210.

Kaplan, M. L., J. W. Zack, V. C. Wang and J. J. Tuccillo, 1982: Initial results from a mesoscale atmospheric simulation system and comparisons with the AVE-SEASAME I data set. Mon. Wea. Rev., 110, 1565-1590.

Keyser, D., and Anthes, R. A., 1977: The applicability of a mixed-layer model of the planetary boundary layer to real-data forecasting. Mon. Wea. Rev., 105, 1351-1371.

Klemp, J. B., and D. R. Durran, 1983: An upper boundary condition permitting internal gravity wave radiation in numerical mesoscale models, Mon. Wea. Rev., 111, 430-444.

Klemp, J. B., and D. K. Lilly, 1978: Numerical simulation of hydrostatic mountain waves. J. Atmos. Sci., 35, 78-107.

Kondo, J., O. Kanechika and N. Yasuda, 1978: Heat and momentum transfers under strong stability in the atmosphere. J. Atmos. Sci., 35, 1012-1021.

Kondratyev, J., 1969: Radiation in the Atmosphere. Academic Press, New York, 342-335, 912 pp.

Kusuda, M., and P. Alpert, 1983: Anti-clockwise rotation of the wind hodograph. Part I: Theoretical study. J. Atmos. Sci., 40, 487-498.

Lavoie, R. L., 1972: A mesoscale numerical model of lake-effect storms. J. Atmos. Sci., 29, 1025-1040.

Lavoie, R. L., 1974: A numerical model of trade wind weather over Oahu. Mon. Wea. Rev., 102, 630-637.

Lenschow, D. H., B. B. Stankov and L. Mahrt, 1979: The rapid morning boundary-layer transition. J. Atmos. Sci., 36, 2108-2124.

Lettau, H. H., and B. Davidson, 1957: Exploring the Atmosphere's First Mile. 2 Volumes, Pergamon Press, New York, 577 pp.

Lilly, D. K., 1965: On the computational stability of numerical solutions of time-dependent non-linear geophysical fluid dynamics problems. Mon. Wea. Rev., 93, 11-26.

Lilly, D. K., 1968: Models of cloud-topped mixed layers under a strong inversion. Quart. J. Roy. Meteor. Soc., 94, 292-309.

Louis, J. F., 1979: A parametric model of vertical eddy fluxes in the atmosphere. Bound.-Layer Meteor., 17, 187-202.

Louis, J. F., M. Tiedtke and J. F. Geleyn, 1982: A short history of the operational planetary boundary layer parameterization at ECMWF. Workshop on Planetary Boundary Layer Parameterization, European Centre for Medium Range Weather Forecasts, 59-79, 260 pp.

Magono, C., and C. Nakamura, 1982: Nocturnal cooling of the Moshiri Basin, Hokkaido in Midwinter. J. Meteor. Soc. Japan, 60, 1106-1116.

Mahrer, Y., and R. A. Pielke, 1975: A numerical study of the air flow over mountains using the two-dimensional version of the University of Virginia mesoscale model. J. Atmos. Sci., 32, 2144-2155.

Mahrer, Y., and R. A. Pielke, 1976: Numerical simulation of the air flow over Barbados. Mon. Wea. Rev., 104, 1392-1402.

Mahrer, Y., and R. A. Pielke, 1977a: A numerical study of the airflow over the irregular terrain. Contr. Atmos. Phys., 50, 98-113.

Mahrer, Y., and R. A. Pielke, 1977b: The effects of topography on the sea and land breezes in a two dimensional numerical model. Mon. Wea. Rev., 105, 1151-1162.

Mahrer, Y., and R. A. Pielke, 1978: A test of an upstream spline interpolation technique for the advective terms in a numerical mesoscale model. Mon. Wea. Rev., 106, 818-830.

Mahrt, L., and D. H. Lenschow, 1976: Growth dynamics of the convective mixed layer. J. Atmos. Sci., 33, 41-51.

Mahrt, L., J. C. Andre and R. C. Heald, 1982: On the depth of the nocturnal boundary layer. J. Appl. Meteor., 21, 90-92.

Malcher, J. M., and H. Kraus, 1983: Low-level jet phenomena described by an integrated dynamical PBL model. Bound.-Layer Meteor., 27, 327-343.

Manabe, S., D. H. Hahn and J. L. Holloway, Jr., 1974: The seasonal
          variation of the tropical circulation as simulated by a
          global model of the atmosphere. J. Atmos. Sci., 31,
          43-83.

Mandelbrot, B. B., 1975: Stochastic models for the earth's relief,
          the shape and the fractal dimension of the coastlines, and
          the number-area rule for islands. Proc. Nat. Acad. Sci.
          USA, 72, No. 10, 3825-3828.

Mannouji, N., 1982: A numerical experiment on the mountain and
          valley winds. J. Meteor. Soc. Japan, 60, 1085-1105.

Mass, C., 1982: The topographically forced diurnal circulation of
          western Washington State and their influence on
          precipitation. Mon. Wea. Rev., 110, 170-183.

McDonald, J., 1960: Direct absorption of solar radiation by
          atmospheric water vapor. J. Meteor., 17, 319-328.

Melgarejo, J. W., and J. W. Deardorff, 1974: Stability functions
          for the boundary-layer resistance laws based upon observed
          boundary-layer heights. J. Atmos. Sci, 31, 1324-1333.

Mesinger, F., 1982: Estimate of truncation error problems of the
          calculation of the pressure gradient force in sigma
          coordinate models. Geophys. Astrophys. Fluid Dynamics,
          19, 105-117.

Mesinger, F., and A. Arakawa, 1976: Numerical methods used in
          atmospheric models. GARP publication series, No. 17,
          Vol. 1, WMO/ICSU Joint Organizing Committee, Geneva,
          64 pp.

Miyakoda, K., and J. Sirutis, 1977: Comparative integrations of
          global models with various parameterized processes of
          subgrid vertical transports: Description of the
          parameterizations. Contr. Atmos. Phys., 50, 445-487.

Monin, A. S., and A. M. Obukhov, 1954: Basic laws of turbulent
          mixing in the atmosphere near the ground. Tr. Nauk SSSR
          Geofiz. Inst., No. 24 (51), 163-187.

Nakamura, H., 1978: Dynamical effects of mountains on the general
          circulation of the atmosphere: I. Development of
          finite-difference schemes suitable for incorporating
          mountains. J. Meteor. Soc. Japan, 56, 317-340.

Navon, I. M., and H. A. Riphagen, 1979: An implicit compact
          fourth-order algorithm for solving the shallow-water
          equations in conservation-law form. Mon. Wea. Rev., 107,
          1107-1127.

Nickerson, E. C., 1979: On the numerical simulation of airflow and clouds over mountainous terrain. <u>Contr</u>. <u>Atmos</u>. <u>Phys</u>., <u>52</u>, 161-177.

Nickerson, E. C., and V. E. Smiley, 1975: Surface layer and energy budget parameterizations for mesoscale models. <u>J</u>. <u>Appl</u>. <u>Meteor</u>., <u>14</u>, 297-300.

O'Brien, J. J., 1970: A note on the vertical structure of the eddy exchange coefficient in the planetary boundary layer. <u>J</u>. <u>Atmos</u>. <u>Sci</u>., <u>27</u>, 1213-1215.

Orlanski, I., 1975: A rational subdivision of scales for atmospheric processes. <u>Bull</u>. <u>Amer</u>. <u>Met</u>. <u>Soc</u>., <u>56</u>, 527-530.

Orlanski, I., 1976: A simple boundary conditions for unbounded hyperbolic flows. <u>J</u>. <u>Comput</u>. <u>Phys</u>., <u>21</u>, 251-269.

Paegle, J., W. G. Zdunkowski and R. M. Welch, 1976: Implicit differencing of primitive equations of the boundary layer. <u>Mon</u>. <u>Wea</u>. <u>Rev</u>., <u>104</u>, 1321-1324.

Paulson, C. A., 1970: The mathematical representation of wind speed and temperature profiles in the unstable atmospheric surface layer. <u>J</u>. <u>Appl</u>. <u>Meteor</u>., <u>9</u>, 857-861.

Phillips, N. A., 1957: A coordinate system having some special advantages for numerical forecasting. <u>J</u>. <u>Meteor</u>., <u>14</u>, 184-185.

Phillips, N. A., 1959: An example of non-linear computational instability. <u>The Atmosphere and the Sea in Motion</u>, Rossby Memorial Volume, Rockefeller Institute Press, 501-504, 509 pp.

Phillips, N. A., 1974: Application of Arakawa's energy conserving layer model to operational weather prediction. NMC Note No. 104, U.S. Dept. of Commerce, 40 pp.

Pielke, R. A., 1973: A three dimensional numerical model of the sea breezes over south Florida. Ph.D. dissertation, The Pennsylvania State University, 135 pp.

Pielke, R. A., 1981: Mesoscale numerical modeling. <u>Advances in Geophysics</u>, Vol. 23, Academic Press, 186-344.

Pielke, R. A., and Y. Mahrer, 1975: Technique to represent the heated-planetary boundary layer in mesoscale models with coarse vertical resolution. <u>J</u>. <u>Atmos</u>. <u>Sci</u>., <u>32</u>, 2288-2308.

Raddatz, R. L., and M. L. Khanderkar, 1979: Upslope enhanced extreme rainfall events over the Canadian western plains: A mesoscale numerical simulation. Mon. Wea. Rev., 107, 650-661.

Randall, D. A., 1982: Performance of the PBL parameterizations in the GLAS and UCLA models. Workshop on Planetary Boundary Layer Parameterization, European Centre for Medium Range Weather Forecasts, 81-117, 260 pp.

Richtmyer, R. D., and K. W. Morton, 1967: Difference methods for initial value problems. Interscience, New York, 405 pp.

Ross, B. B., and I. Orlanski, 1982: The evolution of an observed cold front. Part I: Numerical simulation. J. Atmos. Sci., 39, 296-327.

Sadourny, R., 1975: The dynamics of finite-difference models of the shallow-water equations. J. Atmos. Sci., 32, 680-689.

Schlesinger, M. E., J.-T. Chang and C.-S. Hwang, 1981: Development of an improved version of the OSU two-level atmospheric general circulation model. A proposal for research on the dynamics of climate, 1 March 1982-28 February 1985. The Climatic Research Institute, Oregon State University, Corvallis, G1-G16.

Smith, F. B., and D. J. Carson, 1977: Some thoughts on the specification of the boundary layer relevant to numerical modelling. Bound.-Layer Meteor., 12, 307-330.

Staley, D. O., 1959: The low-level sea breeze of northwest Washington. J. Meteor., 16, 364-370.

Stull, R. B., 1973: Inversion rise model based on penetrative convection. J. Atmos. Sci., 31, 1324-1333.

Stull, R. B., 1976: Mixed-layer depth model based on turbulent energetics. J. Atmos. Sci., 33, 1268-1099.

Suarez, M. J., and A. Arakawa, 1979: Description and preliminary results of the 9-level UCLA general circulation model. Fourth Conf. on Numerical Weather Prediction. Silver Spring, Amer. Meteor. Soc., 290-297.

Suarez, M. J., A. Arakawa and D. A. Randall, 1983: The parameterization of the planetary boundary layer in the UCLA general circulation model: Formulation and results. Mon. Wea. Rev., 111, 2224-2243.

Sundqvist, H., 1975: On truncation errors in sigma-system models. Atmosphere, 13, 81-95.

Swinbank, W. C., 1970: Structure of wind and the shearing stress in the planetary boundary layer. Arch. Met. Geophys., Ser. A, 19, 1-12.

Tennekes, H., 1973: A model for the dynamics of the inversion above a convective boundary layer. J. Atmos. Sci., 30, 558-567.

Tennekes, H., and A. G. M. Driedonks, 1981: Basic entrainment equations for the atmospheric boundary layer. Bound.-Layer Meteor., 20, 515-531.

Thrope, A. J., and T. H. Guymer, 1977: The nocturnal jet. Quart. J. Roy. Meteor. Soc., 103, 633-653.

Tiedtke, M., J. F. Geleyn, A. Hollingworth and J. F. Louis, 1979: ECMWF model - Parameterization of sub-grid scale processes. Tech. Rept. No. 10, European Centre for Medium Range Weather Forecasts, 46 pp.

Tomine, K., and S. Abe, 1982: A trial to reduce truncation errors of the pressure gradient force in the sigma coordinate systems. J. Meteor. Soc. Japan, 60, 709-716.

Townsend, A. A., 1964: Natural convection in water over an ice surface. Quart. J. Roy. Meteor. Soc., 90, 248-259.

Warner, T. T., R. A. Anthes and A. L. McNab, 1978: Numerical simulations with a three-dimensional mesoscale model. Mon. Wea. Rev., 106, 1079-1099.

Washington, W. M., and D. L. Williamson, 1977: A description of the NCAR global circulation models. Methods in Computational Physics, Vol. 17, Academic Press, 111-172, 337 pp.

Whiteman, C. D., 1982: Breakup of temperature inversions in deep mountain valleys: Part I. Observations. J. Appl. Meteor., 21, 270-289.

Williamson, D., 1969: Numerical integration of fluid flow over triangular grids. Mon. Wea. Rev., 97, 885-895.

Yaglom, A. M., 1977: Comments on wind and temperature flux-profile relationships. Bound.-Layer Meteor., 11, 89-102.

Yamada, T., 1978: A three-dimensional numerical study of complex atmospheric circulations produced by terrain. Proc. Amer. Met. Soc. Conf. Sierra Nevada Meteor., 61-67.

Young, G. S., and Pielke, R. A., 1983: Application of terrain height variance spectra to mesoscale modelling. J. Atmos. Sci., 40, 2555-2560.